國立臺灣大學工學院土木工程學系

碩士論文

Department of Civil Engineering

College of Engineering

National Taiwan University

Master's Thesis

雙向地震下非對稱房屋結構的黏彈塑性分析

Viscoelastoplastic analysis of asymmetric building structures under bidirectional seismic excitation

陳政源

Cheng-Yuan Chen

指導教授: 劉立偉 博士

Advisor: Li-Wei Liu, Ph.D.

中華民國 113 年 7 月

July 2024

doi:10.6342/NTU202402645

doi:10.6342/NTU202402645

Acknowledgements

在就讀研究所的這兩年，首先我要衷心的感謝我的指導教授劉立偉教授。您對學術的熱情和嚴謹的態度，一直是我在研究這條路上的榜樣，當我研究上遭遇困難時，您總是隨時願意與我討論，並且不厭其煩的教導我，您的豐厚研究經驗使我在研究上少走了許多彎路，令我不斷進步並且獲得了許多寶貴的學術知識。您總是鼓勵我，給我許多的信心，使我在研究上不斷克服困難，並且堅信自己的研究是走在世界的頂端，我非常感謝您對我的關心與教導。

同時，我要感謝我的口試委員，蔡克銓講座教授、張家銘教授、陳東陽講座教授。你們的寶貴建議與指教，使本論文內容更加完善，並提供我後續研究的指引方向，令我受益良多。

謝謝 912 研究室的簡大哥、景諺、泊赫、泓瑋、豪哥、達哥、彭大哥、亦德，謝謝大家的陪伴，讓我度過了這段歡樂且難忘的時光，有你們的陪伴使我這兩年充滿了許多回憶。謝謝凱哥、禾哥、霖哥、吉米哥、日哥，在我還是剛進研究室的菜鳥時，就找我一起打遊戲、組模型、吃宵夜、做研究，使我很快的適應研究生的生活。

我也要謝謝我朋友們的陪伴，謝謝大學同學們總是邀約我一起出去玩、聚餐，使我可以適當的放鬆心情，並且在我研究遇到困難時給予幫助。謝謝在我就讀研究所期間陪伴並且鼓勵我的朋友們，你們的陪伴和鼓勵總是能使我的壓力得到釋

doi:10.6342/NTU202402645

放。

最後，我要感謝我的家人們。感謝爸爸和媽媽，讓我在求學的生涯中可以無所顧慮，並且給我無限的支持與鼓勵，使我可以專心的完成學業。也感謝所有給予我鼓勵的家人們，你們的鼓勵使我更有信心並且是我能堅持下去的重要動力。

doi:10.6342/NTU202402645

摘要

本研究旨在研究房屋結構在雙向地震作用下的受震反應，提出了一個非對稱房屋結構的黏彈塑性模式以分析其受震反應，此模式考慮兩向層間剪力（位移）與扭矩（扭角）的關係，包含：各向勁度不對稱、走動硬軟化、非等向降伏面與阻尼現象。為了要能夠精確計算出房屋結構的地震反應歷時，本研究使用狀態空間表示法，根據精確的判斷準則，將複雜的黏彈塑性動態系統細分為一個彈性項與多個塑性相動態系統，接著再針對每一相求解對應的房屋結構動態反應。本研究發現，在有樓層進入塑性態時，可以再進一步將計算塑性相動態系統反應分解成：先計算樓層塑性內變數，再計算整棟房屋的動態反應；並且發現模式具有李群（Lie group）和李代數 (Lie algebra) 的內在對稱性，因此可推得塑性內變數單步解析解，進而獲得整棟房屋的動態反應單步解析解。此計算方法也經由誤差分析，驗證其精確性。接下來，本研究根據提出之非對稱房屋結構黏彈塑性模式，考慮 921 集集地震事件全台灣所有地震測站歷時，分析房屋結構其受震後的反應。先以原始地震歷時分析比較單向地震分析及雙向地震分析之反應；接著經由計算出全台灣地震測站歷時所得之房屋塑性當量圖，以分析房屋結構的塑性損傷。此外，也進行地震力入射角對於房屋結構反應的影響；並且進行最大地表加速度分析探討房屋結構隨著譜加速度增加，其速度脈衝型地震與非速度脈衝型地震作用下的反應。研究結果顯示，房屋結構若以單向地震分析，確實相較雙向地震力分析有錯估的情勢；並且使用單向地震力分析建築結構時其塑性損傷會嚴重的低估，其

doi:10.6342/NTU202402645

總層間位移反應及總層間剪力反應平均來看也是相對低估，由此可知以雙向水平地震分析更能貼近房屋結構的受震情況。再者，經由地震力入射角分析也可以看出非對稱房屋對於地震力入射角之考量有一定的影響。此外，非對稱房屋結構經由最大地表加速度分析，顯示某些速度脈衝地震確實造成較大的房屋結構反應。

關鍵字：非對稱建築結構、黏彈塑性、雙向地震、內部對稱性

doi:10.6342/NTU202402645

Abstract

This study aims to investigate the seismic response of asymmetric building structures under bidirectional earthquake excitations. A viscoelastoplastic model of the building structures is proposed taking into account an anisotropic stiffness between the interstory two-directional shears, torque and the interstory two-directional displacement and rotation; a anisotropic yield surface; kinematic hardening and softening; and the damping effects. To accurately calculate the time history of seismic responses for asymmetric building structures, the conventional formulation of the model is rearranged; the state-space representation approach is employed; and the internal symmetry of the model is explored in this study. According to careful derivation about the switching of the plastic mechanism, the complex viscoelastoplastic dynamical system is decomposed into an viscoelastic phase and multiple viscoelastoplastic phases, and then the dynamical responses of the building structure for each part are solved separately. In each viscoelastoplastic phase, the response of the building is decomposed into two steps including the calcula-

doi:10.6342/NTU202402645

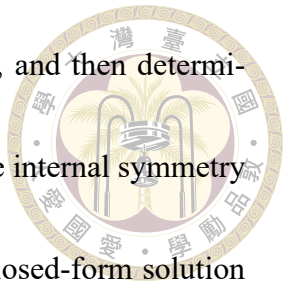

tion of the plastic internal variables based on the internal symmetry, and then determinate of the total responses via the state-space representation. Since the internal symmetry of the Lie group SO(3,1) and the Lie algebra so(3,1), provides the closed-form solution for the plastic internal variables in each single step, and consequently the closed-form response of the building structure in each single step is obtained. The accuracy of this calculation method is also verified through error analysis. Next, based on the proposed viscoelastoplastic model for asymmetric building structures and considering the ground motion time histories recorded at all seismic stations in Taiwan during the 1999 Chi-Chi earthquake event, the seismic responses of building structures were analyzed. First, the original ground motion time histories were used to compare the responses from unidirectional and bidirectional seismic analyses. Then, the plastic ductility demand contours for building structures in Taiwan were computed from the recorded ground motions to assess the plastic damage. Furthermore, the influence of the incidence angle of seismic excitations on the structural responses was investigated. A peak ground acceleration analysis was also performed to study the responses of building structures under velocity pulse-like and non-velocity pulse-like earthquakes as the peak ground acceleration increases. The results show that if building structures are analyzed using unidirectional seismic excitations, their responses would indeed be underestimated compared to those from bidirectional seis-

doi:10.6342/NTU202402645

mic analyses. The plastic damage would be severely underestimated when using unidirectional seismic analysis, and the total interstory drift and shear responses would also be underestimated on average. This indicates that bidirectional horizontal seismic analysis can better capture the actual seismic responses of building structures. Additionally, the analysis of the incidence angle of seismic excitations also reveals that the consideration of incidence angles has a certain influence on the responses of asymmetric building structures. Moreover, the peak ground acceleration analysis for asymmetric building structures shows that some velocity pulse-like earthquakes indeed cause larger structural responses.

Keywords: Asymmetric building structures, Viscoelastoplastic, Bidirectional earthquakes, Internal symmetry

doi:10.6342/NTU202402645

doi:10.6342/NTU202402645

Contents

doi:10.6342/NTU202402645

doi:10.6342/NTU202402645

doi:10.6342/NTU202402645

doi:10.6342/NTU202402645

doi:10.6342/NTU202402645

doi:10.6342/NTU202402645

List of Figures

doi:10.6342/NTU202402645

doi:10.6342/NTU202402645

doi:10.6342/NTU202402645

doi:10.6342/NTU202402645

doi:10.6342/NTU202402645

doi:10.6342/NTU202402645

doi:10.6342/NTU202402645

doi:10.6342/NTU202402645

doi:10.6342/NTU202402645

doi:10.6342/NTU202402645

doi:10.6342/NTU202402645

doi:10.6342/NTU202402645

List of Tables

doi:10.6342/NTU202402645

doi:10.6342/NTU202402645

Denotation

$\mathbf{q}$	Generalized displacement vector
$\mathbf{q}^e$	Generalized elastic displacement vector
$\mathbf{q}^p$	Generalized plastic displacement vector
$\mathbf{Q}$	Generalized force vector
$\mathbf{Q}^{EP}$	Generalized elastoplastic force vector
$\mathbf{Q}_a$	Generalized active force vector
$\mathbf{Q}_b$	Generalized back force vector
k_e	Generalized elastic stiffness
k_p	Generalized kinematic stiffness
Q_y	Interstory yielding shear force
$\dot{\lambda}$	Equivalent plastic strain rate
λ	Equivalent plastic strain rate

doi:10.6342/NTU202402645

f	Yield criteria
m_s	Mass of building structures
$\mathbf{F}$	External force vector
c	Damping coefficient
$\mathbf{P}_s$	Momentum vector
q_y	Yielding displacement
X_0	Integrating factor
$\mathbf{X}$	The augmented stress vector
$\mathbf{A}$	State matrix
$\mathbf{g}$	Minkoeski matrix
$\mathbf{G}$	State transition matrix
ξ	Damping ratio of building structures
$\mathbf{C}$	Damping coefficient matrix
$\mathbf{K}_e$	Generalized elastic stiffness matrix
$\mathbf{K}_p$	Generalized kinematic stiffness matrix
$\mathbf{m}_s$	Mass matrix
$\mathbf{Y}$	Yield matrix

doi:10.6342/NTU202402645

Chapter 1 Introduction

1.1 Motivation and objectives

The impact of seismic behavior on building structures has long been a focus and hotspot of research. With the frequent occurrence of earthquakes, seismic analysis of building structures has become particularly important. Currently, mainstream structural seismic analysis methods primarily rely on finite element software such as Etabs, SAP2000, Abaqus, and PISA3D. These software provide powerful tools for simulating the response of building structures under seismic actions. However, these methods usually require substantial computational resources, especially when performing nonlinear analysis, where the complexity of iterative calculations makes the analysis time-consuming. On the other hand the studies show that existing finite element methods, when dealing with structural behavior in the nonlinear stage, usually require setting plastic hinges to calculate the plastic behavior of the structure, and there has always been a lack of an accurate plasticity mechanics theoretical model to analyze the behavior of structures after entering the nonlinear stage. Moreover, traditional seismic analysis methods typically only consider unidirectional seismic forces, but actual seismic actions are multidirectional, making bidirectional seismic force analysis more consistent with real situations. However, the application of bidirectional seismic force analysis is relatively less common and computationally inten-

doi:10.6342/NTU202402645

sive, urgently requiring more effective analytical methods to address this issue. Against this background, this study proposes a three-component bilinear viscoelastic-plastic model to simulate asymmetric building structures, where the three components refer to bidirectional horizontal seismic forces and torsional moment. This model considers the influence of inertial forces by paralleling with viscous damping and connecting in series with mass elements, thereby simulating the seismic response of symmetric and asymmetric building structures. Based on the high-precision integration method of Lie group internal symmetry, the behavior of structures after entering the plastic stage can be solved without nonlinear iterations, ensuring that when structures enter the plastic stage under seismic action, the shear path remains on the yield surface. Using elastoplastic switching theory, the system is divided into two stages, and combined with incremental analysis methods and state-space representation to solve for the response of the building structure system. This model is not only accurate but also considers the coupling effects in bidirectional horizontal and torsional directions. Therefore, the motivation of this research is to address the issues of high computational cost and insufficient accuracy in existing methods for analyzing bidirectional seismic forces. The objectives is to propose a high-performance and high-precision model to accurately simulate the seismic response of building structures, considering multiple dimensions, and not only elastic but also viscoelastoplastic responses. This aims to provide theoretical foundations and practical guidance for seismic analysis.

doi:10.6342/NTU202402645

1.2 Literature review

1.2.1 General seismic analysis tools

The seismic behavior of building structures has been a widely studied and highly concerned topic. Currently, the mainstream methods for analyzing the seismic response of building structures are mainly based on finite element software, such as Etabs, SAP2000, Abaqus, PISA3D, and other finite element method software. Arvindreddy et al. [4], Divya et al. [10], Guleria et al. [13], and Rathod et al. [40] proposed using Etabs software to analyze the seismic behavior of building structures. Meanwhile, Abbas et al. [1], Ismaei et al. [21], and Yilmaz et al. [50] used SAP2000 software to analyze the behavior of building structures after seismic events. Genikomsou et al. [12] and Li et al. [25] used Abaqus software to analyze the seismic behavior of building structures. Lin et al. [27], Tsai et al. [47], and Lin et al. [26] used PISA3D software to analyze the seismic behavior of building structures. When calculating structural responses using finite element software, plastic hinges are usually set up to calculate the plastic behavior of the structure when its behavior enters the inelastic stage. Complex nonlinear iterations are required during analysis, with common methods including Newton's iteration method and the arc-length method. It is well known that nonlinear analysis requires a large amount of computational time.

1.2.2 Simplified analysis methods

The response of building structures under seismic forces has always been a popular research topic among scholars. Due to the large amount of computational time required

doi:10.6342/NTU202402645

for seismic dynamic analysis using common analysis software such as Etabs, SAP2000, and Abaqus, many simplified analysis methods have been proposed. Common methods include the capacity spectrum method proposed by ATC40 [8], which determines performance points through pushover analysis, and the nonlinear static pushover analysis method proposed by FEMA-356 [11], which links actual demand with capacity for response evaluation. Chopra et al. [6] also proposed a method based on modal pushover analysis to estimate the demand of buildings under seismic action. Although traditional static pushover analysis is simple, it is difficult to accurately consider higher-order modal effects and dynamic behavior. To address this issue, Chopra et al. combined pushover analysis with modal decomposition theory. By decomposing the system into multiple single-degree-of-freedom subsystems, performing pushover analysis separately, and finally superimposing modal responses to obtain overall demand estimation, this method achieved an acceptable error range in inelastic response. However, these pushover methods can only perform unidirectional pushover. For asymmetric building structures, Chopra et al. [7] extended their previous modal pushover analysis method to asymmetric structures. Lin et al. [28] also proposed a simplified 2D modal stick analysis method for evaluating the overall response of asymmetric buildings under seismic action. This method greatly reduces analysis complexity by introducing an equivalent single-degree-of-freedom model and applying pushover-torque relationship curves while considering coupling effects in horizontal and torsional directions.

1.2.3 Simplified model considering precise plastic behavior

Furthermore, when using finite element software to calculate structural responses as mentioned above, plastic hinges are usually set up to calculate the plastic behavior of the

doi:10.6342/NTU202402645

structure when its behavior enters the inelastic stage. The criteria commonly used for plastic analysis when members yield are Von Mises, Tresca yield criterion, and Drucker–Prager yield criterion, as mentioned in [51] and [36]. Therefore, many studies have also proposed accurate plasticity theory models to analyze the behavior of structures or materials after entering inelasticity. In the fields of materials, components, and even building structures, literature has gradually proposed using physical meaning models based on plasticity theory to calculate their responses. We know that plasticity theory is the most important foundation for all calculations. In describing material behavior, Prandt et al. [39], Ishlinsky et al. [20], Whiteman et al. [48], and Iwan et al. [22] all used parallel elastoplastic components to form plastic models for analyzing the elastoplastic behavior of materials.

The elastoplastic behavior of materials, components, or building structures is quite complex. Therefore, Hong et al. [14] proposed the elastoplastic switch theory, which explicitly distinguishes elastoplastic systems into elastic systems and plastic systems using yield conditions and strain conditions.

Hong et al. [16] proposed combining the fully elastoplastic model based on the concept of Lie group symmetry with Minkowski spacetime and the Lorentz group to solve for closed-form solutions of system responses. They also proposed closed-form solutions for bilinear elastoplastic models based on the concept of Lie group symmetry combined with Minkowski spacetime and the Lorentz group [15]. This is a high-precision algorithm that does not require nonlinear iteration and has exact solutions.

Liu et al. [31] proposed a high-precision numerical integration method based on Lie symmetry to solve for nonlinear behavior of systems. This method can avoid nonlinear

doi:10.6342/NTU202402645

iteration and has derived closed-form solutions. Based on this concept, Hong et al. [17] extended their material model to building structure models. This model is a three-degree-of-freedom static model, including two horizontal directions and one torsional direction, used to analyze the behavior of building structures under bidirectional lateral forces and torsion. The simplified plastic models proposed so far are limited to static analysis. However, the seismic behavior of building structures still needs to be analyzed through dynamic behavior to more accurately simulate the seismic response of building structures. Liu et al. [30] proposed a two-dimensional oscillator combining bilinear elastoplasticity and discussed the stability of oscillating systems under tuned loads. In addition, Liu et al. [32] proposed a two-dimensional friction model based on the concept of bilinear elastoplasticity to model the base friction isolation system of structures. Furthermore, Liu et al. [33] applied bilinear elastoplastic models and friction models to the modeling of functionally supported bridges, using bilinear elastoplastic models to model bridge piers and friction models to model functional supports.

1.2.4 State-space representation

When performing dynamic analysis, direct numerical analysis often encounters problems with overly complex mathematical expressions that are difficult to calculate numerically. Therefore, many studies have proposed using state-space representation for numerical solutions. This theory has been widely applied in many studies. Traditional vibration system solutions are obtained through direct numerical or theoretical solving of equations of motion, while Wang et al. [46] transferred the equations of motion to state space for numerical solutions. Xiong et al. [49] used state-space representation for numerical studies of isolated convex friction systems. Brewick et al. [5] applied state-space-based iden-

doi:10.6342/NTU202402645

tification to estimate nominal model parameters of structures under full-scale dynamic testing. State-space representation makes it easier for us to understand the relationship between input and output parameters.

As can be seen, by applying precise plasticity mechanics models combined with some mathematical methods, we can effectively solve system problems. We can apply this concept to the analysis of building structures.

1.2.5 Seismic analysis method

We have already introduced some tools for analysis above. First, we review some common seismic input methods for building structure seismic analysis. The most common is unidirectional seismic input, as mentioned by De et al. [9] and [28]. Some literature also proposes analysis using combined bidirectional earthquakes, the concept of which is to perform independent analysis in two directions for actual or synthetic bidirectional earthquakes, and then superimpose the results. Anastassiadis et al. [3] proposed performing independent pushover analysis in two directions and then combining responses using SRSS (Square Root of Sum of Squares) or CQC (Complete Quadratic Combination) methods. Next is bidirectional seismic analysis, which is direct analysis with simultaneous bidirectional input. Hong et al. [17] also proposed an accurate bilinear elastoplastic plasticity mechanics model considering bidirectional lateral forces and torque for simulating the static response of asymmetric building structures. Reyes et al. [41] further extended the modal pushover analysis method to three-dimensional cases, considering the influence of bidirectional seismic input and the coupling effects of different modes and two horizontal seismic components. Lin et al. [29] proposed a simplified 3D modal stick analysis method for studying buildings that are asymmetric in both plane and vertical directions un-

doi:10.6342/NTU202402645

der bidirectional seismic excitation, considering bidirectional horizontal earthquakes and torsional effects, and studying the influence of asymmetry on seismic response. Kim et al. [24] proposed a new three-dimensional model for simulating the mechanical behavior of reinforced concrete slab-beam-column components under bidirectional cyclic lateral forces. This model couples multiple components such as joint regions, beams, columns, and slabs, effectively capturing their interaction effects.

1.2.6 Unidirectional seismic analysis and bidirectional seismic analysis

Previous literature also mentioned that unidirectional seismic force analysis leads to serious misjudgments compared to bidirectional seismic force analysis. Magliulo et al. [35] studied the dynamic response of asymmetric three-dimensional reinforced concrete buildings under bidirectional seismic excitation. Traditional seismic analysis usually only considers unidirectional seismic input, ignoring the multi-directionality of actual seismic motions. Their three-dimensional building structure finite element model showed that bidirectional seismic excitation significantly increases displacement and internal force demands compared to unidirectional analysis, especially under eccentric torsional effects. Peruvs et al. [38] addressed the nonlinear torsional response problem of single-story structures under bidirectional excitation. When structures have stiffness center eccentricity, they developed a numerical model considering torsion-bending coupling effects based on plastic hinge theory to simulate the dynamic behavior of single-story structures under bidirectional seismic action. Results showed that traditional unidirectional analysis failed to capture torsional effects, greatly underestimating displacement demands and damage levels under bidirectional excitation. Sucuouglu et al. [44] proposed an interstory

doi:10.6342/NTU202402645

drift ratio-based scaling method for bidirectional earthquake motions. Traditional scaling methods usually only consider single-component earthquakes, ignoring the bidirectionality of seismic motions. This new method simultaneously scales both horizontal components of seismic motion, using target interstory drift ratios to ensure that the structure's interstory drift response is close to the expected design target in bidirectional cases. Acharjya et al. [2] explored the performance of using paired spectrum-compatible earthquake motions to estimate structural responses under bidirectional seismic excitation. Key findings include: using paired spectrum-compatible earthquake motions can more accurately predict bidirectional structural responses such as torsional effects and maximum strain/displacement, while using single spectrum-compatible earthquake motions may underestimate these responses, especially for plan-asymmetric structures. Bidirectional analysis is more time-consuming and computationally intensive compared to unidirectional analysis. Therefore, some literature proposes using unidirectional analysis to find the optimal bidirectional analysis response. Roy et al. [42] explored how to use unidirectional seismic analysis to estimate structural responses under bidirectional excitation, identifying a preferred seismic incidence angle. They proposed an angle identification method based on limit response, selecting the angle that produces the maximum response in unidirectional analysis as the preferred angle. By comparing a large number of unidirectional and bidirectional analysis results, they verified the effectiveness of this method in estimating limit responses (such as displacement and acceleration) under bidirectional excitation.

1.2.7 Effect of incident angle of seismic force

When actual seismic waves arrive, they may not necessarily pass through the main axis of the building structure, but rather enter from various angles of the building. There-

doi:10.6342/NTU202402645

fore, some literature also analyzes the incidence angle of seismic forces. As mentioned above, if unidirectional analysis is chosen to approximate bidirectional response, the incidence angle response is crucial. This also means that studying the influence of incidence angles in bidirectional seismic force analysis is a necessary research topic. Therefore, the literature also discusses the influence of seismic wave incidence angles. Hussain et al. [19] explored the impact of bidirectional seismic incidence angles on structural dynamic responses. In reality, seismic motions propagate at a certain angle along the horizontal plane, rather than simple orthogonal decomposition. The study conducted systematic parametric analysis on different types of structural models (such as shear walls and frames), inputting bidirectional seismic excitation with different incidence angles. The research found that changes in incidence angles significantly affect the maximum displacement and internal force demands of structures, and the degree of influence increases with increasing structural asymmetry. This finding emphasizes the importance of fully considering incidence angles in bidirectional seismic input analysis.

1.2.8 Influence of peak ground acceleration

Velocity pulse-type earthquakes have been a widely studied topic in past research, as mentioned by Luo et al.[34], Ji et al.[23], and Ruiz et al.[43]. Some studies have also proposed using peak ground acceleration (PGA) for parametric analysis to investigate structural responses. Tsai et al.[45] used near-fault earthquakes with varying PGA to conduct parametric analysis on friction pendulum bearing bridges, finding that the response increased with increasing PGA. Hsu et al.[18] used near-fault earthquakes with varying PGA to perform parametric analysis on bidirectionally coupled sliding bearing bridges, also observing a trend of increasing response with increasing PGA. Perrault et al.[37]

doi:10.6342/NTU202402645

analyzed relative roof displacement with respect to PGA, showing a trend of increasing relative roof displacement with increasing PGA. Therefore, this study will employ this method to attempt a parametric analysis of PGA for both velocity pulse and non-velocity pulse earthquake time histories, and investigate the seismic response of building structures to velocity pulse-type earthquakes.

1.3 Outlines

This thesis is divided into six chapters, structured as follows: Chapter 1: Briefly explains the motivation and purpose. It includes a literature review, first reviewing past methods of building structural analysis, then introducing the importance of bidirectional seismic analysis and the influence of incidence angles. Finally, it introduces the scope and organization of this thesis. Chapter 2: Proposes a two-component viscoelastoplastic model to simulate symmetric building structures, including model establishment, theoretical derivation, and algorithm. Chapter 3: Based on the two-component viscoelastoplastic model proposed in Chapter 2, conducts seismic analysis of symmetric building structures, comparing bidirectional and unidirectional earthquakes, analyzing the influence of incidence angles, calculating the distribution of plastic equivalents Taiwan under a 921 Chi-Chi earthquake event, and its impact on spectral acceleration. Chapter 4: Proposes a three-component viscoelastoplastic model to simulate asymmetric building structures, including model establishment, theoretical derivation, and algorithm. Chapter 5: Based on the three-component viscoelastoplastic model proposed in Chapter 4, conducts seismic analysis of asymmetric building structures, comparing bidirectional and unidirectional earthquakes, analyzing the influence of incidence angles, calculating the distribution of plastic equivalents Taiwan under a 921 Chi-Chi earthquake event, and its impact on spec-

doi:10.6342/NTU202402645

tral acceleration. Chapter 6: Conclusions and future works This chapter describes the research findings of this thesis and how to further expand and develop this research.

doi:10.6342/NTU202402645

Chapter 2 Mathematical modeling on symmetric building structure

In this study, we focus not only on the viscoelastic behavior of building structures but also on their viscoelastoplastic behavior. The spring component of the mechanical element we propose is a bilinear elastoplastic model that considers the same stiffness in different directions. In the symmetric building structure model, we consider bidirectional interstory displacement, and the building structure is subjected to seismic ground motion.

2.1 Bilinear viscoelastoplastic of a single-story in symmetric building structures

As previously mentioned, we will develop a bilinear viscoelastoplastic model to simulate the response of symmetric building structures. Here, we will detail how to establish a bilinear viscoelastoplastic model for a single-story asymmetric building structure. First, we can derive the equation of motion for symmetric building structure as follows:

$$m_s\ddot{\mathbf{q}} + \mathbf{Q} = \mathbf{F}. \tag{2.1}$$

doi:10.6342/NTU202402645

where

$$\mathbf{q} = \begin{bmatrix} q_1 \\ q_2 \\ q_3 \end{bmatrix},$$

$$\mathbf{Q} = \begin{bmatrix} Q_1 \\ Q_2 \\ Q_3 \end{bmatrix},$$

$$\mathbf{F} = \begin{bmatrix} F_1 \\ F_2 \\ F_3 \end{bmatrix},$$

Among these, m_s is the mass of the building structure. **q** is the generalized displacement, q_1 is the interstory displacement in the 1st direction, q_2 is the interstory displacement in the 2nd direction. **Q** is the generalized force, Q_1 is the interstory shear force in the 1st direction, Q_2 is the interstory shear force in the 2nd direction. **F** is the external force vector, F_1 is the external force in the 1st direction, F_2 is the external force in the 2nd direction.

The model proposed in this study considers not only elasticity but also elastoplasticity. For the elastoplastic part, we applied the bilinear elastoplastic model from plasticity theory to simulate the elastoplastic behavior of the building structure. The bilinear elastoplastic model consists of an elastic part and a plastic part. The elastic part is composed of an elastic spring, while the plastic part consists of a plastic spring and a yield switch.

doi:10.6342/NTU202402645

Therefore, we can decompose the generalized displacement $\mathbf{q}$ into two parts: elastic displacement $\mathbf{q}^e$ and plastic displacement $\mathbf{q}^p$. As mentioned earlier, the model proposed in this study also considers the contribution of viscosity. Thus, we use a viscous damper to simulate the inherent damping of the building structure. Combining the viscous damper in parallel with the bilinear elastoplastic model results in the viscoelastoplastic model. The composition of the generalized shear force includes the elastoplastic shear force contributed by the elastoplastic model and the viscous damping force. The elastoplastic shear force of the building structure $\mathbf{Q}^{EP}$ is decomposed as active shear force $\mathbf{Q}_a$, and back shear force $\mathbf{Q}_b$. Considering all of the above, we can establish the mechanical components as shown in Figure 2.1, and we can express the viscoelastoplastic model mathematically as follows:

$$\mathbf{q} = \mathbf{q}^e + \mathbf{q}^p, \tag{2.2}$$

$$\mathbf{Q} = \mathbf{Q}^{EP} + c\dot{\mathbf{q}}, \tag{2.3}$$

$$\mathbf{Q}^{EP} = \mathbf{Q}_a + \mathbf{Q}_b, \tag{2.4}$$

$$\mathbf{Q}^{EP} = k_e \mathbf{q}^e, \tag{2.5}$$

$$\dot{\mathbf{Q}}_b = k_p \dot{\mathbf{q}}^p, \tag{2.6}$$

$$Q_y \dot{\mathbf{q}}^p = \mathbf{Q}_a \dot{\lambda}, \tag{2.7}$$

doi:10.6342/NTU202402645

$$f\dot{\lambda} = 0, \tag{2.8}$$

$$f = \|\mathbf{Q}_a\| - Q_y \leq 0, \tag{2.9}$$

$$\dot{\lambda} \geq 0, \tag{2.10}$$

The Hooke's law of the elastic displacement is stated in Eq. (2.5) where the k_e is elastic stiffness of building structures. Eq. (2.7) shows the plastic flow rule which relates the plastic displacement rate $\dot{\mathbf{q}}^p$ with the active shear force $\mathbf{Q}_a$ multiplied by the rate of plastic equivalent $\dot{\lambda}$. The kinematic hardening rule in Eq. (2.6) describes the back shear force which is proportional to the rate of generalized plastic displacement where the k_p is kinematic-hardening stiffness. Eq. (2.8)- Eq. (2.10) are the complementary trios where Eq. (2.9) shows that the $||\mathbf{Q}_a||$ cannot exceed the yielding force Q_y, Eq. (2.10) means that the rate of plastic equivalent is non-negative, and the alternative condition Eq. (2.8) means that $f\dot{\lambda}$ must be zero for each case. Further, the bilinear elastoplastic model in

doi:10.6342/NTU202402645

Eq. (2.2)-Eq. (2.10) can be represented as a compact formulation as follows:

$$\dot{\mathbf{q}} = \frac{\dot{\mathbf{Q}}^{EP}}{k_e} + \dot{\mathbf{q}}^p, \tag{2.11}$$

$$\dot{\mathbf{Q}}_a = k_e\dot{\mathbf{q}} - (k_p + k_e)\dot{\mathbf{q}}^p, \tag{2.12}$$

$$\dot{\mathbf{Q}}_a = k_e\dot{\mathbf{q}} - (k_p + k_e)\frac{\dot{\lambda}}{Q_y}\mathbf{Q}_a, \tag{2.13}$$

$$Q_y\dot{\mathbf{q}}^p = \mathbf{Q}_a\dot{\lambda}, \tag{2.14}$$

$$f\dot{\lambda} = 0, \tag{2.15}$$

$$f = \|\mathbf{Q}_a\| - Q_y \leq 0, \tag{2.16}$$

$$\dot{\lambda} \geq 0. \tag{2.17}$$

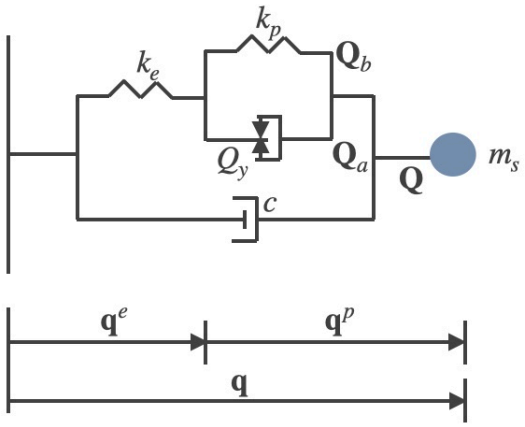

Figure 2.1: Mechanical element of the two-component symmetric building structure

2.2 The straining conditions and the sufficient and necessary conditions for the viscoelastoplastic model

In order to provide a more detailed description of the viscoelastoplastic behavior of this model, we refer to the associated plastic flow rules as shown in Eq. (2.7), and the

doi:10.6342/NTU202402645

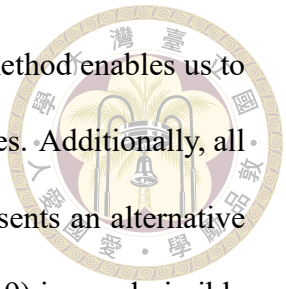

complementary trio, Eqs. (2.8) to Eq. (2.10) proposed in [14]. This method enables us to better describe the viscoelastoplastic behavior of the building structures. Additionally, all these conditions need to be simultaneously satisfied. Eq. (2.8) represents an alternative condition, meaning that either $f = 0$ or $\dot{\lambda} = 0$ can be chosen. Eq. (2.9) is an admissible condition, while Eq. (2.10) ensures non-negative dissipation, meaning that the system will not have dissipations with negative energy. The following is a theoretical derivation. To accurately determine the system's switching to judge whether the system is in a viscoelastic or viscoelastoplastic state, the core idea is to combine the complementary triad as a switching mechanism. When the yield condition $(f = 0)$ is satisfied, it leads to $\dot{f} = 0$, therefore we have

$$\dot{f} = \mathbf{Q}_a^{\mathrm{T}} \dot{\mathbf{Q}}_a = 0.$$

Substituting Eq. (2.13) into the above equations, we obtain:

$$(k_e + k_p)\dot{\lambda} = k_e \mathbf{Q}_a^{\mathrm{T}} \dot{\mathbf{q}}. \tag{2.18}$$

Since $\mathbf{Q}_a^{\mathrm{T}} \dot{\mathbf{q}} \geq 0$ for $\dot{\mathbf{q}} \neq 0$, Eq. (2.15) is satisfied and we can obtain the straining conditions $\dot{\lambda}$,

$$\dot{\lambda} = \frac{\beta}{Q_y} \mathbf{Q}_a^{\mathrm{T}} \dot{\mathbf{q}} > 0, \tag{2.19}$$

where $\beta = \frac{k_e}{k_e + k_p}$.

Therefore, we prove that,

$$\text{if} \quad f = 0 \quad \text{and} \quad \mathbf{Q}_a^{\mathrm{T}} \dot{\mathbf{q}} > 0 \quad \text{then} \quad \dot{\lambda} = \frac{\beta}{Q_y} \mathbf{Q}_a^{\mathrm{T}} \dot{\mathbf{q}} > 0.$$

doi:10.6342/NTU202402645

On the contray, if $\dot{\lambda} > 0$, Eq. (4.15) request $f = 0$, hence we obtain $\dot{f} = 0$ again. Further, this brings us to obtain the following condition,

$$\text{if} \quad \dot{\lambda} = 0 \quad \text{then} \quad f = 0 \quad \text{and} \quad \mathbf{Q}_a^{\mathrm{T}} \dot{\mathbf{q}} > 0.$$

In summary, we have the sufficient and necessary condition of the viscoelastoplastic model.

$$\left\{ f = 0 \text{ and } \mathbf{Q}_a^{\mathrm{T}} \dot{\mathbf{q}} > 0 \right\} \Leftrightarrow \left\{ \dot{\lambda} = \frac{\beta}{Q_y} \mathbf{Q}_a^{\mathrm{T}} \dot{\mathbf{q}} \right\} \Leftrightarrow \{ \dot{\lambda} > 0 \}.$$

It is logically equivalent to the following on-off criterion of the viscoelastoplastic model.

$$\dot{\lambda} = \begin{cases} \frac{\beta}{Q_y} \mathbf{Q}_a^{\mathrm{T}} \dot{\mathbf{q}} & \text{if} \quad f = 0 \quad \text{and} \quad \mathbf{Q}_a^{\mathrm{T}} \dot{\mathbf{q}} > 0, \\ 0 & \text{if} \quad f < 0 \quad \text{or} \quad \mathbf{Q}_a^{\mathrm{T}} \dot{\mathbf{q}} \leq 0. \end{cases} \tag{2.20}$$

Based on the above derivation, we can know that this bilinear viscoelastoplastic model combined with plastic flow rules and complementary trio can more completely describe the viscoelastoplastic behavior of the building structure.

2.3 Two-phase dynamicalal systems

From the preceding section, it is evident that this model involves numerous complex equations. Therefore, to provide a clearer description of the system's viscoelastic and viscoelastoplastic states, we further divide the system into two phases systems: viscoelastic (VE) phase ($\dot{\lambda} = 0$) and viscoelastoplastic (VEP) phase ($\dot{\lambda} > 0$). In the previous section, we have already discussed the complementary trio. Here, we can describe it as a two-phase switching system, where the system is considered as the off phase when it's in the viscoelastic state, and as the on phase when it's in the viscoelastoplastic state. We can

doi:10.6342/NTU202402645

illustrate this relationship graphically as shown in Figure 2.2.and we can also represent it in tabular form as shown in Table 2.1.

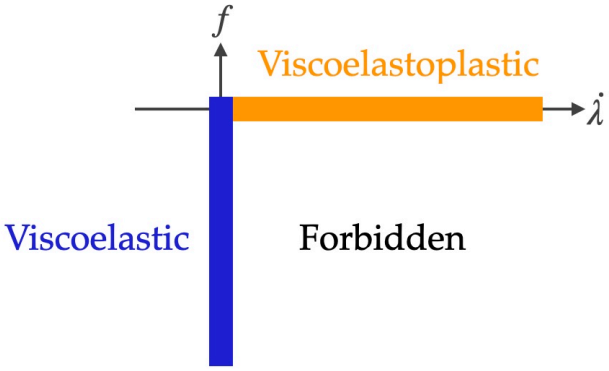

Figure 2.2: Complementary trio relations and two-phase switching

Table 2.1: The relationship between the two-phase system and the complementary trio

	$\dot{\lambda} = 0$	$\dot{\lambda} > 0$
$f < 0$	Viscoelastic-phase	Forbidden
$f = 0$	Viscoelastic-phase	Viscoelastoplastic-phase

doi:10.6342/NTU202402645

2.3.1 Viscoelastic-phase (off-phase)

For case of $\dot{\lambda} = 0$ the formulation of the model in the viscoelastic phase is:

$$\begin{aligned} & m_s \ddot{\mathbf{q}} + \mathbf{Q} = \mathbf{F}, \\ & f = \|\mathbf{Q}_a\| - Q_y \leq 0, \\ & \dot{\lambda} = 0, \\ & \dot{\mathbf{q}}^p = \mathbf{0}, \\ & \dot{\mathbf{Q}}_b = \mathbf{0}, \\ & \mathbf{Q}_a = \mathbf{Q} - \mathbf{Q}_b - c\dot{\mathbf{q}}. \end{aligned} \tag{2.21}$$

Since all of the above equations are linear, the system is linear in viscoelastic phase.

2.3.2 Viscoelastoplastic-phase (on-phase)

For case of $\dot{\lambda} > 0$ the formulation of the model in the viscoelastoplastic phase is:

$$\begin{aligned} & m_s \ddot{\mathbf{q}} + \mathbf{Q} = \mathbf{F}, \\ & f = \|\mathbf{Q}_a\| - Q_y = 0, \\ & \dot{\lambda} > 0, \\ & Q_y \dot{\mathbf{q}}^p = \mathbf{Q}_a \dot{\lambda}, \\ & \dot{\mathbf{q}}^p = \frac{\dot{\mathbf{Q}}_b}{k_p}, \\ & \dot{\mathbf{Q}}_b = k_p \dot{\mathbf{q}}^p, \\ & \mathbf{Q} = \mathbf{Q}_a + \mathbf{Q}_b + c\dot{\mathbf{q}}. \end{aligned} \tag{2.22}$$

doi:10.6342/NTU202402645

Since the formulation of $\dot{\lambda}$ as shown in Eq. (2.19) contain $\mathbf{Q}_a$ in the denominator and the numerator, the system is nonlinear in viscoelastoplastic phase.

2.4 Numerical integration based on internal symmetry

This section aims to address difficult of numerical integration caused by the nonlinear term in Eq. (2.22) when the system is in the viscoelastoplastic phase. Firstly, from Eq. (2.9), we know that when the system is in the plastic phase, $f = 0$, implying $\mathbf{Q}_a^{\mathrm{T}}\mathbf{Q}_a = Q_y^2$. Here, we discuss symmetric building structures, which means that the stiffness in all directions and the radius of the yield surface are the same. Therefore, the yield surface in the $\mathbf{Q}_a$ space can be an circle, as shown in Figure 2.3. To solve for $\mathbf{Q}_a$, we transform the $\mathbf{Q}_a^*$ into augmented force space, where Minkowski spacetime is an inverted circle cone as depicted in Figure 2.5. Next, we will proceed with the theoretical derivation of transforming the $\mathbf{Q}_a$ space into Minkowski spacetime.

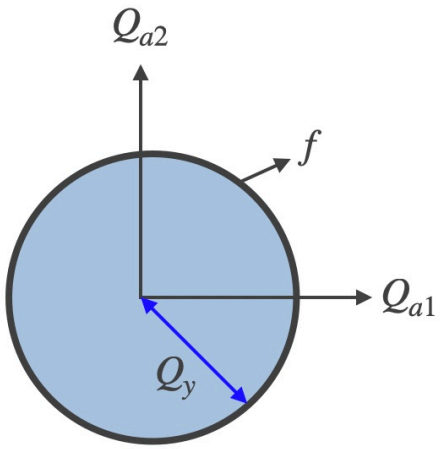

Figure 2.3: Schematic diagram of active shear force space for symmetric structures

doi:10.6342/NTU202402645

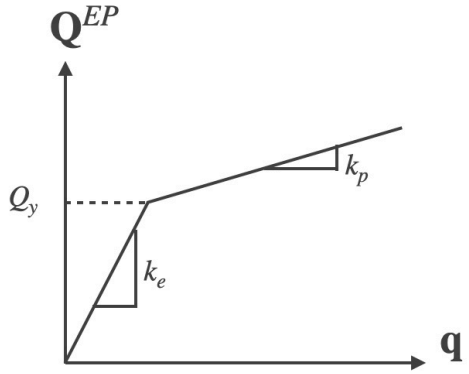

Figure 2.4: Bilinear displacement-force curves of symmetric building structures

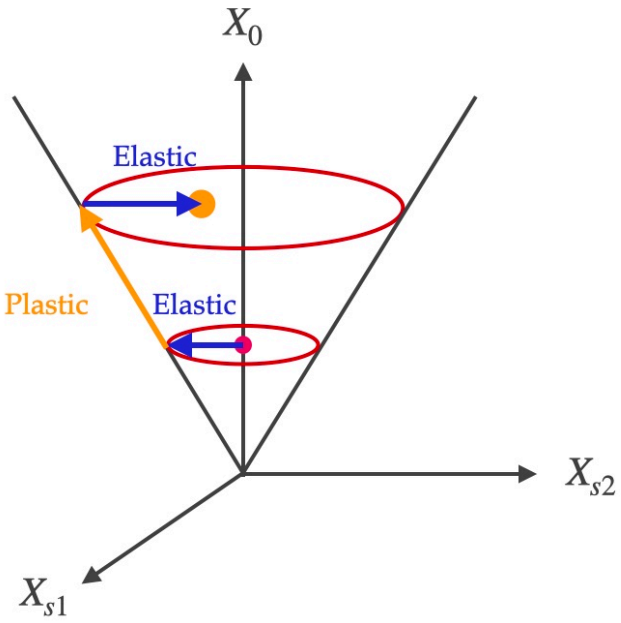

Figure 2.5: Augmented force space of symmetric building structures

2.4.1 Internal symmetry in Minkowski spacetime

First, we start from Eq. (2.13), which is as follows:

$$\dot{\mathbf{Q}}_a + (k_e + k_p)\frac{\dot{\lambda}\mathbf{Q}_a}{Q_y} = k_e\dot{\mathbf{q}}.$$

If the integrating factor as $X_0 = \exp(\frac{\lambda}{\beta q_y})$ is found and multiplies by Eq. (2.13) we have:

$$X_0\dot{\mathbf{Q}}_a + (k_e + k_p)X_0\frac{\dot{\lambda}\mathbf{Q}_a}{Q_y} = k_e X_0\dot{\mathbf{q}}. \tag{2.23}$$

doi:10.6342/NTU202402645

Eq. (2.23) can also be rewritten as follows:

$$X_0\dot{\mathbf{Q}}_a + X_0\frac{\dot{\lambda}\mathbf{Q}_a}{\beta q_y} = k_e X_0\dot{\mathbf{q}}. \tag{2.24}$$

Then, dividing Eq. (2.24) by Q_y, we have:

$$\frac{d}{dt}\left[\frac{X_0\mathbf{Q}_a}{Q_y}\right] = \frac{1}{q_y}X_0\dot{\mathbf{q}}. \tag{2.25}$$

Next, differentiating X_0 yields the following relationship:

$$\frac{d}{dt}\left[X_0\right] = \frac{\dot{\lambda}}{\beta q_y}X_0 = \frac{X_0}{Q_y q_y}(\mathbf{Q}_a)^{\mathsf{T}}\dot{\mathbf{q}} = \frac{X_0}{Q_y q_y}(\dot{\mathbf{q}})^{\mathsf{T}}\mathbf{Q}_a. \tag{2.26}$$

The augmented force vector is defined by:

$$\mathbf{X} = \begin{bmatrix}\mathbf{X}_s\\ X_0\end{bmatrix} = \begin{bmatrix}\frac{X_0\mathbf{Q}_a}{Q_y}\\ \exp(\frac{\lambda}{\beta q_y})\end{bmatrix}. \tag{2.27}$$

We refer to it as the (2+1)-dimensional augmented force vector. We now transform the elastoplastic bilinear model to defined in the generalized force space into model within the augmented force space $\mathbf{X}$. Combining Eq. (2.25) and Eq. (2.26), we obtain the dynamical system of augmented force under viscoelastoplastic phase as follows:

$$\frac{d}{dt}\begin{bmatrix}\frac{X_0\mathbf{Q}_a}{Q_y}\\ X_0\end{bmatrix} = \frac{1}{q_y}\begin{bmatrix}0 & \dot{\mathbf{q}}\\ \dot{\mathbf{q}}^{\mathsf{T}} & 0\end{bmatrix}\begin{bmatrix}\frac{X_0\mathbf{Q}_a}{Q_y}\\ X_0\end{bmatrix} =: \mathbf{AX}, \tag{2.28}$$

where

$$\mathbf{A} = \frac{1}{q_y}\begin{bmatrix}0 & \dot{\mathbf{q}}\\ \dot{\mathbf{q}}^{\mathsf{T}} & 0\end{bmatrix},$$

doi:10.6342/NTU202402645

and **g** is the Minkowski metric as follows:

$$\mathbf{g} = \begin{bmatrix} \mathbf{I} & \mathbf{0} \\ \mathbf{0} & -1 \end{bmatrix}.$$

According to Eq. (2.16), the Minkowski metric **g** and Eq. (2.27), we further distinguish between two correspondences

$$\|\mathbf{Q}_a\| = Q_y \Longleftrightarrow \mathbf{XgX} = 0,$$

$$\|\mathbf{Q}_a\| < Q_y \Longleftrightarrow \mathbf{XgX} < 0.$$

As shown in Figure 2.3, the generalized active force vector in generalized active force space corresponds to an augmented force vector **X** on the cone of Minkowski spacetime $\mathbb{M}^{2+1}$. Note that the outside of the cone is uninhabitable. By using the coordinates, we convert the non-liner model to a system $\dot{\mathbf{X}} = \mathbf{AX}$, and state matrix **A** satisfies

$$\mathbf{A}^{\mathrm{T}}\mathbf{g} + \mathbf{gA} = \mathbf{0}. \tag{2.29}$$

Therefore, **A** is an element of the real Lie algebra so(2,1).

In the viscoelastoplastic phase, the solution of Eq. (2.28) can be expressed by the following augmented force transformation formula:

$$\mathbf{X}(t) = \left[\mathbf{G}(t)\mathbf{G}^{-1}(t_1)\right]\mathbf{X}(t_1),$$

where $\mathbf{G}(t)$ is the fundamental solution of Eq. (2.28) and it satisfies

$$\dot{\mathbf{G}}(t) = \mathbf{AG},$$

doi:10.6342/NTU202402645

$$\mathbf{G}(0) = \mathbf{I}_3.$$

Based on the above mentioned property on $\mathbf{G}(t)$

$$\mathbf{G}^{\mathrm{T}}(t)\mathbf{g}\mathbf{G}(t) = \mathbf{g}. \tag{2.30}$$

Hence,the fundamental solution $\mathbf{G}(t)$ is an element of Lie algebra so(2,1). In the case of constant vector $\dot{\mathbf{q}}$, $\mathbf{A}$ is a constant matrix, and the system Eq. (2.28) become linear. Then the matrix exponent $\exp(\mathbf{A}\Delta t)$ can be used to play the role of the fundamental solution $\mathbf{G}(t_{i+1}, t_i)$ in the period of t_i to $t_{i+1} = t_i + \Delta t$, i.e.

$$\mathbf{G}(t_{i+1}, t_i) = \exp(\mathbf{A}\Delta t) = \begin{bmatrix} \mathbf{I}_n + \frac{a-1}{\|\dot{\mathbf{q}}(t_i)\|^2}\dot{\mathbf{q}}(t_i)\dot{\mathbf{q}}^{\mathrm{T}}(t_i) & \frac{b}{\|\dot{\mathbf{q}}(t_i)\|}\dot{\mathbf{q}}(t_i) \\ \frac{b}{\|\dot{\mathbf{q}}(t_i)\|}\dot{\mathbf{q}}^{\mathrm{T}}(t_i) & a \end{bmatrix}, \tag{2.31}$$

where

$$a = \cosh\left(\frac{\|\dot{\mathbf{q}}(t_i)\|}{q_y}\Delta t\right), \tag{2.32}$$

$$b = \sinh\left(\frac{\|\dot{\mathbf{q}}(t_i)\|}{q_y}\Delta t\right). \tag{2.33}$$

Substituting the above expression into Eq. (2.28) and Eq. (2.31), we obtain:

$$\mathbf{X}(t_{i+1}) = \mathbf{G}(t_{i+1}, t_i)\mathbf{X}(t_i), \tag{2.34}$$

$$\begin{bmatrix} \frac{X_0(t_{i+1})\mathbf{Q}_a(t_{i+1})}{Q_y} \\ X_0(t_{i+1}) \end{bmatrix} = \begin{bmatrix} \mathbf{I}_n + \frac{a-1}{\|\dot{\mathbf{q}}(t_i)\|^2}\dot{\mathbf{q}}(t_i)\dot{\mathbf{q}}^{\mathrm{T}}(t_i) & \frac{b}{\|\dot{\mathbf{q}}(t_i)\|}\dot{\mathbf{q}}(t_i) \\ \frac{b}{\|\dot{\mathbf{q}}(t_i)\|}\dot{\mathbf{q}}^{\mathrm{T}}(t_i) & a \end{bmatrix} \begin{bmatrix} X_0(t_i)\frac{\mathbf{Q}_a(t_i)}{Q_y} \\ X_0(t_i) \end{bmatrix}. \tag{2.35}$$

doi:10.6342/NTU202402645

From Eq. (2.35), we have obtained the closed-form solution for $\mathbf{Q}_a$ as follows:

$$\mathbf{Q}_a(t_{i+1}) = \frac{X_0(t_{i+1})\mathbf{Q}_a(t_{i+1})}{Q_y}\frac{Q_y}{X_0(t_{i+1})}. \tag{2.36}$$

In the above derivation, we utilized the transformation of $\mathbf{Q}_a$ space to augmented force space and employed the Group-preserving integration (GPI) method to derive the closed-form solution for $\mathbf{Q}_a$. That will be advantageous for solving the viscoelastoplastic-phase system. In the next section, we will represent the two-phase system in the form of state-space representation, it will become clearer why we need to solve for $\mathbf{Q}_a$ and how we address the nonlinear behavior in the viscoelastoplastic-phase.

2.5 State-space representation

From Section 2.3, we can divide the entire system into two phases for analysis, namely the viscoelastic-phase and the viscoelastoplastic-phase. In this section, we represent the system using the state-space representation method, which is a highly advantageous tool for analyzing dynamic systems. Additionally, when the system enters the viscoelastoplastic-phase, we utilize the closed-form solution derived in Section 2.4, denoted as $\mathbf{Q}_a$, in conjunction with the state-space representation method for analysis.The following, we will proceed with the matrix derivation of the state-space representation method for the two-phase system.

From Eq. (2.21) and Eq. (2.22), we can derive the equation of motion for the two-phase system as follows:

$$m_s\ddot{\mathbf{q}} + \mathbf{Q} = \mathbf{F}.$$

doi:10.6342/NTU202402645

Next, we define the momentum equation for the two-phase system as follows:

$$\mathbf{P}_s = m_s \dot{\mathbf{q}}. \tag{2.37}$$

We differentiate Eq. (2.21) as follows:

$$\dot{\mathbf{P}}_s = m_s \ddot{\mathbf{q}}. \tag{2.38}$$

Substituting Eq. (2.38) into the equation of motion, we get:

$$\dot{\mathbf{P}}_s = -\mathbf{Q} + \mathbf{F}. \tag{2.39}$$

Next, we will derive the state-space representation for the two-phase system separately.

2.5.1 Viscoelastic-phase

From Section 2.3.1, we know that when the system is in the viscoelastic-phase, it can be represented by Eq. (2.21). First, we substitute Eq. (2.5) into Eq. (2.3) to obtain $\mathbf{Q} = k_e \mathbf{q}^e + c\dot{\mathbf{q}}$, and then we differentiate it as follows:

$$\dot{\mathbf{Q}} = k_e \dot{\mathbf{q}}^e + c\ddot{\mathbf{q}}. \tag{2.40}$$

From Eq. (2.2), we know that $\dot{\mathbf{q}}^e = \dot{\mathbf{q}} - \dot{\mathbf{q}}^p$. Substituting this into Eq. (2.40), we get:

$$\dot{\mathbf{Q}} = k_e(\dot{\mathbf{q}} - \dot{\mathbf{q}}^p) + c\ddot{\mathbf{q}}. \tag{2.41}$$

doi:10.6342/NTU202402645

Since $\dot{\mathbf{q}}^p = \mathbf{0}$ from Eq. (2.8), Eq. (2.41) can be rewritten as follows:

$$\dot{\mathbf{Q}} = k_e\dot{\mathbf{q}} + c\ddot{\mathbf{q}}. \tag{2.42}$$

From the equation of motion, we know that $\ddot{\mathbf{q}} = -\frac{1}{m_s}\mathbf{Q} + \frac{1}{m_s}\mathbf{F}$, and from Eq. (2.37), we know that $\dot{\mathbf{q}} = \frac{1}{m_s}\mathbf{P}_s$. Therefore, Eq. (2.42) can be rewritten as follows:

$$\dot{\mathbf{Q}} = \frac{k_e}{m_s}\mathbf{P}_s - \frac{c}{m_s}\mathbf{Q} + \frac{c}{m_s}\mathbf{F}. \tag{2.43}$$

Using the state-space representation, we can express Eq. (2.37), Eq. (2.39), and Eq. (2.43) as follows:

$$\begin{bmatrix} \dot{\mathbf{P}}_s \\ \dot{\mathbf{q}} \\ \dot{\mathbf{Q}} \end{bmatrix} = \begin{bmatrix} \mathbf{0} & \mathbf{0} & -\mathbf{I} \\ \frac{1}{m_s}\mathbf{I} & \mathbf{0} & \mathbf{0} \\ \frac{k_e}{m_s}\mathbf{I} & \mathbf{0} & -\frac{c}{m_s}\mathbf{I} \end{bmatrix} \begin{bmatrix} \mathbf{P}_s \\ \mathbf{q} \\ \mathbf{Q} \end{bmatrix} + \begin{bmatrix} \mathbf{F} \\ \mathbf{0} \\ \frac{c}{m_s}\mathbf{F} \end{bmatrix}. \tag{2.44}$$

Eq. (2.44) can also be expressed as follows:

$$\frac{d}{dt}\mathbf{z}_{\mathrm{e}}(t) = \mathbf{A}_{\mathrm{e}}\mathbf{z}_{\mathrm{e}}(t) + \mathbf{u}_{\mathrm{e}}(t), \tag{2.45}$$

where $\mathbf{z}_{\mathrm{e}}(t)$ is the state matrix for viscoelastic-phase, $\mathbf{u}_{\mathrm{e}}(t)$ is the input matrix for viscoelastic-phase and $\mathbf{A}_{\mathrm{e}}$ is the constant matrix for the viscoelastic-phase and

$$\mathbf{z}_{\mathrm{e}} = \begin{bmatrix} \mathbf{P}_s \\ \mathbf{q} \\ \mathbf{Q} \end{bmatrix}, \mathbf{A}_{\mathrm{e}} = \begin{bmatrix} \mathbf{0} & \mathbf{0} & -\mathbf{I} \\ \frac{1}{m_s}\mathbf{I} & \mathbf{0} & \mathbf{0} \\ \frac{k_e}{m_s}\mathbf{I} & \mathbf{0} & -\frac{c}{m_s}\mathbf{I} \end{bmatrix}, \mathbf{u}_{\mathrm{e}} = \begin{bmatrix} \mathbf{F} \\ \mathbf{0} \\ \frac{c}{m_s}\mathbf{F} \end{bmatrix}. \tag{2.46}$$

So far, we have derived the state-space representation for the viscoelastic-phase. Furthermore, from Eq. (2.21), we know that the viscoelastic-phase system must satisfy the

doi:10.6342/NTU202402645

following equations simultaneously:

$$\dot{\mathbf{q}}^p = \mathbf{0},$$

$$\dot{\mathbf{Q}}_b = \mathbf{0},$$

$$\mathbf{Q}_a = \mathbf{Q} - \mathbf{Q}_b - c\dot{\mathbf{q}}.$$

We have completed the derivation of the state-space representation for the viscoelastic-phase system. Next, we will derive the state-space representation for the viscoelastoplastic-phase system.

2.5.2 Viscoelastoplastic-phase

From Section 2.3.2, we know that when the system is in the viscoelastoplastic-phase, it can be represented by Eq. (2.22). First, from Eq. (2.3) and Eq. (2.4), we know that $\mathbf{Q} = \mathbf{Q}_a + \mathbf{Q}_b + c\dot{\mathbf{q}}$. We substitute this into Eq. (2.39) as follows:

$$\dot{\mathbf{P}}_s = -\mathbf{Q}_a - \mathbf{Q}_b - c\dot{\mathbf{q}} + \mathbf{F}. \tag{2.47}$$

We know from Eq. (2.37) that $\dot{\mathbf{q}} = \frac{1}{m_s}\mathbf{P}_s$. Substituting this into Eq. (2.47), we get:

$$\dot{\mathbf{P}}_s = -\mathbf{Q}_a - \mathbf{Q}_b - \frac{c}{m_s}\mathbf{P}_s + \mathbf{F}. \tag{2.48}$$

doi:10.6342/NTU202402645

In Section 2.4, we have already solved for the closed form of $\mathbf{Q}_a$, so $\dot{\mathbf{Q}}_a$ is known. From Eq. (2.12), we can know $\dot{\mathbf{q}}^p$ as follows:

$$\dot{\mathbf{q}}^p = \frac{k_e}{k_e + k_p}\dot{\mathbf{q}} - \frac{1}{k_e + k_p}\dot{\mathbf{Q}}_a. \tag{2.49}$$

We can also know $\dot{\mathbf{Q}}_b$ from Eq. (2.6) as follows:

$$\begin{aligned} \dot{\mathbf{Q}}_b, &= \frac{k_e k_p}{k_e + k_p}\dot{\mathbf{q}} - \frac{k_p}{k_e + k_p}\dot{\mathbf{Q}}_a, \\ &= \frac{k_e k_p}{(k_e + k_p)m_s}\mathbf{P}_s - \frac{k_p}{k_e + k_p}\dot{\mathbf{Q}}_a. \end{aligned} \tag{2.50}$$

Using the state-space representation, we can express Eq. (2.37), Eq. (2.48), and Eq. (2.50) as follows:

$$\begin{bmatrix} \dot{\mathbf{P}}_s \\ \dot{\mathbf{q}} \\ \dot{\mathbf{Q}}_b \end{bmatrix} = \begin{bmatrix} -\frac{c}{m_s}\mathbf{I} & \mathbf{0} & -\mathbf{I} \\ \frac{1}{m_s}\mathbf{I} & \mathbf{0} & \mathbf{0} \\ \frac{k_e k_p}{(k_e+k_p)m_s}\mathbf{I} & \mathbf{0} & \mathbf{0} \end{bmatrix} \begin{bmatrix} \mathbf{P}_s \\ \mathbf{q} \\ \mathbf{Q}_b \end{bmatrix} + \begin{bmatrix} -\mathbf{Q}_a + \mathbf{F} \\ \mathbf{0} \\ -\frac{kp}{k_e+k_p}\dot{\mathbf{Q}}_a \end{bmatrix}. \tag{2.51}$$

Eq. (2.51) can also be expressed as follows:

$$\frac{d}{dt}\mathbf{z}_{\mathrm{p}}(t) = \mathbf{A}_{\mathrm{p}}\mathbf{z}_{\mathrm{p}}(t) + \mathbf{u}_{\mathrm{p}}(t), \tag{2.52}$$

where $\mathbf{z}_{\mathrm{p}}(t)$ is the state matrix for viscoelastoplastic-phase, $\mathbf{u}_{\mathrm{p}}(t)$ is the input matrix for viscoelastoplastic-phase and $\mathbf{A}_{\mathrm{p}}$ is the constant matrix for the viscoelastoplastic-phase and

$$\mathbf{z}_{\mathrm{p}} = \begin{bmatrix} \mathbf{P}_s \\ \mathbf{q} \\ \mathbf{Q}_b \end{bmatrix}, \mathbf{A}_{\mathrm{p}} = \begin{bmatrix} -\frac{c}{m_s}\mathbf{I} & \mathbf{0} & -\mathbf{I} \\ \frac{1}{m_s}\mathbf{I} & \mathbf{0} & \mathbf{0} \\ \frac{k_e k_p}{(k_e+k_p)m_s}\mathbf{I} & \mathbf{0} & \mathbf{0} \end{bmatrix}, \mathbf{u}_{\mathrm{p}} = \begin{bmatrix} -\mathbf{Q}_a + \mathbf{F} \\ \mathbf{0} \\ -\frac{kp}{k_e+k_p}\dot{\mathbf{Q}}_a \end{bmatrix}. \tag{2.53}$$

doi:10.6342/NTU202402645

So far, we have derived the state-space representation for the viscoelastoplastic-phase. Furthermore, from Eq. (2.22), we know that the viscoelastoplastic-phase system must satisfy the following equations simultaneously:

$$Q_y \dot{\mathbf{q}}^p = \mathbf{Q}_a \dot{\lambda},$$

$$\dot{\mathbf{q}}^p = \frac{\dot{\mathbf{Q}}_b}{k_p},$$

$$\dot{\mathbf{Q}}_b = k_p \dot{\mathbf{q}}^p,$$

$$\mathbf{Q} = \mathbf{Q}_a + \mathbf{Q}_b + c\dot{\mathbf{q}}.$$

By now, we have derived the state-space representation for the viscoelastoplastic-phase, and the viscoelastoplastic-phase system is now a linear system. In this section, we utilize the closed-form solution derived in Section 2.4 to address the complex nonlinear terms arising from the viscoelastoplastic-phase. With the state-space representations for the viscoelastic-phase and viscoelastoplastic-phases established, we can better solve this bilinear viscoelastoplastic model since all nonlinear terms have been eliminated. In the next section, we will introduce how to solve this state-space representation.

2.6 Incremental analysis method

In Section 2.5, the state-space representation for the two-phase system has been derived. In this section, we will explain the use of the incremental analysis method to analyze

doi:10.6342/NTU202402645

its state-space representation. The incremental analysis, as the name suggests, involves step-by-step consideration of each increment, and analyzing the system's response at each step. In the case of the two-phase system, we take Δt as a small increment, representing the time interval for the external force input to the system. Therefore, we know that this increment is constant. Furthermore, because Δt is a constant, it is possible to violate the admissible condition at fixed time intervals. This occurs because the transition from the viscoelastic-phase to the viscoelastoplastic-phase may not necessarily happen exactly at the onset of plasticity. Therefore, we may encounter a violation of the admissible condition. Here, we provide a clearer explanation with a diagram, as shown in Figure 2.6. In the figure, we define t_k as the last point in the viscoelastic-phase, and t_{k+1} as the next point in time at a fixed time interval. At t_{k+1}, the system has already entered the viscoelastoplastic-phase, but we can observe from the graph that a violation of the admissible condition occurs at this time, i.e., $f > 0$. This is because t_{k+1} may not be the correct onset time for entering the plastic state. Therefore, we must first find the onset time t_s. Here, we divide the system into three elements: the viscoelastic-phase module, the viscoelastoplastic-phase module, and the viscoelastoplastic pull-back module. The viscoelastoplastic pull-back module is used to find the system's response at the time of t_s to address the situation described above. Now, we will proceed with the introduction to the incremental analysis method for these three elements.

In Section 2.5, we initially divide the viscoelastoplastic system into two phases. However, due to the need for viscoelastoplastic pull-back when the viscoelastic-phase transitions into the viscoelastoplastic-phase, the two-phase system is further divided into three modules for analysis. Next, we will introduce the linear time-invariant (LTI) system, followed by the introduction of the three modules separately.

doi:10.6342/NTU202402645

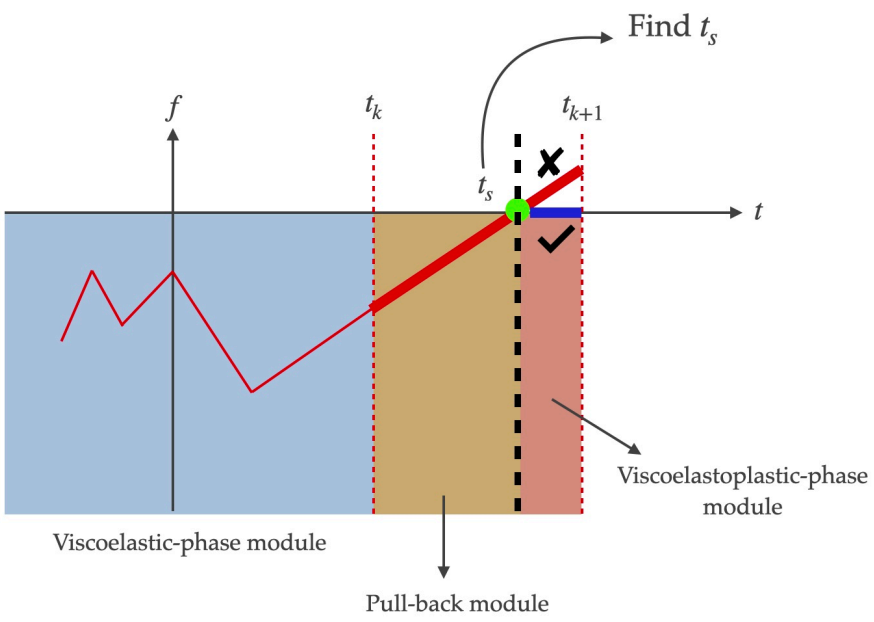

Figure 2.6: Scheme diagram about the computational idea from VE phase to VEP phase

2.6.1 Linear time-invariant (LTI) system

First, we will proceed with the solution of the linear time-invariant (LTI) system, which is represented mathematically as follows.

$$\frac{d}{dt}\mathbf{z}_{\mathrm{s}}(t) = \mathbf{A}_{\mathrm{s}}\mathbf{z}_{\mathrm{s}}(t) + \mathbf{u}_{\mathrm{s}}(t), \tag{2.54}$$

where $\mathbf{z}_{\mathrm{s}}(t)$ is the state matrix for LTI system, $\mathbf{u}_{\mathrm{s}}(t)$ is the input vector for LTI system and $\mathbf{A}_{\mathrm{s}}$ is the constant matrix for LTI system. Its solution can be represented as follows:

$$\mathbf{z}_{\mathrm{s}}(t) = \exp\left(\mathbf{A}_{\mathrm{s}}\left(t - t_i\right)\right)\mathbf{z}_{\mathrm{s}}\left(t_i\right) + \int_{t_i}^{t} \exp(\mathbf{A}_{\mathrm{s}}(t-\tau))\mathbf{u}_{\mathrm{s}}(\tau)d\tau. \tag{2.55}$$

If the time increment is Δt, and we have already obtained $\mathbf{z}_{\mathrm{s}}\left(t_i\right)$ and $\mathbf{u}_{\mathrm{s}}(t_i)$, with the time interval $(t_i, t_i + \Delta t)$, and $\mathbf{u}_{\mathrm{s}}(t_i + \Delta t)$ is a constant, then the solution of the linear

doi:10.6342/NTU202402645

time-invariant (LTI) system at this time is as follows:

$$\mathbf{z}_{\mathrm{s}}\left(t_i+\Delta t\right)=\exp(\mathbf{A}_{\mathrm{s}}(\Delta t))\mathbf{z}_{\mathrm{s}}\left(t_i\right)+\int_{t_i}^{t_i+\Delta t}\exp\left(\mathbf{A}_{\mathrm{s}}\left(t_i+\Delta t-\tau\right)\right)d\tau\mathbf{u}_{\mathrm{s}}\left(t_i\right). \quad (2.56)$$

Next, integrating Eq. (2.56), we have:

$$\mathbf{z}_{\mathrm{s}}\left(t_i+\Delta t\right)=\exp(\mathbf{A}_{\mathrm{s}}\Delta t)\mathbf{z}_{\mathrm{s}}\left(t_i\right)+\left[\sum_{n=0}^{\infty}\left(\frac{\Delta t^{n+1}}{(n+1)!}\right)\mathbf{A}_{\mathrm{s}}^{n}\right]\mathbf{u}_{\mathrm{s}}\left(t_i\right). \quad (2.57)$$

Above, we have completed the derivation of the solution for the time-invariant (LTI) system. Next, we will apply the result of Eq. (2.57) to the three modules.

2.6.2 Viscoelastic-phase module

If the time increment is Δt, and we have already obtained $\mathbf{z}_{\mathrm{e}}\left(t_i\right)$ and $\mathbf{u}_{\mathrm{e}}(t_i)$, with the time interval $(t_i, t_i+\Delta t)$, and $\mathbf{u}_{\mathrm{e}}(t_i+\Delta t)$ is a constant, then the solution of the viscoelastic phase system at this time is as follows:

$$\mathbf{z}_{\mathrm{e}}\left(t_i+\Delta t\right)=\exp(\mathbf{A}_{\mathrm{e}}(\Delta t))\mathbf{z}_{\mathrm{e}}\left(t_i\right)+\int_{t_i}^{t_i+\Delta t}\exp\left(\mathbf{A}_{\mathrm{e}}\left(t_i+\Delta t-\tau\right)\right)d\tau\mathbf{u}_{\mathrm{e}}\left(t_i\right). \quad (2.58)$$

Next, integrating Eq. (2.58), we have:

$$\mathbf{z}_{\mathrm{e}}\left(t_i+\Delta t\right)=\exp(\mathbf{A}_{\mathrm{e}}\Delta t)\mathbf{z}_{\mathrm{e}}\left(t_i\right)+\left[\sum_{n=0}^{\infty}\left(\frac{\Delta t^{n+1}}{(n+1)!}\right)\mathbf{A}_{\mathrm{e}}^{n}\right]\mathbf{u}_{\mathrm{e}}\left(t_i\right). \quad (2.59)$$

We have now introduced the incremental analysis method for the viscoelastic- phase module. Next, we will introduce the viscoelastoplastic module.

doi:10.6342/NTU202402645

2.6.3 Viscoelastoplastic-phase module

If the time increment is Δt, and we have already obtained $\mathbf{z}_{\mathrm{p}}(t_i)$ and $\mathbf{u}_{\mathrm{p}}(t_i)$, with the time interval $(t_i, t_i + \Delta t)$, and $\mathbf{u}_{\mathrm{p}}(t_i + \Delta t)$ is a constant, then the solution of the viscoelastoplastic phase system at this time is as follows:

$$\mathbf{z}_{\mathrm{p}}(t_i + \Delta t) = \exp(\mathbf{A}_{\mathrm{p}}(\Delta t))\mathbf{z}_{\mathrm{p}}(t_i) + \int_{t_i}^{t_i+\Delta t} \exp\left(\mathbf{A}_{\mathrm{p}}(t_i + \Delta t - \tau)\right) d\tau \mathbf{u}_{\mathrm{p}}(t_i). \quad (2.60)$$

Next, integrating Eq. (2.60), we have:

$$\mathbf{z}_{\mathrm{p}}(t_i + \Delta t) = \exp(\mathbf{A}_{\mathrm{p}}\Delta t)\mathbf{z}_{\mathrm{p}}(t_i) + \left[\sum_{n=0}^{\infty}\left(\frac{\Delta t^{n+1}}{(n+1)!}\right)\mathbf{A}_{\mathrm{p}}^{n}\right]\mathbf{u}_{\mathrm{p}}(t_i). \quad (2.61)$$

We have now introduced the incremental analysis method for the viscoelastoplastic-phase module. Next, we will introduce the viscoelastoplastic pull-back module.

2.6.4 Viscoelastoplastic pull-back module

As shown in Figure 2.6, switching from the viscoelastic-phase system to the viscoelastoplastic-phase system at fixed time intervals may lead to a violation of the admissible condition. Therefore, we must first find the time t_s when entering the viscoelastoplastic-phase.. We divide Δt into ten equal parts and then use the viscoelastic-phase module to calculate $\mathbf{z}_{\mathrm{e}}(t_k + 0.1\Delta t)$. At this time, we check the admissible condition f. If $f(t_k + 0.1\Delta t) < 0$, it means the system has not yet yielded. We can further calculate $\mathbf{z}_{\mathrm{e}}(t_k + 0.2\Delta t)$ using the viscoelastic-phase module and check the admissible condition f again. If $f(t_k + 0.2\Delta t) < 0$, we continue to divide the time interval. If $f(t_k + 0.2\Delta t) > 0$, it means $t_s \in (t_k, t_k + 0.2\Delta t)$. Then we divide the time interval $0.2\Delta t$ into ten equal parts again

doi:10.6342/NTU202402645

until $f = 0$. At this time, the time is the time of the first entry into the viscoelastoplastic-phase. The flowchart is depicted in Figure 2.7. The above derivation has provided solutions for the three modules using the incremental analysis method. The next section will introduce the algorithm and its process for combining these three modules.

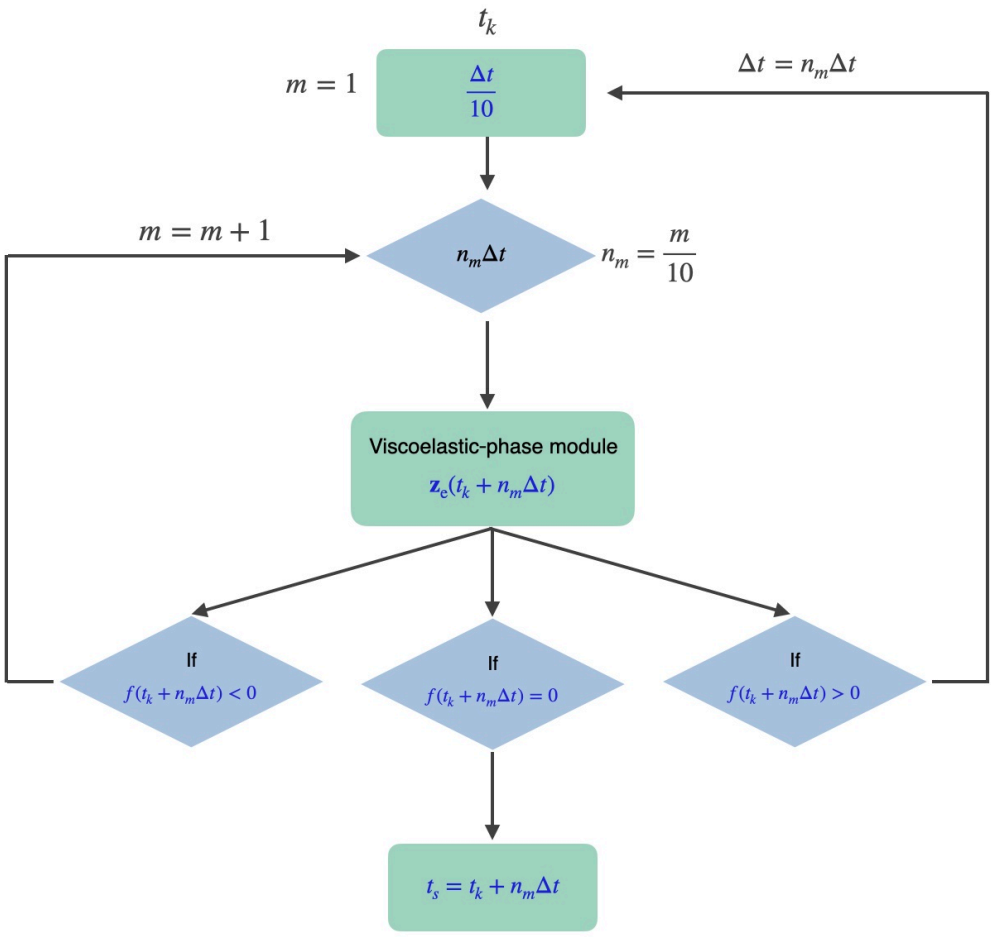

Figure 2.7: Flowchat of pull back module in the VEP phase

2.7 Algorithm

In this section, we will introduce the entire system algorithm process. The analysis methods for the three modules have been explained in section 2.6. Next, we will combine the three modules and incorporate judgment conditions to analyze the system. From section 2.3, we know that the system can be divided into two phases: the viscoelastic-phase

doi:10.6342/NTU202402645

and the viscoelastoplastic-phase. There are two very important judgment conditions: the floor shear force admissible condition and the straining condition. These two judgment conditions can help us determine the state of the system and satisfy the requirements of the complementary trio simultaneously. Here, we define the viscoelastoplastic indicator as **Iflage**. When **Iflage** $= 0$, the system is in the viscoelastic-phase, and when **Iflage** $= 1$, the system is in the viscoelastoplastic-phase. This viscoelastoplastic indicator facilitates us in conveniently determining the state of the system. First, we need to solve the initial value problem of the differential equation, so we set the initial condition $\mathbf{z} = \mathbf{0}$. Next is the detailed algorithm process.

When the system is at time t_i, if **Iflage** $= 0$, the system is in the viscoelastic-phase. Therefore, we calculate the response at t_{i+1} based on the viscoelastic-phase module. First, we need to confirm whether t_{i+1} violates the floor shear force admissible condition. If $f(t_{i+1}) \leq 0$, the calculation result at this time is reasonable for the viscoelastic-phase module **Iflage** $= 0$, and we proceed to the next time for calculation. If $f > 0$, the situation of violating the admissible condition mentioned in Section 2.6 occurs. Therefore, we need to enter the viscoelastoplastic pull-back module to find t_s. Once t_s is found, we enter the viscoelastic-phase module for calculation. At this time, **Iflage** $= 0$. Next, we need to follow the procedure mentioned in Section 2.4 to transform the $\mathbf{Q}_a$ space into Minkowski spacetime and calculate the closed-form $\mathbf{Q}_a$. Then, we proceed to calculate the response at t_{i+1} based on the viscoelastoplastic-phase module, where **Iflage** $= 1$, and then continue to the calculation of the next time.

When the system is at time t_i, if **Iflage** $= 1$, the system is in the viscoelastoplastic-phase. At this time, we first confirm the straining condition. If the straining condition $s(t_i) < 0$, we calculate the response at t_{i+1} based on the viscoelastic-phase module.

doi:10.6342/NTU202402645

Then, we confirm whether t_{i+1} violates the floor shear force admissible condition. If $f(t_{i+1}) \leq 0$, the calculation result at this time is reasonable for the viscoelasti-phase module **Iflage** $= 0$, and we proceed to the next time for calculation. If $f > 0$, the situation of violating the admissible condition mentioned in Section 2.6 occurs. Therefore, we need to enter the viscoelastoplastic pull-back module to find t_s. Once t_s is found, we enter the viscoelastic-phase module for calculation. At this time, **Iflage** $= 0$. Next, we need to follow the procedure mentioned in Section 2.4 to transform the $\mathbf{Q}_a$ space into Minkowski spacetime and calculate the closed-form $\mathbf{Q}_a$. Then, we proceed to calculate the response at t_{i+1} based on the viscoelastoplastic-phase module, where **Iflage** $= 1$, and then continue to the calculation of the next time. If the straining condition $s(t_i) > 0$, we directly calculate the closed-form $\mathbf{Q}_a$ and then proceed to calculate the response at t_{i+1} based on the viscoelastoplastic-phase modudle, where **Iflage** $= 1$, and then continue to the calculation of the next time.

Here is a flowchart to better understand this algorithm process, as shown in Figure 2.8.

doi:10.6342/NTU202402645

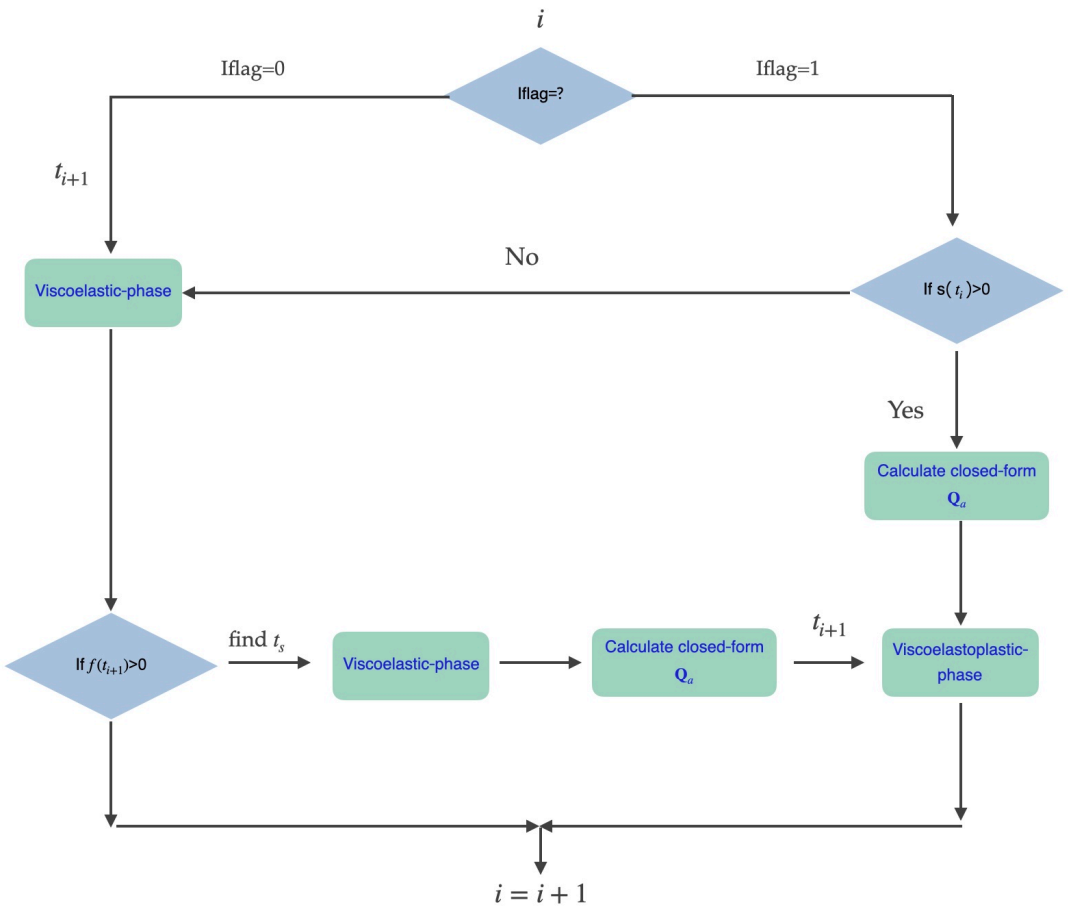

Figure 2.8: Viscoelastoplastic model analysis algorithm flowchart

doi:10.6342/NTU202402645

Chapter 3 Seismic behavior of symmetric building structures

This section will implement the mathematical model proposed in Chapter 2 using MATLAB, and the entire analysis procedure will follow the algorithm flow established in Sec 2.7. A single-story, bi-directionally symmetric building structure is considered for earthquake excitation analysis. The structure dimensions are 5m in both directions, and the story height is 3.6m, with fixed supports. The column cross-section dimensions are $0.5m \times 0.5m$, with a total of four columns. The beam cross-section dimensions are $0.25m \times 0.5m$, and the floor slab is a 15cm thick rigid slab. All materials are reinforced concrete, with a unit weight of 2400 $(\frac{kgf}{m^3})$ for reinforced concrete, a design compressive strength of 210 $(\frac{kgf}{cm^2})$, and a column stiffness reduction factor of 0.8. The damping ratio for the entire structure is 5%. It is assumed that the mass of the structure is concentrated at the floor slab centroid.

Based on the provided information, the necessary parameters for the analysis model can be obtained. The structural mass is $m_s = 2409.785933$ $\left(\frac{\text{kgf}-\text{s}^2}{\text{m}}\right)$. The elastic lateral stiffness is $k_e = 7454411.908$ $\left(\frac{kgf}{m}\right)$. The post-yield stiffness $k_p = 0.05k_e$. The structural

doi:10.6342/NTU202402645

damping coefficient $c = 2\xi\sqrt{k_e m_s}$ $\left(\frac{kgf-s}{m}\right)$. The story yield shear force $Q_y = C_s \times W$, where W is the structural weight, and C_s is taken as 0.12 based on empirical data. Based on the building structural parameters, we can determine that the natural period of the symmetric building structures in both horizontal directions is $T_n = 0.1129\ (s)$.

This section will perform earthquake excitation analysis using the above structural parameters. First, the complementary trio will be used to verify whether the algorithm flow proposed in Sec 2.7 is correct. After confirming the accuracy of the algorithm, the peak responses of the symmetric building structure under bi-directional and uni-directional earthquake excitations will be compared. Furthermore, the plastic equivalent responses of this building structure at various stations across Taiwan during the 921 Chi-Chi earthquake event will be analyzed. Subsequently, an analysis considering the angle of incidence of the earthquake excitations will be conducted.

In this section, the ground motion records used for the analysis are the east-west and north-south horizontal acceleration signals recorded at ten stations during the 921 Chi-Chi earthquake event, provided by the PEER Center (Pacific Earthquake Engineering Research Center). The stations are CHY041, TCU084, CHY028, TCU052, TCU068, TCU065, TCU079, CHY101, TCU071, and TCU129.

3.1 Complementary trio checking of symmetric structures

Before conducting structural response analysis, it is necessary to verify the correctness of the algorithm flow proposed in Sec 2.7. We will use the complementary trio conditions mentioned in Sec 2.2 to confirm the validity of the algorithm, which involves checking the non-negative dissipation $\dot{\lambda} \geq 0$, the admissible condition $f \leq 0$, and the

doi:10.6342/NTU202402645

alternative condition $f\dot{\lambda} = 0$. The verification method is to input the aforementioned bidirectional ground motion records into our proposed analysis model, and after the analysis, check if the complementary trio conditions are satisfied. From Figures 3.1 to 3.10, it can be observed that all selected seismic records satisfied the complementary trio conditions. Therefore, we can confirm the accuracy of this algorithm and proceed with the subsequent analyses with confidence.Additionally, all analyzed seismic acceleration records are the original seismic acceleration records.

After confirming that the complementary trio conditions are satisfied, we can essentially verify the correctness of the entire algorithm. To further validate this, we can check whether the path of $\mathbf{Q}_a$ always remains within or on the yield surface, without any instances of exceeding it. In this case, considering that the building structure we are studying has symmetric properties with equal stiffness in all directions, and without accounting for any eccentricity effects, we have only considered the bi-directional response. The yield surface of this structure is designed as a two-dimensional circular yield surface, implying that the structure has the same yield strength in any direction.From Figure 3.11 to Figure 3.20, it can be clearly observed that the $\mathbf{Q}_a$ paths induced by each earthquake time history are confined within the yield surface. This observation further confirms the correctness and robustness of the proposed algorithm flow. Specifically, each path demonstrates the force-displacement response of the structure under seismic action, and there are no phenomena of exceeding the yield surface. During the seismic action, the $\mathbf{Q}_a$ paths are all on or within the yield surface, which is entirely consistent with the constraints of our proposed model. In other words, it accurately describes the viscoelastoplastic behavior of the building structure after being subjected to an earthquake. The acquisition of these results not only demonstrates the theoretical rigor of the algorithm but also reflects its effectiveness in

doi:10.6342/NTU202402645

practical applications. For engineering practice, the ability to accurately predict structural behavior under seismic action is crucial, and our algorithm has shown powerful capabilities in this regard. Through these illustrations, one can intuitively understand the dynamic process of structural response.In summary, through the examination and analysis of the $\mathbf{Q}_a$ paths, we can confidently confirm the correctness of the proposed algorithm. These results once again emphasize the importance of considering the bi-directional response of structures under seismic loads in engineering design and analysis. These research findings provide important references for future structural analysis, particularly valuable when dealing with dynamic loads such as earthquakes.

doi:10.6342/NTU202402645

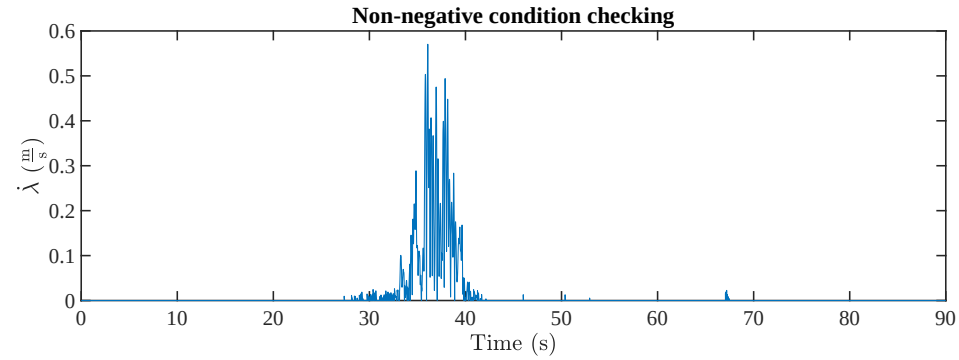

(a) The history of $\dot{\lambda}$ value

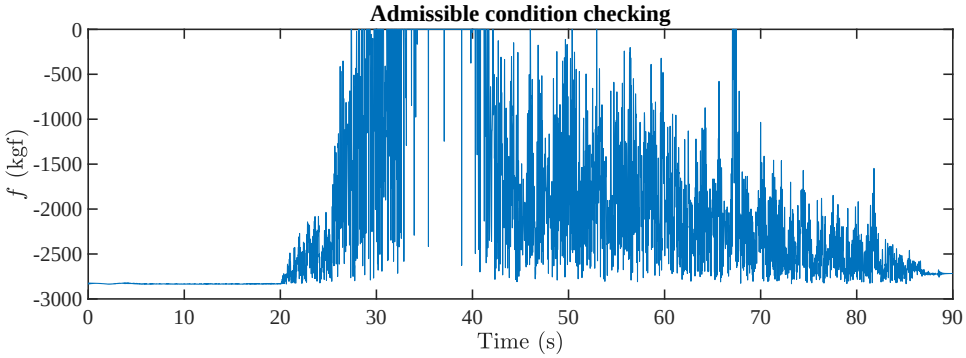

(b) The history of f value

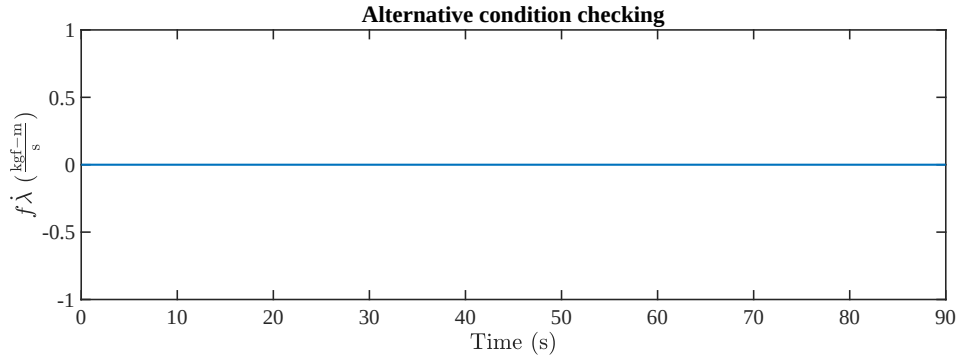

(c) The history of $f\dot{\lambda}$ value

Figure 3.1: The response of $\dot{\lambda}$, f, $f\dot{\lambda}$ of symmetric building structures under the seismic record of the CHY028 station during Chi-Chi earthquake

doi:10.6342/NTU202402645

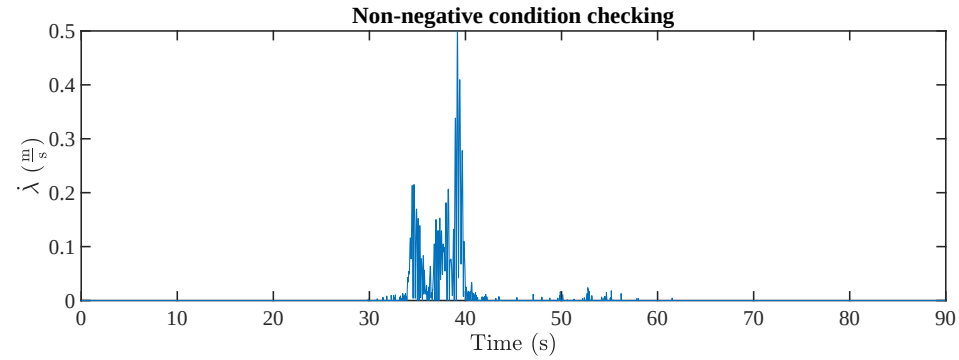

(a) The history of $\dot{\lambda}$ value

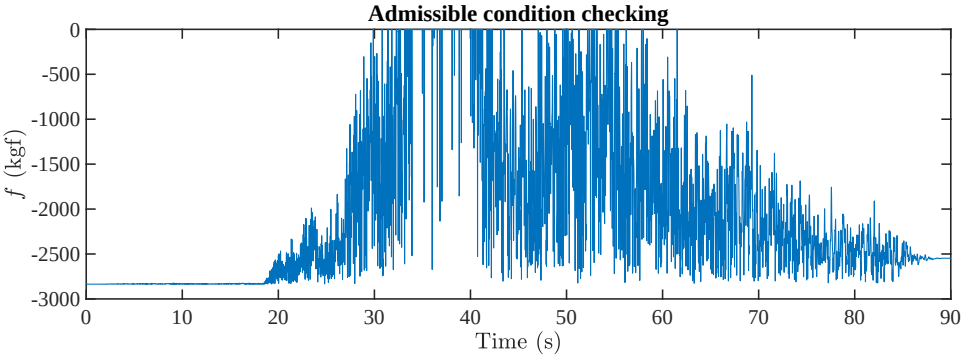

(b) The history of f value)

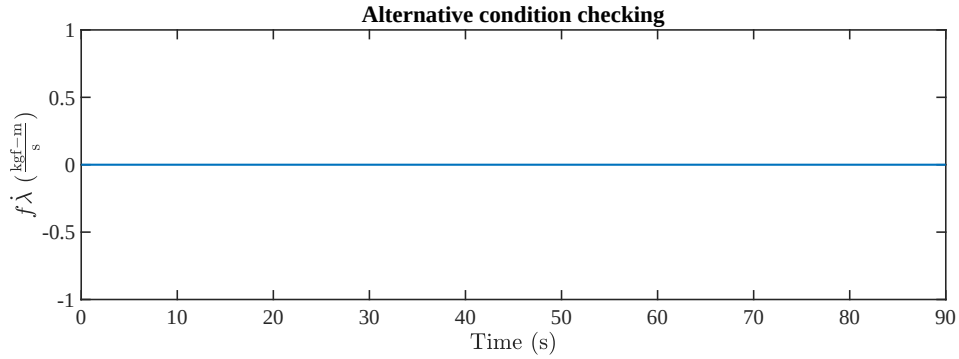

(c) The history of $f\dot{\lambda}$ value

Figure 3.2: The response of $\dot{\lambda}$, f, $f\dot{\lambda}$ of symmetric building structures under the seismic record of the CHY041 station during Chi-Chi earthquake

doi:10.6342/NTU202402645

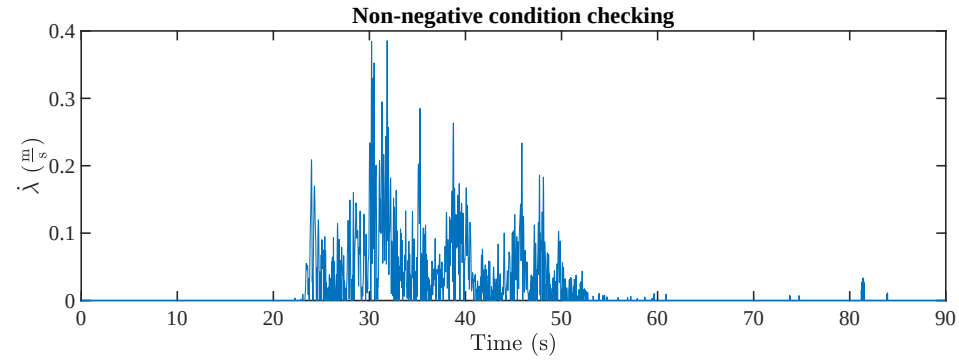

(a) The history of $\dot{\lambda}$ value

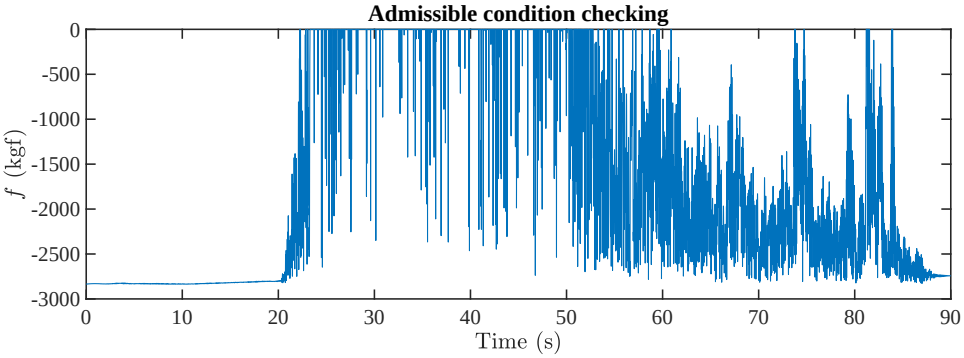

(b) The history of f value

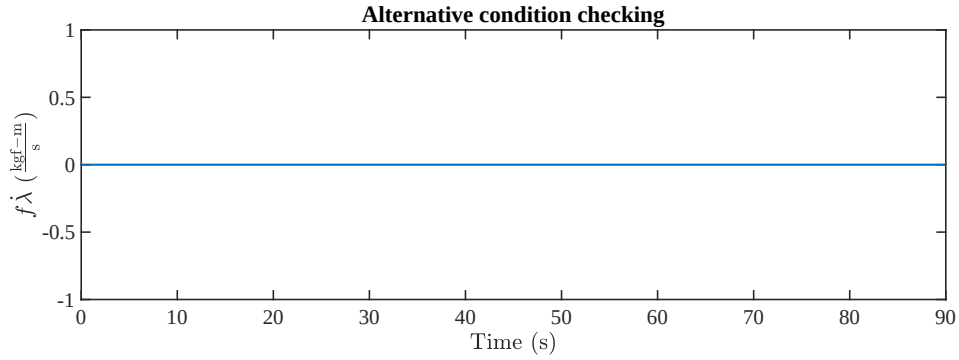

(c) The history of $f\dot{\lambda}$ value

Figure 3.3: The response of $\dot{\lambda}$, f, $f\dot{\lambda}$ of symmetric building structures under the seismic record of the TCU071 station during Chi-Chi earthquake

doi:10.6342/NTU202402645

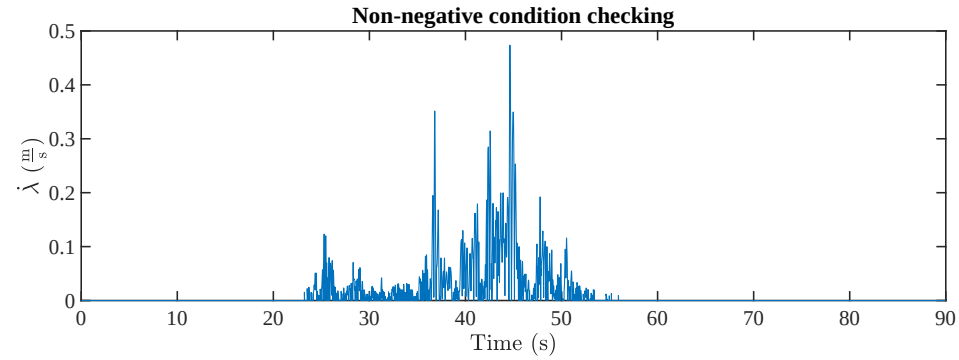

(a) The history of $\dot{\lambda}$ value

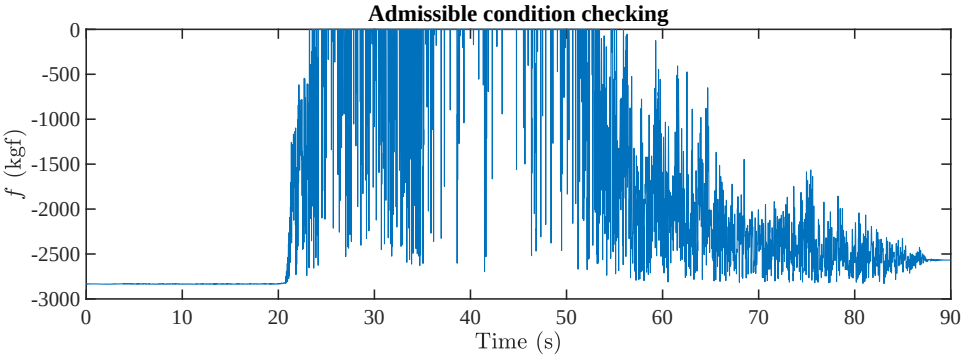

(b) The history of f value

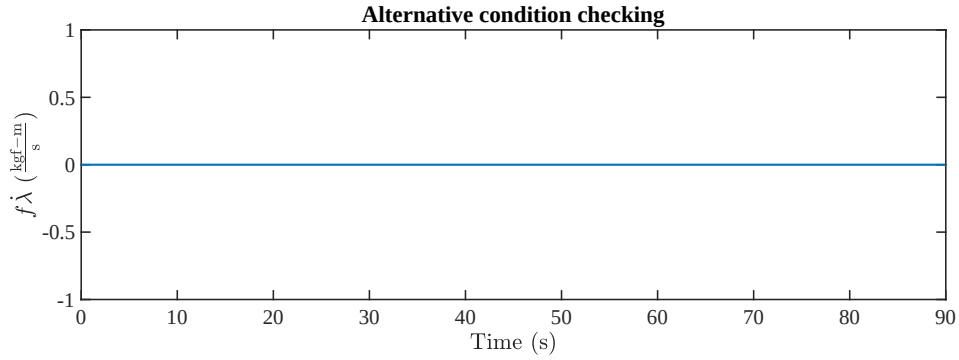

(c) The history of $f\dot{\lambda}$ value

Figure 3.4: The response of $\dot{\lambda}$, f, $f\dot{\lambda}$ of symmetric building structures under the seismic record of the TCU079 station during Chi-Chi earthquake

doi:10.6342/NTU202402645

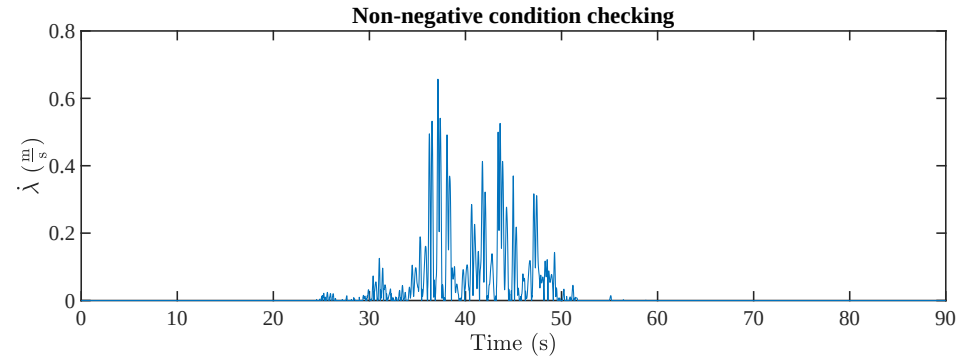

(a) The history of $\dot{\lambda}$ value

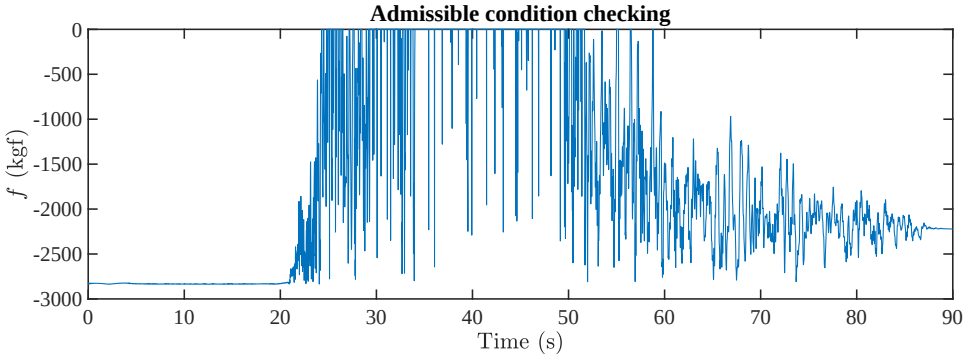

(b) The history of f value

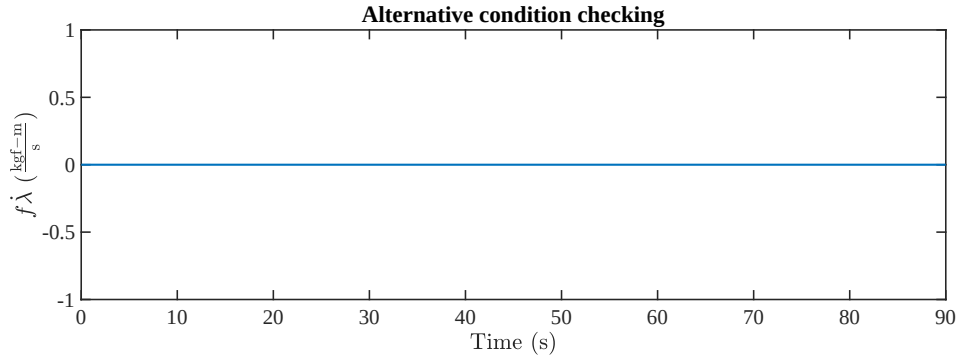

(c) The history of $f\dot{\lambda}$ value

Figure 3.5: The response of $\dot{\lambda}$, f, $f\dot{\lambda}$ of symmetric building structures under the seismic record of the TCU084 station during Chi-Chi earthquake

doi:10.6342/NTU202402645

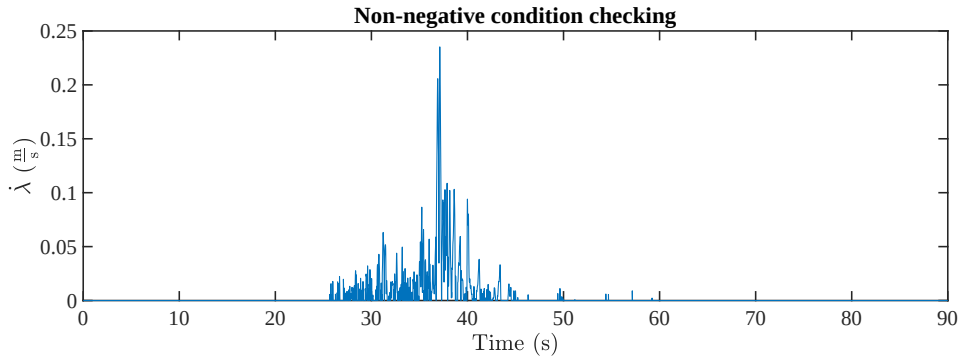

(a) The history of $\dot{\lambda}$ value

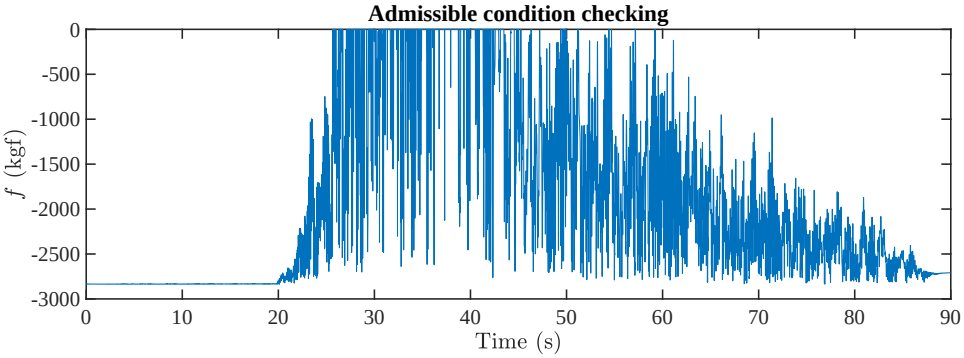

(b) The history of f value

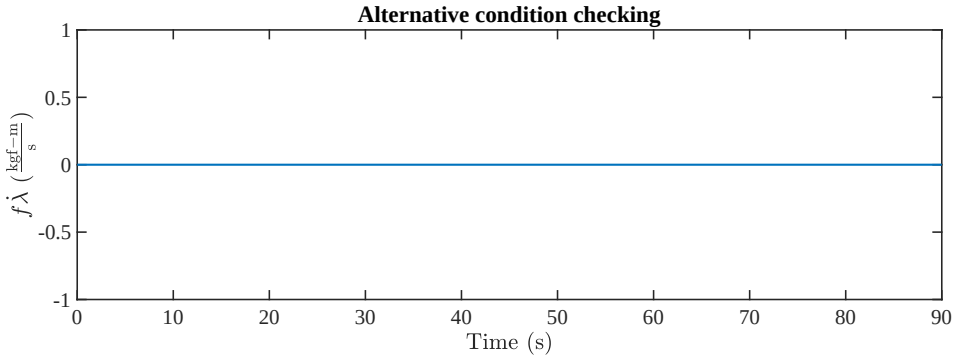

(c) The history of $f\dot{\lambda}$ value

Figure 3.6: The response of $\dot{\lambda}$, f, $f\dot{\lambda}$ of symmetric building structures under the seismic record of the CHY101 station during Chi-Chi earthquake

doi:10.6342/NTU202402645

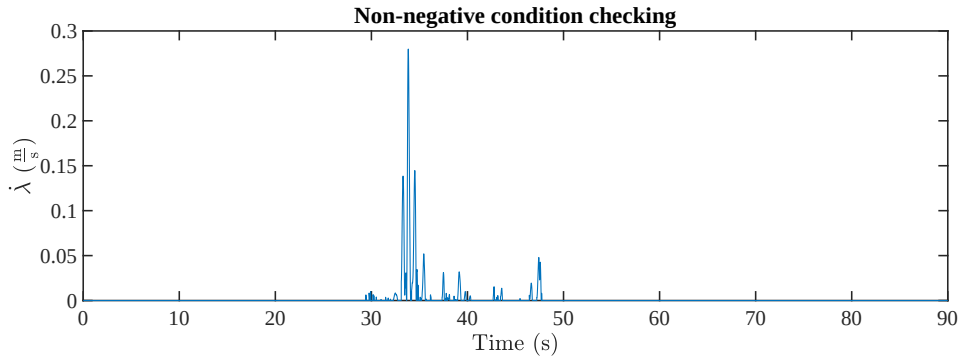

(a) The history of $\dot{\lambda}$ value

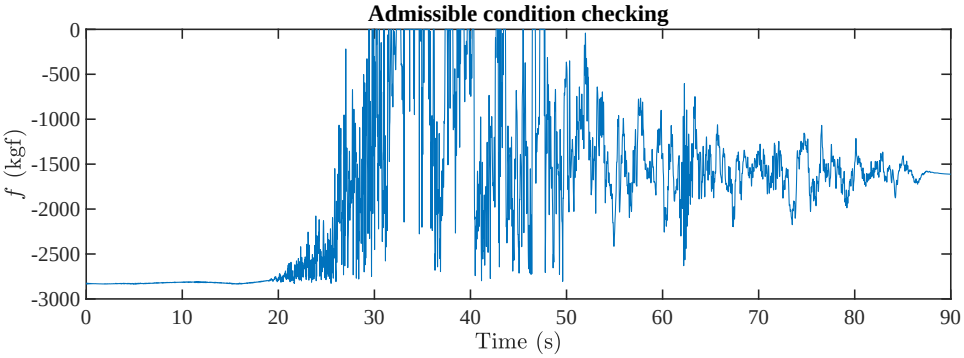

(b) The history of f value

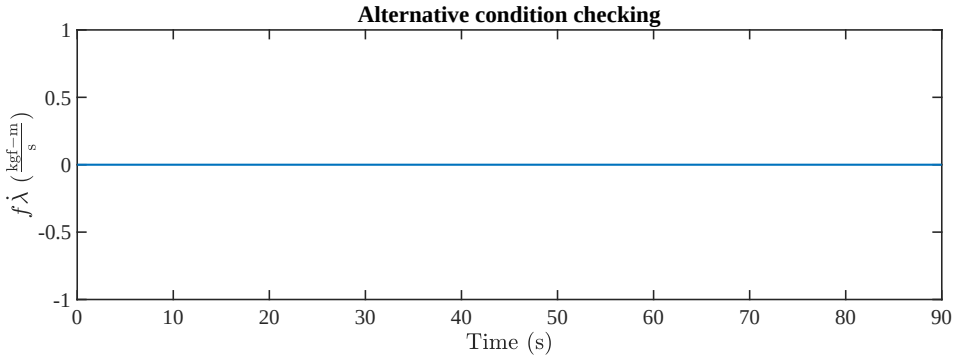

(c) The history of $f\dot{\lambda}$ value

Figure 3.7: The response of $\dot{\lambda}$, f, $f\dot{\lambda}$ of symmetric building structures under the seismic record of the TCU052 station during Chi-Chi earthquake

doi:10.6342/NTU202402645

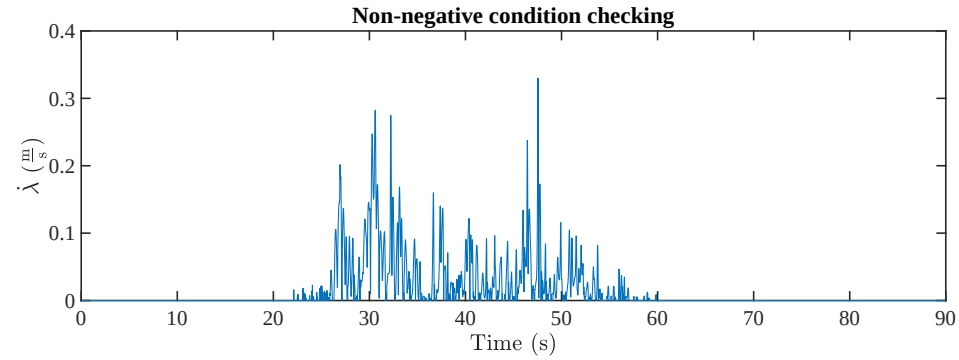

(a) The history of $\dot{\lambda}$ value

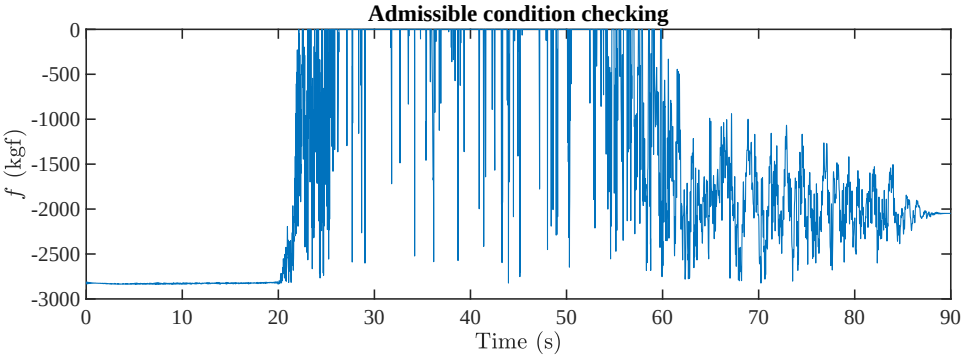

(b) The history of f value

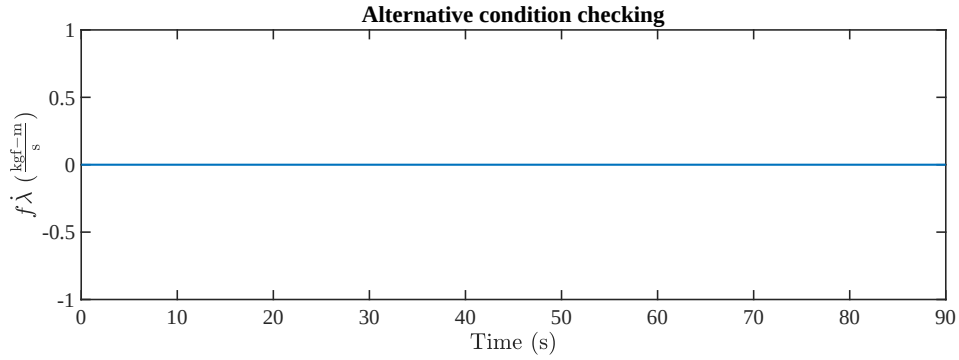

(c) The history of $f\dot{\lambda}$ value

Figure 3.8: The response of $\dot{\lambda}$, f, $f\dot{\lambda}$ of symmetric building structures under the seismic record of the TCU065 station during Chi-Chi earthquake

doi:10.6342/NTU202402645

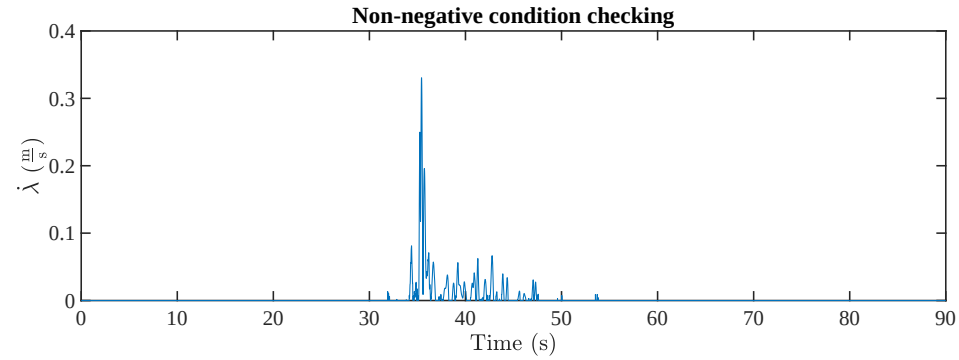

(a) The history of $\dot{\lambda}$ value

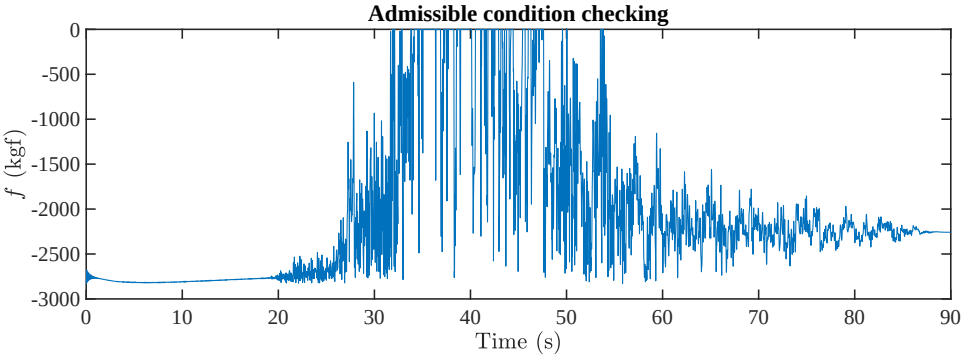

(b) The history of f value

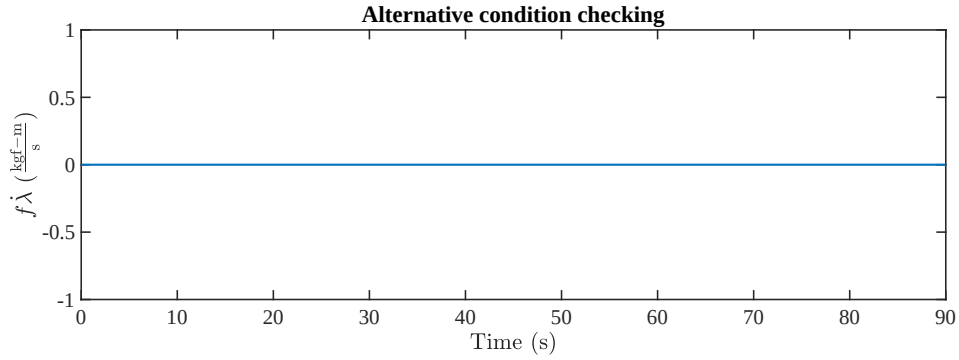

(c) The history of $f\dot{\lambda}$ value

Figure 3.9: The response of $\dot{\lambda}$, f, $f\dot{\lambda}$ of symmetric building structures under the seismic record of the TCU068 station during Chi-Chi earthquake

doi:10.6342/NTU202402645

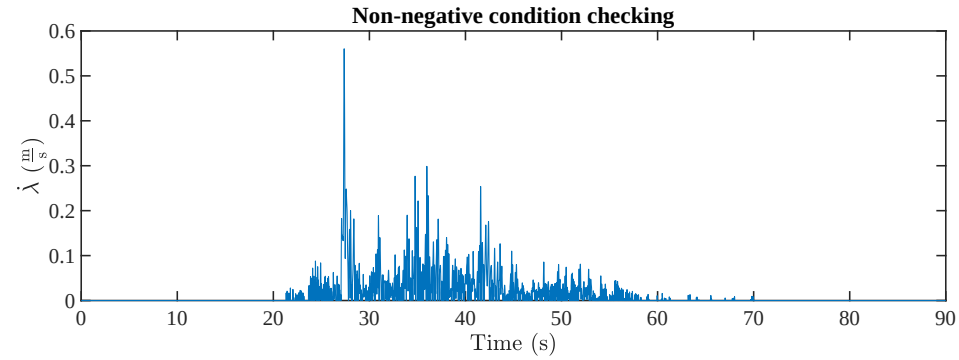

(a) The history of $\dot{\lambda}$ value

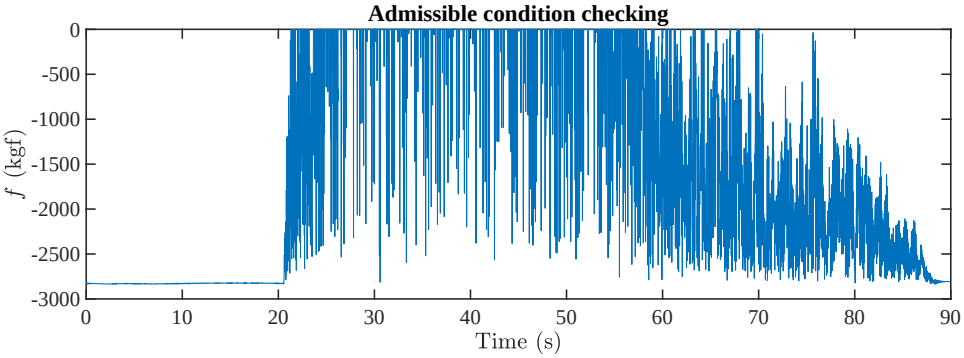

(b) The history of f value

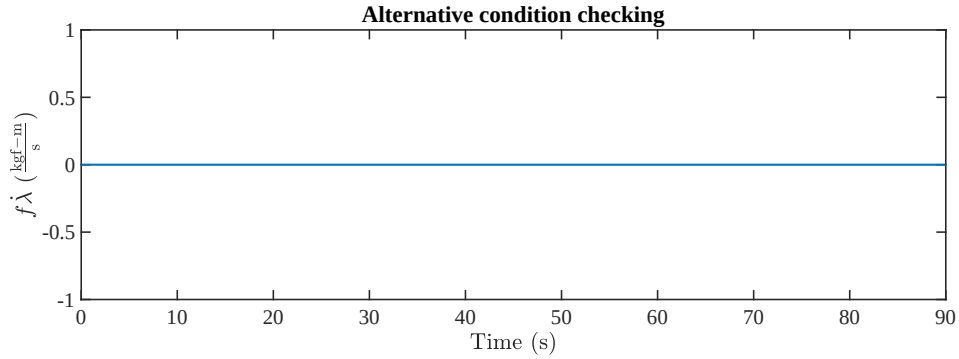

(c) The history of $f\dot{\lambda}$ value

Figure 3.10: The response of $\dot{\lambda}$, f, $f\dot{\lambda}$ of symmetric building structures under the seismic record of the TCU129 station during Chi-Chi earthquake

doi:10.6342/NTU202402645

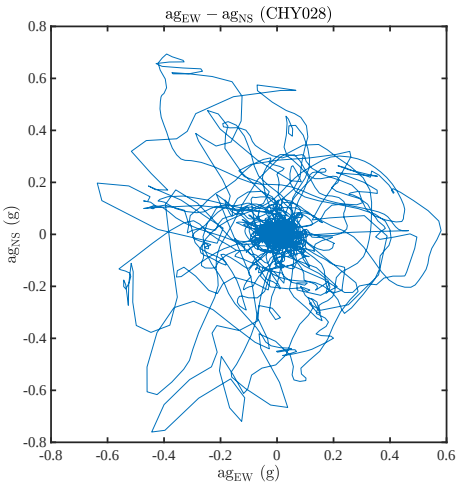

(a) Bidirectional plot of ground acceleration

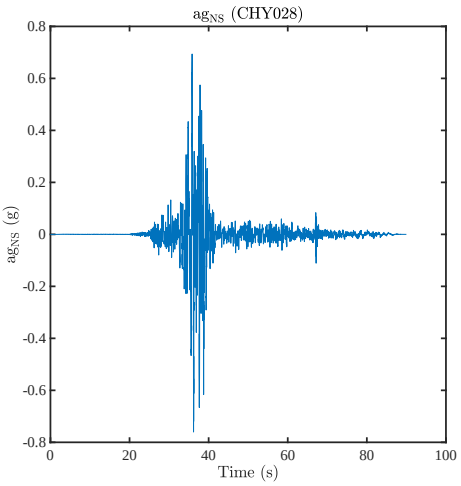

(b) N-S ground acceleration history

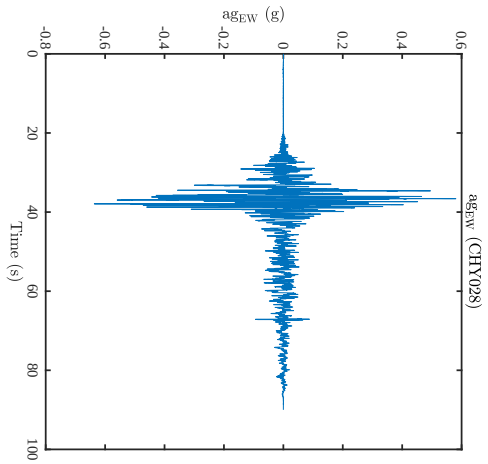

(c) E-W ground acceleration history

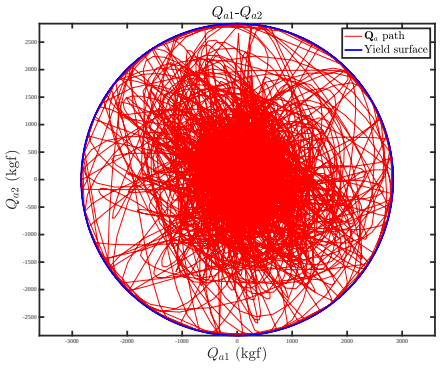

(d) Trajectory of $\mathbf{Q}_a$ for symmetric building structures

Figure 3.11: Ground acceleration at CHY028 station of Chi-Chi earthquake and trajectory of $\mathbf{Q}_a$ for symmetric building structures under bidirectional acceleration at CHY028 station of the Chi-Chi earthquake event

doi:10.6342/NTU202402645

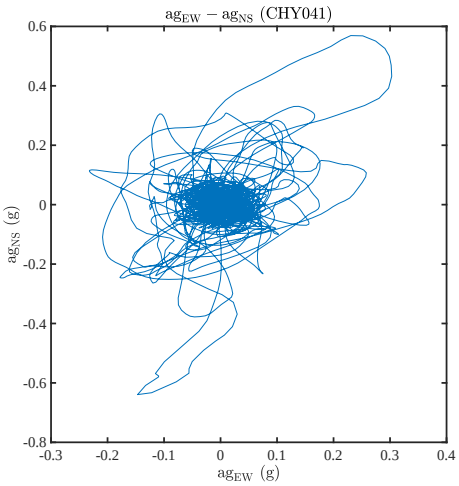

(a) Bidirectional plot of ground acceleration

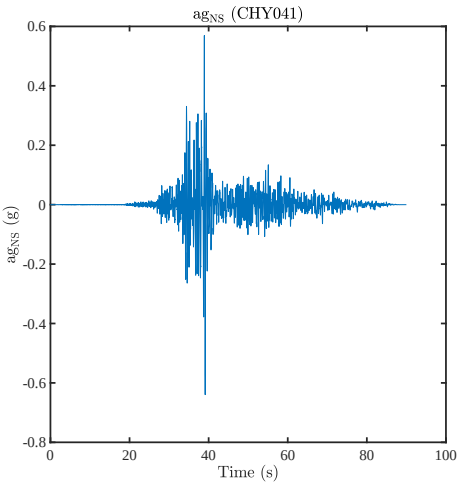

(b) N-S ground acceleration history

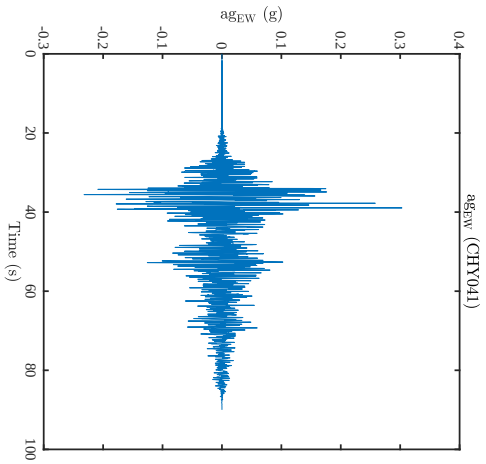

(c) E-W ground acceleration history

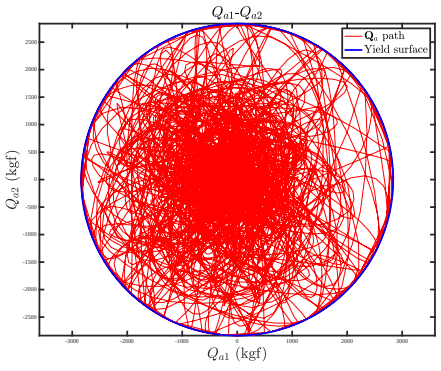

(d) Trajectory of $\mathbf{Q}_a$ for symmetric building structures

Figure 3.12: Ground acceleration at CHY041 station of Chi-Chi earthquake and trajectory of $\mathbf{Q}_a$ for symmetric building structures under bidirectional acceleration at CHY041 station of the Chi-Chi earthquake event

doi:10.6342/NTU202402645

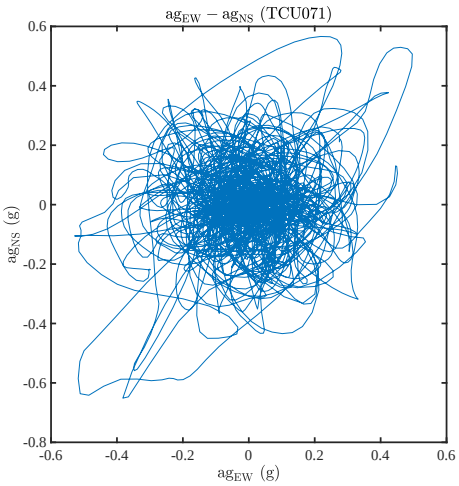

(a) Bidirectional plot of ground acceleration

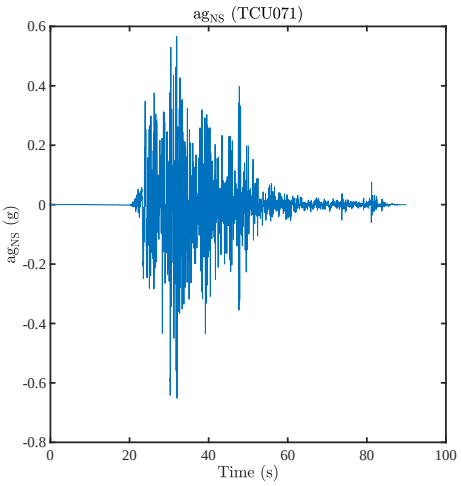

(b) N-S ground acceleration history

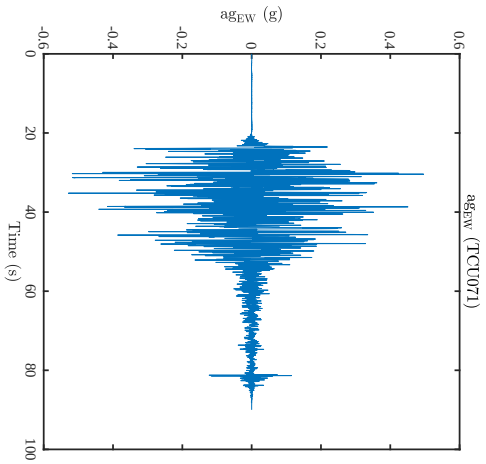

(c) E-W ground acceleration history

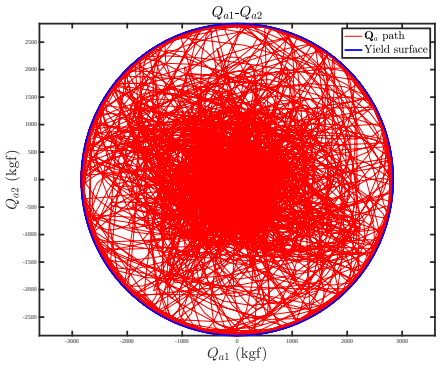

(d) Trajectory of $\mathbf{Q}_a$ for symmetric building structures

Figure 3.13: Ground acceleration at TCU071 station of Chi-Chi earthquake and trajectory of $\mathbf{Q}_a$ for symmetric building structures under bidirectional acceleration at TCU071 station of the Chi-Chi earthquake event

doi:10.6342/NTU202402645

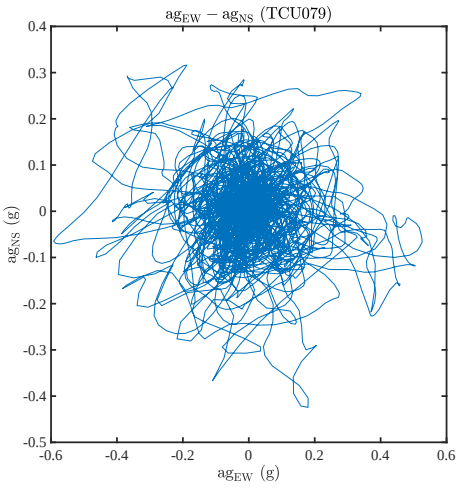

(a) Bidirectional plot of ground acceleration

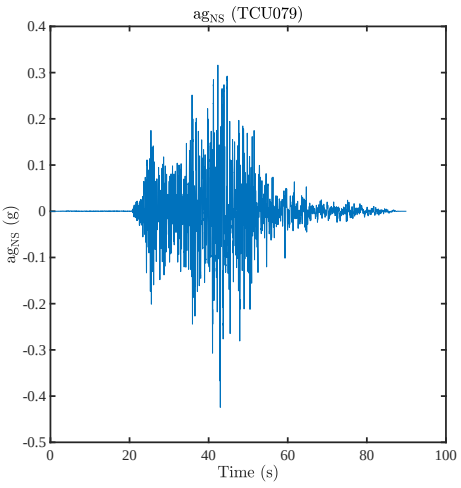

(b) N-S ground acceleration history

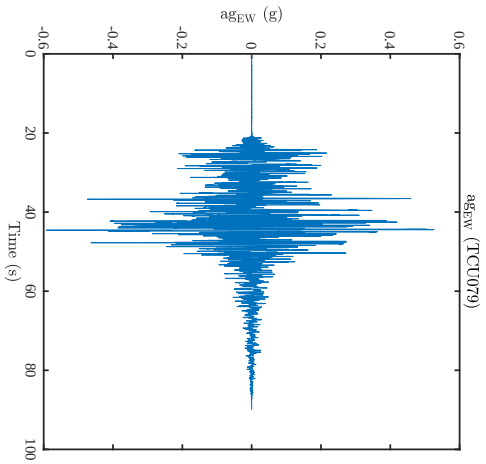

(c) E-W ground acceleration history

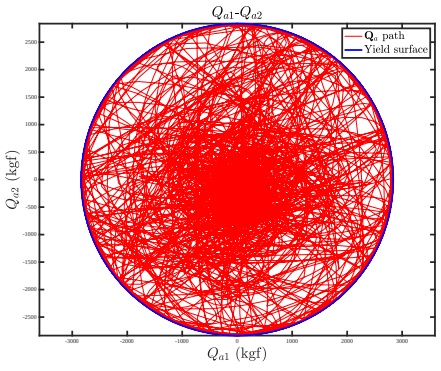

(d) Trajectory of $\mathbf{Q}_a$ for symmetric building structures

Figure 3.14: Ground acceleration at TCU079 station of Chi-Chi earthquake and trajectory of $\mathbf{Q}_a$ for symmetric building structures under bidirectional acceleration at TCU079 station of the Chi-Chi earthquake event

doi:10.6342/NTU202402645

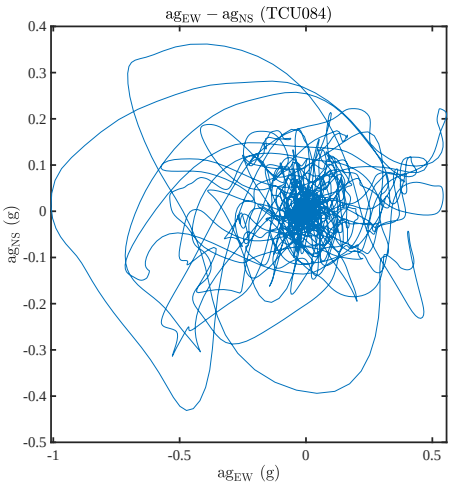

(a) Bidirectional plot of ground acceleration

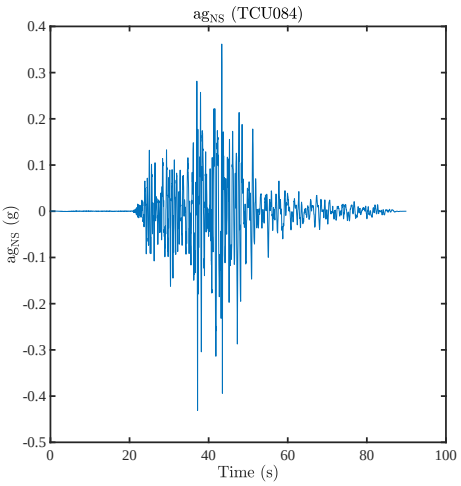

(b) N-S ground acceleration history

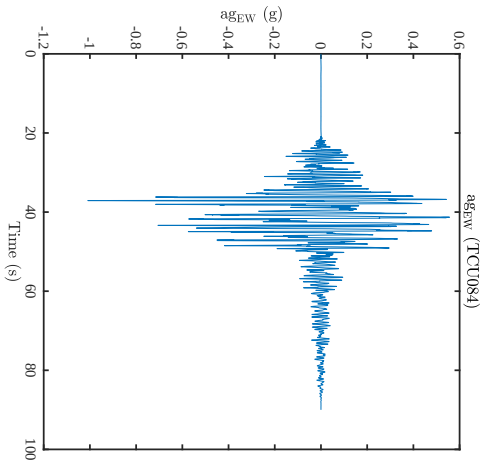

(c) E-W ground acceleration history

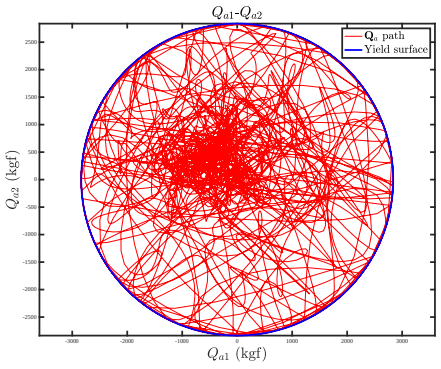

(d) Trajectory of $\mathbf{Q}_a$ for symmetric building structures

Figure 3.15: Ground acceleration at TCU084 station of Chi-Chi earthquake and trajectory of $\mathbf{Q}_a$ for symmetric building structures under bidirectional acceleration at TCU084 station of the Chi-Chi earthquake event

doi:10.6342/NTU202402645

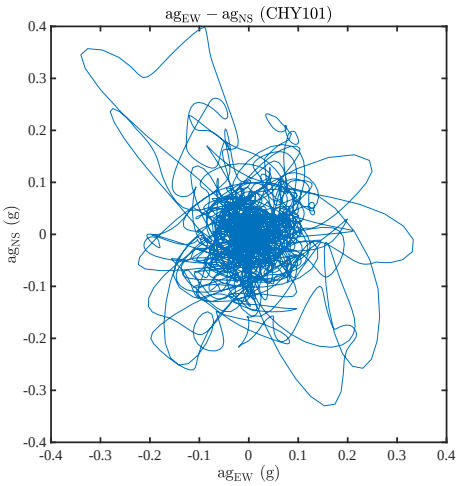

(a) Bidirectional plot of ground acceleration

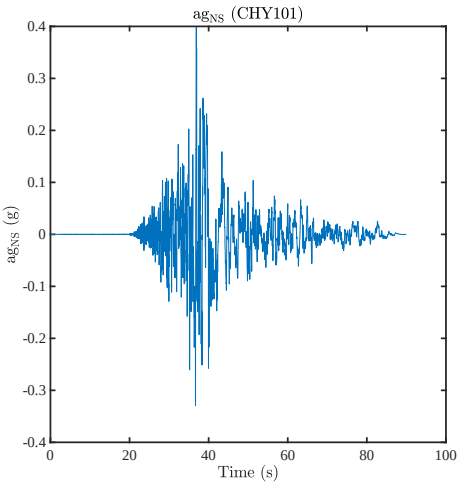

(b) N-S ground acceleration history

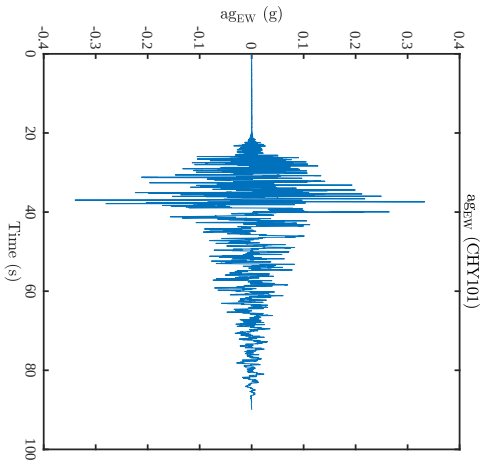

(c) E-W ground acceleration history

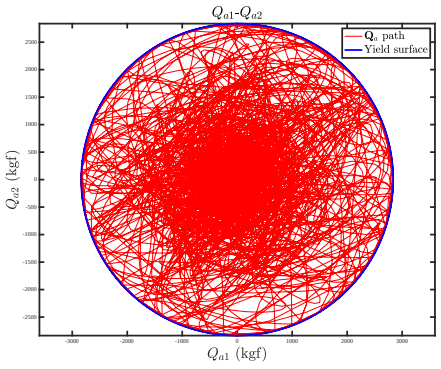

(d) Trajectory of $\mathbf{Q}_a$ for symmetric building structures

Figure 3.16: Ground acceleration at CHY101 station of Chi-Chi earthquake and trajectory of $\mathbf{Q}_a$ for symmetric building structures under bidirectional acceleration at CHY101 station of the Chi-Chi earthquake event

doi:10.6342/NTU202402645

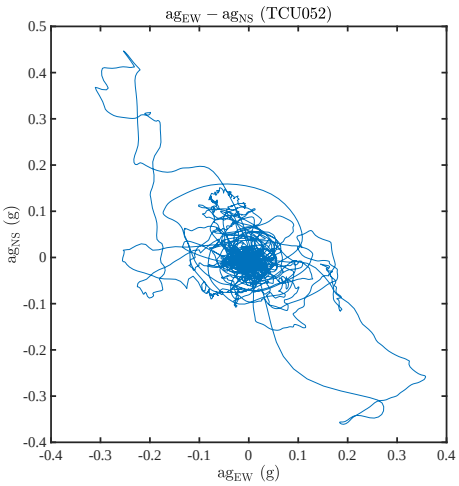

(a) Bidirectional plot of ground acceleration

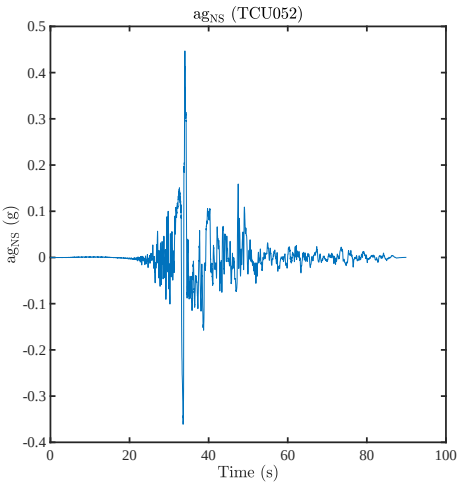

(b) N-S ground acceleration history

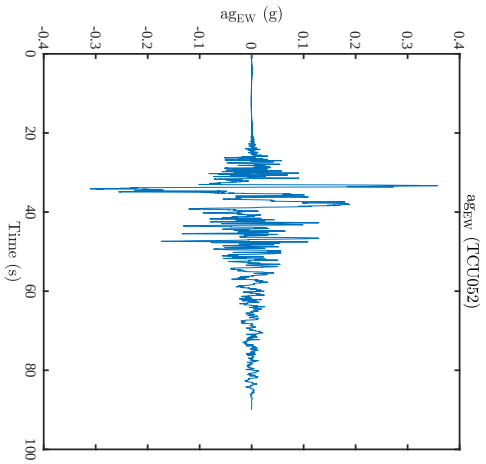

(c) E-W ground acceleration history

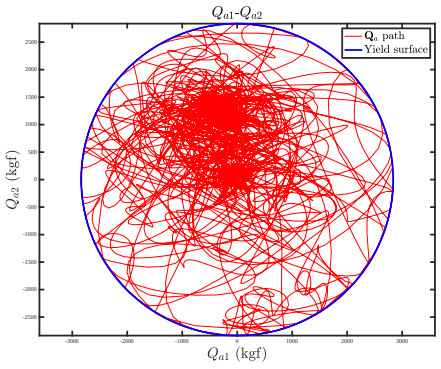

(d) Trajectory of $\mathbf{Q}_a$ for symmetric building structures

Figure 3.17: Ground acceleration at TCU052 station of Chi-Chi earthquake and trajectory of $\mathbf{Q}_a$ for symmetric building structures under bidirectional acceleration at TCU052 station of the Chi-Chi earthquake event

doi:10.6342/NTU202402645

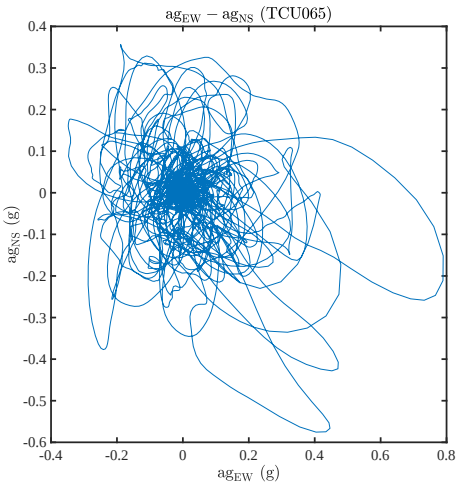

(a) Bidirectional plot of ground acceleration

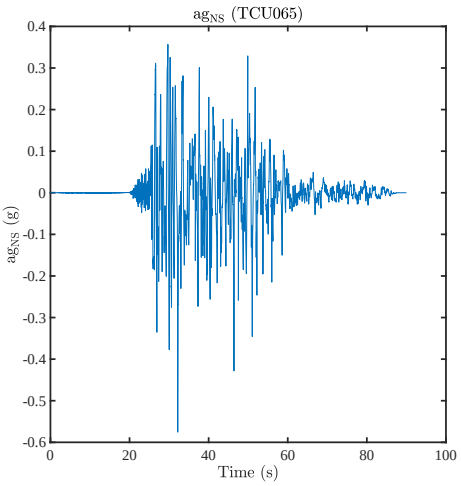

(b) N-S ground acceleration history

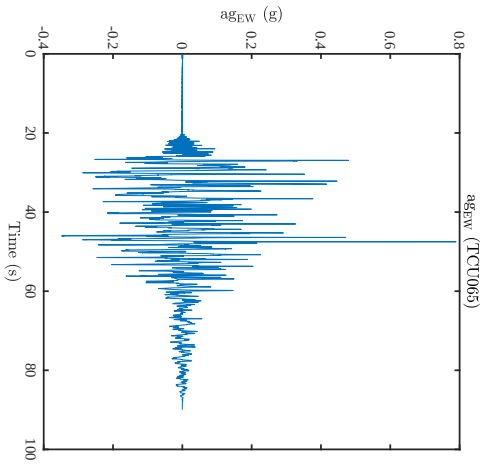

(c) E-W ground acceleration history

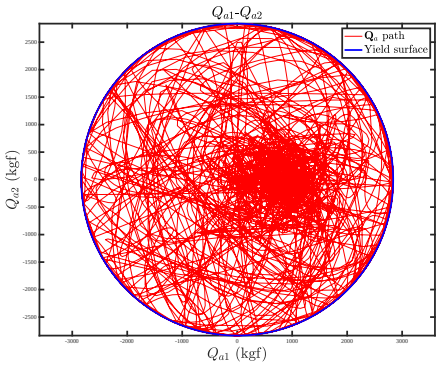

(d) Trajectory of $\mathbf{Q}_a$ for symmetric building structures

Figure 3.18: Ground acceleration at TCU065 station of Chi-Chi earthquake and trajectory of $\mathbf{Q}_a$ for symmetric building structures under bidirectional acceleration at TCU065 station of the Chi-Chi earthquake event

doi:10.6342/NTU202402645

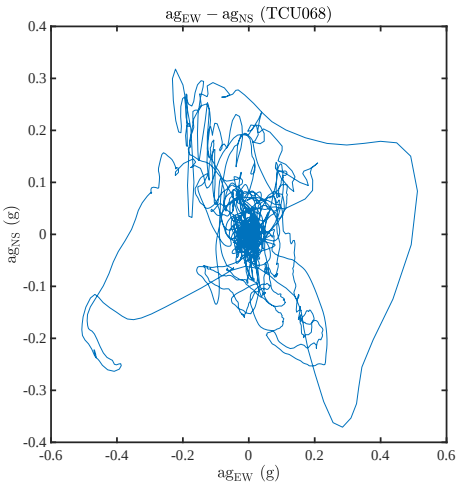

(a) Bidirectional plot of ground acceleration

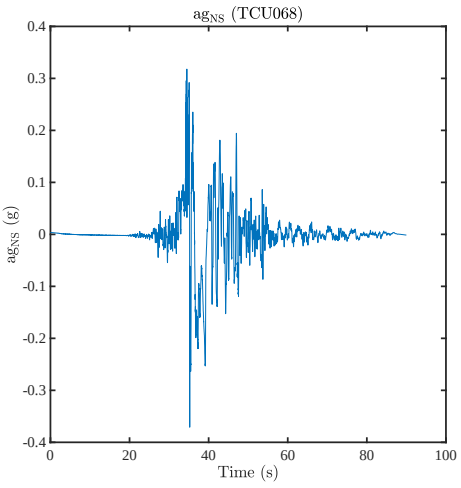

(b) N-S ground acceleration history

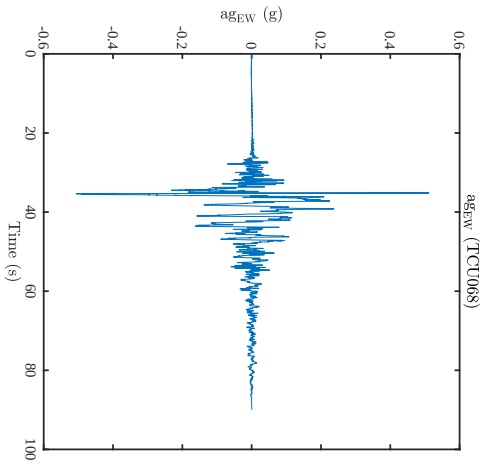

(c) E-W ground acceleration history

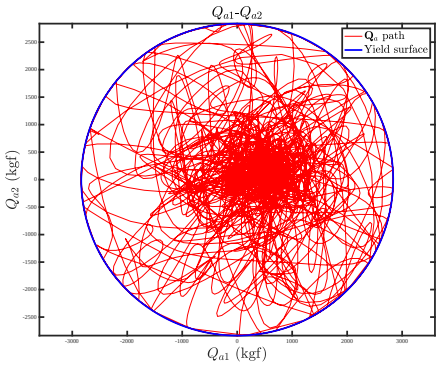

(d) Trajectory of $\mathbf{Q}_a$ for symmetric building structures

Figure 3.19: Ground acceleration at TCU068 station of Chi-Chi earthquake and trajectory of $\mathbf{Q}_a$ for symmetric building structures under bidirectional acceleration at TCU068 station of the Chi-Chi earthquake event

doi:10.6342/NTU202402645

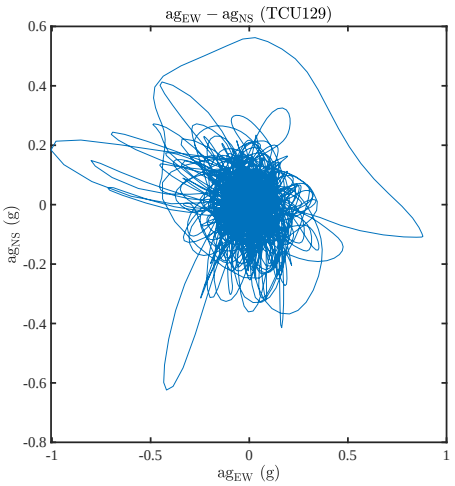

(a) Bidirectional plot of ground acceleration

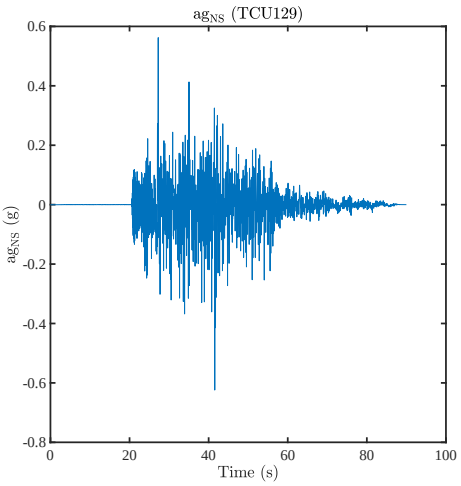

(b) N-S ground acceleration history

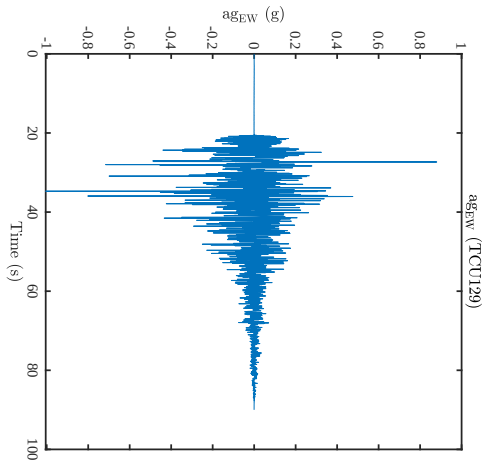

(c) E-W ground acceleration history

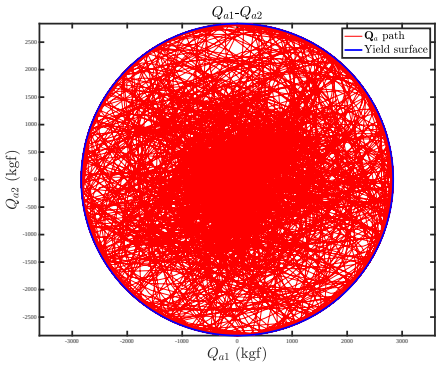

(d) Trajectory of $\mathbf{Q}_a$ for symmetric building structures

Figure 3.20: Ground acceleration at TCU129 station of Chi-Chi earthquake and trajectory of $\mathbf{Q}_a$ for symmetric building structures under bidirectional acceleration at TCU129 station of the Chi-Chi earthquake event

doi:10.6342/NTU202402645

3.2 Responses of the symmetric building structure under bidirectional and unidirectional earthquake excitations

In this section, we will compare the differences in peak responses between bidirectional and unidirectional seismic analyses. First, we will use the viscoelastoplastic model proposed in this study to perform a unidirectional seismic analysis on an symmetric building structure. Then, we will conduct a bidirectional seismic analysis. Finally, we will compare the differences between the bidirectional and unidirectional seismic analyses. The structural mass is $m_s = 2409.785933 \quad \left(\frac{\text{kgf}-\text{s}^2}{\text{m}}\right)$. The elastic lateral stiffness is $k_e = 7454411.908 \quad \left(\frac{kgf}{m}\right)$. The post-yield stiffness $k_p = 0.05k_e$. The structural damping coefficient $c = 2\xi\sqrt{k_e m_s} \quad \left(\frac{kgf-s}{m}\right)$. The story yield shear force $Q_y = C_s \times W$, where W is the structural weight, and C_s is taken as 0.12 based on empirical data.

3.2.1 Approximate analysis of symmetric building structures under unidirectional earthquake

For the unidirectional analysis, we input the structural parameters of the symmetric building into the viscoelastoplastic model. We then select earthquake acceleration time histories from one station and input them individually into the viscoelastoplastic model for analysis. In this case, we choose the earthquake acceleration data from the TCU084 station during the Chi-Chi earthquake event as input for analysis.

First, we input only the E-W direction acceleration data from the TCU084 station into the viscoelastoplastic model, record the interstory displacement time history and interstory shear force time history, and examine the peak responses. Next, we input only the N-S

doi:10.6342/NTU202402645

direction acceleration data from the TCU084 station into the viscoelastoplastic model, record the displacement time history and shear force time history, and examine the peak responses.

The results of the E-W direction unidirectional analysis are shown in Figures 3.21 to 3.22. Figure 3.21 shows the interstory displacement time history with a peak interstory displacement of 0.073 m. Figure 5.22 shows the interstory shear force time history with a peak interstory shear force of 30791.569 kgf.

The results of the N-S direction unidirectional analysis are shown in Figures 3.23 to 3.24. Figure 3.23 shows the interstory displacement time history with a peak interstory displacement of 0.018 m. Figure 3.24 shows the interstory shear force time history with a peak interstory shear force of 9405.018 kgf.

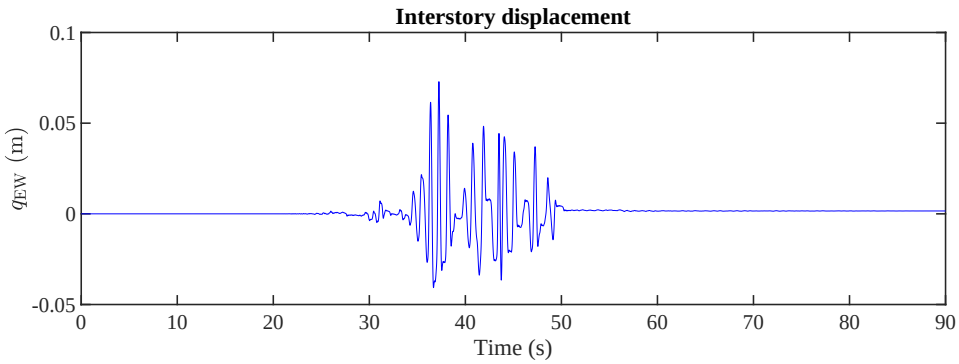

Figure 3.21: Interstory displacement time history for E-W unidirectional analysis of symmetric building structures

doi:10.6342/NTU202402645

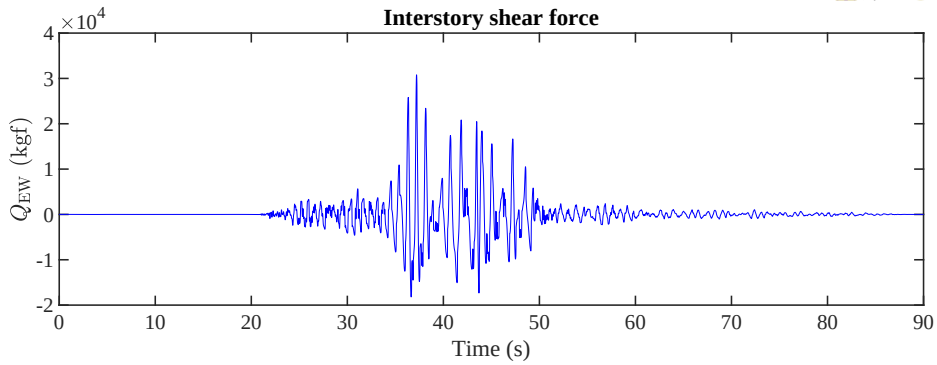

Figure 3.22: Interstory shear force time history for E-W unidirectional analysis of symmetric building structures

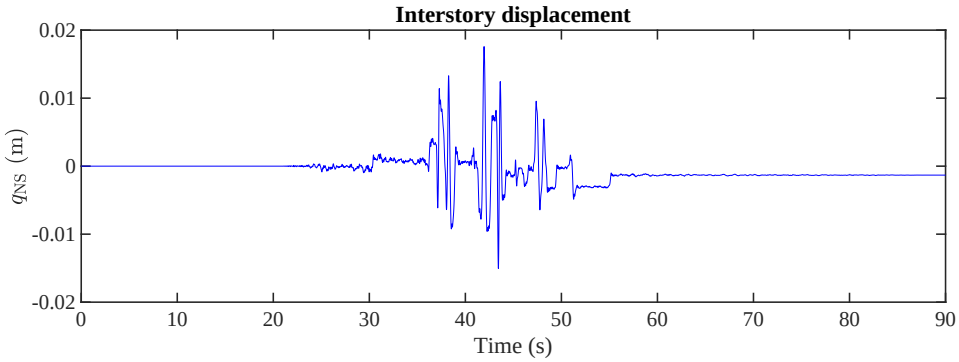

Figure 3.23: Interstory displacement time history for N-S unidirectional analysis of symmetric building structures

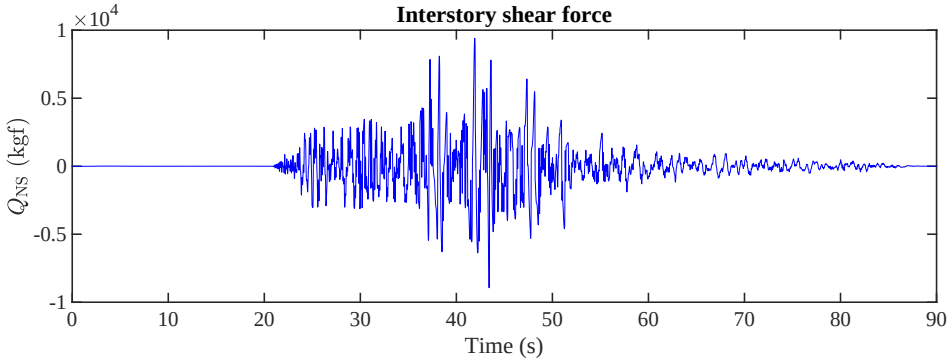

Figure 3.24: Interstory shear force time history for N-S unidirectional analysis of symmetric building structures

3.2.2 Accurate analysis of symmetric building structures under bidirectional earthquake

For the bidirectional analysis, we input the structural parameters of the symmetric building into the viscoelastoplastic model. We then select earthquake acceleration time

doi:10.6342/NTU202402645

histories from one station and input them simultaneously in both directions into the viscoelastoplastic model for analysis. In this case, we choose the earthquake acceleration data from the TCU084 station during the Chi-Chi earthquake event as input for analysis.

We input both the E-W and N-S direction acceleration data from the TCU084 station simultaneously into the viscoelastoplastic model, record the bidirectional interstory displacement time history and bidirectional interstory shear force time history, and examine the peak responses.

The results of the bidirectional analysis are shown in Figures 5.25 to 5.28. Figure 5.25 shows the E-W direction interstory displacement time history from the bidirectional analysis, with a peak interstory displacement of 0.074 m. Figure 5.25 shows the N-S direction interstory displacement time history from the bidirectional analysis, with a peak interstory displacement of 0.024 m. Figure 5.26 shows the E-W direction interstory shear force time history from the bidirectional analysis, with a peak interstory shear force of 30687.607 kgf. Figure 5.26 shows the N-S direction interstory shear force time history from the bidirectional analysis, with a peak interstory shear force of 11880.063 kgf.

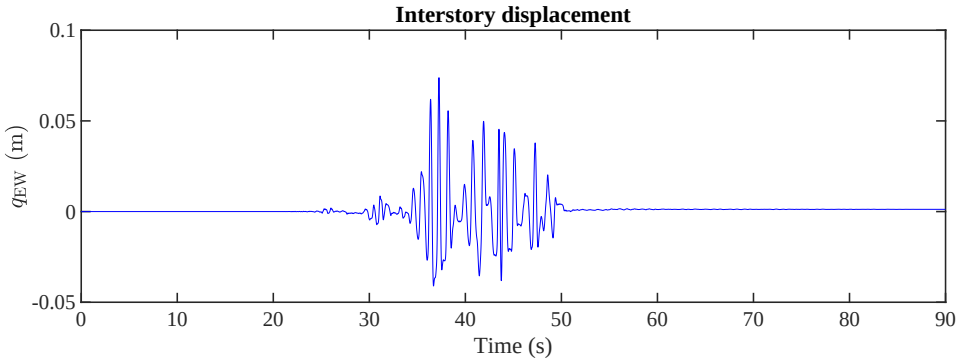

Figure 3.25: Interstory displacement time history for E-W bidirectional analysis of symmetric building structures

doi:10.6342/NTU202402645

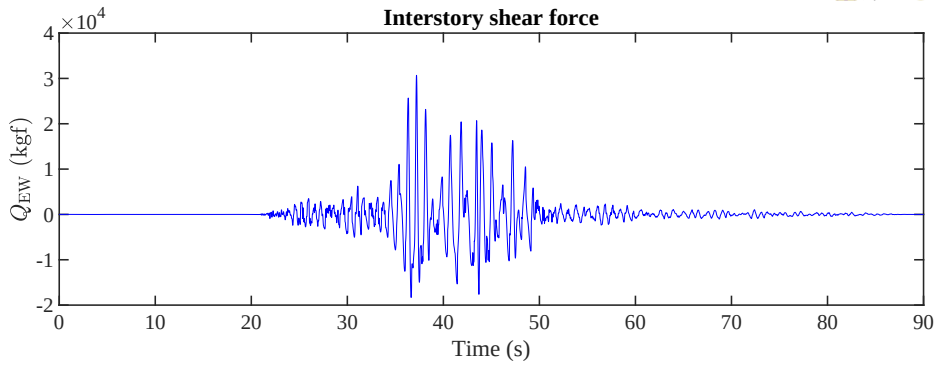

Figure 3.26: Interstory shear force time history for E-W bidirectional analysis of symmetric building structures

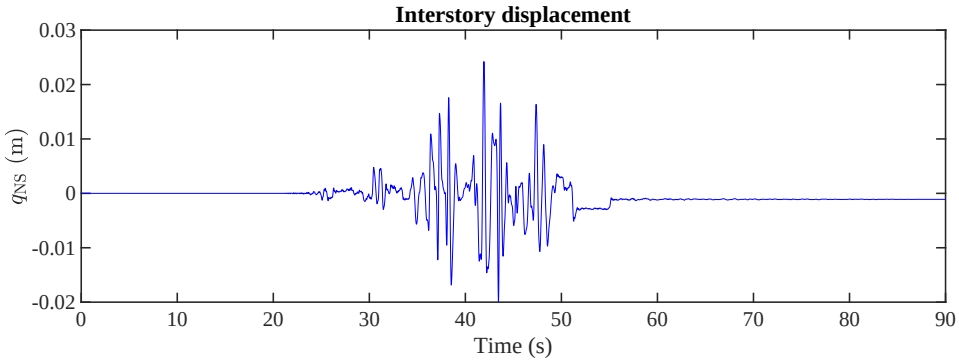

Figure 3.27: Interstory displacement time history for N-S bidirectional analysis of symmetric building structures

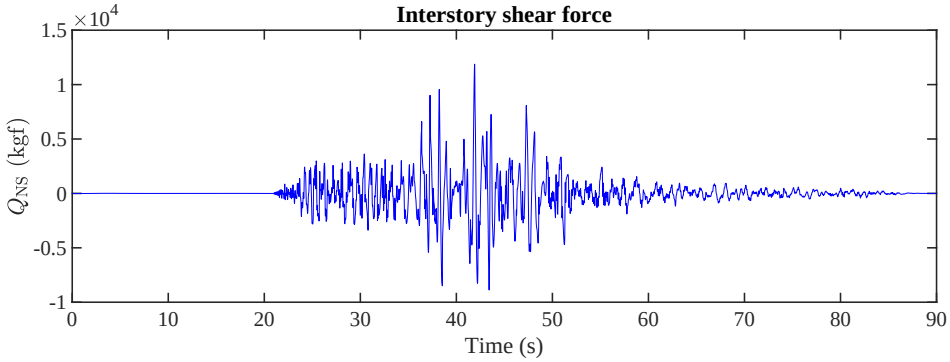

Figure 3.28: Interstory shear force time history for N-S bidirectional analysis of symmetric building structures

3.2.3 Comparisons of unidirectional and bidirectional analysis for symmetric building structures

Sections 3.2.1 and 3.2.2 analyze the peak responses of interstory displacement and interstory shear force for an symmetric structure using unidirectional and bidirectional

doi:10.6342/NTU202402645

analyses, respectively. The results show that the unidirectional analysis underestimates the peak inter-story displacement in the E-W direction by 1.35% and in the N-S direction by 25% compared to the bidirectional analysis. The peak interstory shear force in the E-W direction is overestimated by 0.3% in the unidirectional analysis, while in the N-S direction, it is overestimated by 20.83%.

These results suggest that unidirectional analysis may significantly underestimate or miscalculate the seismic response of building structures. To further investigate and validate these findings, this subsection compares the differences in peak responses between bidirectional and unidirectional seismic analyses. We examine the impact of these differences on the total number of viscoelastoplastic-phase time steps, equivalent, peak interstory displacement response, and peak interstory shear force response for symmetric building structures.

The bidirectional seismic analysis uses acceleration data from 10 stations during the 1999 Chi-Chi earthquake event. For each station, we input the E-W and N-S acceleration time histories simultaneously into the viscoelastoplastic model and record the peak responses. For the unidirectional seismic analysis, we input the acceleration data from the same 10 stations separately, using only the E-W or only the N-S acceleration time history. When comparing the analysis results, we compare the peak responses of the two unidirectional analyses with the total response of the bidirectional analysis.

First, from Figure 3.29, we can see that for the acceleration time histories of these 10 stations, unidirectional analysis, whether using East-West or North-South input, significantly underestimates the total number of viscoelastoplastic-phase time steps occurrences in the building structure compared to bidirectional analysis. On average, using only unidi-

doi:10.6342/NTU202402645

rectional E-W analysis underestimates the total number of viscoelastoplastic-phase time steps occurrences by 33.158%, while using only unidirectional N-S analysis underestimates it by 41.049% compared to bidirectional analysis. This indicates that bidirectional analysis more accurately captures the total number of viscoelastoplastic-phase time steps occurrences in the building structure.

Next, Figure 3.30 shows the plastic equivalent response of the building structure. The plastic equivalent can be considered as a damage indicator for the building structure after an earthquake. The results show that unidirectional analysis significantly underestimates the plastic equivalent of the building structure after seismic activity compared to bidirectional analysis. On average, using only unidirectional E-W analysis underestimates the plastic equivalent by 40.949%, while using only unidirectional N-S analysis underestimates it by 58.574% compared to bidirectional analysis. This demonstrates that bidirectional analysis more accurately reflects the degree of damage to the building structure after an earthquake.

Furthermore, Figure 3.31 shows that the peak displacements from unidirectional analysis are significantly lower than those from bidirectional analysis. On average, using only unidirectional E-W analysis underestimates the interstory displacement by 23.927%, while using only unidirectional N-S analysis underestimates it by 40.357% compared to bidirectional analysis. This implies that bidirectional analysis is more accurate in capturing the interstory displacement of the building structure after seismic activity.

Finally, Figure 3.32 shows that the peak interstory shear forces from unidirectional analysis are generally lower than those from bidirectional analysis. However, exceptions are the N-S interstory shear force for TCU071, which is overestimated by 2.14%, and the

doi:10.6342/NTU202402645

E-W interstory shear force for TCU129, which is overestimated by 0.668%. On average, using only unidirectional E-W analysis underestimates the interstory shear force by 19.216%, while using only unidirectional N-S analysis underestimates it by 33.579% compared to bidirectional analysis. This indicates that bidirectional analysis is more accurate in capturing the interstory shear force of the building structure after seismic activity.

Here we calculate the formula for the underestimation effect as follows:

$$\text{Underestimation effect} = \left(\frac{\text{Unidirectional analysis} - \text{Bidirectional analysis}}{\text{Bidirectional analysis}} \right) 100\%. \tag{3.1}$$

In conclusion, bidirectional seismic analysis significantly outperforms unidirectional seismic analysis in capturing the behavior of building structures after seismic activity, showing higher accuracy in terms of the total number of viscoelastoplastic-phase time steps occurrences, plastic equivalent, interstory displacement, and peak interstory shear force responses. Therefore, to more accurately assess the impact of earthquakes on building structures, it is essential to adopt bidirectional seismic analysis.

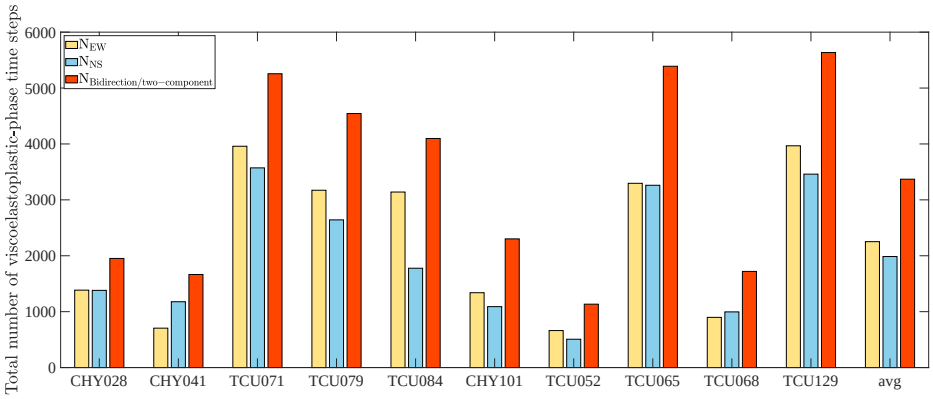

Figure 3.29: Total number of viscoelastoplastic-phase time steps for symmetric building structures

doi:10.6342/NTU202402645

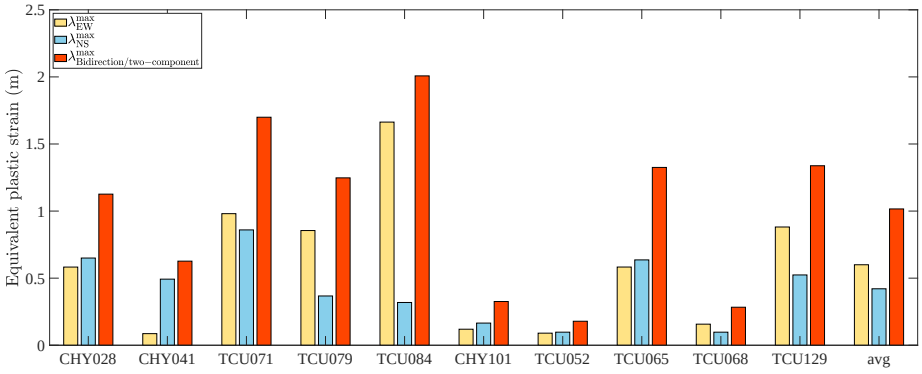

Figure 3.30: Equivalent plastic strain of symmetric building structures

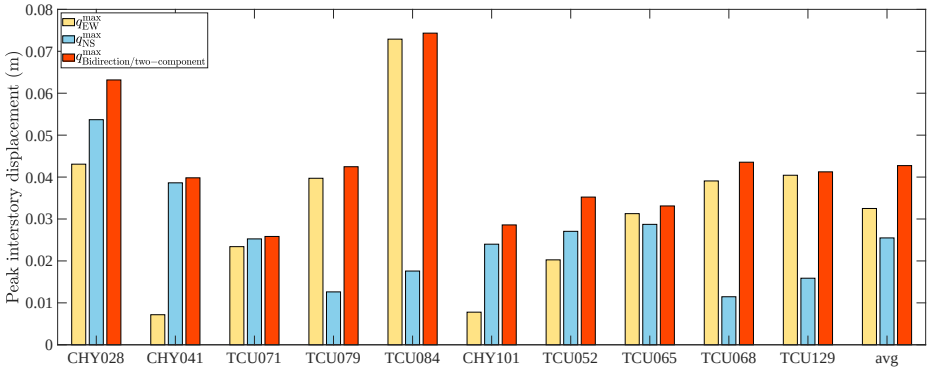

Figure 3.31: Peak interstory displacement of symmetric building structures

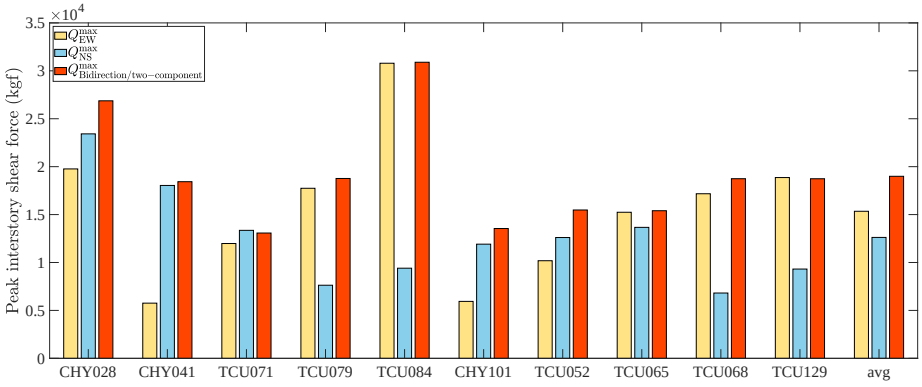

Figure 3.32: Peak interstory shear force of symmetric building structures

doi:10.6342/NTU202402645

3.3 The plastic equivalent of Taiwan under the 921 Chi-Chi earthquake event

In this section, we utilized data from the 921 Chi-Chi earthquake provided by the PEER Center (Pacific Earthquake Engineering Research Center), which includes bidirectional horizontal ground acceleration time histories from 295 stations, to conduct a plastic equivalent analysis across Taiwan. This extensive dataset provides us with a comprehensive understanding of seismic responses in various regions of Taiwan.

We input the parameters of symmetric building structures into the viscoelastoplastic model developed in this study. This model considers the viscoelastoplastic behavior of building structures, allowing for a more accurate simulation of actual structural responses under strong seismic actions. By inputting bidirectional horizontal acceleration time histories, we recorded the plastic equivalent values of symmetric building structures after the earthquake. This method enables us to evaluate the plastic damage experienced by buildings in different directions.

The analysis process is as follows: first, we recorded the latitude and longitude coordinates corresponding to each station, then converted these coordinates into x-y coordinates for representation on a plane map. Next, we recorded the plastic equivalent response values at each station's location. Finally, we presented the data in the form of an plastic equivalent distribution, intuitively displaying the damage distribution across Taiwan.

This result reflects the degree of plastic damage that symmetric building structures throughout Taiwan might suffer under the Chi-Chi earthquake event. It provides us with a valuable tool to roughly predict the potential damage levels in various regions during fu-

doi:10.6342/NTU202402645

ture similar earthquakes. This predictive capability has significant implications for earthquake hazard prediction and analysis.

As shown in Figure 3.33, the analysis results indicate that areas with higher plastic equivalent values are mainly concentrated in the central region, especially near Taichung and Nantou. The red dot in the figure marks the location of the earthquake epicenter. This finding reveals the damage distribution of symmetric building structures across Taiwan, with areas near the epicenter exhibiting the most severe plastic damage. The central region experienced the most significant impact, which is closely related to the propagation characteristics of seismic waves.

Notably, our analysis results highly correspond with the actual observed damage after the 921 Chi-Chi earthquake. This consistency not only verifies the accuracy of the viscoelastoplastic model proposed in this study but also demonstrates its practical value in conducting large-scale damage estimation. This finding is significant for the field of earthquake engineering as it provides a reliable tool for assessing the seismic resistance of existing building structures and formulating more targeted earthquake disaster mitigation strategies. It offers scientific evidence for urban planners and decision-makers to improve the overall seismic resilience of cities.

In summary, this study not only confirms the effectiveness of the proposed viscoelastoplastic model in analyzing large-scale damage estimation but also provides new insights for future earthquake engineering research and practice. We hope to further enhance our ability to predict and mitigate earthquake disasters, ultimately contributing to the construction of safer and more resilient urban environments.

doi:10.6342/NTU202402645

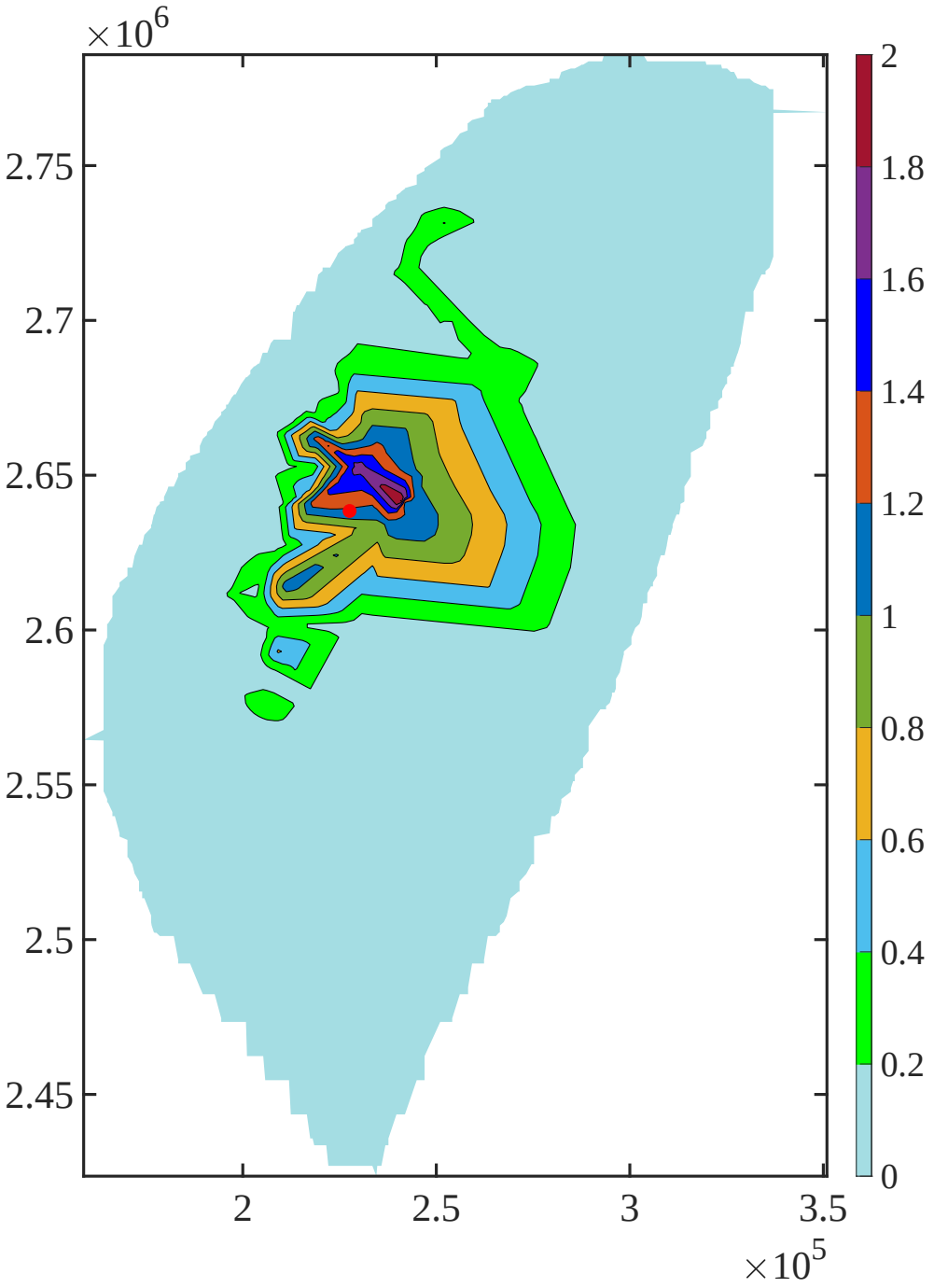

Figure 3.33: The plastic equivalent distribution

doi:10.6342/NTU202402645

3.3.1 CPU time for viscoelastoplastic analysis of symmetric building structures

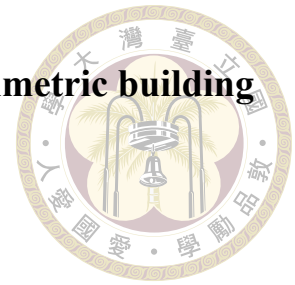

Section 3.3 We analyzed the equivalent plastic strain response of symmetric structures using acceleration data recorded from 295 stations during the Chi-Chi earthquake event in Taiwan. In this subsection, we document the time taken to analyze these 295 stations. We used a 2020 iMac computer with a 3.8 GHz 8-core Intel Core i7 processor for the calculations. The computation time for each station is shown in Figure 3.34. The results indicate that using the viscoelastoplastic model proposed in this study, the average computation time for analyzing the acceleration time histories of 295 stations was 8.30154936 seconds. This high performance can be attributed to several factors:

1. Our model considers two-dimensional responses, simplifying computational complexity while maintaining accuracy. 2. Accurate viscoelastoplastic behavior: The model incorporates precise representations of viscoelastoplastic behavior, enhancing the accuracy of results. 3. Elimination of complex nonlinear iterations: When symmetric building structures enter plastic states due to seismic excitation, our model does not require complex nonlinear iterations. This feature significantly reduces the computational burden. 4. Optimized algorithm: We proposed an algorithm flow that ensures all computational results satisfy the conditions of the viscoelastoplastic model. Based on this algorithm flow, we developed an efficient numerical method and optimized code, further reducing computation time.

To better understand this performance, traditional nonlinear analysis methods might require hours or even days of computation time for such a large dataset. Our model achieves comparable accuracy in just a few seconds, representing a significant advance-

doi:10.6342/NTU202402645

ment in computational efficiency.

These results strongly demonstrate that the viscoelastoplastic model proposed in this study is an efficient and accurate simplified model. It can quickly process large datasets while maintaining high precision, making it a valuable tool for seismic analysis and design of symmetric building structures. This model opens up new possibilities for large-scale seismic risk assessment and real-time structural health monitoring systems, where computational efficiency is crucial. In future work.

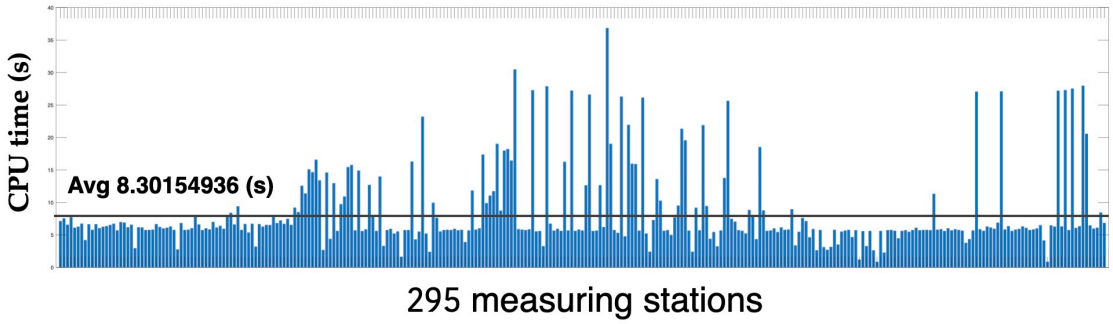

Figure 3.34: CPU time for viscoelastoplastic analysis of symmetric building structures

3.4 Analysis of incident angle of seismic excitations on symmetric building structures

In section 3.2, we learned that bidirectional analysis can more accurately capture the seismic response of symmetric building structures. This section will further explore the seismic behavior of symmetric building structures during earthquakes. The transmission of seismic forces actually occurs in the form of waves, while past structural analyses have mostly been conducted assuming seismic forces are transmitted through the principal axes. However, when seismic waves are transmitted to a building structure, they may not necessarily pass through the principal axes, but often have a certain angle of incidence. Therefore, this section will explore the impact of considering the angle of incidence of

doi:10.6342/NTU202402645

seismic waves on the seismic response of symmetric building structures, examining the responses of both bidirectional coupled (BDC) seismic analysis and biunidirectional uncoupled (BUU) seismic force analysis.

3.4.1 Biunidirectional uncoupled analysis of symmetric building structures

On the other hand, in the biunidirectional uncoupled (BUU) seismic analysis, we independently input the two acceleration time history data from the same station into the model, considering an angle of incidence for the analysis. The simplified concept is shown in Figure 3.35. We can express the form of external force input as follows:

$$\ddot{u}_{g_{\mathrm{EW}}}(\theta) = \ddot{u}_{g_{\mathrm{EW}}} \cos\theta, \tag{3.2}$$

$$\ddot{u}_{g_{\mathrm{NS}}}(\theta) = \ddot{u}_{g_{\mathrm{NS}}} \sin\theta, \tag{3.3}$$

where $\ddot{u}_{g_{\mathrm{EW}}}(\theta)$ represents the seismic force acceleration input of the east-west seismic wave with an incidence angle to the principal axis, and $\ddot{u}_{g_{\mathrm{NS}}}(\theta)$ represents the seismic force acceleration input of the north-south seismic wave with an incidence angle to the principal axis. During analysis, the two acceleration time history data are independently input into the model, considering the incidence angle between the seismic wave and the principal axis from 0° to 360° at one-degree intervals. The peak structural responses for each degree are recorded, including the peak interstory displacement and peak interstory shear force. The results of the two independent unidirectional analyses are then combined by taking the square root of the sum of their squares to represent the total structural response. These are represented in polar coordinates to show the structural response considering 360 degrees of incidence angles, exploring the impact of the incidence angle and comparing it with the

doi:10.6342/NTU202402645

results of bidirectional coupled (BDC) seismic analysis. The biunidirectional uncoupled (BUU) peak interstory displacement response and peak interstory shear force response are as follows:

$$q_{\max} = \sqrt{(q_{\mathrm{EW}}^{\max})^2 + (q_{\mathrm{NS}}^{\max})^2}, \tag{3.4}$$

$$Q_{\max} = \sqrt{(Q_{\mathrm{EW}}^{\max})^2 + (Q_{\mathrm{NS}}^{\max})^2}. \tag{3.5}$$

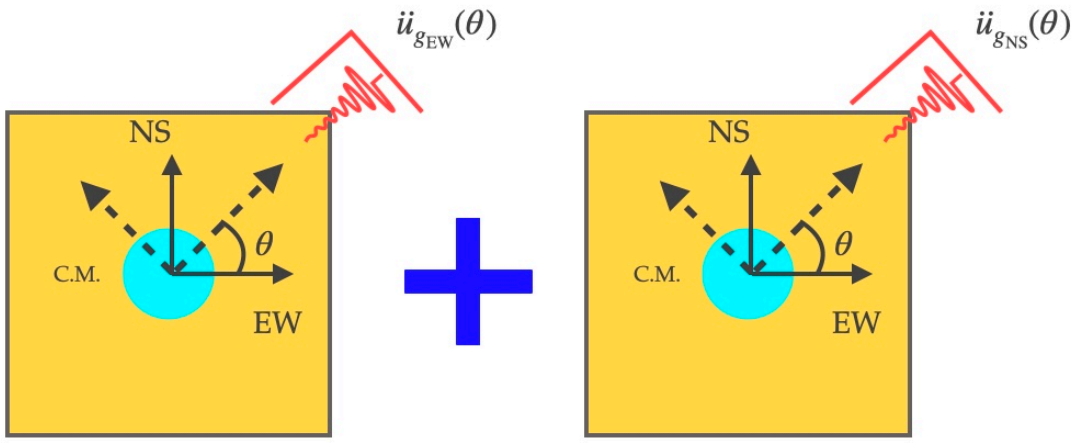

Figure 3.35: Schematic diagram of biunidirectional uncoupled (BUU) analysis of symmetric building structures

3.4.2 Bidirectional coupled analysis of symmetric building structures

In bidirectional coupled (BDC) seismic analysis, we simultaneously input the bidirectional horizontal acceleration time history data from the same station into the model, considering an angle of incidence for the analysis. The simplified concept is shown in

doi:10.6342/NTU202402645

Figure 3.36. We can express the form of external force input as follows:

$$\begin{bmatrix} \ddot{u}_{g_{\mathrm{EW}}}(\theta) \\ \ddot{u}_{g_{\mathrm{NS}}}(\theta) \end{bmatrix} = \begin{bmatrix} \cos\theta & -\sin\theta \\ \sin\theta & \cos\theta \end{bmatrix} \begin{bmatrix} \ddot{u}_{g_{\mathrm{EW}}} \\ \ddot{u}_{g_{\mathrm{NS}}} \end{bmatrix}, \tag{3.6}$$

where $\ddot{u}_{g_{\mathrm{EW}}}(\theta)$ represents the seismic force acceleration input of the east-west seismic wave with an incidence angle to the principal axis, and $\ddot{u}_{g_{\mathrm{NS}}}(\theta)$ represents the seismic force acceleration input of the north-south seismic wave with an incidence angle to the principal axis. During analysis, the bidirectional horizontal acceleration time history data are simultaneously input into the model, considering the incidence angle between the seismic wave and the principal axis from 0° to 360° at one-degree intervals. The peak structural responses for each degree are recorded, specifically the peak interstory displacement and peak interstory shear force for each degree. These are represented in polar coordinates to show the structural response considering 360 degrees of incidence angles, exploring the impact of the incidence angle and comparing it with the results of biunidirectional uncoupled (BUU) seismic analysis. The bidirectional coupled (BDC) peak interstory displacement response and peak interstory shear force response are expressed as follows:

$$q_{\max} = \max_{\forall t} \left(\sqrt{(q_{\mathrm{EW}}(t))^2 + (q_{\mathrm{NS}}(t))^2} \right), \tag{3.7}$$

$$Q_{\max} = \max_{\forall t} \left(\sqrt{(Q_{\mathrm{EW}}(t))^2 + (Q_{\mathrm{NS}}(t))^2} \right). \tag{3.8}$$

doi:10.6342/NTU202402645

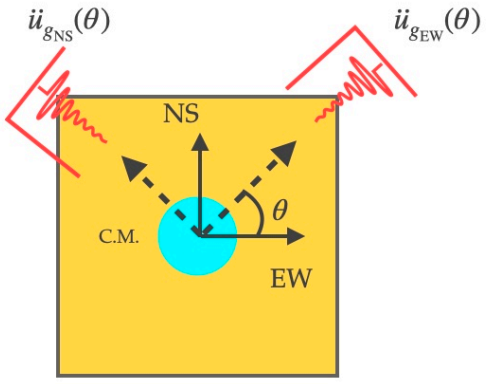

Figure 3.36: Schematic diagram of bidirectional coupled (BDC) analysis of symmetric building structures

3.4.3 Comparisons of biunidirectional uncoupled (BUU) analysis and bidirectional coupled (BDC) analysis for symmetric building structures

We analyzed the acceleration data from 10 stations during the 1999 Chi-Chi earthquake event, with results shown in Figures 3.37-3.56. The results indicate that for symmetric building structures, when using bidirectional couples (BDC) analysis, the angle of incidence of the earthquake has almost no effect on the structural response, whether in terms of peak interstory displacement response or peak interstory shear force response. Consequently, the peak value graphs for interstory displacement and interstory shear force considering 360 degrees of incidence angles are almost circular. This situation is consistently demonstrated in the results analyzed from the acceleration data of all 10 stations using bidirectional earthquake input with consideration of incidence angles. When considering the angle of incidence for interstory displacement response, unidirectional analysis shows a significant underestimation compared to bidirectional coupled (BDC) analysis. For interstory shear force response considering the angle of incidence, most angles also show that biunidirectional uncoupled (BUU) analysis significantly underestimates com-

doi:10.6342/NTU202402645

pared to bidirectional coupled (BDC) analysis. However, at certain angles, such as for TCU071, TCU079, TCU065, and TCU129, overestimation occurs. These results clearly demonstrate that using unidirectional analysis alone can seriously underestimate or misestimate the structural response. Therefore, the accuracy and importance of bidirectional analysis become more significant. In conclusion, bidirectional coupled (BDC) analysis considering the angle of incidence of seismic waves can provide a more accurate assessment of structural seismic response, offering important reference value for earthquake engineering design and evaluation. Through the above analysis and graphical presentation, we can intuitively see the impact of seismic wave incidence angles on structural response, emphasizing the importance of bidirectional coupled (BDC) analysis.

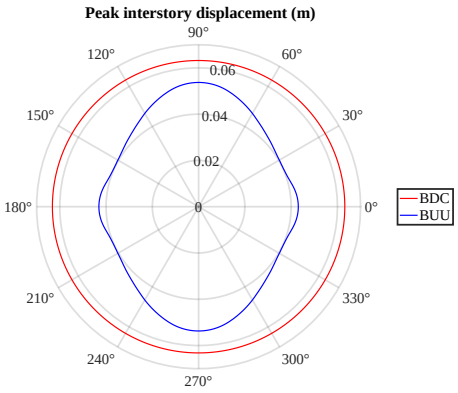

Figure 3.37: Peak interstory displacement responses of symmetric building structures under different incidence angles (CHY028)

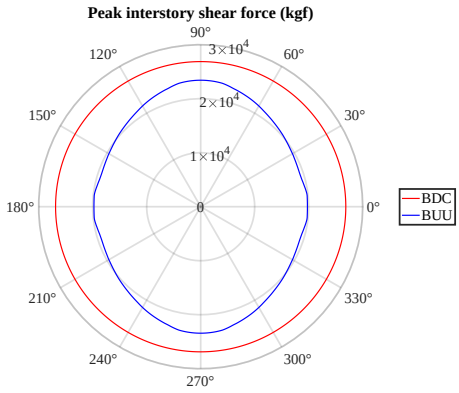

Figure 3.38: Peak interstory shear force responses of symmetric building structures under different incidence angles (CHY028)

doi:10.6342/NTU202402645

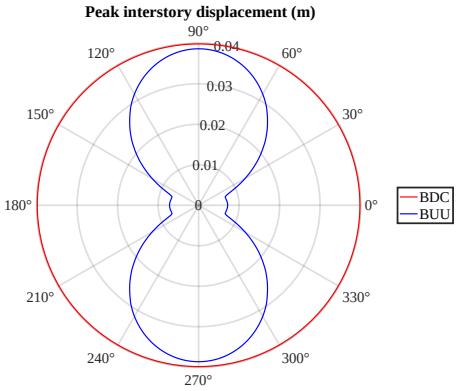

Figure 3.39: Peak interstory displacement responses of symmetric building structures under different incidence angles (CHY041)

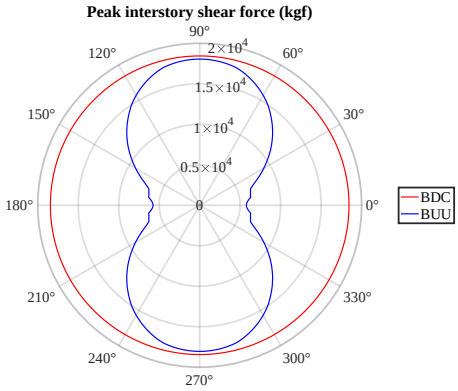

Figure 3.40: Peak interstory shear force responses of symmetric building structures under different incidence angles (CHY041)

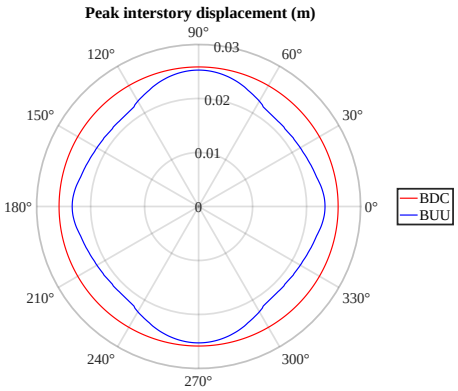

Figure 3.41: Peak interstory displacement responses of symmetric building structures under different incidence angles (TCU071)

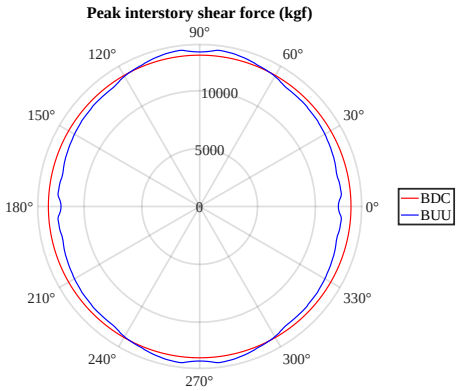

Figure 3.42: Peak interstory shear force responses of symmetric building structures under different incidence angles (TCU071)

doi:10.6342/NTU202402645

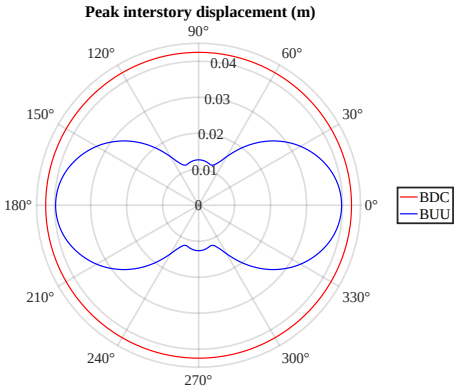

Figure 3.43: Peak interstory displacement responses of symmetric building structures under different incidence angles (TCU079)

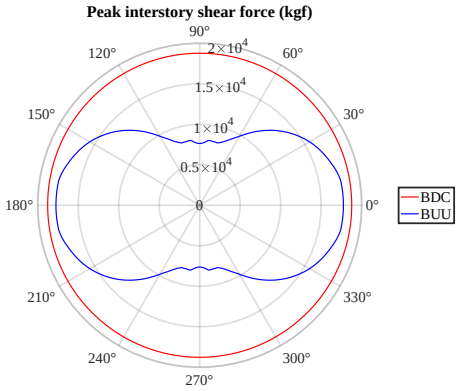

Figure 3.44: Peak interstory shear force responses of symmetric building structures under different incidence angles (TCU079)

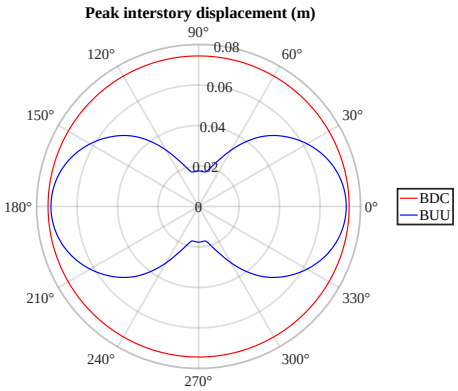

Figure 3.45: Peak interstory displacement responses of symmetric building structures under different incidence angles (TCU084)

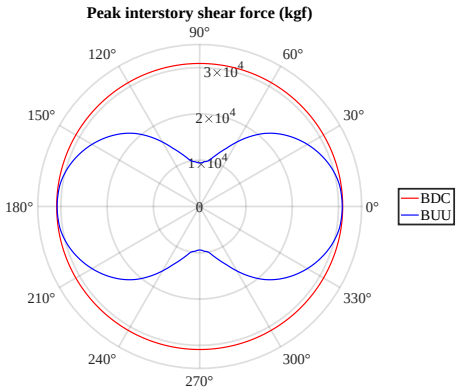

Figure 3.46: Peak interstory shear force responses of symmetric building structures under different incidence angles (TCU084)

doi:10.6342/NTU202402645

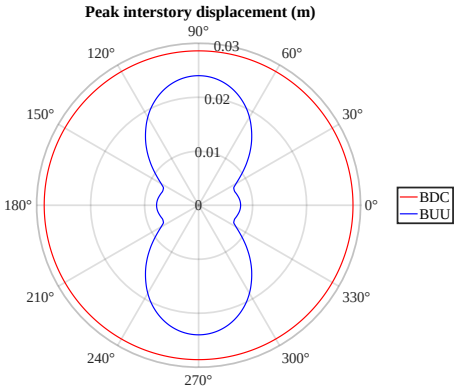

Figure 3.47: Peak interstory displacement responses of symmetric building structures under different incidence angles (CHY101)

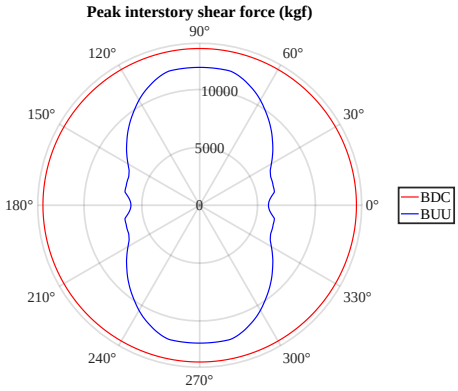

Figure 3.48: Peak interstory shear force responses of symmetric building structures under different incidence angles (CHY101)

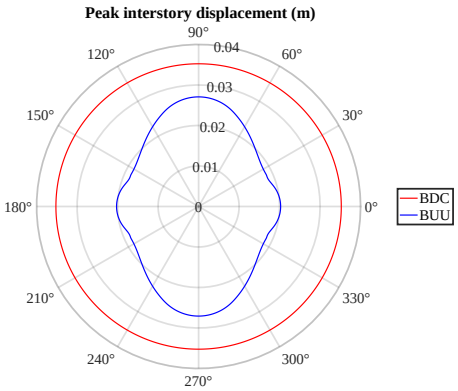

Figure 3.49: Peak interstory displacement responses of symmetric building structures under different incidence angles (TCU052)

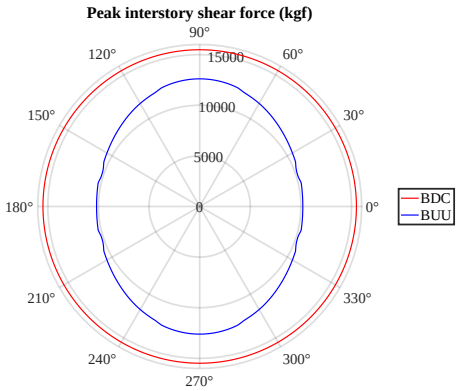

Figure 3.50: Peak interstory shear force responses of symmetric building structures under different incidence angles (TCU052)

doi:10.6342/NTU202402645

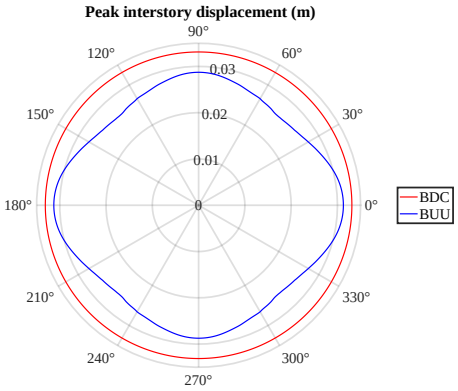

Figure 3.51: Peak interstory displacement responses of symmetric building structures under different incidence angles (TCU065)

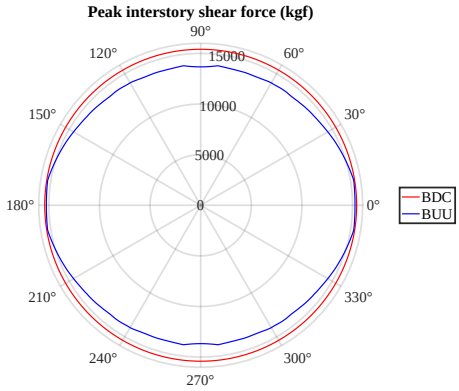

Figure 3.52: Peak interstory shear force responses of symmetric building structures under different incidence angles (TCU065)

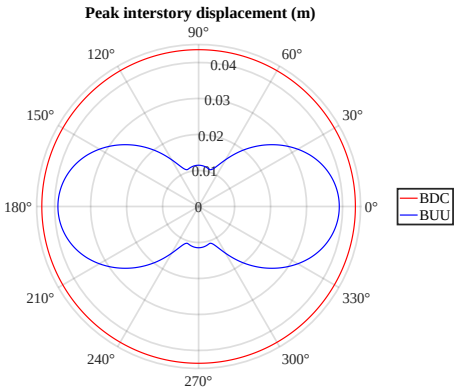

Figure 3.53: Peak interstory displacement responses of symmetric building structures under different incidence angles (TCU068)

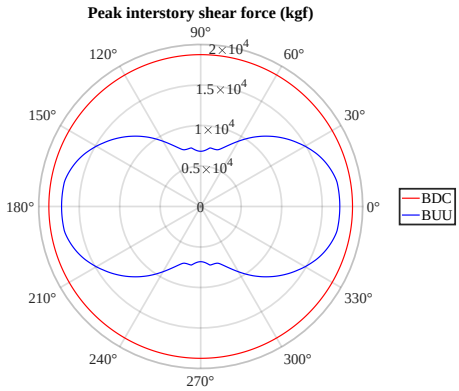

Figure 3.54: Peak interstory shear force responses of symmetric building structures under different incidence angles (TCU068)

doi:10.6342/NTU202402645

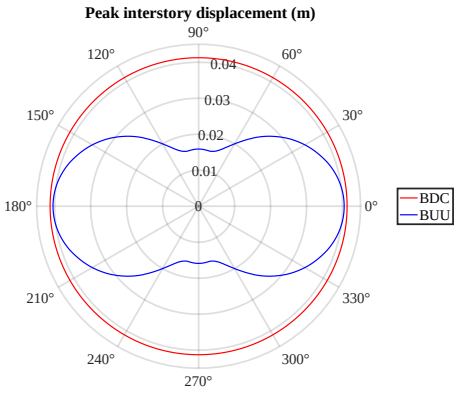

Figure 3.55: Peak interstory displacement responses of symmetric building structures under different incidence angles (TCU129)

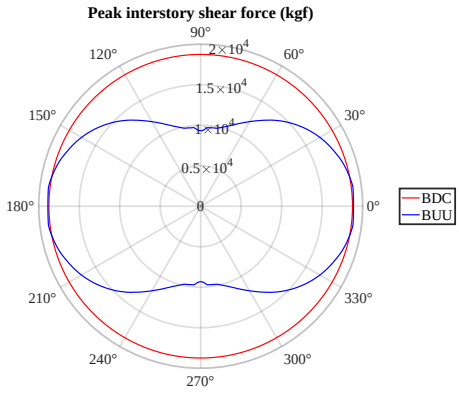

Figure 3.56: Peak interstory shear force responses of symmetric building structures under different incidence angles (TCU129)

3.5 Influence of seismic peak ground acceleration for symmetric building structures

This section utilizes acceleration data from 10 stations during the 1999 Chi-Chi earthquake event for detailed analysis and study of peak ground acceleration effects. In this study, the peak ground acceleration range is from 0.1g to 1g, with parametric analysis conducted at 0.1g intervals. The selected analysis parameters include: Equivalent plastic strain, interstory displacement, interstory shear force, and equivalent plastic strain rate. The analysis results are shown in Figures 3.57 to 3.67. The analysis results show that regardless of equivalent plastic strain, interstory displacement, interstory shear force, or equivalent plastic strain rate, as the peak ground acceleration increases, the overall response trend of these parameters increases. Particularly in Figures 3.67a to 3.67d, we conducted an integrated analysis aimed at determining the response impact of velocity pulse-type earthquake acceleration time histories on building structures. In this part of

doi:10.6342/NTU202402645

the study, five non-velocity pulse-type earthquake acceleration time histories (CHY028, CHY041, TCU071, TCU079, TCU084) and five velocity pulse-type earthquake acceleration time histories (CHY101, TCU052, TCU065, TCU068, TCU129) were selected. All responses are plotted on the same graph for comparison and analysis. It can be clearly seen from the graphs that records marked as ”pulse” (such as CHY101, TCU052, etc.) usually lead to larger responses, especially in terms of interstory displacement and interstory shear force. In Figures 3.67b and 3.67c, these pulse-type records show significantly higher displacement responses at high PGA values compared to non-pulse records. This emphasizes the significant impact of velocity pulses in near-fault earthquakes on symmetric building structures, potentially leading to greater interstory displacement demands and energy input. The results indicate that the behavior of symmetric structures varies greatly under different earthquake records, highlighting the importance of considering multiple earthquake scenarios. Near-fault effects (pulse-type records) may require special attention and additional design considerations to address larger displacement demands. Moreover, although it is known that earthquakes with velocity pulses cause greater displacement demands on symmetric structures, Figures 3.67a and 3.67d show that there are no significant trend changes in equivalent plastic strain and equivalent plastic strain rate. This is because the earthquake waveform and its overall time history process are related; larger interstory displacement and interstory shear force do not necessarily lead to larger plastic equivalent responses. However, we can infer from this that earthquakes with velocity pulses do indeed cause more pronounced overall responses in building structures. These findings emphasize the necessity of incorporating the effects of velocity pulse-type earthquakes in structural design to ensure buildings maintain adequate safety and stability during such seismic events. Future research should further explore responses under different structural

doi:10.6342/NTU202402645

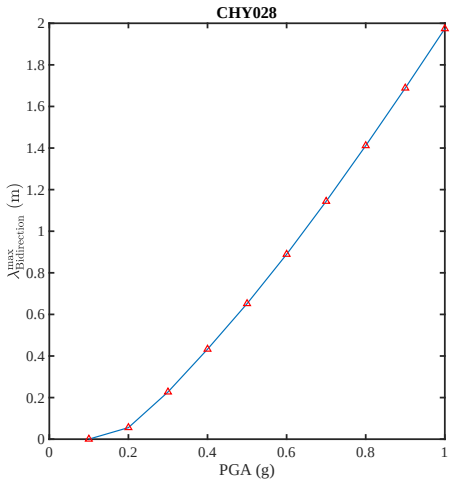

(a) Equivalent plastic strain

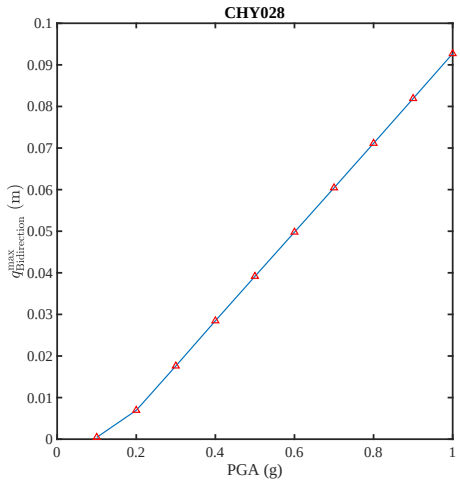

(b) Peak interstory displacement

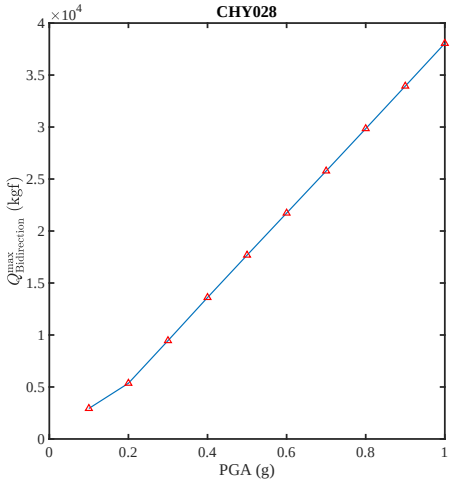

(c) Peak interstory shear force

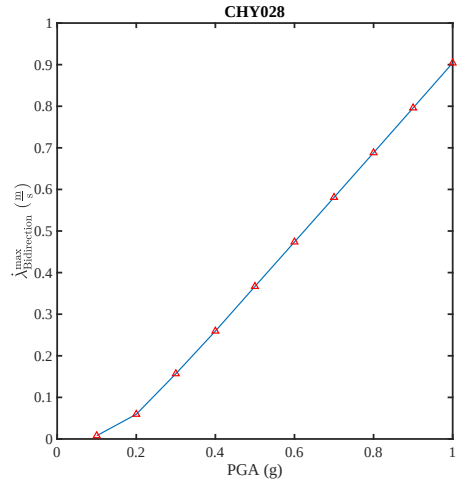

(d) Equivalent plastic strain rate

Figure 3.57: Analysis results of symmetric building structures under different peak ground accelerations (PGA) at CHY028 station

types and design parameters to provide more comprehensive design guidance.

doi:10.6342/NTU202402645

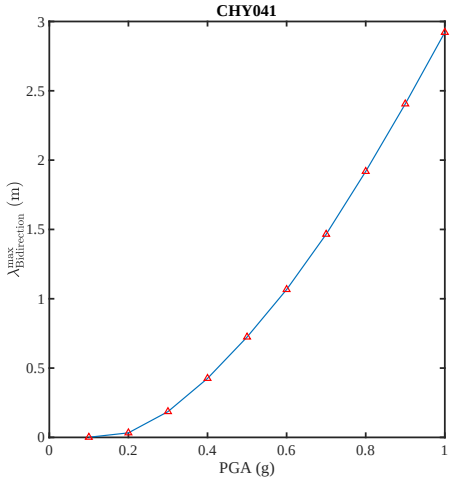

(a) Equivalent plastic strain

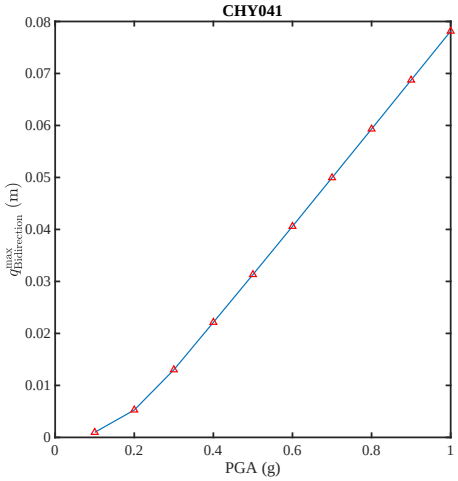

(b) Peak interstory displacement

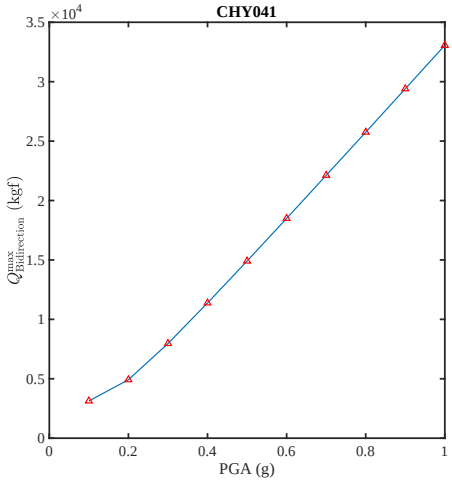

(c) Peak interstory shear force

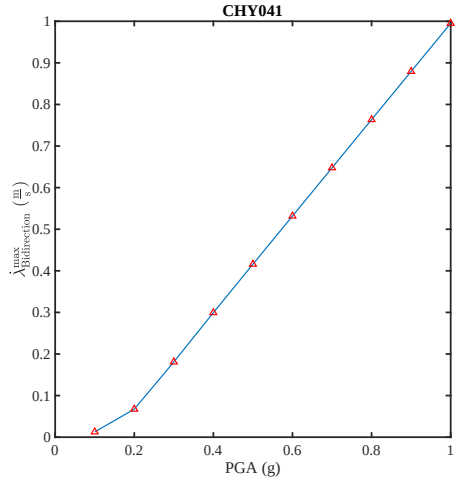

(d) Equivalent plastic strain rate

Figure 3.58: Analysis results of symmetric building structures under different peak ground accelerations (PGA) at CHY041 station

doi:10.6342/NTU202402645

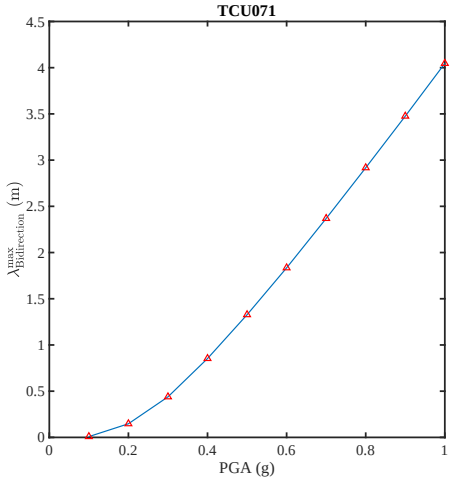

(a) Equivalent plastic strain

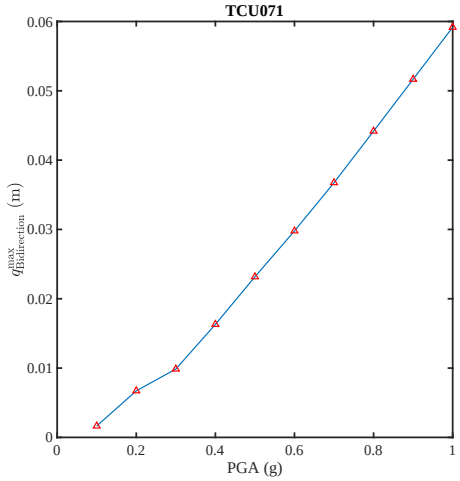

(b) Peak interstory displacement

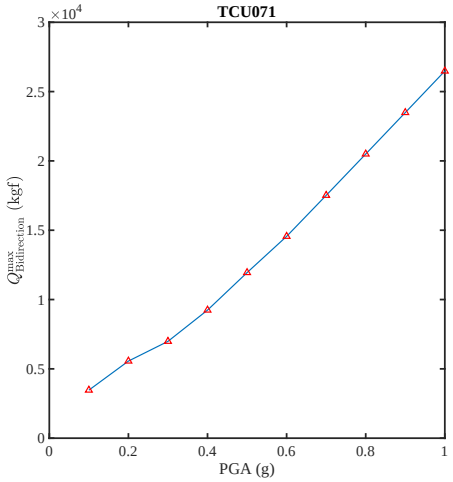

(c) Peak interstory shear force

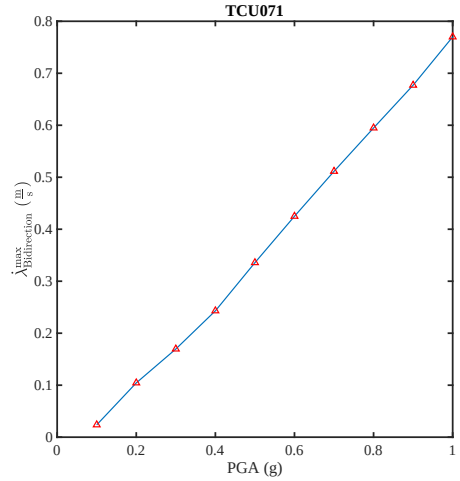

(d) Equivalent plastic strain rate

Figure 3.59: Analysis results of symmetric building structures under different peak ground accelerations (PGA) at TCU071 station

doi:10.6342/NTU202402645

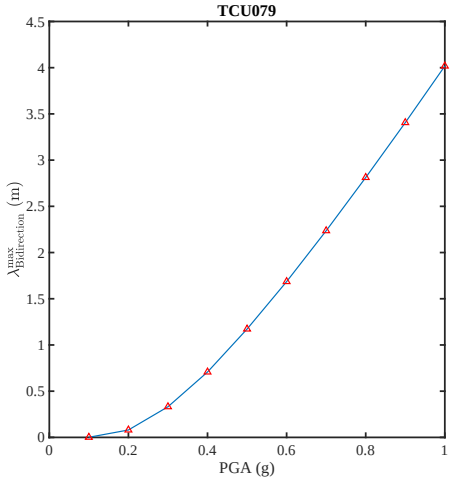

(a) Equivalent plastic strain

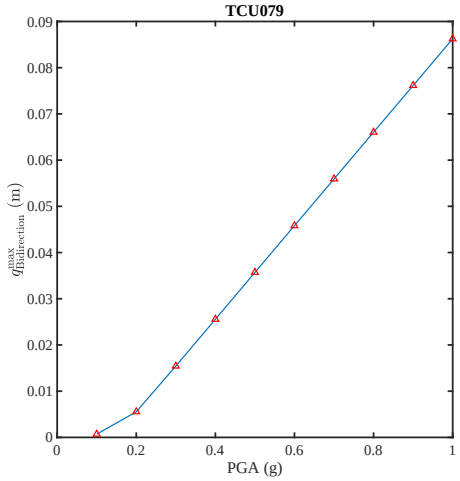

(b) Peak interstory displacement

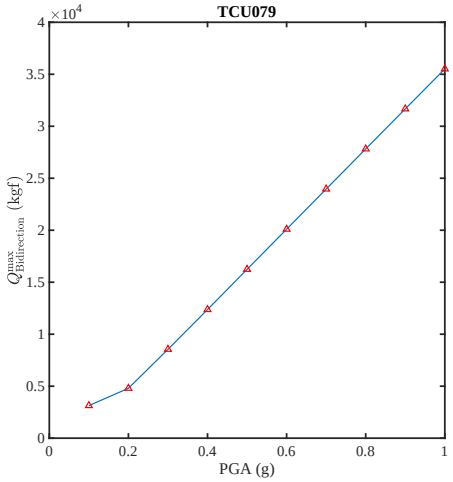

(c) Peak interstory shear force

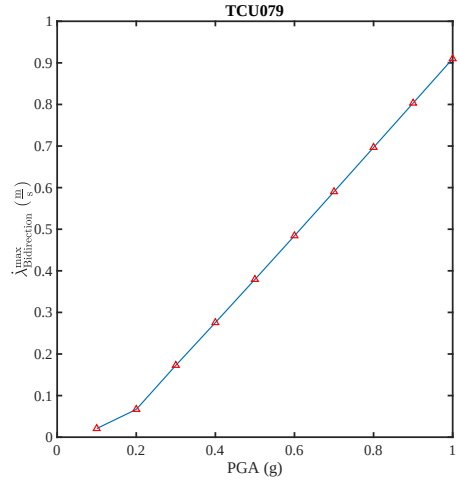

(d) Equivalent plastic strain rate

Figure 3.60: Analysis results of symmetric building structures under different peak ground accelerations (PGA) at TCU079 station

doi:10.6342/NTU202402645

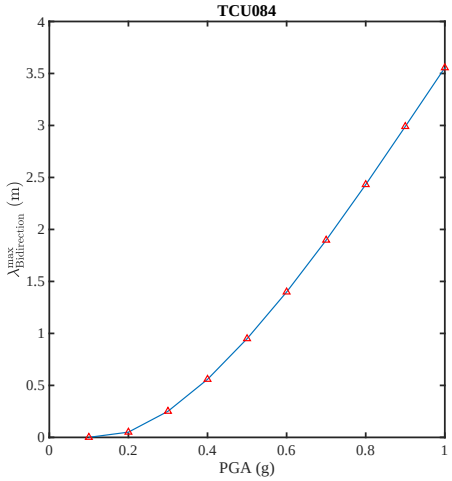

(a) Equivalent plastic strain

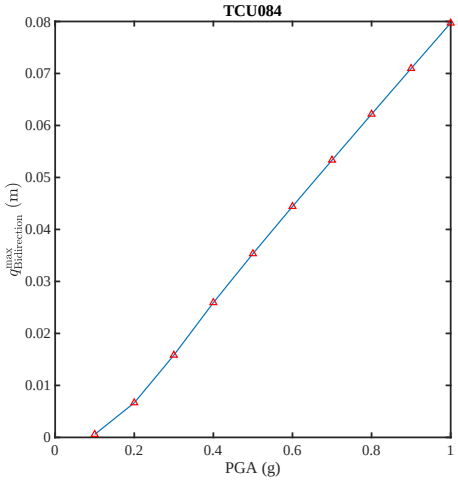

(b) Peak interstory displacement

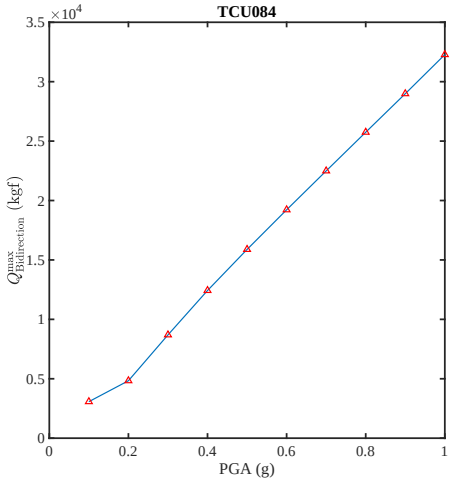

(c) Peak interstory shear force

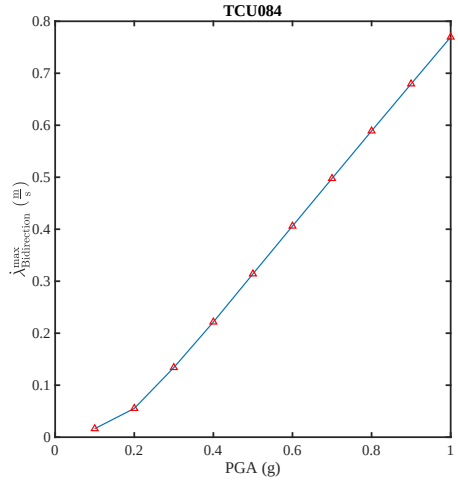

(d) Equivalent plastic strain rate

Figure 3.61: Analysis results of symmetric building structures under different peak ground accelerations (PGA) at TCU084 station

doi:10.6342/NTU202402645

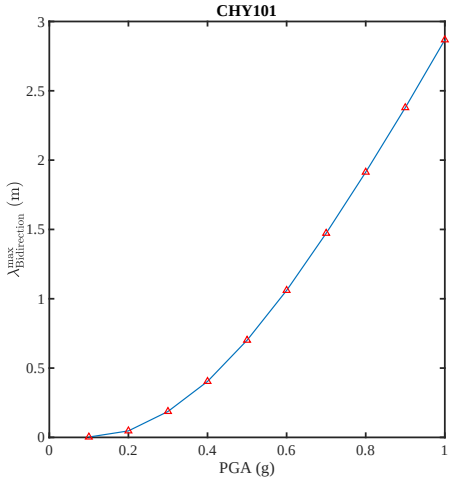

(a) Equivalent plastic strain

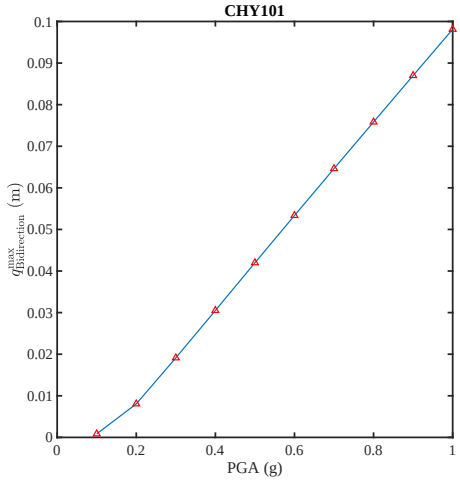

(b) Peak interstory displacement

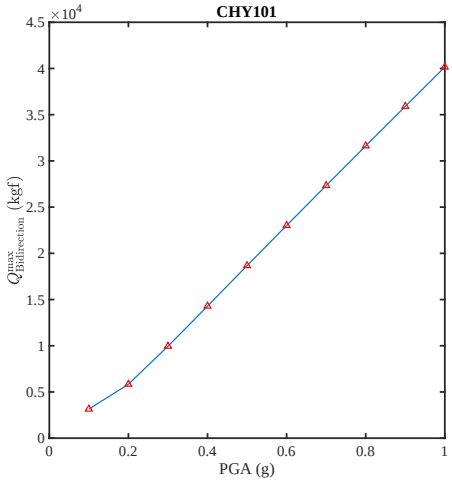

(c) Peak interstory shear force

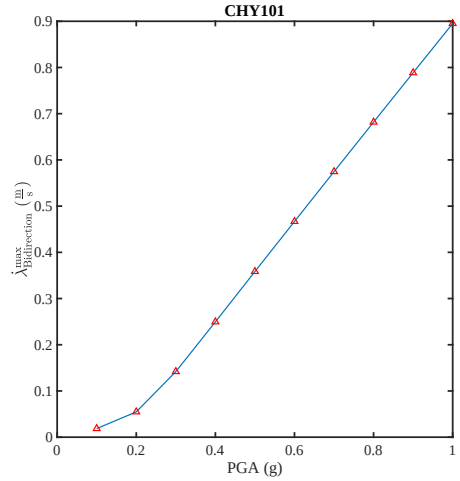

(d) Equivalent plastic strain rate

Figure 3.62: Analysis results of symmetric building structures under different peak ground accelerations (PGA) at CHY101 station

doi:10.6342/NTU202402645

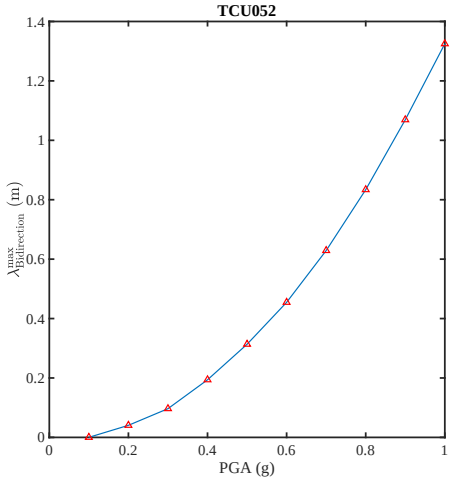

(a) Equivalent plastic strain

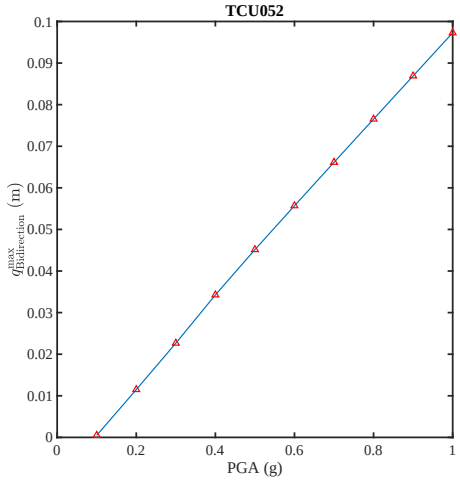

(b) Peak interstory displacement

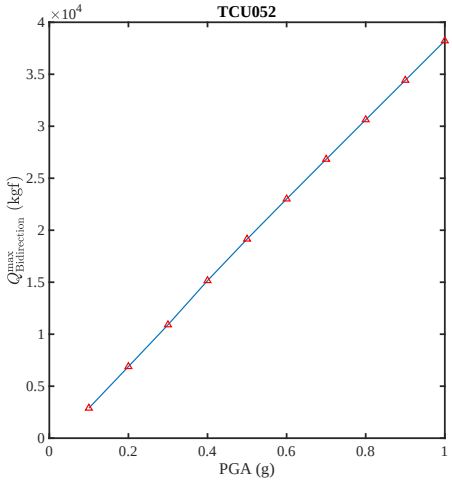

(c) Peak interstory shear force

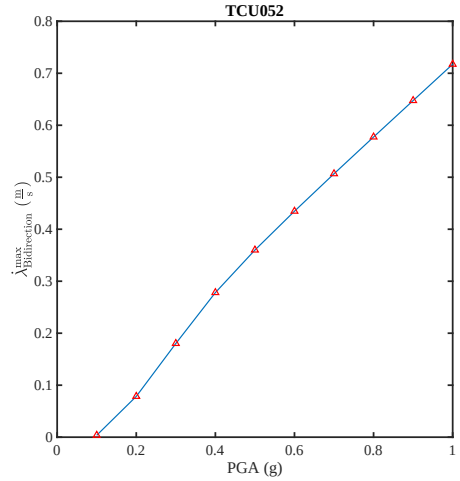

(d) Equivalent plastic strain rate

Figure 3.63: Analysis results of symmetric building structures under different peak ground accelerations (PGA) at TCU052 station

doi:10.6342/NTU202402645

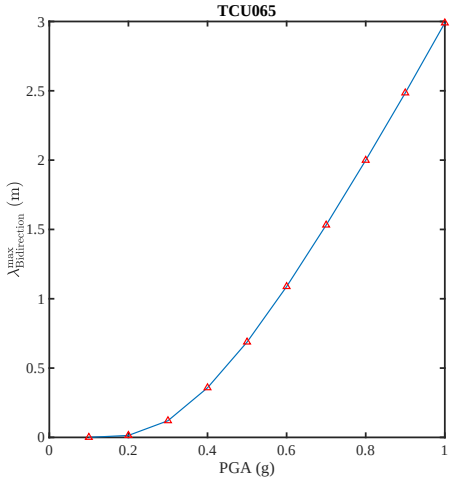

(a) Equivalent plastic strain

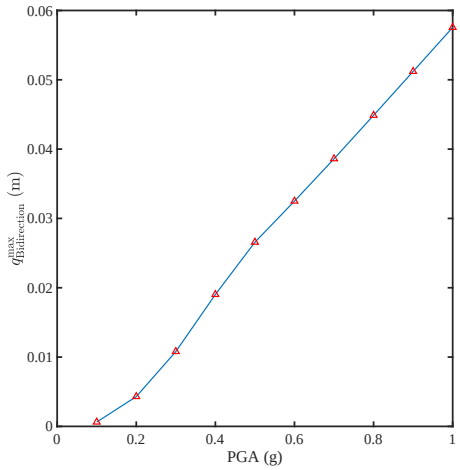

(b) Peak interstory displacement

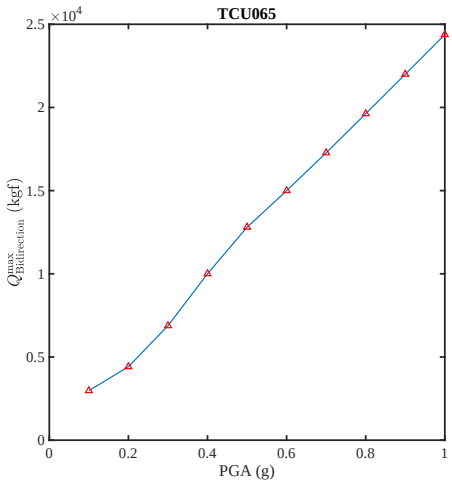

(c) Peak interstory shear force

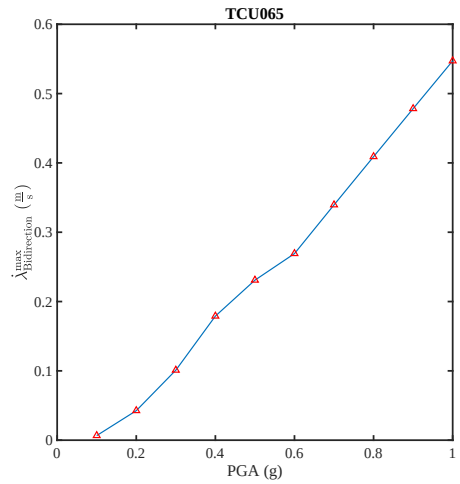

(d) Equivalent plastic strain rate

Figure 3.64: Analysis results of symmetric building structures under different peak ground accelerations (PGA) at TCU065 station

doi:10.6342/NTU202402645

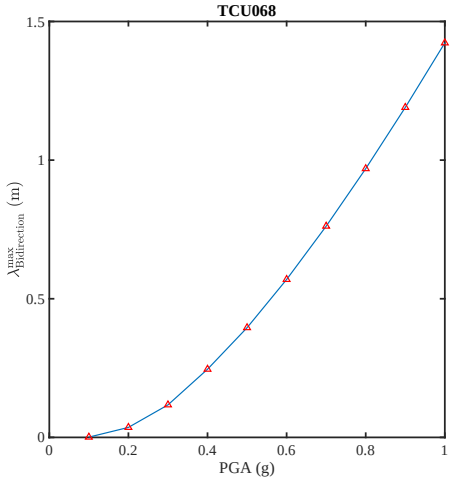

(a) Equivalent plastic strain

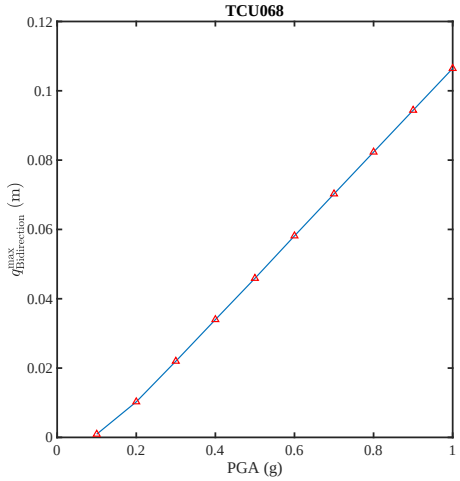

(b) Peak interstory displacement

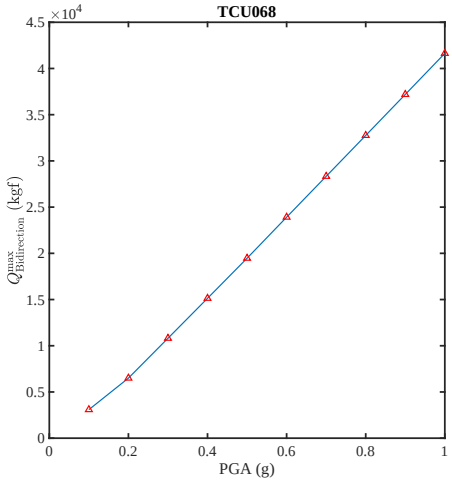

(c) Peak interstory shear force

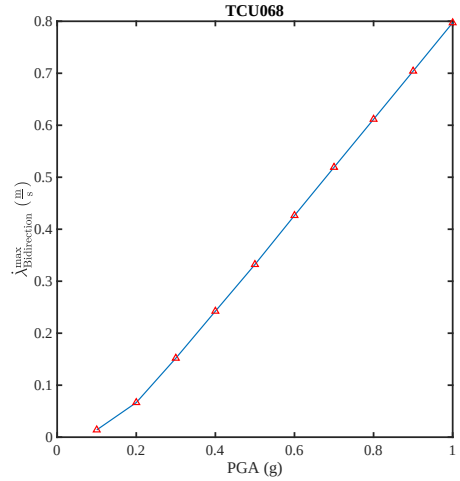

(d) Equivalent plastic strain rate

Figure 3.65: Analysis results of symmetric building structures under different peak ground accelerations (PGA) at TCU068 station

doi:10.6342/NTU202402645

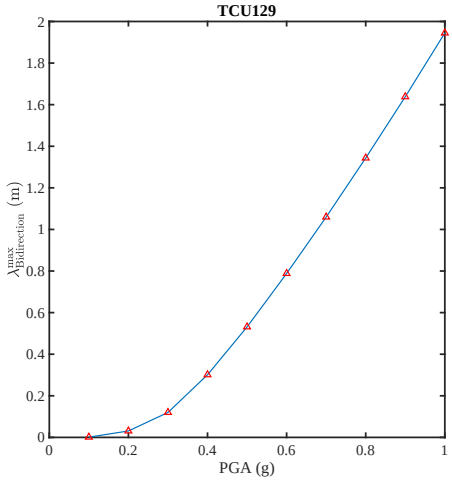

(a) Equivalent plastic strain

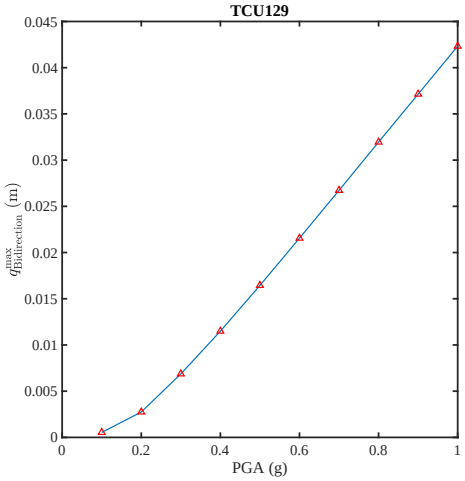

(b) Peak interstory displacement

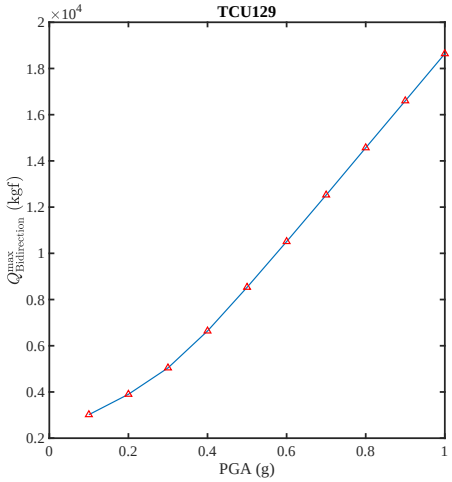

(c) Peak interstory shear force

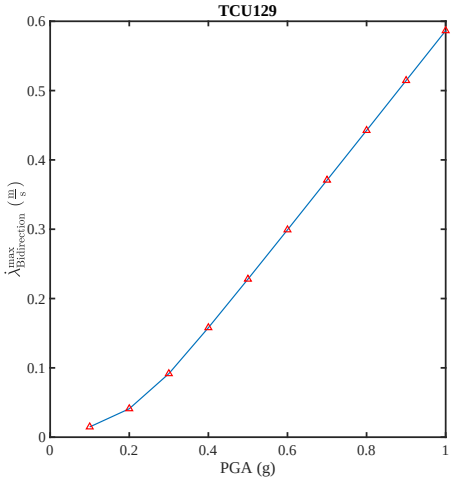

(d) Equivalent plastic strain rate

Figure 3.66: Analysis results of symmetric building structures under different peak ground accelerations (PGA) at TCU129 station

doi:10.6342/NTU202402645

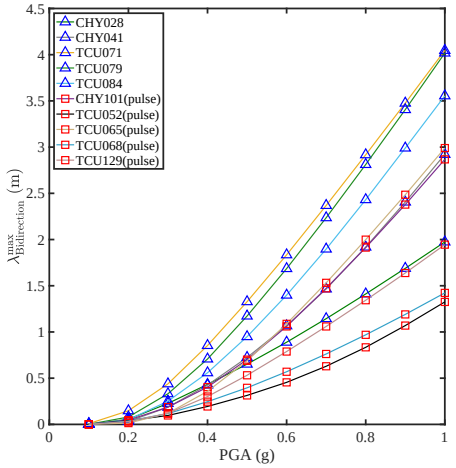

(a) Equivalent plastic strain

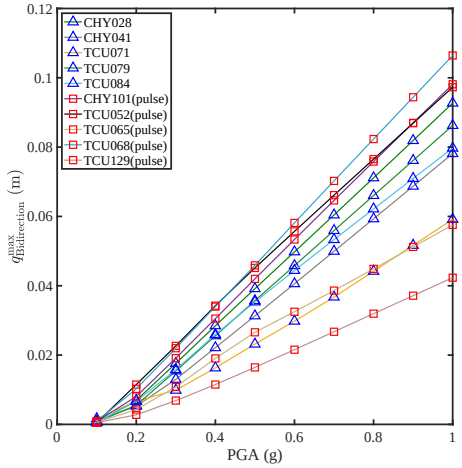

(b) Peak interstory displacement

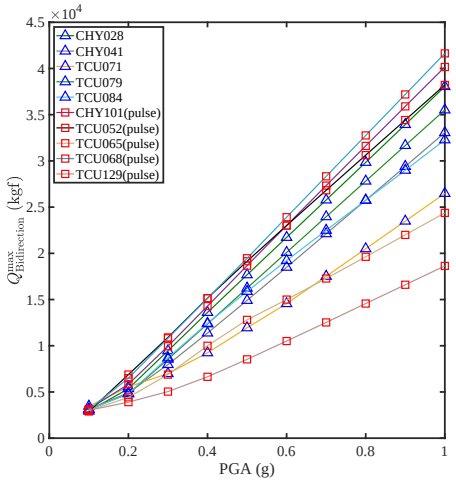

(c) Peak interstory shear force

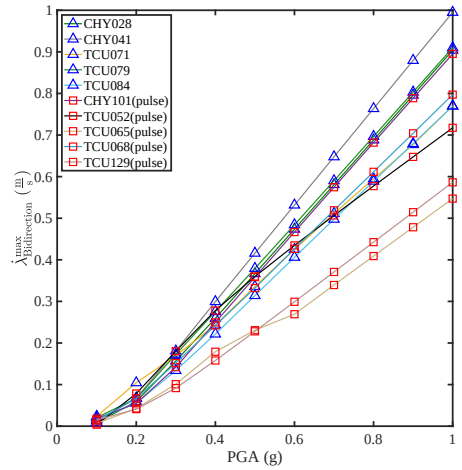

(d) Equivalent plastic strain rate

Figure 3.67: Comparisons of symmetric structure responses under different peak ground accelerations at 10 stations for pulse-like and non-pulse-like earthquakes

doi:10.6342/NTU202402645

Chapter 4 Mathematical modeling on asymmetric building structure

In this study we focus not only on viscoelastic behavior but also on viscoelastoplastic behavior of the building structures, the spring component in our proposed mechanical element is a bilinear elastoplastic model that considers different stiffness in all directions. In the building structures model, we consider bidirectional interstory displacement and twist angle and the building structures suffers the earthquake ground motion.

4.1 Bilinear viscoelastoplastic of a single-story in asymmetric building structures

As previously mentioned, we will develop a bilinear viscoelastoplastic model to simulate the response of asymmetric building structures. Here, we will detail how to establish a bilinear viscoelastoplastic model for a single-story asymmetric building structure. First, we can derive the equation of motion for this asymmetric building structure as follows:

$$\mathbf{m}_s\ddot{\mathbf{q}} + \mathbf{Q} = \mathbf{F}. \tag{4.1}$$

doi:10.6342/NTU202402645

where

$$\mathbf{m}_s = \begin{bmatrix} m_1 & 0 & 0 \\ 0 & m_2 & 0 \\ 0 & 0 & I_o \end{bmatrix},$$

$$\mathbf{q} = \begin{bmatrix} q_1 \\ q_2 \\ q_3 \end{bmatrix},$$

$$\mathbf{Q} = \begin{bmatrix} Q_1 \\ Q_2 \\ Q_3 \end{bmatrix},$$

$$\mathbf{F} = \begin{bmatrix} F_1 \\ F_2 \\ F_3 \end{bmatrix},$$

Among these, $\mathbf{m}_s$ is the mass matrix of the building structure, m_1 and m_2 are the masses of the building structure, and I_o is the rotational inertia of the building structure.**q** is the generalized displacement, q_1 is the interstory displacement in the 1st direction, q_2 is the interstory displacement in the 2nd direction, q_3 is the twist angle. **Q** is the generalized force, Q_1 is the interstory shear force in the 1st direction, Q_2 is the interstory shear force in the 2nd direction, Q_3 is the torque. **F** is the external force vector, F_1 is the external force in the 1st direction, F_2 is the external force in the 2nd direction, F_3 is the external

doi:10.6342/NTU202402645

torque.

The model proposed in this study considers not only elasticity but also elastoplasticity. For the elastoplastic part, we applied the bilinear elastoplastic model from plasticity theory to simulate the elastoplastic behavior of the building structure. The bilinear elastoplastic model consists of an elastic part and a plastic part. The elastic part is composed of an elastic spring, while the plastic part consists of a plastic spring and a yield switch. Therefore, we can decompose the generalized displacement $\mathbf{q}$ into two parts: elastic displacement $\mathbf{q}^e$ and plastic displacement $\mathbf{q}^p$. As mentioned earlier, the model proposed in this study also considers the contribution of viscosity. Thus, we use a viscous damper to simulate the inherent damping of the building structure. Combining the viscous damper in parallel with the bilinear elastoplastic model results in the viscoelastoplastic model. The composition of the generalized shear force includes the elastoplastic shear force contributed by the elastoplastic model and the viscous damping force. The elastoplastic shear force of the building structure $\mathbf{Q}^{EP}$ is decomposed as active shear force $\mathbf{Q}_a$, and back shear force $\mathbf{Q}_b$. Considering all of the above, we can establish the mechanical components as shown in Figure 4.1, and we can express the viscoelastoplastic model mathematically as follows:

$$\mathbf{q} = \mathbf{q}^e + \mathbf{q}^p, \tag{4.2}$$

$$\mathbf{Q} = \mathbf{Q}^{EP} + \mathbf{C}\dot{\mathbf{q}}, \tag{4.3}$$

doi:10.6342/NTU202402645

$$\mathbf{Q}^{EP} = \mathbf{Q}_a + \mathbf{Q}_b, \tag{4.4}$$

$$\mathbf{Q}^{EP} = \mathbf{K}_e \mathbf{q}^e, \tag{4.5}$$

$$\dot{\mathbf{Q}}_b = \mathbf{K}_p \dot{\mathbf{q}}^p, \tag{4.6}$$

$$Q_y \dot{\mathbf{q}}^p = \mathbf{Q}_a^* \dot{\lambda}, \tag{4.7}$$

$$f\dot{\lambda} = 0, \tag{4.8}$$

$$f = \sqrt{\mathbf{Q}_a^{\mathrm{T}} \mathbf{Y} \mathbf{Q}_a} - Q_y \leq 0, \tag{4.9}$$

$$\dot{\lambda} \geq 0, \tag{4.10}$$

where

$$\mathbf{Y} = (\mathbf{N}^{-1})^{\mathrm{T}} \mathbf{N},$$

$$\mathbf{K}_p = k_p \mathbf{N},$$

$$\mathbf{Q}_a^* = \mathbf{N}^{-1} \mathbf{Q}_a,$$

doi:10.6342/NTU202402645

$$\dot{\mathbf{q}}^p = \frac{\dot{\lambda}}{Q_y}\mathbf{N}^{-1}\mathbf{Q}_a,$$

where $\mathbf{Y}$ is yield matrix.

The Hooke's law of the elastic displacement is stated in Eq. (4.5) where the $\mathbf{K}_e$ is elastic stiffness of building structures. Eq. (4.7) shows the plastic flow rule which relates the plastic displacement rate $\dot{\mathbf{q}}^p$ with the active shear force $\mathbf{Q}_a^*$ multiplied by the rate of plastic equivalent $\dot{\lambda}$. The kinematic hardening rule in Eq. (4.6) describes the back shear force which is proportional to the rate of generalized plastic displacement where the $\mathbf{K}_p$ is kinematic-hardening stiffness. Eq. (4.8)- Eq. (4.10) are the complementary trios where Eq. (4.9) shows that the $||\mathbf{Q}_a^*||$ cannot exceed the yielding force Q_y, Eq. (4.10) means that the rate of plastic equivalent is non-negative, and the alternative condition Eq. (4.8) means that $f\dot{\lambda}$ must be zero for each case. Further, the bilinear elastoplastic model in Eq. (4.2)-Eq. (4.10) can be represented as a compact formulation as follows:

$$\dot{\mathbf{q}} = \mathbf{K}_e^{-1}\dot{\mathbf{Q}}^{\mathrm{EP}} + \dot{\mathbf{q}}^p, \tag{4.11}$$

$$\dot{\mathbf{Q}}_a = \mathbf{K}_e\dot{\mathbf{q}} - (\mathbf{K}_p + \mathbf{K}_e)\dot{\mathbf{q}}^p, \tag{4.12}$$

$$\dot{\mathbf{Q}}_a^* = \mathbf{N}^{-1}\mathbf{K}_e\dot{\mathbf{q}} - (\mathbf{N}^{-1}\mathbf{K}_e + k_p\mathbf{I})\frac{\dot{\lambda}}{Q_y}\mathbf{Q}_a^*, \tag{4.13}$$

$$Q_y\dot{\mathbf{q}}^p = \mathbf{Q}_a^*\dot{\lambda}, \tag{4.14}$$

$$f\dot{\lambda} = 0, \tag{4.15}$$

$$f = \sqrt{\mathbf{Q}_a^{\mathrm{T}}\mathbf{Y}\mathbf{Q}_a} - Q_y \leq 0, \tag{4.16}$$

$$\dot{\lambda} \geq 0. \tag{4.17}$$

doi:10.6342/NTU202402645

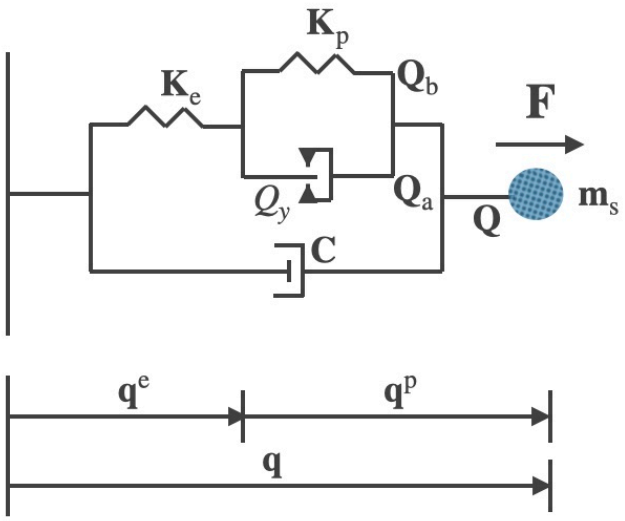

Figure 4.1: Mechanical element of the three-component asymmetric building structure

4.2 The straining conditions and the sufficient and necessary conditions for the viscoelastoplastic model

In order to provide a more detailed description of the viscoelastoplastic behavior of this model. We use the complementary trio relationship to better describe the viscoelastoplastic behavior of the building structures. Additionally, all these conditions need to be simultaneously satisfied. Eq. (4.8) represents an alternative condition, meaning that either $f = 0$ or $\dot{\lambda} = 0$ can be chosen. Eq. (4.9) is an admissible condition, while Eq. (4.10) ensures non-negative dissipation, meaning that the system will not have dissipations with negative energy.The following is a theoretical derivation. To accurately determine the system's switching to judge whether the system is in a viscoelastic or viscoelastoplastic state, the core idea is to combine the complementary trio as a switching mechanism. When the yield condition $(f = 0)$ is satisfied, it leads to $\dot{f} = 0$, therefore we have

$$\dot{f} = (\mathbf{Q}_a^*)^{\mathrm{T}} \dot{\mathbf{Q}}_a^* = 0.$$

doi:10.6342/NTU202402645

Substituting Eq. (4.13) into the above equations, we obtain:

$$(\mathbf{Q}_a^*)^{\mathrm{T}}\mathbf{N}^{-1}\mathbf{K}_e\dot{\mathbf{q}} - (\mathbf{Q}_a^*)^{\mathrm{T}}(\mathbf{N}^{-1}\mathbf{K}_e + k_p\mathbf{I})\frac{\dot{\lambda}}{Q_y}\mathbf{Q}_a^* = 0. \tag{4.18}$$

Since $(\mathbf{Q}_a^*)^{\mathrm{T}}(\mathbf{N}^{-1}\mathbf{K}_e + k_p\mathbf{I})\mathbf{Q}_a^* \geq 0$ for $\mathbf{Q}_a^* \neq 0$, Eq. (4.15) is satisfied and we can obtain the straining conditions $\dot{\lambda}$,

$$\dot{\lambda} = \frac{Q_y(\mathbf{Q}_a^*)^{\mathrm{T}}\mathbf{N}^{-1}\mathbf{K}_e\dot{\mathbf{q}}}{(\mathbf{Q}_a^*)^{\mathrm{T}}(\mathbf{N}^{-1}\mathbf{K}_e + k_p\mathbf{I})\mathbf{Q}_a^*} > 0. \tag{4.19}$$

Therefore, we prove that,

$$\text{if} \quad f = 0 \quad \text{and} \quad (\mathbf{Q}_a^*)^{\mathrm{T}}\mathbf{N}^{-1}\mathbf{K}_e\dot{\mathbf{q}} > 0 \quad \text{then} \quad \dot{\lambda} = \frac{Q_y(\mathbf{Q}_a^*)^{\mathrm{T}}\mathbf{N}^{-1}\mathbf{K}_e\dot{\mathbf{q}}}{(\mathbf{Q}_a^*)^{\mathrm{T}}(\mathbf{N}^{-1}\mathbf{K}_e + k_p\mathbf{I})\mathbf{Q}_a^*} > 0.$$

On the contray, if $\dot{\lambda} > 0$, Eq. (4.15) request $f = 0$, hence we obtain $\dot{f} = 0$ again. Further, this brings us to obtain the following condition,

$$\text{if} \quad \dot{\lambda} = 0 \quad \text{then} \quad f = 0 \quad \text{and} \quad (\mathbf{Q}_a^*)^{\mathrm{T}}\mathbf{N}^{-1}\mathbf{K}_e\dot{\mathbf{q}} > 0.$$

In summary, we have the sufficient and necessary condition of the viscoelastoplastic model.

$$\left\{f = 0 \text{ and } (\mathbf{Q}_a^*)^{\mathrm{T}}\mathbf{N}^{-1}\mathbf{K}_e\dot{\mathbf{q}} > 0\right\} \Leftrightarrow \left\{\dot{\lambda} = \frac{Q_y(\mathbf{Q}_a^*)^{\mathrm{T}}\mathbf{N}^{-1}\mathbf{K}_e\dot{\mathbf{q}}}{(\mathbf{Q}_a^*)^{\mathrm{T}}(\mathbf{N}^{-1}\mathbf{K}_e + k_p\mathbf{I})\mathbf{Q}_a^*}\right\} \Leftrightarrow \{\dot{\lambda} > 0\}.$$

It is logically equivalent to the following on-off criterion of the viscoelastoplastic model.

$$\dot{\lambda} = \begin{cases} \frac{Q_y(\mathbf{Q}_a^*)^{\mathrm{T}}\mathbf{N}^{-1}\mathbf{K}_e\mathbf{q}}{(\mathbf{Q}_a^*)^{\mathrm{T}}(\mathbf{N}^{-1}\mathbf{K}_e + k_p\mathbf{I})\mathbf{Q}_a^*} & \text{if} \quad f = 0 \quad \text{and} \quad (\mathbf{Q}_a^*)^{\mathrm{T}}\mathbf{N}^{-1}\mathbf{K}_e\dot{\mathbf{q}} > 0 \\ 0 & \text{if} \quad f < 0 \quad \text{or} \quad (\mathbf{Q}_a^*)^{\mathrm{T}}\mathbf{N}^{-1}\mathbf{K}_e\dot{\mathbf{q}} \leq 0 \end{cases}. \tag{4.20}$$

Based on the above derivation, we can know that this bilinear viscoelastoplastic model combined with plastic flow rules and complementary trio can more completely

doi:10.6342/NTU202402645

describe the viscoelastoplastic behavior of the building structure.

4.3 Two-phase dynamicalal systems

From the preceding section, it is evident that this model involves numerous complex equations. Therefore, to provide a clearer description of the system's viscoelastic and viscoelastoplastic states, we further divide the system into two phases systems: viscoelastic (VE) phase ($\dot{\lambda} = 0$) and viscoelastoplastic (VEP) phase ($\dot{\lambda} > 0$). In the previous section, we have already discussed the complementary trio. Here, we can describe it as a two-phase switching system, where the system is considered as the off phase when it's in the viscoelastic state, and as the on phase when it's in the viscoelastoplastic state. We can illustrate this relationship graphically as shown in Figure 4.2.and we can also represent it in tabular form as shown in Table 4.1.

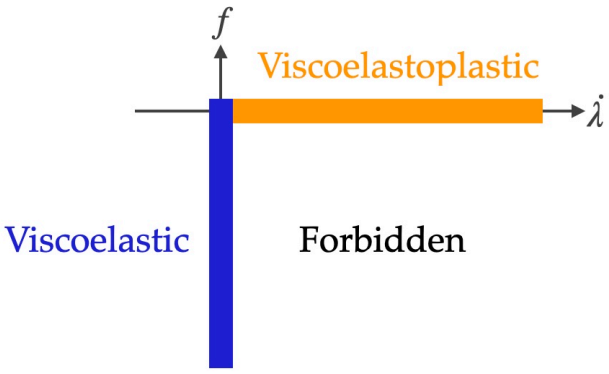

Figure 4.2: Complementary trio relations and two-phase switching

doi:10.6342/NTU202402645

Table 4.1: The relationship between the two-phase system and the complementary trio

	$\dot{\lambda} = 0$	$\dot{\lambda} > 0$
$f < 0$	Viscoelastic-phase	Forbidden
$f = 0$	Viscoelastic-phase	Viscoelastoplastic-phase

4.3.1 Viscoelastic-phase (off-phase)

For case of $\dot{\lambda} = 0$ the formulation of the model in the viscoelastic phase is:

$$\begin{aligned} &\mathbf{m}_s\ddot{\mathbf{q}} + \mathbf{Q} = \mathbf{F}, \\ &f = \|\mathbf{Q}_a^*\| - Q_y \leq 0, \\ &\dot{\lambda} = 0, \\ &\dot{\mathbf{q}}^p = \mathbf{0}, \\ &\dot{\mathbf{Q}}_b = \mathbf{0}, \\ &\mathbf{Q}_a = \mathbf{Q} - \mathbf{Q}_b - \mathbf{C}\dot{\mathbf{q}}. \end{aligned} \tag{4.21}$$

Since all of the above equations are linear, the system is linear in viscoelastic phase.

doi:10.6342/NTU202402645

4.3.2 Viscoelastoplastic-phase (on-phase)

For case of $\dot{\lambda} > 0$ the formulation of the model in the viscoelastoplastic phase is:

$$\begin{aligned}
&\mathbf{m}_s\ddot{\mathbf{q}} + \mathbf{Q} = \mathbf{F},\\
&f = \|\mathbf{Q}_a^*\| - Q_y = 0,\\
&\dot{\lambda} > 0,\\
&Q_y\dot{\mathbf{q}}^p = \mathbf{Q}_a^*\dot{\lambda},\\
&\dot{\mathbf{q}}^p = \mathbf{K}_p^{-1}\dot{\mathbf{Q}}_b,\\
&\dot{\mathbf{Q}}_b = \mathbf{K}_p\dot{\mathbf{q}}^p,\\
&\mathbf{Q} = \mathbf{Q}_a + \mathbf{Q}_b + \mathbf{C}\dot{\mathbf{q}}.
\end{aligned} \tag{4.22}$$

Since the formulation of $\dot{\lambda}$ as shown in Eq. (4.19) contain $\mathbf{Q}_a$ in the denominator and the numerator, the system is nonlinear in viscoelastoplastic phase.

4.4 Numerical integration based on internal symmetry

This section aims to address difficult of numerical integration caused by the nonlinear term in Eq. (4.22) when the system is in the viscoelastoplastic phase. Firstly, from Eq. (4.9), we know that when the system is in the plastic phase, $f = 0$, implying $(\mathbf{Q}_a^*)^{\mathrm{T}}\mathbf{Q}_a^* = Q_y^2$. Here, we discuss asymmetric building structures, which means that the stiffness in all directions and the radius of the yield surface can be different. Therefore, the yield surface in the $\mathbf{Q}_a^*$ space can be an ellipse. To solve for $\mathbf{Q}_a^*$, we transform the $\mathbf{Q}_a^*$ into augmented force space. Next, we will proceed with the theoretical derivation of the Minkowski spacetime.

doi:10.6342/NTU202402645

4.4.1 Internal symmetry in Minkowski spacetime

First, we start from Eq. (4.13), which can be rewritten as follows:

$$\dot{\mathbf{Q}}_a^* + k_p \frac{\dot{\lambda}}{Q_y} \mathbf{Q}_a^* = \mathbf{N}^{-1}\mathbf{K}_e(\dot{\mathbf{q}} - \dot{\mathbf{q}}^p). \tag{4.23}$$

If the integrating factor as $X_0 = \exp(\frac{k_p \lambda}{Q_y})$ is found and multiplies by Eq. (4.23) we have:

$$X_0\dot{\mathbf{Q}}_a^* + k_p X_0 \frac{\dot{\lambda}}{Q_y} \mathbf{Q}_a^* = X_0\mathbf{N}^{-1}\mathbf{K}_e(\dot{\mathbf{q}} - \dot{\mathbf{q}}^p). \tag{4.24}$$

Then, dividing Eq. (4.24) by Q_y, we have:

$$\frac{d}{dt}\left[\frac{X_0\mathbf{Q}_a^*}{Q_y}\right] = \frac{X_0}{Q_y}\mathbf{N}^{-1}\mathbf{K}_e(\dot{\mathbf{q}} - \dot{\mathbf{q}}^p). \tag{4.25}$$

Beside the formulation of $\dot{\lambda}$ in Eq. (4.19),we derive another form of $\dot{\lambda}$ for the expoloration of internal stmmetry.Multipling both sides of Eq. (4.23) by $(\mathbf{Q}_a^*)^{\mathrm{T}}$, we have

$$(\mathbf{Q}_a^*)^{\mathrm{T}}\dot{\mathbf{Q}}_a^* + k_p \frac{\dot{\lambda}}{Q_y}(\mathbf{Q}_a^*)^{\mathrm{T}}\mathbf{Q}_a^* = (\mathbf{Q}_a^*)^{\mathrm{T}}\mathbf{N}^{-1}\mathbf{K}_e(\dot{\mathbf{q}} - \dot{\mathbf{q}}^p). \tag{4.26}$$

In case of $\dot{\lambda} > 0$, we know that $f = 0$, $(\mathbf{Q}_a^*)^{\mathrm{T}}\mathbf{Q}_a^* = Q_y^2$, and $\dot{f} = 0$, $(\mathbf{Q}_a^*)^{\mathrm{T}}\dot{\mathbf{Q}}_a^* = 0$. Substituting them into Eq. (4.26), we get:

$$k_p Q_y \dot{\lambda} = (\mathbf{Q}_a^*)^{\mathrm{T}}\mathbf{N}^{-1}\mathbf{K}_e(\dot{\mathbf{q}} - \dot{\mathbf{q}}^p). \tag{4.27}$$

If $\frac{(\mathbf{Q}_a^*)^{\mathrm{T}}\mathbf{N}^{-1}\mathbf{K}_e(\dot{\mathbf{q}}-\dot{\mathbf{q}}^p)}{k_p} > 0$, then

$$\dot{\lambda} = \frac{(\mathbf{Q}_a^*)^{\mathrm{T}}\mathbf{N}^{-1}\mathbf{K}_e(\dot{\mathbf{q}} - \dot{\mathbf{q}}^p)}{k_p Q_y}. \tag{4.28}$$

doi:10.6342/NTU202402645

Next, differentiating X_0 with respect to time yields the following relationship:

$$\frac{d}{dt}\left[X_0\right] = \frac{k_p\dot{\lambda}}{Q_y}X_0 = \frac{X_0}{Q_y}\frac{(\mathbf{Q}_a^*)^{\mathrm{T}}\mathbf{N}^{-1}\mathbf{K}_e(\dot{\mathbf{q}}-\dot{\mathbf{q}}^p)}{Q_y} = \frac{[\mathbf{N}^{-1}\mathbf{K}_e(\dot{\mathbf{q}}-\dot{\mathbf{q}}^p)]^{\mathrm{T}}}{Q_y}X_0\frac{\mathbf{Q}_a^*}{Q_y}. \tag{4.29}$$

The augmented force vector is defined by:

$$\mathbf{X} = \begin{bmatrix}\mathbf{X}_s \\ X_0\end{bmatrix} = \begin{bmatrix}X_0\frac{\mathbf{Q}_a^*}{Q_y} \\ X_0\end{bmatrix}. \tag{4.30}$$

We refer to it as the (3+1)-dimensional augmented force vector. We now transform the elastoplastic bilinear model to defined in the generalized force space into model within the augmented force space $\mathbf{X}$. Combining Eq. (4.25) and Eq. (4.29), we obtain the dynamical system of augmented force under viscoelastoplastic phase as follows:

$$\frac{d}{dt}\begin{bmatrix}\frac{X_0\mathbf{Q}_a^*}{Q_y} \\ X_0\end{bmatrix} = \frac{1}{Q_y}\begin{bmatrix}0 & \boldsymbol{\eta} \\ \boldsymbol{\eta}^{\mathrm{T}} & 0\end{bmatrix}\begin{bmatrix}X_0\frac{\mathbf{Q}_a^*}{Q_y} \\ X_0\end{bmatrix} =: \mathbf{AX}, \tag{4.31}$$

where $\boldsymbol{\eta} = [\mathbf{N}^{-1}\mathbf{K}_e(\dot{\mathbf{q}}-\dot{\mathbf{q}}^p)]$ and $\mathbf{g}$ is the Minkowski metric as follows:

$$\mathbf{g} = \begin{bmatrix}\mathbf{I} & \mathbf{0} \\ \mathbf{0} & -1\end{bmatrix}.$$

According to Eq. (4.9), the Minkowski metric $\mathbf{g}$ and Eq. (4.30), we further distinguish between two correspondences

$$\|\mathbf{Q}_a^*\| = Q_y \Longleftrightarrow \mathbf{XgX} = 0,$$

$$\|\mathbf{Q}_a^*\| < Q_y \Longleftrightarrow \mathbf{XgX} < 0.$$

The generalized active force vector in generalized active force space corresponds to

doi:10.6342/NTU202402645

an augmented force vector $\mathbf{X}$ of Minkowski spacetime $\mathbb{M}^{3+1}$. By using the coordinates, we convert the non-liner model to a system $\dot{\mathbf{X}} = \mathbf{A}\mathbf{X}$, and state matrix $\mathbf{A}$ satisfies

$$\mathbf{A}^{\mathrm{T}}\mathbf{g} + \mathbf{g}\mathbf{A} = \mathbf{0}, \tag{4.32}$$

Therefore, $\mathbf{A}$ is an element of the real Lie algebra so(3,1).

In the viscoelastoplastic phase, the solution of Eq. (4.31) can be expressed by the following augmented force transformation formula:

$$\mathbf{X}(t) = \left[\mathbf{G}(t)\mathbf{G}^{-1}(t_1)\right]\mathbf{X}(t_1),$$

where $\mathbf{G}(t)$ is the fundamental solution of Eq. (4.31) and it satisfies

$$\dot{\mathbf{G}}(t) = \mathbf{A}\mathbf{G},$$

$$\mathbf{G}(0) = \mathbf{I}_4.$$

Based on the above mentioned property on $\mathbf{G}(t)$

$$\mathbf{G}^{\mathrm{T}}(t)\mathbf{g}\mathbf{G}(t) = \mathbf{g}. \tag{4.33}$$

Hence,the fundamental solution $\mathbf{G}(t)$ is an element of Lie algebra so(3,1). In the case of constant vector $\dot{\boldsymbol{\eta}}$, $\mathbf{A}$ is a constant matrix, and the system Eq. (4.31) become linear. Then the matrix exponent $\exp(\mathbf{A}\Delta t)$ can be used to play the role of the fundamental solution

doi:10.6342/NTU202402645

$\mathbf{G}(t_{i+1}, t_i)$ in the period of t_i to $t_{i+1} = t_i + \Delta t$, i.e.

$$\mathbf{G}(t_{i+1}, t_i) = \exp(\mathbf{A}\Delta t) = \begin{bmatrix} \mathbf{I}_n + \frac{a-1}{\|\boldsymbol{\eta}(t_i)\|^2}\boldsymbol{\eta}(t_i)\boldsymbol{\eta}^{\mathrm{T}}(t_i) & \frac{b}{\|\boldsymbol{\eta}(t_i)\|}\boldsymbol{\eta}(t_i) \\ \frac{b}{\|\boldsymbol{\eta}(t_i)\|}\boldsymbol{\eta}^{\mathrm{T}}(t_i) & a \end{bmatrix}, \tag{4.34}$$

where

$$a = \cosh\left(\frac{\|\boldsymbol{\eta}(t_i)\|}{Q_y}\Delta t\right), \tag{4.35}$$

$$b = \sinh\left(\frac{\|\boldsymbol{\eta}(t_i)\|}{Q_y}\Delta t\right). \tag{4.36}$$

Substituting the above expression into Eq. (4.31) and Eq. (4.34), we obtain:

$$\mathbf{X}(t_{i+1}) = \mathbf{G}(t_{i+1}, t_i)\mathbf{X}(t_i), \tag{4.37}$$

$$\begin{bmatrix} \frac{X_0(t_{i+1})\mathbf{Q}_a^*(t_{i+1})}{Q_y} \\ X_0(t_{i+1}) \end{bmatrix} = \begin{bmatrix} \mathbf{I}_n + \frac{a-1}{\|\boldsymbol{\eta}(t_i)\|^2}\boldsymbol{\eta}(t_i)\boldsymbol{\eta}^{\mathrm{T}}(t_i) & \frac{b}{\|\boldsymbol{\eta}(t_i)\|}\boldsymbol{\eta}(t_i) \\ \frac{b}{\|\boldsymbol{\eta}(t_i)\|}\boldsymbol{\eta}^{\mathrm{T}}(t_i) & a \end{bmatrix} \begin{bmatrix} X_0(t_i)\frac{\mathbf{Q}_a^*(t_i)}{Q_y} \\ X_0(t_i) \end{bmatrix}. \tag{4.38}$$

From Eq. (4.38), we have obtained the closed-form solution for $\mathbf{Q}_a$ as follows:

$$\mathbf{Q}_a(t_{i+1}) = \frac{X_0(t_{i+1})\mathbf{Q}_a^*(t_{i+1})}{Q_y}\frac{Q_y}{X_0(t_{i+1})}. \tag{4.39}$$

In the above derivation, we utilized the transformation of $\mathbf{Q}_a^*$ space to augmented force space and employed the Group-preserving integration (GPI) method to derive the closed-form solution for $\mathbf{Q}_a^*$. That will be advantageous for solving the viscoelastoplastic-phase system. In the next section, we will represent the two-phase system in the form of state-space representation, it will become clearer why we need to solve for $\mathbf{Q}_a^*$ and how

doi:10.6342/NTU202402645

we address the nonlinear behavior in the viscoelastoplastic-phase.

4.5 State-space representation

From Section 4.3, we can divide the entire system into two phases for analysis, namely the viscoelastic phase and the viscoelastoplastic phase. In this section, we represent the system using the state-space representation method, which is a highly advantageous tool for analyzing dynamical systems. Additionally, when the system enters the viscoelastoplastic phase, we utilize the closed-form solution derived in Section 4, denoted as $\mathbf{Q}_a^*$, in conjunction with the state-space representation method for analysis.The following, we will proceed with the matrix derivation of the state-space representation method for the two-phase system. From Eq. (4.21) and Eq. (4.22), we can derive the equation of motion for the two-phase system as follows:

$$\mathbf{m}_s\ddot{\mathbf{q}} + \mathbf{Q} = \mathbf{F}.$$

Next, we define the momentum equation for the two-phase system as follows:

$$\mathbf{P}_s = \mathbf{m}_s\dot{\mathbf{q}}. \tag{4.40}$$

We differentiate Eq. (4.40) wich represent to the time and obtain::

$$\dot{\mathbf{P}}_s = \mathbf{m}_s\ddot{\mathbf{q}}. \tag{4.41}$$

Substituting Eq. (4.41) into the equation of motion Eq. (4.1), we get:

$$\dot{\mathbf{P}}_s = -\mathbf{Q} + \mathbf{F}. \tag{4.42}$$

doi:10.6342/NTU202402645

Next, we will derive the state-space representation for the two-phase system separately.

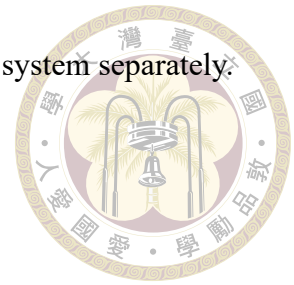

4.5.1 Viscoelastic-phase

From Section 4.3.1, we know that when the system is in the viscoelastic phase, it can be represented by Eq. (4.21). First, we substitute Eq. (4.5) into Eq. (4.3) to obtain $\mathbf{Q} = \mathbf{K}_e\mathbf{q}^e + \mathbf{C}\dot{\mathbf{q}}$, and then we differentiate it as follows:

$$\dot{\mathbf{Q}} = \mathbf{K}_e\dot{\mathbf{q}}^e + \mathbf{C}\ddot{\mathbf{q}}. \tag{4.43}$$

From Eq. (4.2), we know that $\dot{\mathbf{q}}^e = \dot{\mathbf{q}} - \dot{\mathbf{q}}^p$. Substituting this into Eq. (4.43), we get:

$$\dot{\mathbf{Q}} = \mathbf{K}_e(\dot{\mathbf{q}} - \dot{\mathbf{q}}^p) + \mathbf{C}\ddot{\mathbf{q}}. \tag{4.44}$$

Since $\dot{\mathbf{q}}^p = \mathbf{0}$ from Eq. (4.8), Eq. (4.44) can be rewritten as follows:

$$\dot{\mathbf{Q}} = \mathbf{K}_e\dot{\mathbf{q}} + \mathbf{C}\ddot{\mathbf{q}}. \tag{4.45}$$

From the equation of motion, we know that $\ddot{\mathbf{q}} = -\mathbf{m}_s^{-1}\mathbf{Q} + \mathbf{m}_s^{-1}\mathbf{F}$, and from Eq. (4.40), we know that $\dot{\mathbf{q}} = \mathbf{m}_s^{-1}\mathbf{P}_s$. Therefore, Eq. (4.45) can be rewritten as follows:

$$\dot{\mathbf{Q}} = \mathbf{K}_e\mathbf{m}_s^{-1}\mathbf{P}_s - \mathbf{C}\mathbf{m}_s^{-1}\mathbf{Q} + \mathbf{C}\mathbf{m}_s^{-1}\mathbf{F}. \tag{4.46}$$

doi:10.6342/NTU202402645

Using the state-space representation, we can express Eq. (4.40), Eq. (4.42), and Eq. (4.46) as follows:

$$\begin{bmatrix} \dot{\mathbf{P}}_s \\ \dot{\mathbf{q}} \\ \dot{\mathbf{Q}} \end{bmatrix} = \begin{bmatrix} \mathbf{0} & \mathbf{0} & -\mathbf{I} \\ \mathbf{m}_s^{-1} & \mathbf{0} & \mathbf{0} \\ \mathbf{K}_e\mathbf{m}_s^{-1} & \mathbf{0} & -\mathbf{C}\mathbf{m}_s^{-1} \end{bmatrix} \begin{bmatrix} \mathbf{P}_s \\ \mathbf{q} \\ \mathbf{Q} \end{bmatrix} + \begin{bmatrix} \mathbf{F} \\ \mathbf{0} \\ \mathbf{C}\mathbf{m}_s^{-1}\mathbf{F} \end{bmatrix}. \tag{4.47}$$

Eq. (4.47) can also be expressed as follows:

$$\frac{d}{dt}\mathbf{z}_{\mathrm{e}}(t) = \mathbf{A}_{\mathrm{e}}\mathbf{z}_{\mathrm{e}}(t) + \mathbf{u}_{\mathrm{e}}(t), \tag{4.48}$$

where $\mathbf{z}_{\mathrm{e}}(t)$ is the state matrix for viscoelastic phase, $\mathbf{u}_{\mathrm{e}}(t)$ is the input matrix for viscoelastic phase and $\mathbf{A}_{\mathrm{e}}$ is the constant matrix for the viscoelastic phase and

$$\mathbf{z}_{\mathrm{e}} = \begin{bmatrix} \mathbf{P}_s \\ \mathbf{q} \\ \mathbf{Q} \end{bmatrix}, \mathbf{A}_{\mathrm{e}} = \begin{bmatrix} \mathbf{0} & \mathbf{0} & -\mathbf{I} \\ \mathbf{m}_s^{-1} & \mathbf{0} & \mathbf{0} \\ \mathbf{K}_e\mathbf{m}_s^{-1} & \mathbf{0} & -\mathbf{C}\mathbf{m}_s^{-1} \end{bmatrix}, \mathbf{u}_{\mathrm{e}} = \begin{bmatrix} \mathbf{F} \\ \mathbf{0} \\ \mathbf{C}\mathbf{m}_s^{-1}\mathbf{F} \end{bmatrix}. \tag{4.49}$$

So far, we have derived the state-space representation for the viscoelastic phase. Furthermore, from Eq. (4.21), we know that the viscoelastic phase system must satisfy the following equations simultaneously:

$$\dot{\mathbf{q}}^p = \mathbf{0},$$

$$\dot{\mathbf{Q}}_b = \mathbf{0},$$

$$\mathbf{Q}_a = \mathbf{Q} - \mathbf{Q}_b - \mathbf{C}\dot{\mathbf{q}}.$$

doi:10.6342/NTU202402645

We have completed the derivation of the state-space representation for the viscoelastic phase system. Next, we will derive the state-space representation for the viscoelastoplastic phase system.

4.5.2 Viscoelastoplastic-phase

From Sec 4.3.2, we know that when the system is in the viscoelastoplastic phase, it can be represented by Eq. (4.22). First, from Eq. (4.3) and Eq. (4.4), we know that $\mathbf{Q} = \mathbf{Q}_a + \mathbf{Q}_b + \mathbf{C}\dot{\mathbf{q}}$. We substitute this into Eq. (4.42) as follows:

$$\dot{\mathbf{P}}_s = -\mathbf{Q}_a - \mathbf{Q}_b - \mathbf{C}\dot{\mathbf{q}} + \mathbf{F}. \tag{4.50}$$

We know from Eq. (4.50) that $\dot{\mathbf{q}} = \mathbf{m}_s^{-1}\mathbf{P}_s$. Substituting this into Eq. (4.42), we get:

$$\dot{\mathbf{P}}_s = -\mathbf{Q}_a - \mathbf{Q}_b - \mathbf{C}\mathbf{m}_s^{-1}\mathbf{P}_s + \mathbf{F}. \tag{4.51}$$

In Section 4, we have already solved for the closed form of $\mathbf{Q}_a^*$, so $\mathbf{Q}_a$, $\dot{\mathbf{Q}}_a$ and $\dot{\mathbf{Q}}_a^*$ is known. From Eq. (4.12), we can know $\dot{\mathbf{q}}^p$ as follows:

$$\dot{\mathbf{q}}^p = [\mathbf{K}_p + \mathbf{K}_e]^{-1}\mathbf{K}_e\dot{\mathbf{q}} - [\mathbf{K}_p + \mathbf{K}_e]^{-1}\dot{\mathbf{Q}}_a. \tag{4.52}$$

We can also know $\dot{\mathbf{Q}}_b$ from Eq. (4.6) as follows:

$$\begin{aligned}\dot{\mathbf{Q}}_b &= \mathbf{K}_p[\mathbf{K}_p + \mathbf{K}_e]^{-1}\mathbf{K}_e\dot{\mathbf{q}} - \mathbf{K}_p[\mathbf{K}_p + \mathbf{K}_e]^{-1}\dot{\mathbf{Q}}_a, \\ &= \mathbf{K}_p[\mathbf{K}_p + \mathbf{K}_e]^{-1}\mathbf{K}_e\mathbf{m}_s^{-1}\mathbf{P}_s - \mathbf{K}_p[\mathbf{K}_p + \mathbf{K}_e]^{-1}\dot{\mathbf{Q}}_a.\end{aligned} \tag{4.53}$$

doi:10.6342/NTU202402645

Using the state-space representation, we can express Eq. (4.40), Eq. (4.51), and Eq. (4.53) as follows:

$$\begin{bmatrix} \dot{\mathbf{P}}_s \\ \dot{\mathbf{q}} \\ \dot{\mathbf{Q}}_b \end{bmatrix} = \begin{bmatrix} -\mathbf{C}\mathbf{m}_s^{-1} & \mathbf{0} & -\mathbf{I} \\ \mathbf{m}_s^{-1} & \mathbf{0} & \mathbf{0} \\ \mathbf{K}_p[\mathbf{K}_p+\mathbf{K}_e]^{-1}\mathbf{K}_e\mathbf{m}_s^{-1} & \mathbf{0} & \mathbf{0} \end{bmatrix} \begin{bmatrix} \mathbf{P}_s \\ \mathbf{q} \\ \mathbf{Q}_b \end{bmatrix} + \begin{bmatrix} -\mathbf{Q}_a+\mathbf{F} \\ \mathbf{0} \\ -\mathbf{K}_p[\mathbf{K}_p+\mathbf{K}_e]^{-1}\dot{\mathbf{Q}}_a \end{bmatrix}. \quad (4.54)$$

Eq. (4.54) can also be expressed as follows:

$$\frac{d}{dt}\mathbf{z}_{\mathrm{p}}(t) = \mathbf{A}_{\mathrm{p}}\mathbf{z}_{\mathrm{p}}(t) + \mathbf{u}_{\mathrm{p}}(t), \quad (4.55)$$

where $\mathbf{z}_{\mathrm{p}}(t)$ is the state matrix for viscoelastoplastic phase, $\mathbf{u}_{\mathrm{p}}(t)$ is the input matrix for viscoelastoplastic phase and $\mathbf{A}_{\mathrm{p}}$ is the constant matrix for the viscoelastoplastic phase and

$$\mathbf{z}_{\mathrm{p}} = \begin{bmatrix} \mathbf{P}_s \\ \mathbf{q} \\ \mathbf{Q}_b \end{bmatrix}, \mathbf{A}_{\mathrm{p}} = \begin{bmatrix} -\mathbf{C}\mathbf{m}_s^{-1} & \mathbf{0} & -\mathbf{I} \\ \mathbf{m}_s^{-1} & \mathbf{0} & \mathbf{0} \\ \mathbf{K}_p[\mathbf{K}_p+\mathbf{K}_e]^{-1}\mathbf{K}_e\mathbf{m}_s^{-1} & \mathbf{0} & \mathbf{0} \end{bmatrix}, \mathbf{u}_{\mathrm{p}} = \begin{bmatrix} -\mathbf{Q}_a+\mathbf{F} \\ \mathbf{0} \\ -\mathbf{K}_p[\mathbf{K}_p+\mathbf{K}_e]^{-1}\dot{\mathbf{Q}}_a \end{bmatrix}. \quad (4.56)$$

So far, we have derived the state-space representation for the viscoelastoplastic phase. Furthermore, from Eq. (4.22), we know that the viscoelastoplastic phase system must satisfy the following equations simultaneously:

$$Q_y\dot{\mathbf{q}}^p = \mathbf{Q}_a^*\dot{\lambda},$$

$$\dot{\mathbf{q}}^p = \mathbf{K}_p^{-1}\dot{\mathbf{Q}}_b,$$

doi:10.6342/NTU202402645

$$\dot{\mathbf{Q}}_b = \mathbf{K}_p \dot{\mathbf{q}}^p,$$

$$\mathbf{Q} = \mathbf{Q}_a + \mathbf{Q}_b + \mathbf{C}\dot{\mathbf{q}}.$$

By now, we have derived the state-space representation for the viscoelastoplastic-phase, and the viscoelastoplastic-phase system is now a linear system. In this section, we utilize the closed-form solution derived in Section 4.4 to address the complex nonlinear terms arising from the viscoelastoplastic-phase. With the state-space representations for the viscoelastic-phase and viscoelastoplastic-phases established, we can better solve this bilinear viscoelastoplastic model since all nonlinear terms have been eliminated. In the next section, we will introduce how to solve this state-space representation.

4.6 Incremental analysis method

In Section 4.5, the state-space representation for the two-phase system has been derived. In this section, we will explain the use of the incremental analysis method to analyze its state-space representation. The incremental analysis, as the name suggests, involves step-by-step consideration of each increment, and analyzing the system's response at each step. In the case of the two-phase system, we take Δt as a small increment, representing the time interval for the external force input to the system. Therefore, we know that this increment is constant. Furthermore, because Δt is a constant, it is possible to violate the admissible condition at fixed time intervals. This occurs because the transition from the viscoelastic-phase to the viscoelastoplastic-phase may not necessarily happen exactly at the onset of plasticity. Therefore, we may encounter a violation of the admissi-

doi:10.6342/NTU202402645

ble condition. Here, we provide a clearer explanation with a diagram, as shown in Figure 4.3. In the figure, we define t_k as the last point in the viscoelastic-phase, and t_{k+1} as the next point in time at a fixed time interval. At t_{k+1}, the system has already entered the viscoelastoplastic-phase, but we can observe from the graph that a violation of the admissible condition occurs at this time, i.e., $f > 0$. This is because t_{k+1} may not be the correct onset time for entering the plastic state. Therefore, we must first find the onset time t_s. Here, we divide the system into three elements: the viscoelastic-phase module, the viscoelastoplastic-phase module, and the viscoelastoplastic pull-back module. The viscoelastoplastic pull-back module is used to find the system's response at the time of t_s to address the situation described above.Now, we will proceed with the introduction to the incremental analysis method for these three elements.

In Section 4.5, we initially divide the viscoelastoplastic system into two phases. However, due to the need for viscoelastoplastic pull-back when the viscoelastic-phase transitions into the viscoelastoplastic-phase, the two-phase system is further divided into three modules for analysis. Next, we will introduce the linear time-invariant (LTI) system, followed by the introduction of the three modules separately.

doi:10.6342/NTU202402645

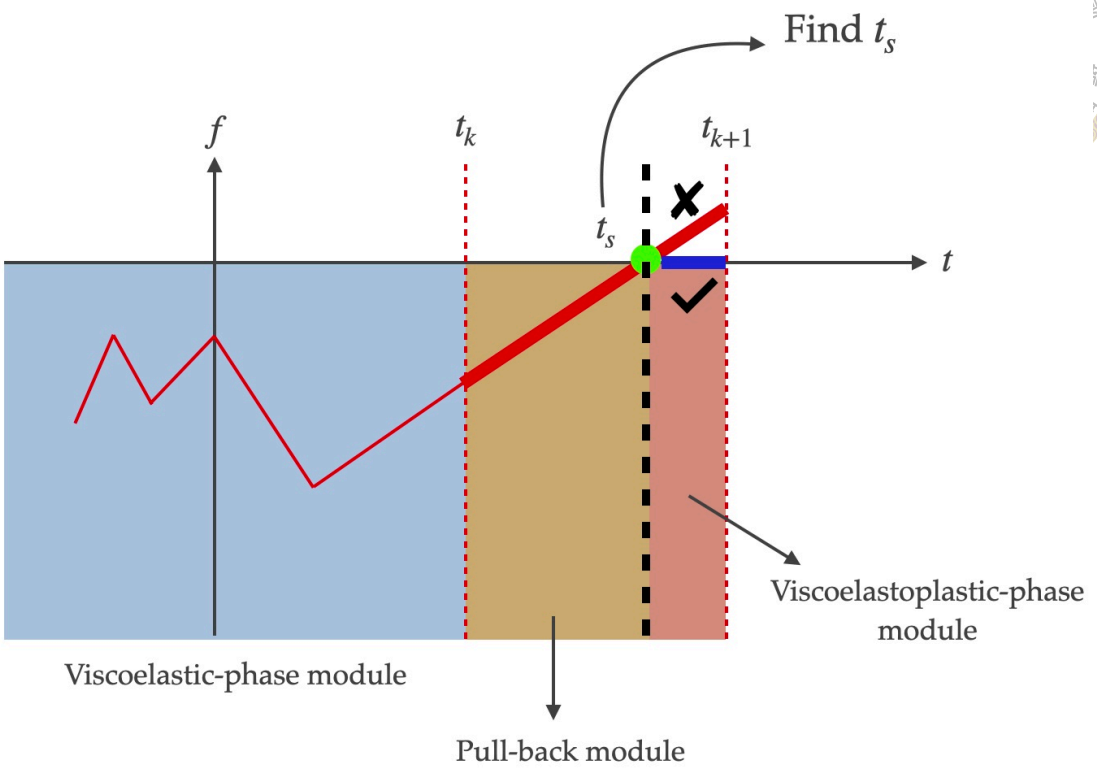

Figure 4.3: Scheme diagram about the computational idea from VE phase to VEP phase

4.6.1 Linear time-invariant (LTI) system

First, we will proceed with the solution of the linear time-invariant (LTI) system, which is represented mathematically as follows.

$$\frac{d}{dt}\mathbf{z}_{\mathrm{s}}(t) = \mathbf{A}_{\mathrm{s}}\mathbf{z}_{\mathrm{s}}(t) + \mathbf{u}_{\mathrm{s}}(t), \tag{4.57}$$

where $\mathbf{z}_{\mathrm{s}}(t)$ is the state matrix for LTI system, $\mathbf{u}_{\mathrm{s}}(t)$ is the input vector for LTI system and $\mathbf{A}_{\mathrm{s}}$ is the constant matrix for LTI system. Its solution can be represented as follows:

$$\mathbf{z}_{\mathrm{s}}(t) = \exp\left(\mathbf{A}_{\mathrm{s}}\left(t - t_i\right)\right)\mathbf{z}_{\mathrm{s}}\left(t_i\right) + \int_{t_i}^{t} \exp(\mathbf{A}_{\mathrm{s}}(t-\tau))\mathbf{u}_{\mathrm{s}}(\tau)d\tau. \tag{4.58}$$

If the time increment is Δt, and we have already obtained $\mathbf{z}_{\mathrm{s}}\left(t_i\right)$ and $\mathbf{u}_{\mathrm{s}}(t_i)$, with the

doi:10.6342/NTU202402645

time interval $(t_i, t_i + \Delta t)$, and $\mathbf{u}_{\mathrm{s}}(t_i + \Delta t)$ is a constant, then the solution of the linear time-invariant (LTI) system at this time is as follows:

$$\mathbf{z}_{\mathrm{s}}\left(t_i + \Delta t\right) = \exp(\mathbf{A}_{\mathrm{s}}(\Delta t))\mathbf{z}_{\mathrm{s}}\left(t_i\right) + \int_{t_i}^{t_i+\Delta t} \exp\left(\mathbf{A}_{\mathrm{s}}\left(t_i + \Delta t - \tau\right)\right) d\tau \mathbf{u}_{\mathrm{s}}\left(t_i\right). \quad (4.59)$$

Next, integrating Eq. (4.59), we have:

$$\mathbf{z}_{\mathrm{s}}\left(t_i + \Delta t\right) = \exp(\mathbf{A}_{\mathrm{s}}\Delta t)\mathbf{z}_{\mathrm{s}}\left(t_i\right) + \left[\sum_{n=0}^{\infty}\left(\frac{\Delta t^{n+1}}{(n+1)!}\right)\mathbf{A}_{\mathrm{s}}^{n}\right]\mathbf{u}_{\mathrm{s}}\left(t_i\right). \quad (4.60)$$

Above, we have completed the derivation of the solution for the Time-Invariant (LTI) system. Next, we will apply the result of Eq. (4.60) to the three modules.

4.6.2 Viscoelastic-phase module

If the time increment is Δt, and we have already obtained $\mathbf{z}_{\mathrm{e}}\left(t_i\right)$ and $\mathbf{u}_{\mathrm{e}}(t_i)$, with the time interval $(t_i, t_i+\Delta t)$, and $\mathbf{u}_{\mathrm{e}}(t_i+\Delta t)$ is a constant, then the solution of the viscoelastic phase system at this time is as follows:

$$\mathbf{z}_{\mathrm{e}}\left(t_i + \Delta t\right) = \exp(\mathbf{A}_{\mathrm{e}}(\Delta t))\mathbf{z}_{\mathrm{e}}\left(t_i\right) + \int_{t_i}^{t_i+\Delta t} \exp\left(\mathbf{A}_{\mathrm{e}}\left(t_i + \Delta t - \tau\right)\right) d\tau \mathbf{u}_{\mathrm{e}}\left(t_i\right). \quad (4.61)$$

Next, integrating Eq. (4.61), we have:

$$\mathbf{z}_{\mathrm{e}}\left(t_i + \Delta t\right) = \exp(\mathbf{A}_{\mathrm{e}}\Delta t)\mathbf{z}_{\mathrm{e}}\left(t_i\right) + \left[\sum_{n=0}^{\infty}\left(\frac{\Delta t^{n+1}}{(n+1)!}\right)\mathbf{A}_{\mathrm{e}}^{n}\right]\mathbf{u}_{\mathrm{e}}\left(t_i\right). \quad (4.62)$$

We have now introduced the incremental analysis method for the viscoelastic-phase module. Next, we will introduce the viscoelastoplastic module.

doi:10.6342/NTU202402645

4.6.3 Viscoelastoplastic-phase module

If the time increment is Δt, and we have already obtained $\mathbf{z}_{\mathrm{p}}(t_i)$ and $\mathbf{u}_{\mathrm{p}}(t_i)$, with the time interval $(t_i, t_i + \Delta t)$, and $\mathbf{u}_{\mathrm{p}}(t_i + \Delta t)$ is a constant, then the solution of the viscoelastoplastic phase system at this time is as follows:

$$\mathbf{z}_{\mathrm{p}}(t_i + \Delta t) = \exp(\mathbf{A}_{\mathrm{p}}(\Delta t))\mathbf{z}_{\mathrm{p}}(t_i) + \int_{t_i}^{t_i+\Delta t} \exp\left(\mathbf{A}_{\mathrm{p}}(t_i + \Delta t - \tau)\right) d\tau \mathbf{u}_{\mathrm{p}}(t_i). \quad (4.63)$$

Next, integrating Eq. (4.63), we have:

$$\mathbf{z}_{\mathrm{p}}(t_i + \Delta t) = \exp(\mathbf{A}_{\mathrm{p}}\Delta t)\mathbf{z}_{\mathrm{p}}(t_i) + \left[\sum_{n=0}^{\infty}\left(\frac{\Delta t^{n+1}}{(n+1)!}\right)\mathbf{A}_{\mathrm{p}}^{n}\right]\mathbf{u}_{\mathrm{p}}(t_i). \quad (4.64)$$

We have now introduced the incremental analysis method for the viscoelastoplastic-phase module. Next, we will introduce the viscoelastoplastic pull-back module.

4.6.4 Viscoelastoplastic pull-back module

As shown in Figure 4.3, switching from the viscoelastic-phase system to the viscoelastoplastic-phase system at fixed time intervals may lead to a violation of the admissible condition. Therefore, we must first find the time t_s when entering the viscoelastoplastic-phase. We divide Δt into ten equal parts and then use the viscoelastic-phase module to calculate $\mathbf{z}_{\mathrm{e}}(t_k + 0.1\Delta t)$. At this time, we check the admissible condition f. If $f(t_k + 0.1\Delta t) < 0$, it means the system has not yet yielded. We can further calculate $\mathbf{z}_{\mathrm{e}}(t_k + 0.2\Delta t)$ using the viscoelastic-phase module and check the admissible condition f again. If $f(t_k + 0.2\Delta t) < 0$, we continue to divide the time interval. If $f(t_k + 0.2\Delta t) > 0$, it means $t_s \in (t_k, t_k + 0.2\Delta t)$. Then we divide the time interval $0.2\Delta t$ into ten equal parts again

doi:10.6342/NTU202402645

until $f = 0$. At this time, the time is the time of the first entry into the viscoelastoplastic-phase. The flowchart is depicted in Figure 4.4. The above derivation has provided solutions for the three modules using the incremental analysis method. The next section will introduce the algorithm and its process for combining these three modules.

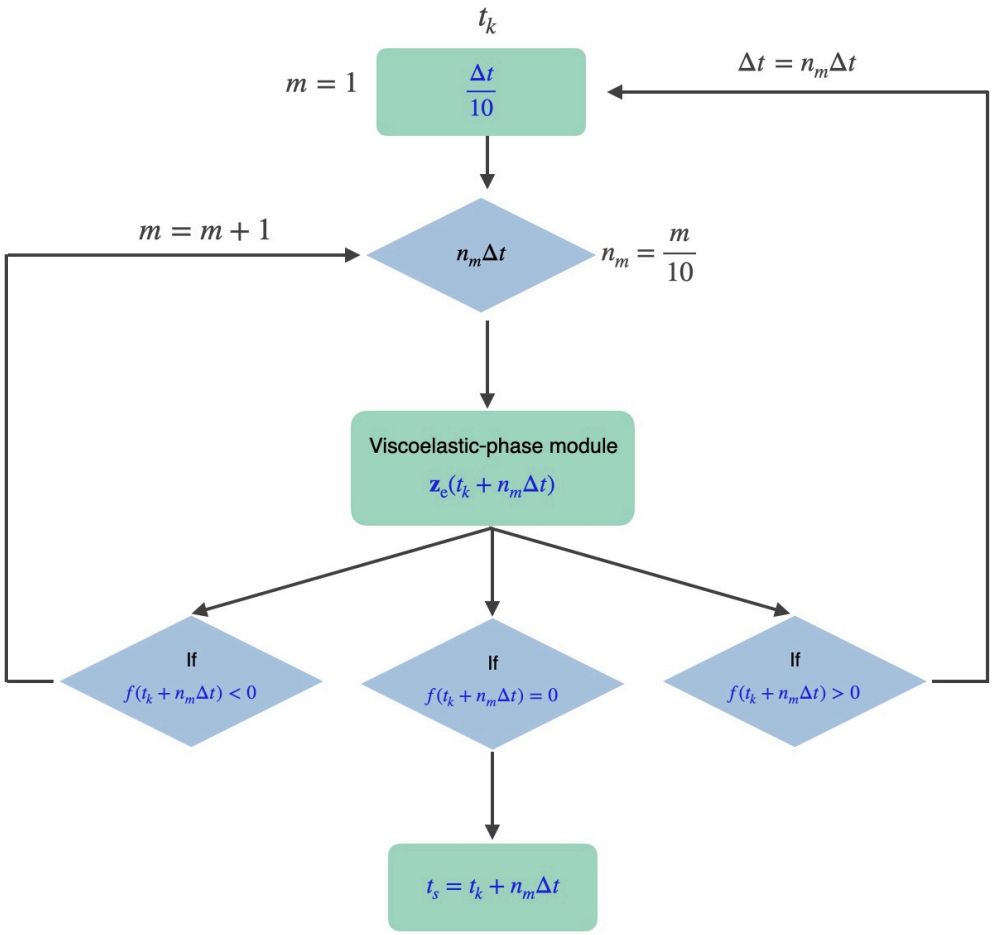

Figure 4.4: Flowchat of pull back module in the VEP phase

4.7 Algorithm

In this section, we will introduce the entire system algorithm process. The analysis methods for the three modules have been explained in section 4.6. Next, we will combine the three modules and incorporate judgment conditions to analyze the system. From sec-

doi:10.6342/NTU202402645

tion 4.3, we know that the system can be divided into two phases: the viscoelastic-phase and the viscoelastoplastic-phase. There are two very important judgment conditions: the floor shear force admissible condition and the straining condition. These two judgment conditions can help us determine the state of the system and satisfy the requirements of the complementary trio simultaneously. Here, we define the viscoelastoplastic indicator as **Iflage**. When **Iflage** $= 0$, the system is in the viscoelastic-phase, and when **Iflage** $= 1$, the system is in the viscoelastoplastic-phase. This viscoelastoplastic indicator facilitates us in conveniently determining the state of the system. First, we need to solve the initial value problem of the differential equation, so we set the initial condition $\mathbf{z} = \mathbf{0}$. Next is the detailed algorithm process.

When the system is at time t_i, if **Iflage** $= 0$, the system is in the viscoelastic-phase. Therefore, we calculate the response at t_{i+1} based on the viscoelastic-phase module. First, we need to confirm whether t_{i+1} violates the floor shear force admissible condition. If $f(t_{i+1}) \leq 0$, the calculation result at this time is reasonable for the viscoelastic-phase module **Iflage** $= 0$, and we proceed to the next time for calculation. If $f > 0$, the situation of violating the admissible condition mentioned in Section 4.6 occurs. Therefore, we need to enter the viscoelastoplastic pull-back module to find t_s. Once t_s is found, we enter the viscoelastic-phase module for calculation. At this time, **Iflage** $= 0$. Next, we need to follow the procedure mentioned in Section 4.4 to transform the $\mathbf{Q}_a$ space into Minkowski spacetime and calculate the closed-form $\mathbf{Q}_a$. Then, we proceed to calculate the response at t_{i+1} based on the viscoelastoplastic-phase module, where **Iflage** $= 1$, and then continue to the calculation of the next time.

When the system is at time t_i, if **Iflage** $= 1$, the system is in the viscoelastoplastic-phase. At this time, we first confirm the straining condition. If the straining condition

doi:10.6342/NTU202402645

$s(t_i) < 0$, we calculate the response at t_{i+1} based on the viscoelastic-phase module. Then, we confirm whether t_{i+1} violates the floor shear force admissible condition. If $f(t_{i+1}) \leq 0$, the calculation result at this time is reasonable for the viscoelasti-phase module **Iflage** $= 0$, and we proceed to the next time for calculation. If $f > 0$, the situation of violating the admissible condition mentioned in Section 4.6 occurs. Therefore, we need to enter the viscoelastoplastic pull-back module to find t_s. Once t_s is found, we enter the viscoelastic-phase module for calculation. At this time, **Iflage** $= 0$. Next, we need to follow the procedure mentioned in Section 4.4 to transform the $\mathbf{Q}_a$ space into Minkowski spacetime and calculate the closed-form $\mathbf{Q}_a$. Then, we proceed to calculate the response at t_{i+1} based on the viscoelastoplastic-phase module, where **Iflage** $= 1$, and then continue to the calculation of the next time. If the straining condition $s(t_i) > 0$, we directly calculate the closed-form $\mathbf{Q}_a$ and then proceed to calculate the response at t_{i+1} based on the viscoelastoplastic-phase modudle, where **Iflage** $= 1$, and then continue to the calculation of the next time.

Here is a flowchart to better understand this algorithm process, as shown in Figure 4.5.

doi:10.6342/NTU202402645

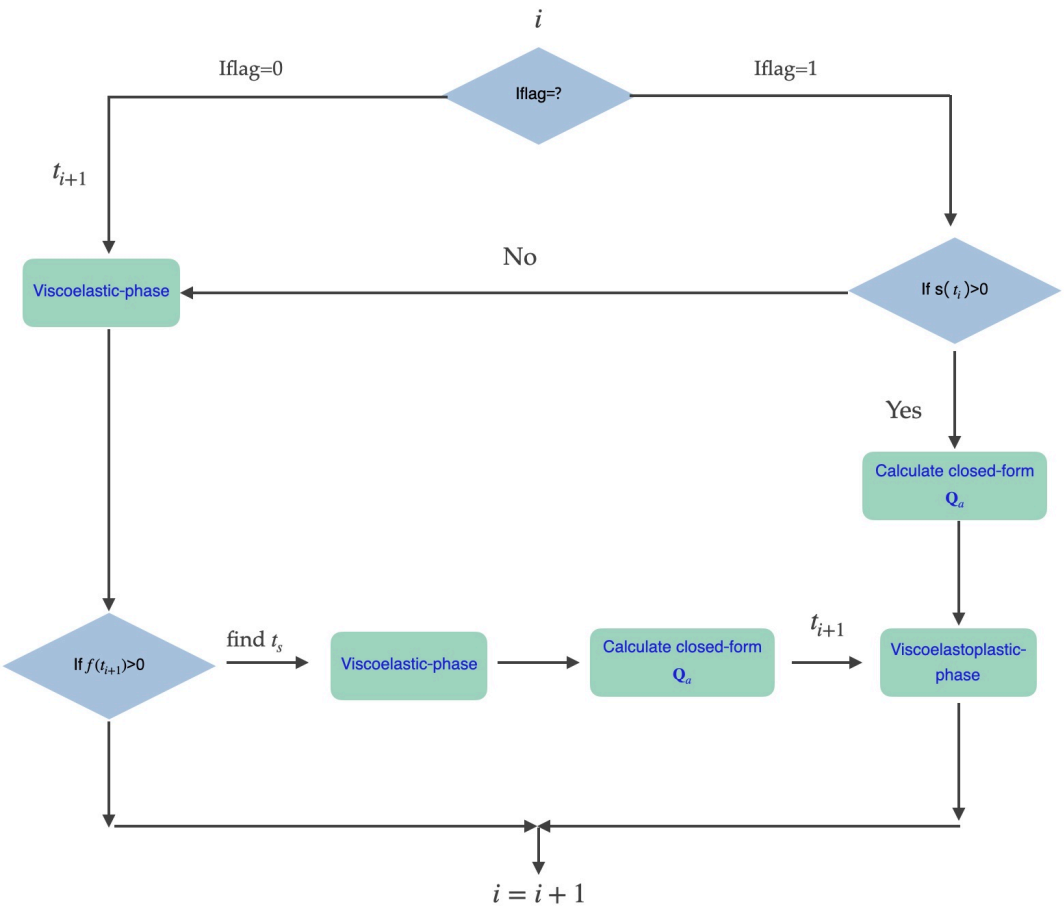

Figure 4.5: Viscoelastoplastic model analysis algorithm flowchart

doi:10.6342/NTU202402645

Chapter 5 Seismic behavior of asymmetric building structures

This section will implement the mathematical model proposed in Chapter 4 using MATLAB, and the entire analysis procedure will follow the algorithm flow established in Sec 4.7. A single-story, bidirectionally asymmetric building structure is considered for earthquake excitation analysis. The structure dimensions are 10m in EW directions, 5m in NS directions and the story height is 3.6m, with fixed supports. The column cross-section dimensions are $0.5m \times 0.3m$, with a total of four columns. The beam cross-section dimensions are $0.25m \times 0.5m$, and the floor slab is a 15cm thick rigid slab. All materials are reinforced concrete, with a unit weight of $2400(\frac{kgf}{m^3})$ for reinforced concrete, a design compressive strength of $210(\frac{kgf}{cm^2})$, and a column stiffness reduction factor of 0.8. The damping ratio for the entire structure is 5%. It is assumed that the mass of the structure is concentrated at the floor slab centroid. Assuming that the eccentricity in both directions

doi:10.6342/NTU202402645

is $e_x = 0.05$ and $e_y = 0.05$.The structural stiffness matrix is

$$\mathbf{K}_e = \begin{bmatrix} k_{xx} & k_{xy} & k_{x\theta} \\ k_{yx} & k_{yy} & k_{y\theta} \\ k_{\theta x} & k_{\theta y} & k_{\theta\theta} \end{bmatrix} = \begin{bmatrix} k_x & 0 & -e_y k_x \\ 0 & k_y & e_x k_y \\ -e_y k_x & e_x k_y & k_\theta + e_y^2 k_x + e_x^2 k_y \end{bmatrix}.$$

Here, subscript x represents the component in 1st direction , subscript y represents the component in 2nd direction, and subscript θ represents the component in 3th direction.

Based on the provided information, the necessary parameters for the analysis model can be obtained. The structural mass is $m_s = 3280.733945 \left(\frac{\text{kgf}-\text{s}^2}{\text{m}}\right)$. The moment of inertia is$I_o = 34174.31193 \left(\text{kgf} - \text{m}^2\right)$.The elastic lateral stiffness is $k_1 = 4472647.145 \left(\frac{kgf}{m}\right)$ in EW-direction, $k_2 = 1610152.972 \left(\frac{kgf}{m}\right)$ in NS-direction, and $k_3 = 19232382.72 \left(\frac{\text{kgf}-\text{m}}{\text{rad}}\right)$ in twist direction. The post-yield stiffness $\mathbf{K}_p = 0.05\mathbf{K}_e$. The structural damping coefficient matrix use Rayleigh damping $\mathbf{C} = \alpha\mathbf{m}_s + \beta\mathbf{K}_e \left(\frac{kgf-s}{m}\right)$. The story yield shear force $Q_y = C_s \times W$, where W is the structural weight, and C_s is taken as 0.12 based on empirical data. Based on the parameters, we can determine that the natural period of the asymmetrical building structures in the E-W direction is $T_{nEW} = 0.17\ (s)$, in the N-S direction is $T_{nNS} = 0.284\ (s)$, and the torsional period is $T_\theta = 0.265\ (s)$.

In this section, the ground motion records used for the analysis are the east-west and north-south horizontal acceleration signals recorded at ten stations during the 921 Chi-Chi earthquake event, provided by the PEER Center (Pacific Earthquake Engineering Research Center). The stations are CHY041, TCU084, CHY028, TCU052, TCU068, TCU065, TCU079, CHY101, TCU071, and TCU129.

doi:10.6342/NTU202402645

5.1 Complementary trio checking of asymmetric structures

Before conducting structural response analysis, it is necessary to verify the correctness of the algorithm flow proposed in Sec 4.7. We will use the complementary tri-variate conditions mentioned in Sec 4.2 to confirm the validity of the algorithm, which involves checking the non-negative dissipation $\dot{\lambda} \geq 0$, the admissible condition $f \leq 0$, and the alternative condition $f\dot{\lambda} = 0$. The verification method is to input the aforementioned bi-directional ground motion records into our proposed analysis model, and after the analysis, check if the complementary trio conditions are satisfied. From Figures 5.1 to 5.10, it can be observed that all selected seismic records satisfied the complementary trio conditions. Therefore, we can confirm the accuracy of this algorithm and proceed with the subsequent analyses with confidence.Additionally, all analyzed seismic acceleration records are the original seismic acceleration records.

After confirming that the complementary triad conditions are satisfied, we can essentially verify the correctness of the entire algorithm. To further validate this, we can check whether the path of $\mathbf{Q}_a$ always remains within or on the yield surface, without any instances of exceeding it. In this case, considering that the building structure we are studying has asymmetric properties with different stiffness in all directions, and accounting for eccentricity effects, we have considered not only the bi-directional horizontal response but also the torsional response. The yield surface of this structure is designed as a three-dimensional ellipsoidal yield surface, implying that the structure has different yield strengths in different directions. From Figure 5.11 to Figure 5.20, it can be clearly observed that the $\mathbf{Q}_a$ paths induced by each earthquake time history are confined within

doi:10.6342/NTU202402645

the yield surface. This observation further confirms the correctness and robustness of the proposed algorithm flow. Specifically, each path demonstrates the force-displacement response of the structure under seismic action, and there are no phenomena of exceeding the yield surface. During the seismic action, the $\mathbf{Q}_a$ paths are all on or within the yield surface, which is entirely consistent with the constraints of our proposed model. In other words, it accurately describes the viscoelastoplastic behavior of the building structure after being subjected to an earthquake. The acquisition of these results not only demonstrates the theoretical rigor of the algorithm but also reflects its effectiveness in practical applications. For engineering practice, the ability to accurately predict structural behavior under seismic action is crucial, and our algorithm has shown powerful capabilities in this regard. Through these illustrations, one can intuitively understand the dynamic process of structural response. In summary, through the examination and analysis of the $\mathbf{Q}_a$ paths, we can confidently confirm the correctness of the proposed algorithm. These results once again emphasize the importance of considering both the bi-directional horizontal response and the torsional response of structures under seismic loads in engineering design and analysis. These research findings provide important references for future structural analysis, particularly valuable when dealing with dynamic loads such as earthquakes.

doi:10.6342/NTU202402645

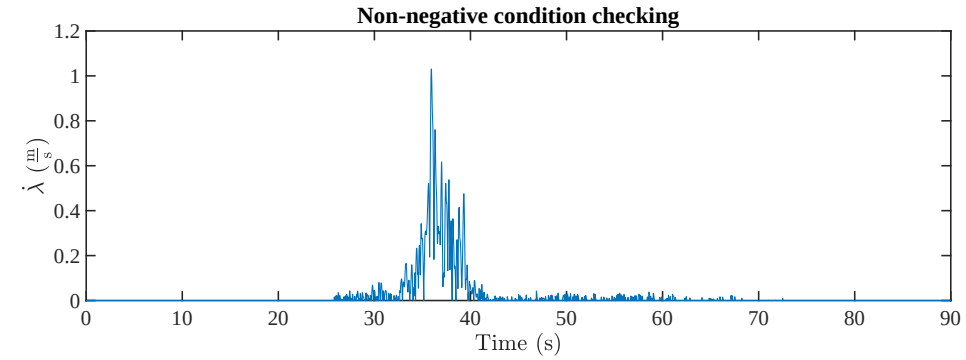

(a) The history of $\dot{\lambda}$ value

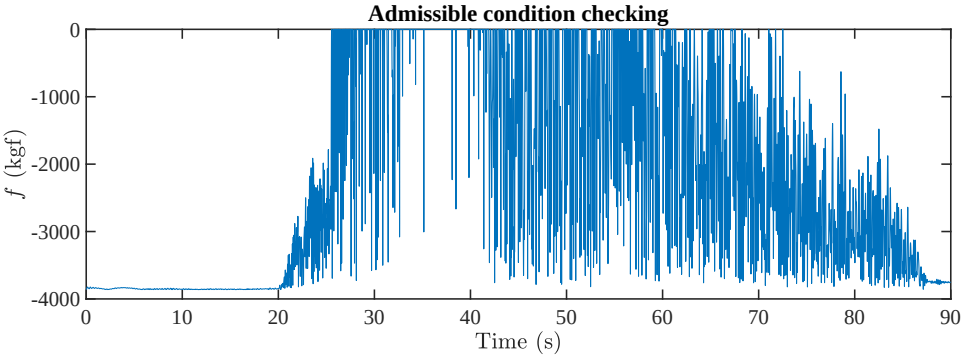

(b) The history of f value

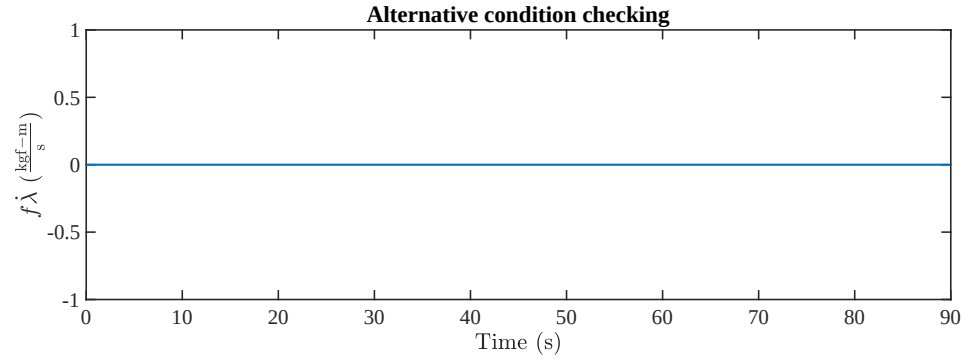

(c) The history of $f\dot{\lambda}$ value

Figure 5.1: The response of $\dot{\lambda}$, f, $f\dot{\lambda}$ of asymmetric building structures under the seismic record of the CHY028 station during Chi-Chi earthquake

doi:10.6342/NTU202402645

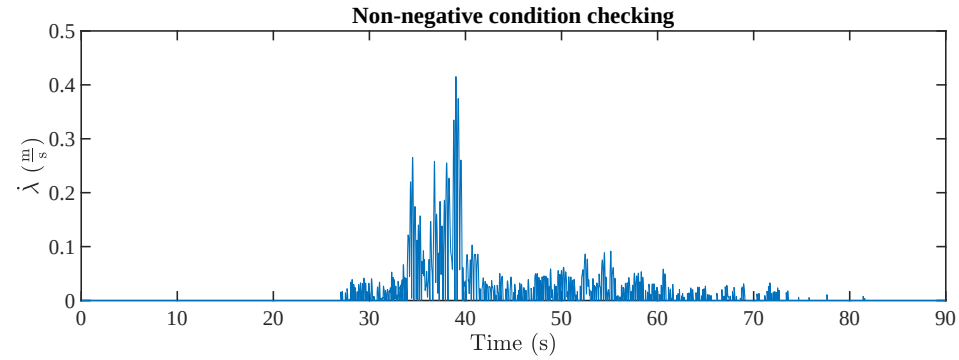

(a) The history of $\dot{\lambda}$ value

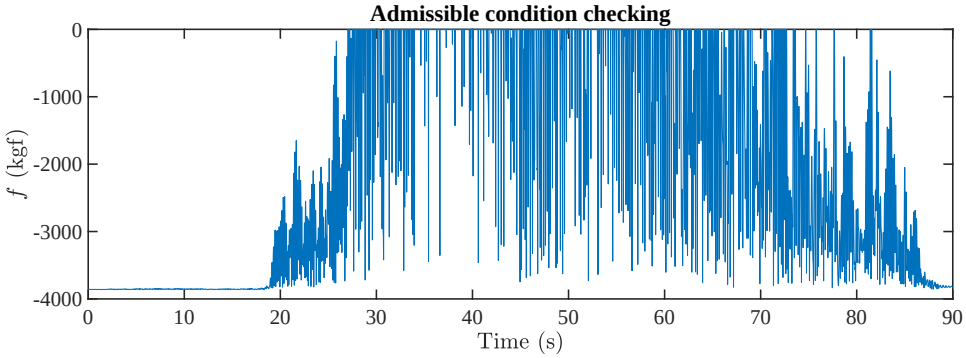

(b) The history of f value)

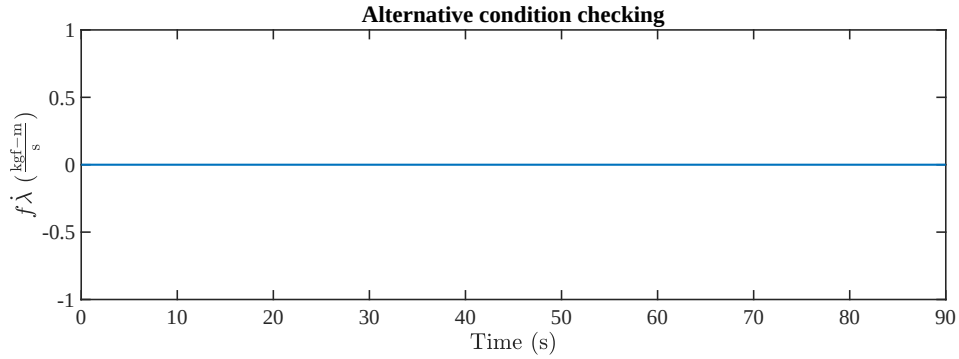

(c) The history of $f\dot{\lambda}$ value

Figure 5.2: The response of $\dot{\lambda}$, f, $f\dot{\lambda}$ of asymmetric building structures under the seismic record of the CHY041 station during Chi-Chi earthquake

doi:10.6342/NTU202402645

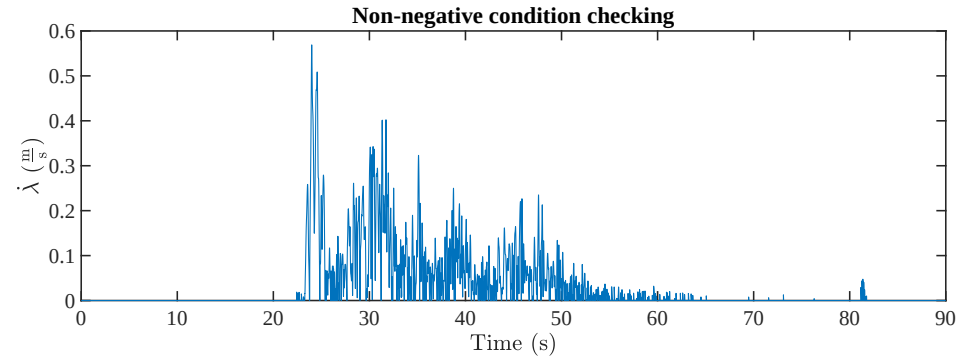

(a) The history of $\dot{\lambda}$ value

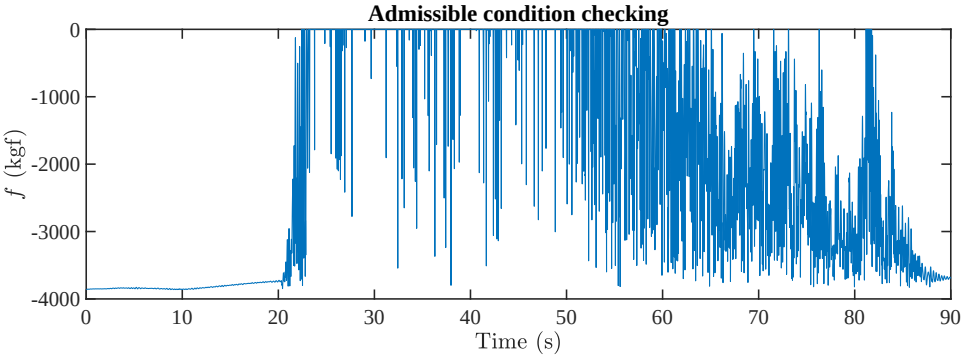

(b) The history of f value

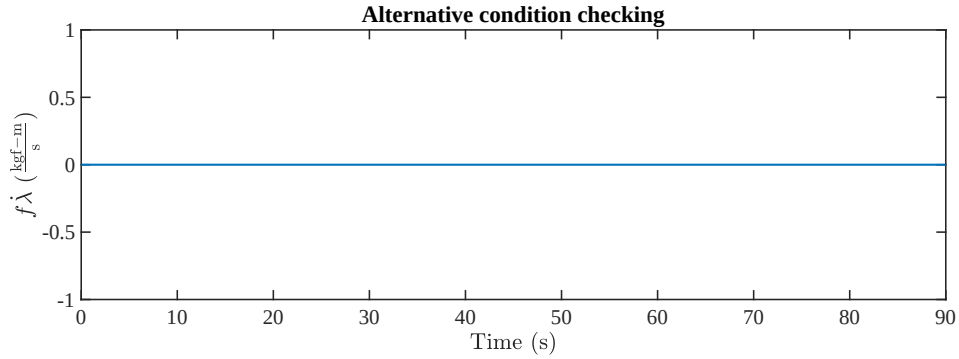

(c) The history of $f\dot{\lambda}$ value

Figure 5.3: The response of $\dot{\lambda}$, f, $f\dot{\lambda}$ of asymmetric building structures under the seismic record of the TCU071 station during Chi-Chi earthquake

doi:10.6342/NTU202402645

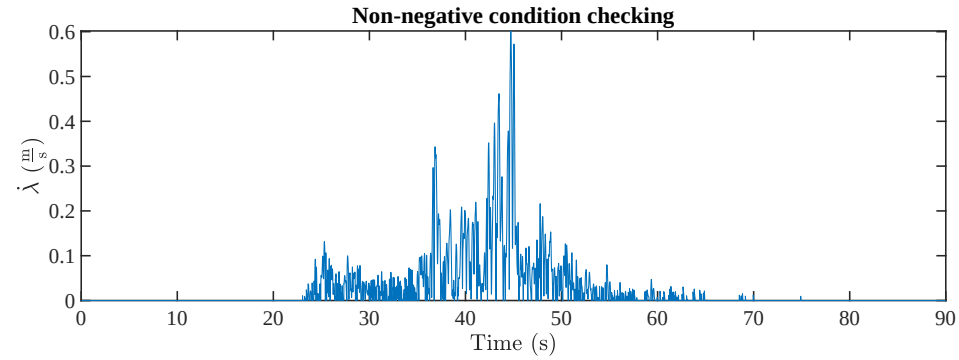

(a) The history of $\dot{\lambda}$ value

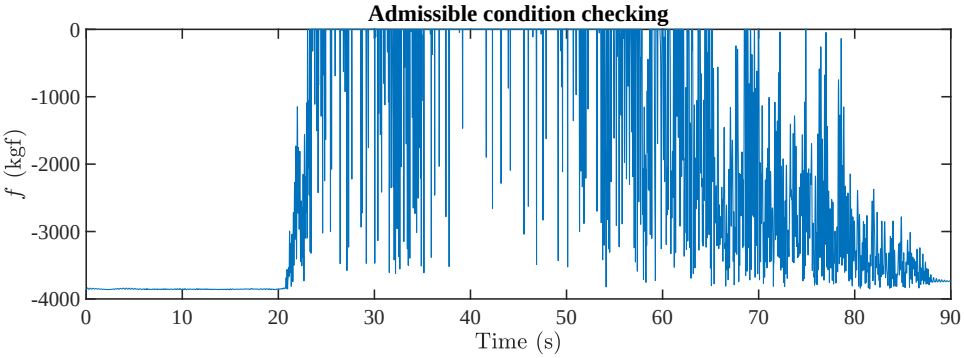

(b) The history of f value

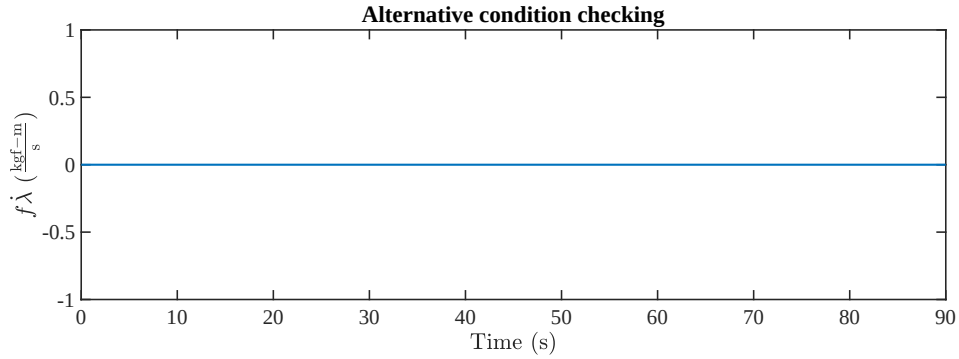

(c) The history of $f\dot{\lambda}$ value

Figure 5.4: The response of $\dot{\lambda}$, f, $f\dot{\lambda}$ of asymmetric building structures under the seismic record of the TCU079 station during Chi-Chi earthquake

doi:10.6342/NTU202402645

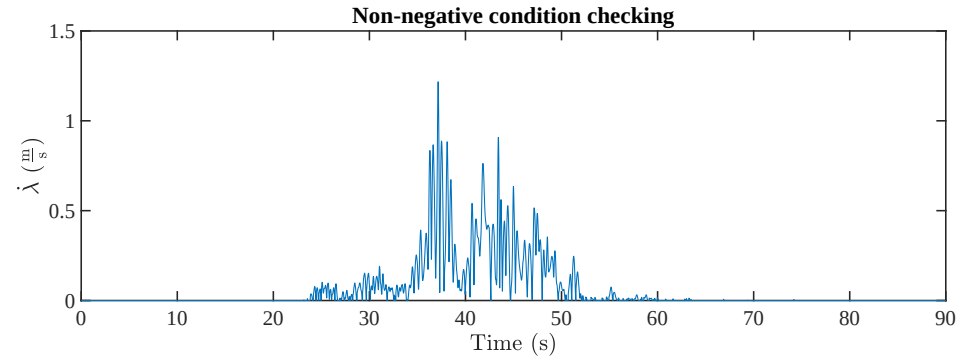

(a) The history of $\dot{\lambda}$ value

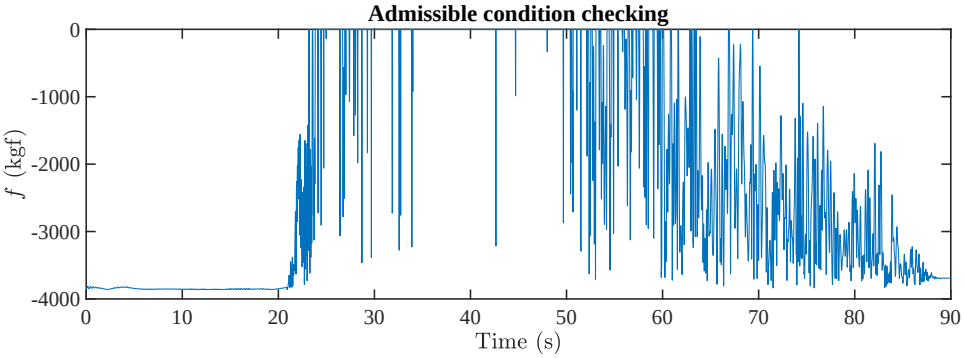

(b) The history of f value

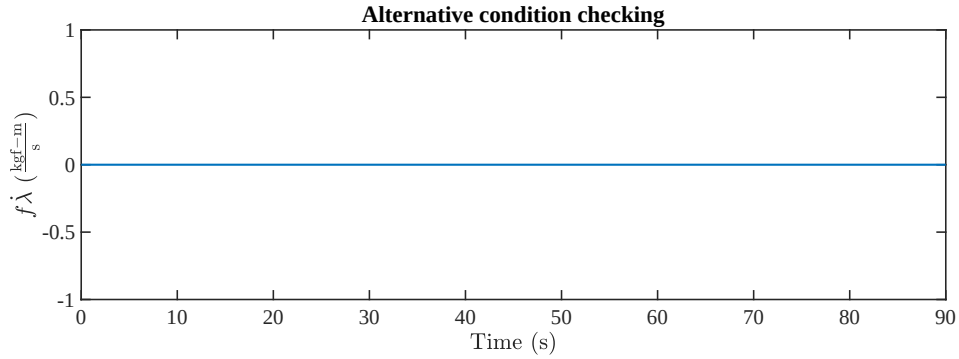

(c) The history of $f\dot{\lambda}$ value

Figure 5.5: The response of $\dot{\lambda}$, f, $f\dot{\lambda}$ of asymmetric building structures under the seismic record of the TCU084 station during Chi-Chi earthquake

doi:10.6342/NTU202402645

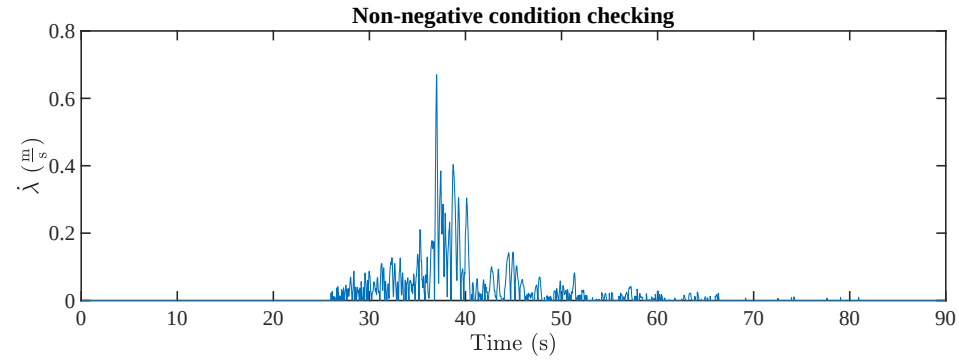

(a) The history of $\dot{\lambda}$ value

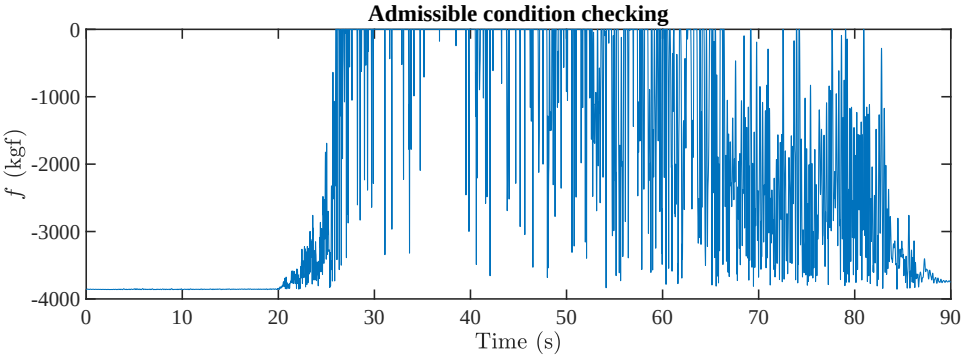

(b) The history of f value

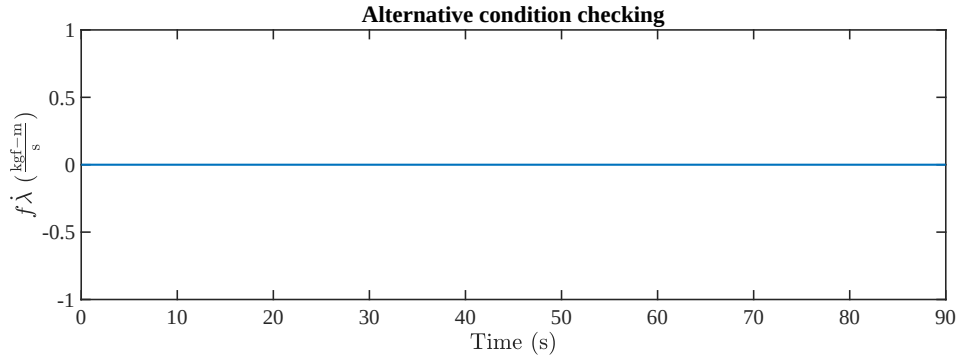

(c) The history of $f\dot{\lambda}$ value

Figure 5.6: The response of $\dot{\lambda}$, f, $f\dot{\lambda}$ of asymmetric building structures under the seismic record of the CHY101 station during Chi-Chi earthquake

doi:10.6342/NTU202402645

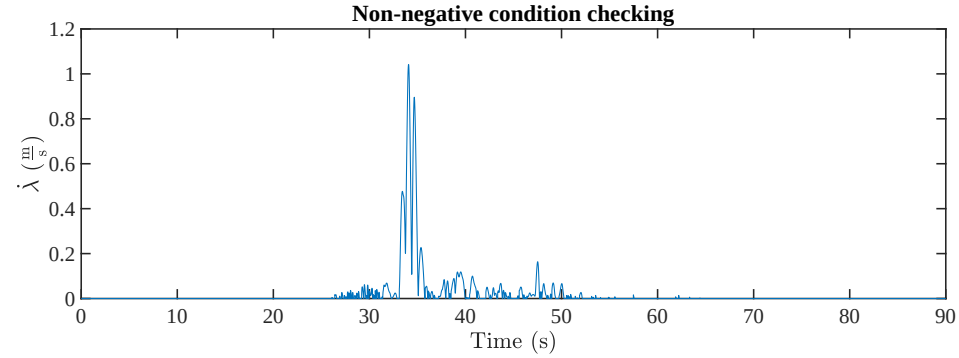

(a) The history of $\dot{\lambda}$ value

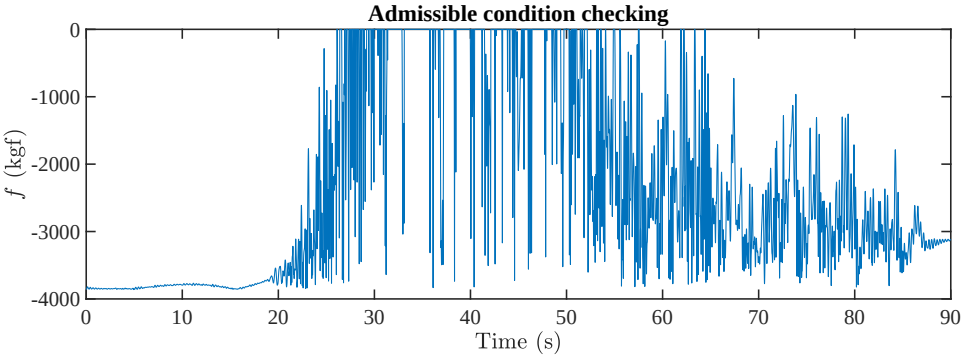

(b) The history of f value

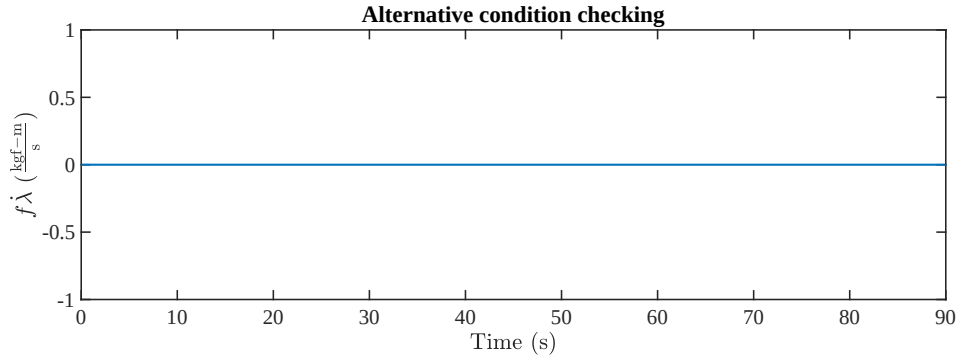

(c) The history of $f\dot{\lambda}$ value

Figure 5.7: The response of $\dot{\lambda}$, f, $f\dot{\lambda}$ of asymmetric building structures under the seismic record of the TCU052 station during Chi-Chi earthquake

doi:10.6342/NTU202402645

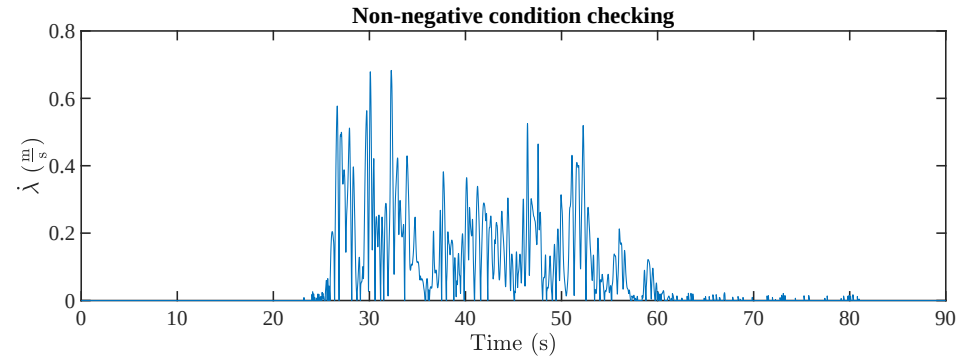

(a) The history of $\dot{\lambda}$ value

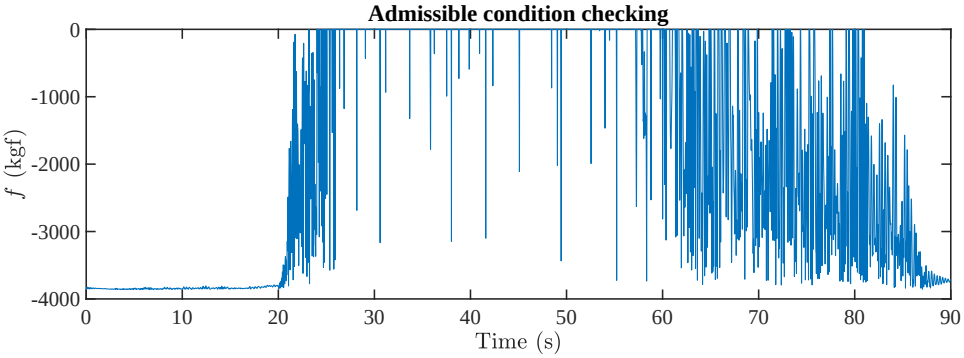

(b) The history of f value

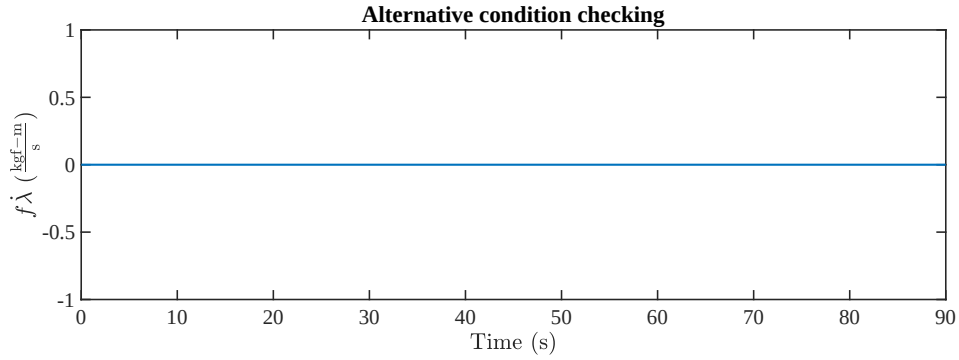

(c) The history of $f\dot{\lambda}$ value

Figure 5.8: The response of $\dot{\lambda}$, f, $f\dot{\lambda}$ of asymmetric building structures under the seismic record of the TCU065 station during Chi-Chi earthquake

doi:10.6342/NTU202402645

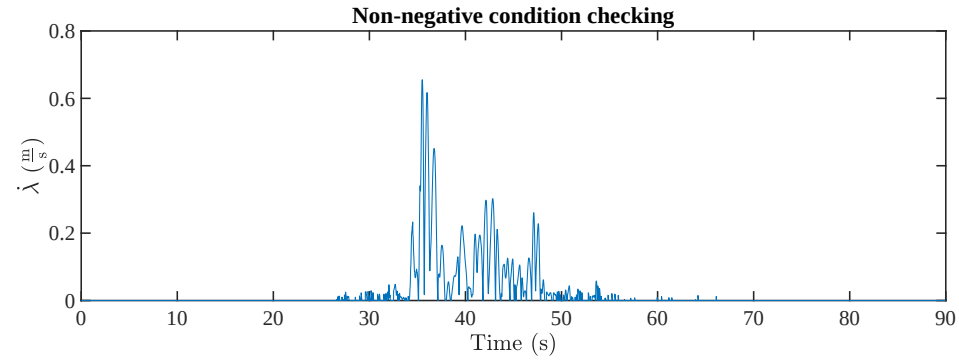

(a) The history of $\dot{\lambda}$ value

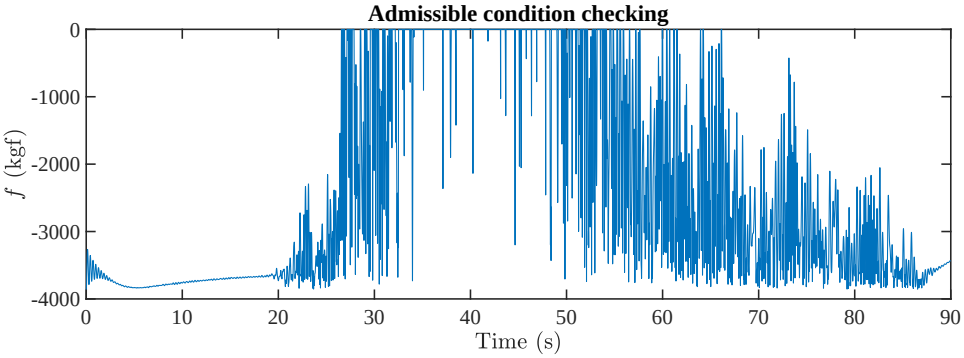

(b) The history of f value

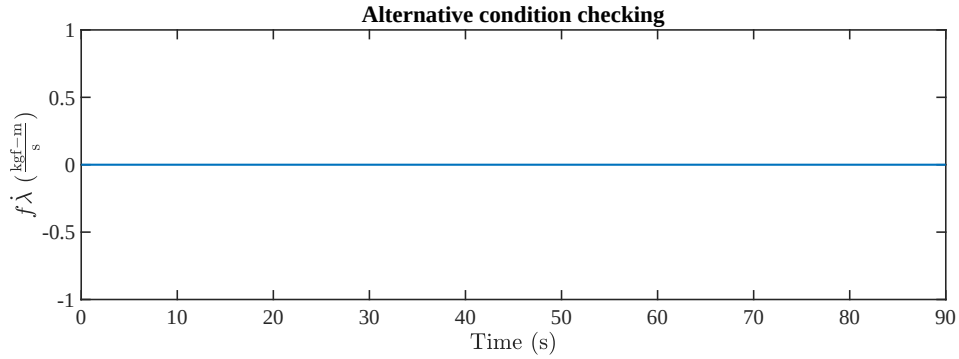

(c) The history of $f\dot{\lambda}$ value

Figure 5.9: The response of $\dot{\lambda}$, f, $f\dot{\lambda}$ of asymmetric building structures under the seismic record of the TCU068 station during Chi-Chi earthquake

doi:10.6342/NTU202402645

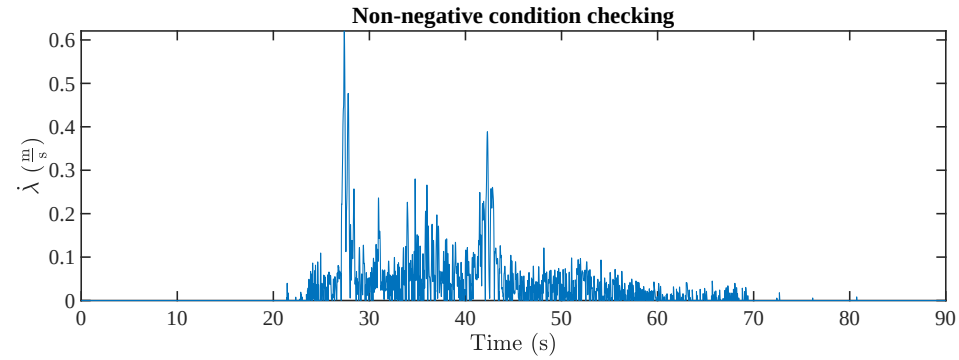

(a) The history of $\dot{\lambda}$ value

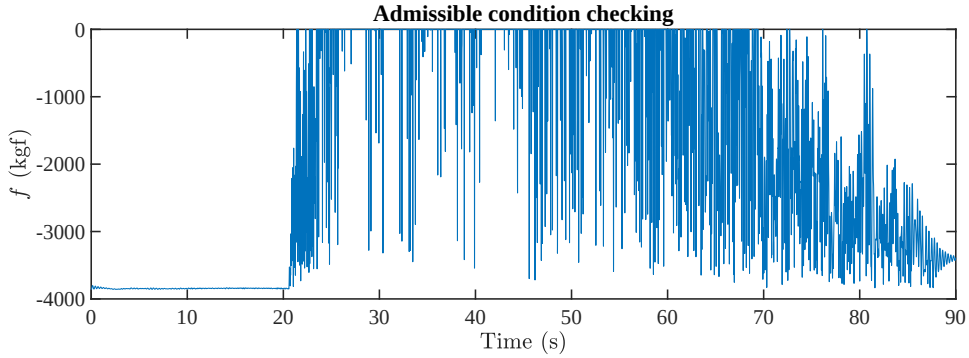

(b) The history of f value

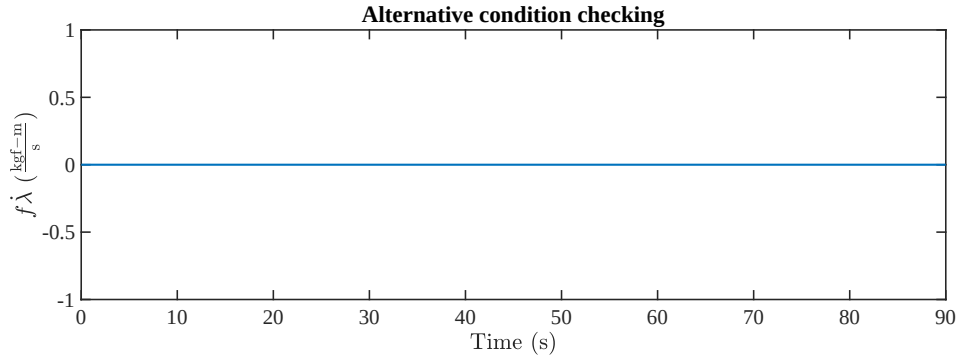

(c) The history of $f\dot{\lambda}$ value

Figure 5.10: The response of $\dot{\lambda}$, f, $f\dot{\lambda}$ of asymmetric building structures under the seismic record of the TCU129 station during Chi-Chi earthquake

doi:10.6342/NTU202402645

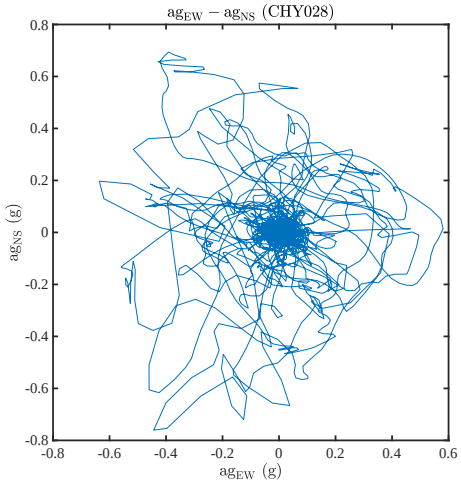

(a) Bidirectional plot of ground acceleration

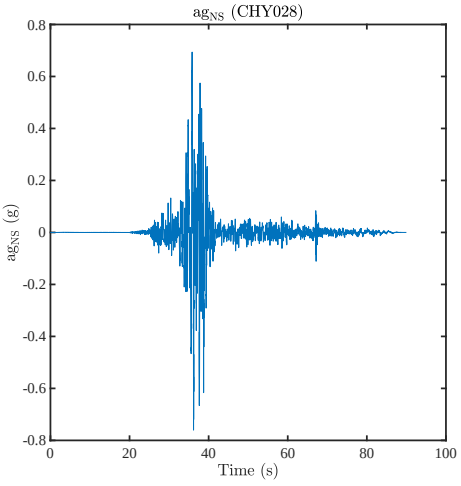

(b) N-S ground acceleration history

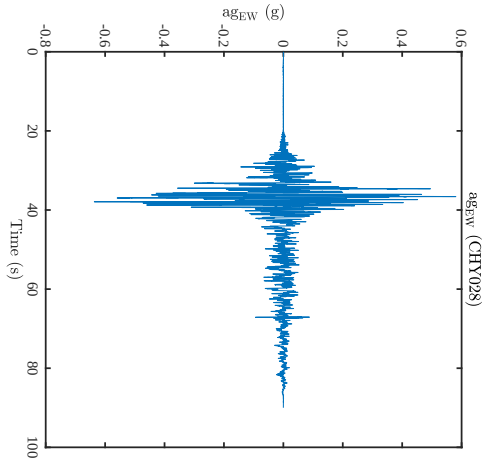

(c) E-W ground acceleration history

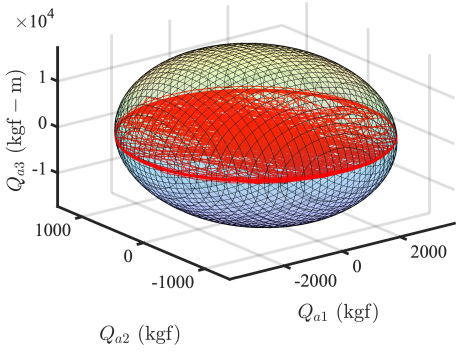

(d) Trajectory of $\mathbf{Q}_a$ for asymmetric building structures

Figure 5.11: Ground acceleration at CHY028 station of Chi-Chi earthquake and trajectory of $\mathbf{Q}_a$ for asymmetric building structures under bidirectional acceleration at CHY028 station of the Chi-Chi earthquake event

doi:10.6342/NTU202402645

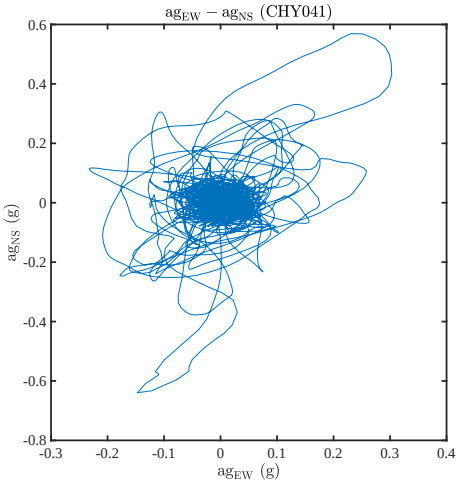

(a) Bidirectional plot of ground acceleration

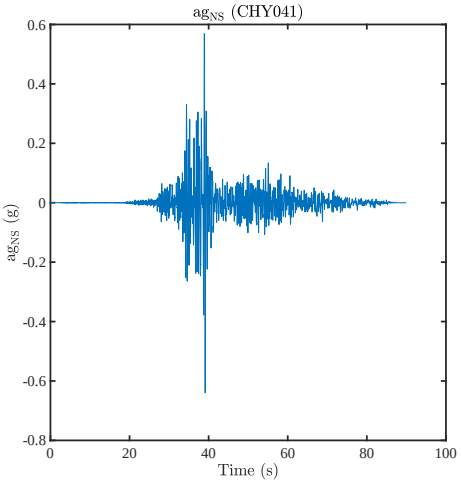

(b) N-S ground acceleration history

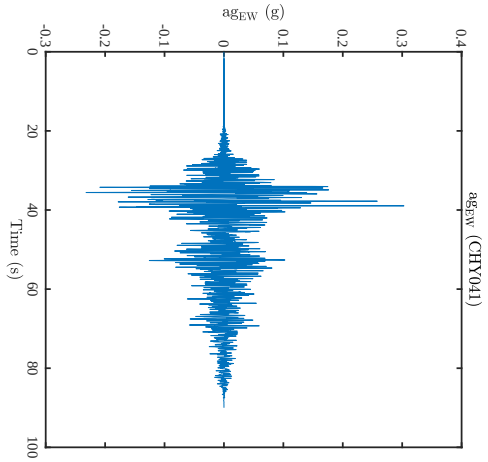

(c) E-W ground acceleration history

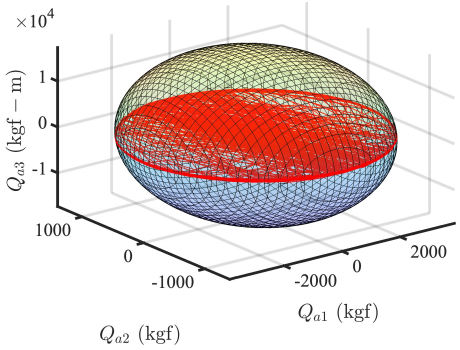

(d) Trajectory of $\mathbf{Q}_a$ for asymmetric building structures

Figure 5.12: Ground acceleration at CHY041 station of Chi-Chi earthquake and trajectory of $\mathbf{Q}_a$ for asymmetric building structures under bidirectional acceleration at CHY041 station of the Chi-Chi earthquake event

doi:10.6342/NTU202402645

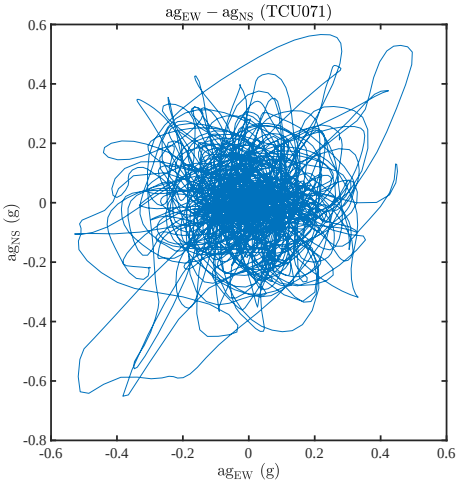

(a) Bidirectional plot of ground acceleration

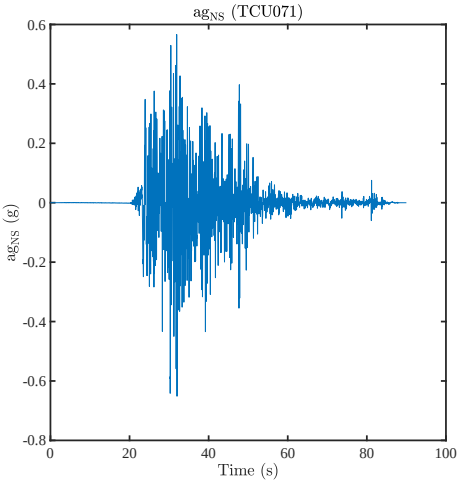

(b) N-S ground acceleration history

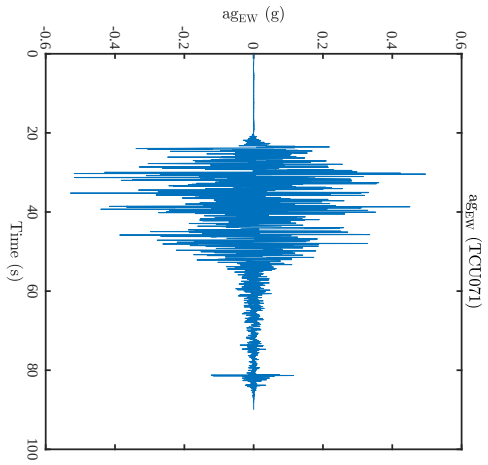

(c) E-W ground acceleration history

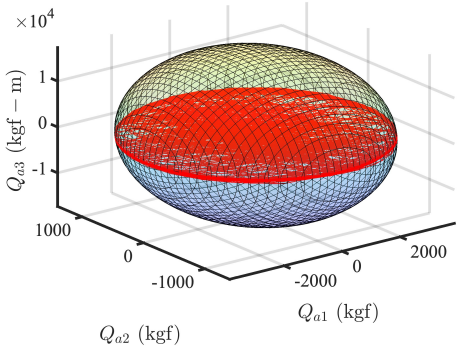

(d) Trajectory of $\mathbf{Q}_a$ for asymmetric building structures

Figure 5.13: Ground acceleration at TCU071 station of Chi-Chi earthquake and trajectory of $\mathbf{Q}_a$ for asymmetric building structures under bidirectional acceleration at TCU071 station of the Chi-Chi earthquake event

doi:10.6342/NTU202402645

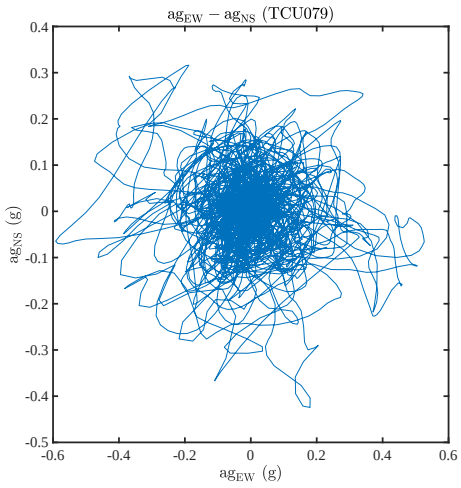

(a) Bidirectional plot of ground acceleration

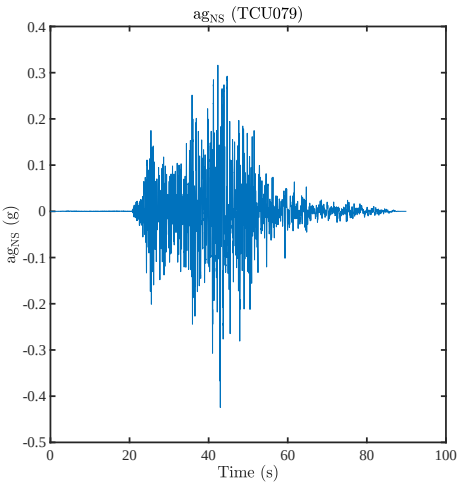

(b) N-S ground acceleration history

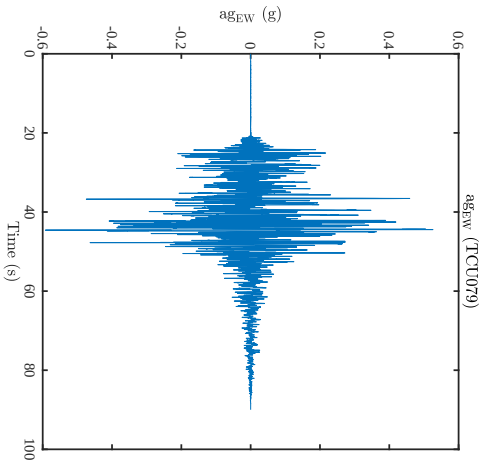

(c) E-W ground acceleration history

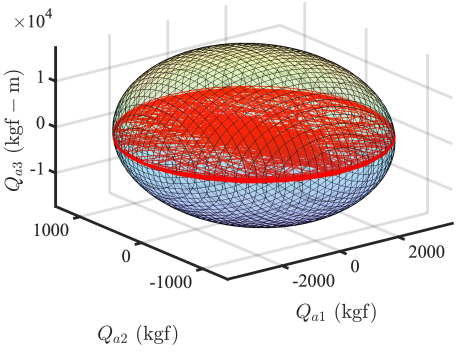

(d) Trajectory of $\mathbf{Q}_a$ for asymmetric building structures

Figure 5.14: Ground acceleration at TCU079 station of Chi-Chi earthquake and trajectory of $\mathbf{Q}_a$ for asymmetric building structures under bidirectional acceleration at TCU079 station of the Chi-Chi earthquake event

doi:10.6342/NTU202402645

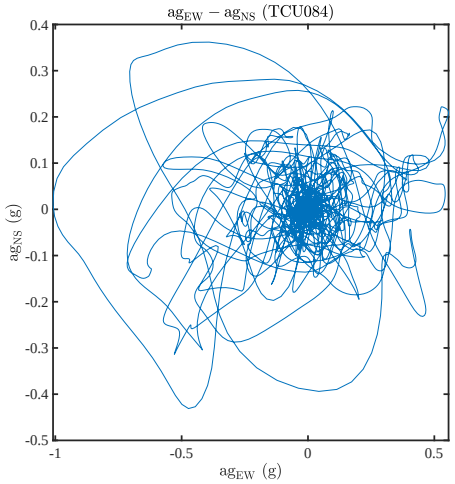

(a) Bidirectional plot of ground acceleration

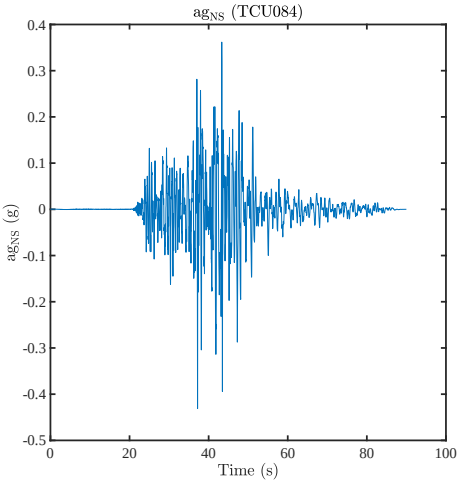

(b) N-S ground acceleration history

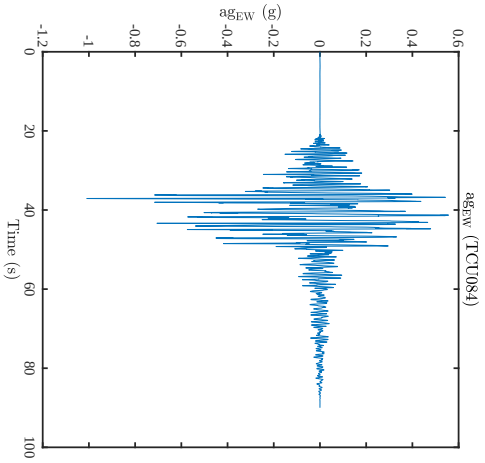

(c) E-W ground acceleration history

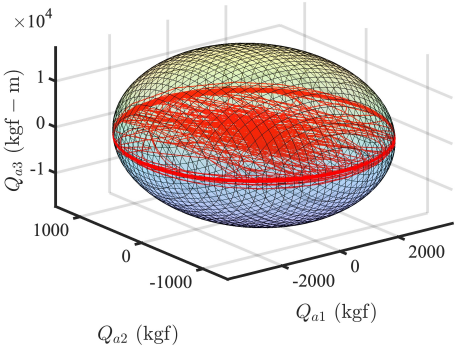

(d) Trajectory of $\mathbf{Q}_a$ for asymmetric building structures

Figure 5.15: Ground acceleration at TCU084 station of Chi-Chi earthquake and trajectory of $\mathbf{Q}_a$ for asymmetric building structures under bidirectional acceleration at TCU084 station of the Chi-Chi earthquake event

doi:10.6342/NTU202402645

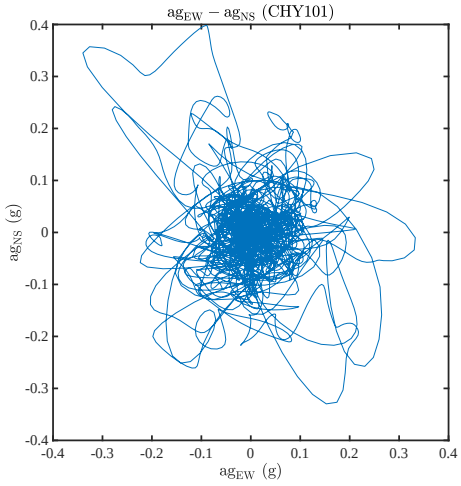

(a) Bidirectional plot of ground acceleration

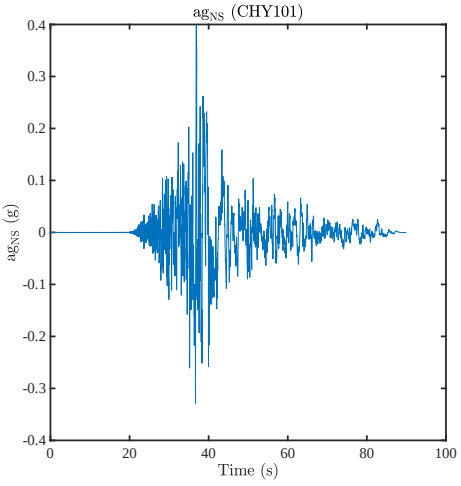

(b) N-S ground acceleration history

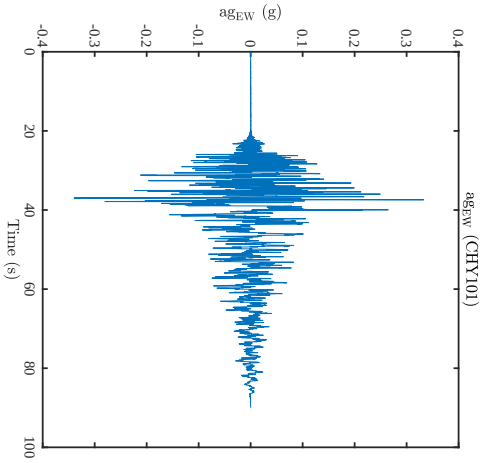

(c) E-W ground acceleration history

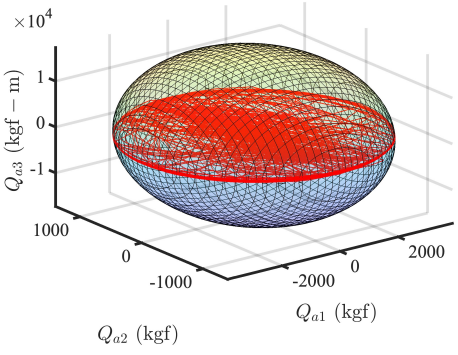

(d) Trajectory of $\mathbf{Q}_a$ for asymmetric building structures

Figure 5.16: Ground acceleration at CHY101 station of Chi-Chi earthquake and trajectory of $\mathbf{Q}_a$ for asymmetric building structures under bidirectional acceleration at CHY101 station of the Chi-Chi earthquake event

doi:10.6342/NTU202402645

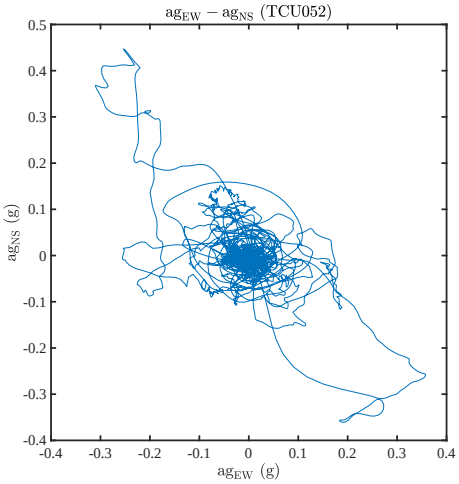

(a) Bidirectional plot of ground acceleration

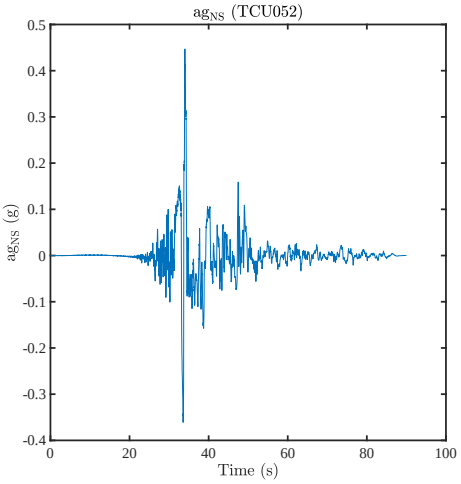

(b) N-S ground acceleration history

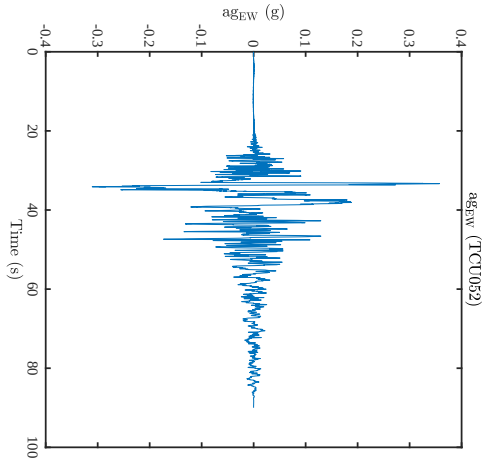

(c) E-W ground acceleration history

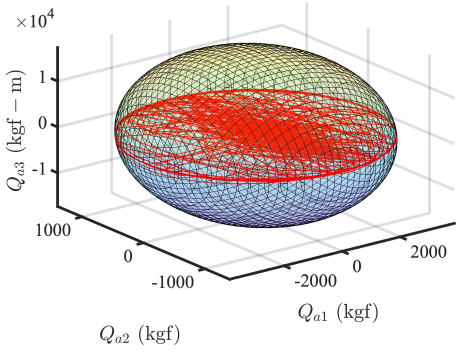

(d) Trajectory of $\mathbf{Q}_a$ for asymmetric building structures

Figure 5.17: Ground acceleration at TCU052 station of Chi-Chi earthquake and trajectory of $\mathbf{Q}_a$ for asymmetric building structures under bidirectional acceleration at TCU052 station of the Chi-Chi earthquake event

doi:10.6342/NTU202402645

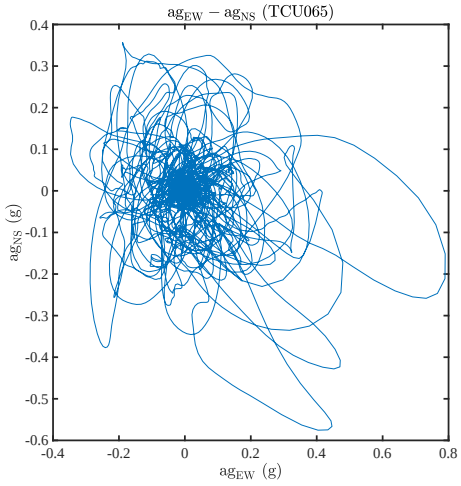

(a) Bidirectional plot of ground acceleration

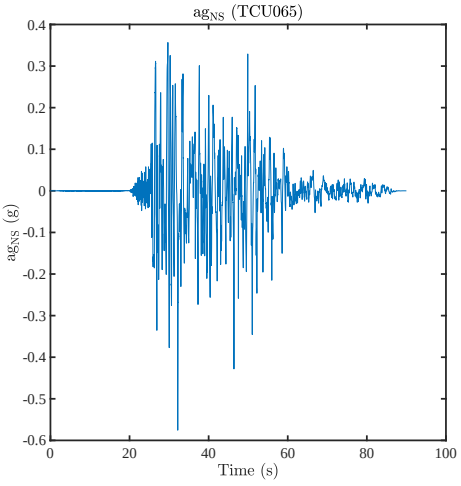

(b) N-S ground acceleration history

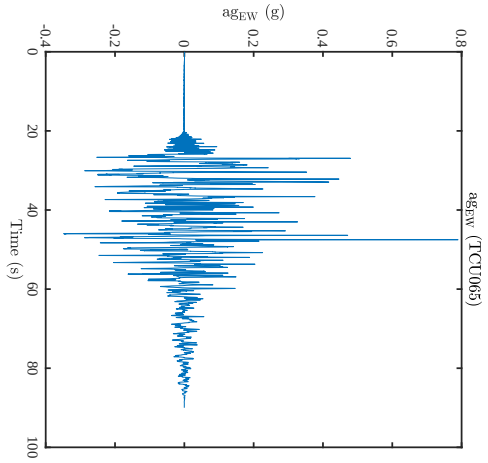

(c) E-W ground acceleration history

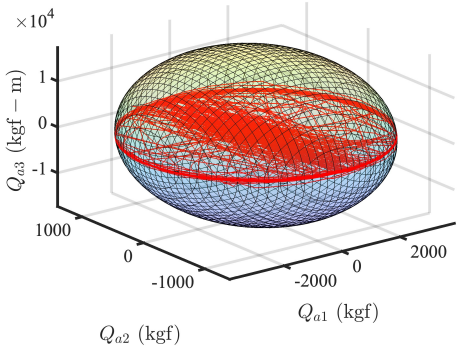

(d) Trajectory of $\mathbf{Q}_a$ for asymmetric building structures

Figure 5.18: Ground acceleration at TCU065 station of Chi-Chi earthquake and trajectory of $\mathbf{Q}_a$ for asymmetric building structures under bidirectional acceleration at TCU065 station of the Chi-Chi earthquake event

doi:10.6342/NTU202402645

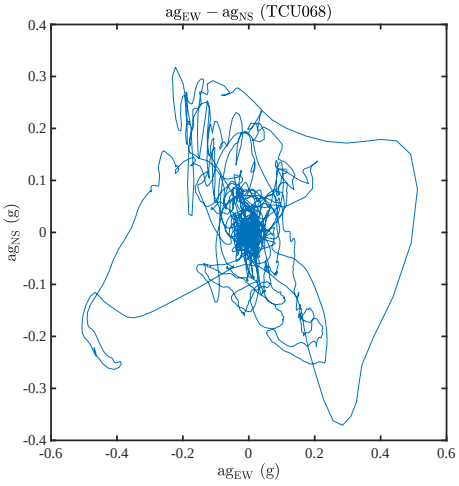

(a) Bidirectional plot of ground acceleration

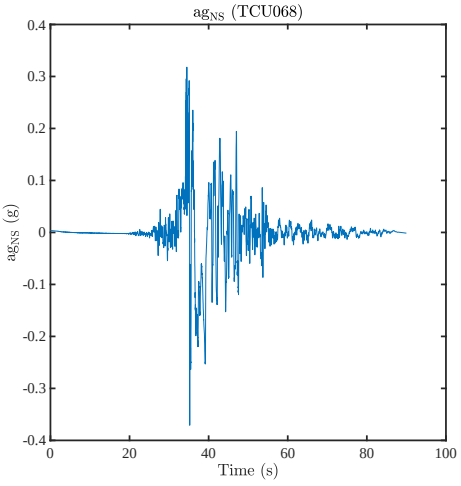

(b) N-S ground acceleration history

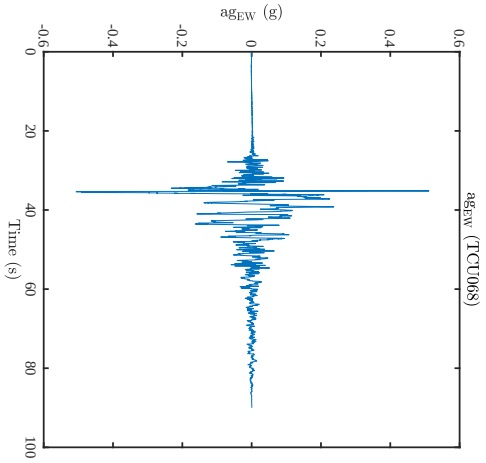

(c) E-W ground acceleration history

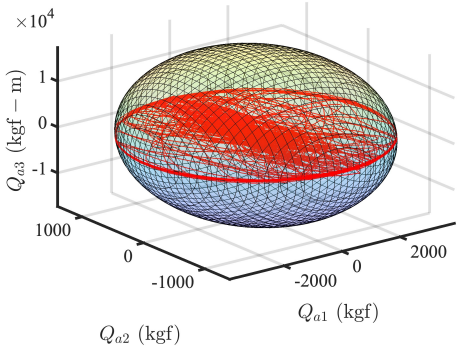

(d) Trajectory of $\mathbf{Q}_a$ for asymmetric building structures

Figure 5.19: Ground acceleration at TCU068 station of Chi-Chi earthquake and trajectory of $\mathbf{Q}_a$ for asymmetric building structures under bidirectional acceleration at TCU068 station of the Chi-Chi earthquake event

doi:10.6342/NTU202402645

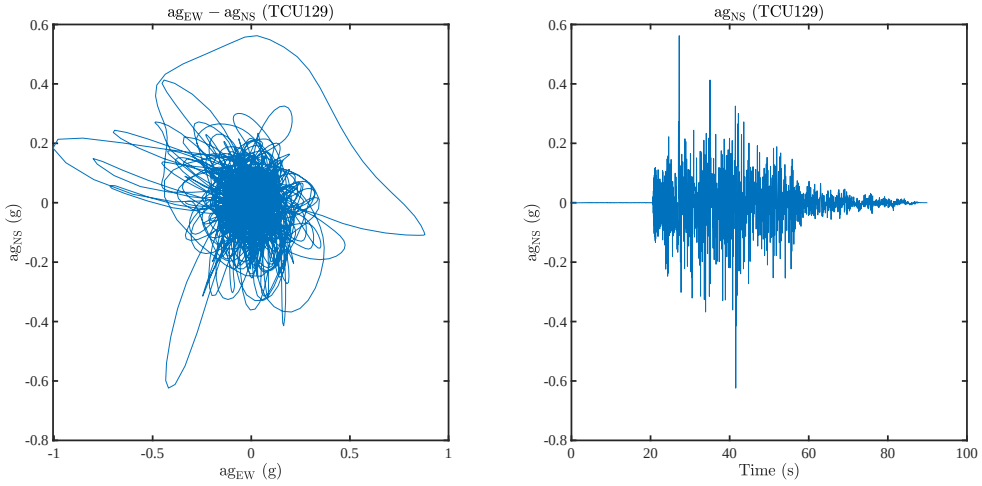

(a) Bidirectional plot of ground acceleration

(b) N-S ground acceleration history

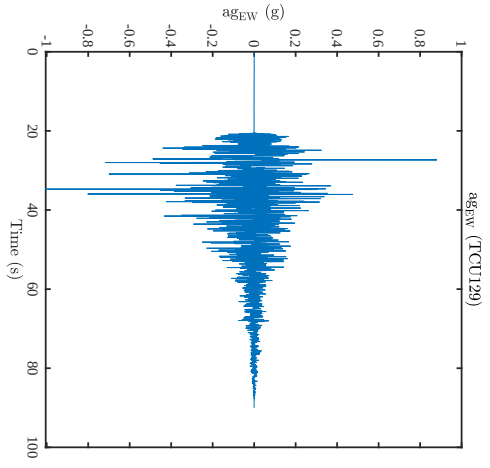

(c) E-W ground acceleration history

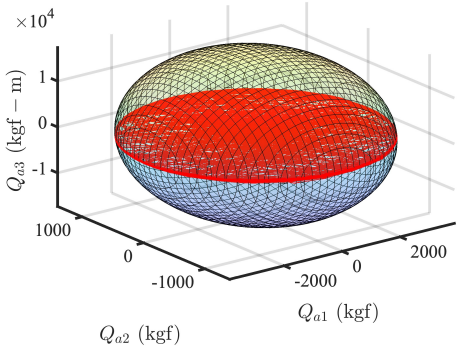

(d) Trajectory of $\mathbf{Q}_a$ for asymmetric building structures

Figure 5.20: Ground acceleration at TCU129 station of Chi-Chi earthquake and trajectory of $\mathbf{Q}_a$ for asymmetric building structures under bidirectional acceleration at TCU129 station of the Chi-Chi earthquake event

doi:10.6342/NTU202402645

5.2 Responses of the asymmetric building structures under earthquake excitations

In this section, we will compare the differences in peak responses between bidirectional and unidirectional seismic analyses. First, we will use the viscoelastoplastic model proposed in this study to perform a unidirectional seismic analysis on an asymmetric building structure. Then, we will conduct a bidirectional seismic analysis. Finally, we will compare the differences between the bidirectional and unidirectional seismic analyses. The parameters for the asymmetric building structure selected for analysis in this section are as follows: The structural mass is $m_s = 3280.733945 \left(\frac{\text{kgf}-\text{s}^2}{\text{m}}\right)$. The moment of inertia is $I_o = 34174.31193 \left(\text{kgf} - \text{m}^2\right)$.The elastic lateral stiffness is $k_1 = 4472647.145 \left(\frac{kgf}{m}\right)$ in EW-direction, $k_2 = 1610152.972 \left(\frac{kgf}{m}\right)$ in NS-direction, and $k_3 = 19232382.72 \left(\frac{\text{kgf}-\text{m}}{\text{rad}}\right)$ in twist direction. The post-yield stiffness $\mathbf{K}_p = 0.05\mathbf{K}_e$. The structural damping coefficient matrix use Rayleigh damping $\mathbf{C} = \alpha\mathbf{m}_s + \beta\mathbf{K}_e \left(\frac{kgf-s}{m}\right)$. The story yield shear force $Q_y = C_s \times W$, where W is the structural weight, and C_s is taken as 0.12 based on empirical data. Consider bidirectional eccentricity of 0.05 meters.

5.2.1 Approximate analysis of asymmetric building structures under unidirectional earthquake

For the unidirectional analysis, we input the structural parameters of the asymmetric building into the viscoelastoplastic model. We then select earthquake acceleration time histories from one station and input them individually into the viscoelastoplastic model for analysis. In this case, we choose the earthquake acceleration data from the TCU084 station during the Chi-Chi earthquake event as input for analysis.

doi:10.6342/NTU202402645

First, we input only the E-W direction acceleration data from the TCU084 station into the viscoelastoplastic model, record the interstory displacement time history and interstory shear force time history, and examine the peak responses. Next, we input only the N-S direction acceleration data from the TCU084 station into the viscoelastoplastic model, record the displacement time history and shear force time history, and examine the peak responses.

The results of the E-W direction unidirectional analysis are shown in Figures 5.21 to 5.22. Figure 5.21 shows the interstory displacement time history with a peak interstory displacement of 0.1498 m. Figure 5.22 shows the interstory shear force time history with a peak interstory shear force of 39487.276 kgf.

The results of the N-S direction unidirectional analysis are shown in Figures 5.23 to 5.24. Figure 5.23 shows the interstory displacement time history with a peak interstory displacement of 0.077 m. Figure 5.24 shows the interstory shear force time history with a peak interstory shear force of 8075.434 kgf.

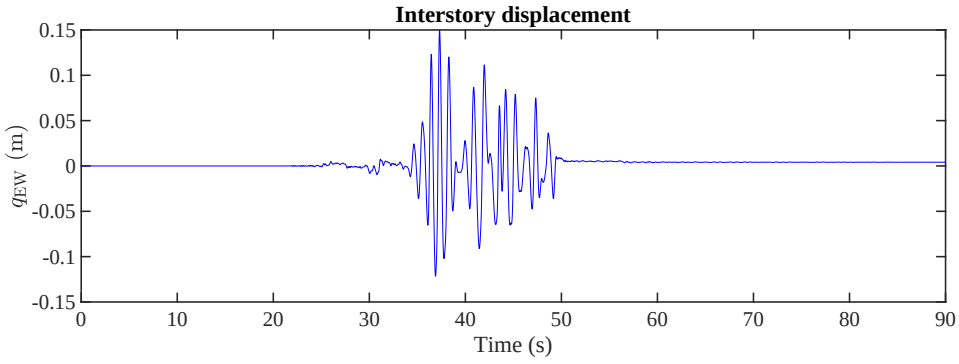

Figure 5.21: Interstory displacement time history for E-W unidirectional analysis of asymmetric building structures

doi:10.6342/NTU202402645

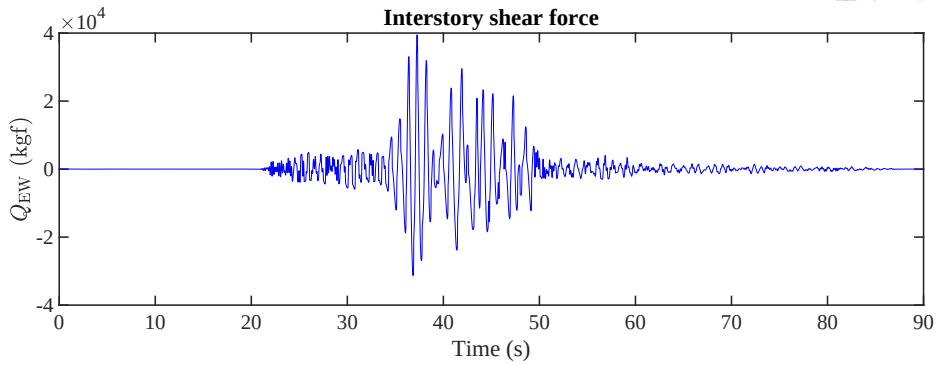

Figure 5.22: Interstory shear force time history for E-W unidirectional analysis of asymmetric building structures

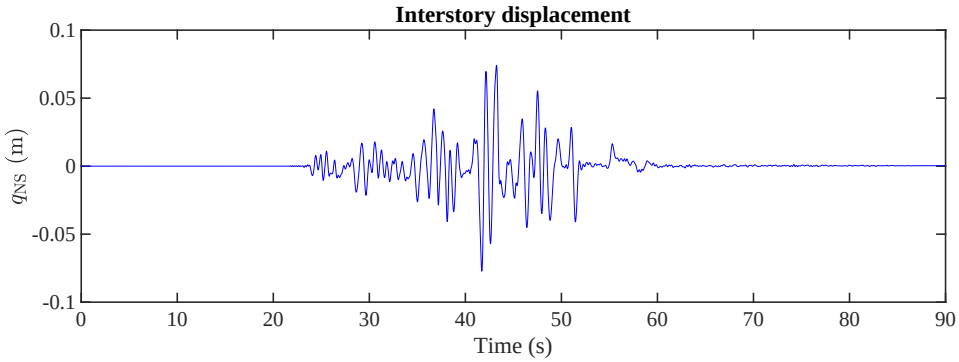

Figure 5.23: Interstory displacement time history for N-S unidirectional analysis of asymmetric building structures

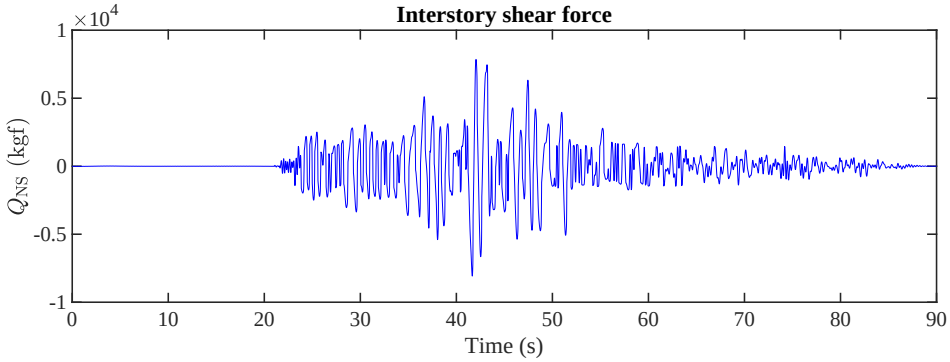

Figure 5.24: Interstory shear force time history for N-S unidirectional analysis of asymmetric building structures

5.2.2 Accurate analysis of asymmetric building structures under bidirectional earthquake

For the bidirectional analysis, we input the structural parameters of the asymmetric building into the viscoelastoplastic model. We then select earthquake acceleration time

doi:10.6342/NTU202402645

histories from one station and input them simultaneously in both directions into the viscoelastoplastic model for analysis. In this case, we choose the earthquake acceleration data from the TCU084 station during the Chi-Chi earthquake event as input for analysis.

We input both the E-W and N-S direction acceleration data from the TCU084 station simultaneously into the viscoelastoplastic model, record the bidirectional interstory displacement time history and bidirectional interstory shear force time history, and examine the peak responses.

The results of the bidirectional analysis are shown in Figures 5.25 to 5.28. Figure 5.25 shows the E-W direction interstory displacement time history from the bidirectional analysis, with a peak interstory displacement of 0.1528 m. Figure 5.25 shows the N-S direction interstory displacement time history from the bidirectional analysis, with a peak interstory displacement of 0.086 m. Figure 5.26 shows the E-W direction interstory shear force time history from the bidirectional analysis, with a peak interstory shear force of 40123.7658 kgf. Figure 5.26 shows the N-S direction interstory shear force time history from the bidirectional analysis, with a peak interstory shear force of 7995.416 kgf.

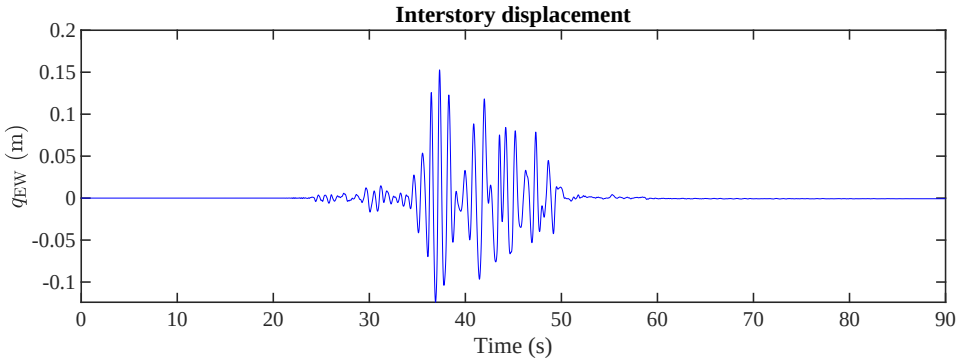

Figure 5.25: Interstory displacement time history for E-W bidirectional analysis of asymmetric building structures

doi:10.6342/NTU202402645

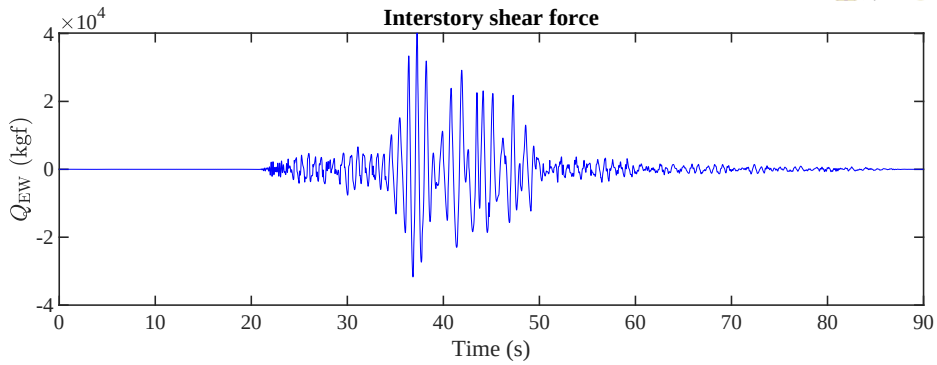

Figure 5.26: Interstory shear force time history for E-W bidirectional analysis of asymmetric building structures

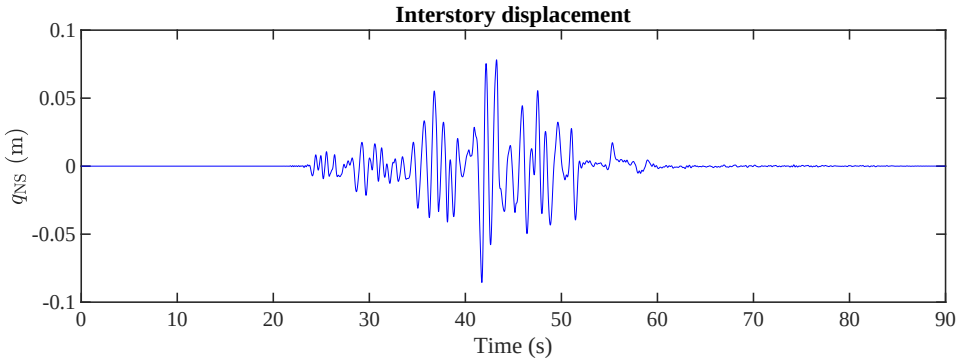

Figure 5.27: Interstory displacement time history for N-S bidirectional analysis of asymmetric building structures

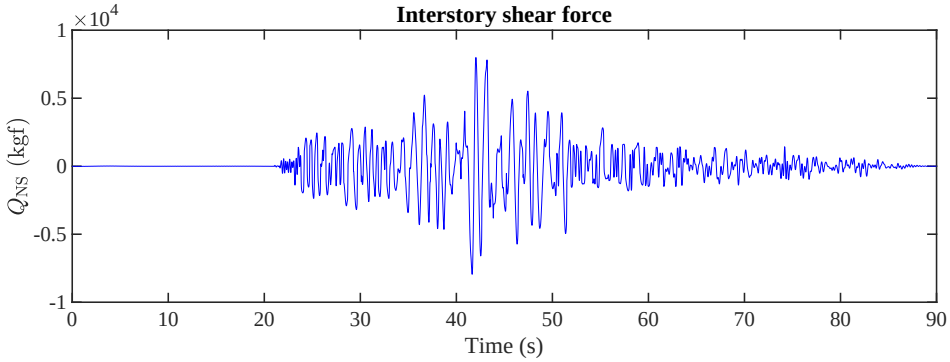

Figure 5.28: Interstory shear force time history for N-S bidirectional analysis of asymmetric building structures

5.2.3 Comparisons of unidirectional and bidirectional analysis for asymmetric building structures

Sections 5.2.1 and 5.2.2 analyze the peak responses of interstory displacement and interstory shear force for an asymmetric structure using unidirectional and bidirectional

doi:10.6342/NTU202402645

analyses, respectively. The results show that the unidirectional analysis underestimates the peak inter-story displacement in the E-W direction by 1.96% and in the N-S direction by 10.47% compared to the bidirectional analysis. The peak interstory shear force in the E-W direction is underestimated by 1.59% in the unidirectional analysis, while in the N-S direction, it is overestimated by 1%.

These results suggest that unidirectional analysis may significantly underestimate or miscalculate the seismic response of building structures. To further investigate and validate these findings, this subsection compares the differences in peak responses between bidirectional and unidirectional seismic analyses. We examine the impact of these differences on the total number of viscoelastoplastic-phase time steps occurrences, peak plastic equivalent, peak interstory displacement response, and peak interstory shear force response for asymmetric building structures.

The bidirectional seismic analysis uses acceleration data from 10 stations during the 1999 Chi-Chi earthquake event. For each station, we input the E-W and N-S acceleration time histories simultaneously into the viscoelastoplastic model and record the peak responses. For the unidirectional seismic analysis, we input the acceleration data from the same 10 stations separately, using only the E-W or only the N-S acceleration time history. When comparing the analysis results, we compare the peak responses of the two unidirectional analyses with the total response of the bidirectional analysis.

First, Figure 5.29 shows that for the acceleration time histories of these 10 stations, unidirectional analysis, whether using E-W or N-S input, significantly underestimates the total number of viscoelastoplastic-phase time steps occurrences in the building structure compared to bidirectional analysis. On average, using only unidirectional E-W analy-

doi:10.6342/NTU202402645

sis underestimates the total number of viscoelastoplastic-phase time steps occurrences by 56.111%, while using only unidirectional N-S analysis underestimates it by 15.644% compared to bidirectional analysis. This indicates that bidirectional analysis more accurately captures the total number of viscoelastoplastic-phase time steps occurrences in the building structure.

Next, Figure 5.30 shows the plastic equivalent response of the building structure. The plastic equivalent can be considered as a damage indicator for the building structure after an earthquake. The results show that unidirectional analysis significantly underestimates the plastic equivalent of the building structure after seismic activity compared to bidirectional analysis. On average, using only unidirectional E-W analysis underestimates the plastic equivalent by 63.975%, while using only unidirectional N-S analysis underestimates it by 30.727% compared to bidirectional analysis. This demonstrates that bidirectional analysis more accurately reflects the degree of damage to the building structure after an earthquake.

Furthermore, Figure 5.31 shows that the peak interstory displacements from unidirectional analysis are significantly lower than those from bidirectional analysis. However, an exception is the N-S Peak interstory displacement for CHY101, which is overestimated by 0.141%. On average, using only unidirectional E-W analysis underestimates the Peak interstory displacement by 55.632%, while using only unidirectional N-S analysis underestimates it by 11.146% compared to bidirectional analysis. This implies that bidirectional analysis is more accurate in capturing the Peak interstory displacement of the building structure after seismic activity.

Finally, Figure 5.32 shows that the Peak interstory shear forces from unidirectional

doi:10.6342/NTU202402645

analysis are generally lower than those from bidirectional analysis. However, an exception is the E-W peak interstory shear force for CHY101, which is overestimated by 1.399%. On average, using only unidirectional E-W analysis underestimates the peak interstory shear force by 11.74%, while using only unidirectional N-S analysis underestimates it by 43.098% compared to bidirectional analysis. This indicates that bidirectional analysis is more accurate in capturing the peak interstory shear force of the building structure after seismic activity.

Here we calculate the formula for the underestimation effect as follows:

$$\text{Underestimation effect} = \left(\frac{\text{Unidirectional analysis} - \text{Bidirectional analysis}}{\text{Bidirectional analysis}} \right) 100\%. \tag{5.1}$$

In conclusion, bidirectional seismic analysis significantly outperforms unidirectional seismic analysis in capturing the behavior of building structures after seismic activity, showing higher accuracy in terms of the total number of viscoelastoplastic-phase time steps occurrences, plastic equivalent, peak interstory displacement, and peak interstory shear force responses. Therefore, to more accurately assess the impact of earthquakes on building structures, it is essential to adopt bidirectional seismic analysis.

doi:10.6342/NTU202402645

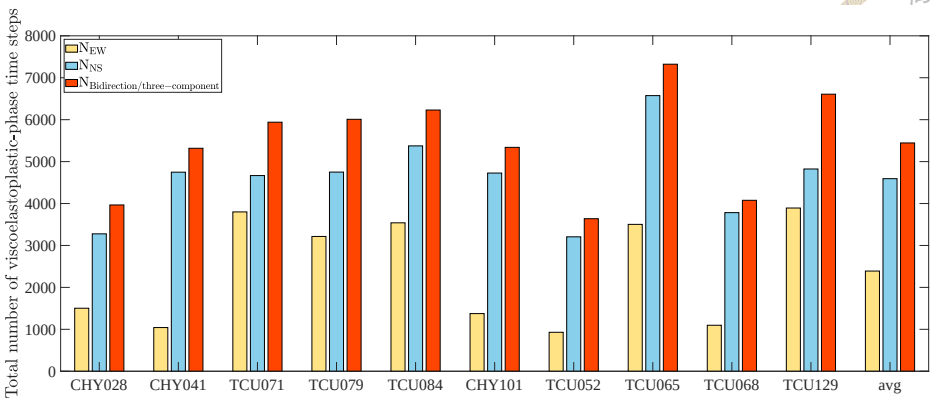

Figure 5.29: Total number of viscoelastoplastic-phase time steps for asymmetric building structures

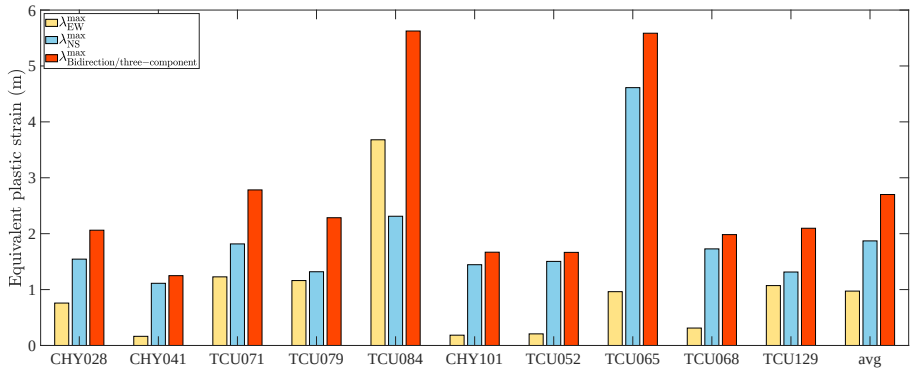

Figure 5.30: Equivalent plastic strain of asymmetric building structures

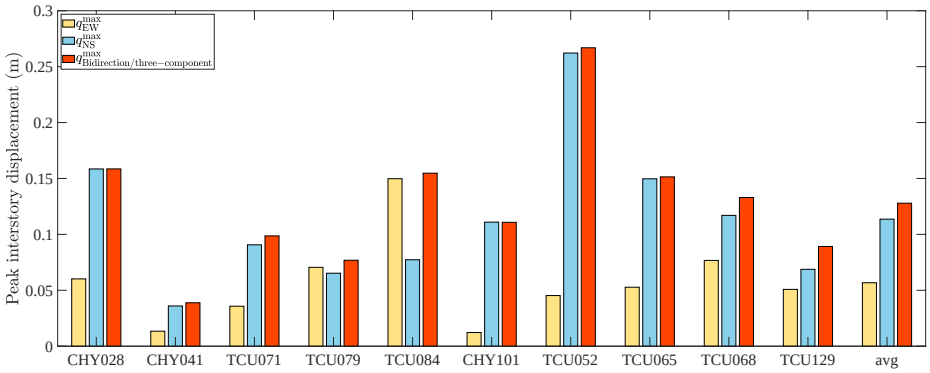

Figure 5.31: Peak interstory displacement of asymmetric building structures

doi:10.6342/NTU202402645

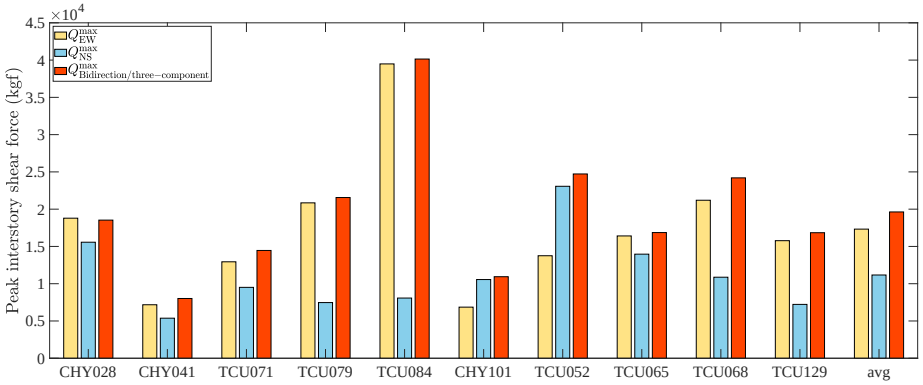

Figure 5.32: Peak interstory shear force of asymmetric building structures

5.3 The plastic equivalent of Taiwan under the 921 Chi-Chi earthquake event

In this section, we utilized data from the 921 Chi-Chi earthquake provided by the PEER Center (Pacific Earthquake Engineering Research Center), which includes bidirectional horizontal ground acceleration time histories from 295 stations, to conduct a plastic equivalent analysis across Taiwan. This extensive dataset provides us with a comprehensive understanding of seismic responses in various regions of Taiwan.

We input the parameters of asymmetric building structures into the viscoelastoplastic model developed in this study. This model considers the viscoelastoplastic behavior of building structures, allowing for a more accurate simulation of actual structural responses under strong seismic actions. By inputting bidirectional horizontal acceleration time histories, we recorded the plastic equivalent values of asymmetric building structures after the earthquake. This method enables us to evaluate the plastic damage experienced by buildings in different directions.

The analysis process is as follows: first, we recorded the latitude and longitude co-

doi:10.6342/NTU202402645

ordinates corresponding to each station, then converted these coordinates into x-y coordinates for representation on a plane map. Next, we recorded the plastic equivalent response values at each station's location. Finally, we presented the data in the form of an plastic equivalent distribution, intuitively displaying the damage distribution across Taiwan.

This result reflects the degree of plastic damage that asymmetric building structures throughout Taiwan might suffer under the Chi-Chi earthquake event. It provides us with a valuable tool to roughly predict the potential damage levels in various regions during future similar earthquakes. This predictive capability has significant implications for earthquake hazard prediction and analysis.

As shown in Figure 5.33, the analysis results indicate that areas with higher plastic equivalent values are mainly concentrated in the central region, especially near Taichung and Nantou. The red dot in the figure marks the location of the earthquake epicenter. This finding reveals the damage distribution of asymmetric building structures across Taiwan, with areas near the epicenter exhibiting the most severe plastic damage. The central region experienced the most significant impact, which is closely related to the propagation characteristics of seismic waves.

Notably, our analysis results highly correspond with the actual observed damage after the 921 Chi-Chi earthquake. This consistency not only verifies the accuracy of the viscoelastoplastic model proposed in this study but also demonstrates its practical value in conducting large-scale damage estimation. This finding is significant for the field of earthquake engineering as it provides a reliable tool for assessing the seismic resistance of existing building structures and formulating more targeted earthquake disaster mitigation strategies. It offers scientific evidence for urban planners and decision-makers to improve

doi:10.6342/NTU202402645

the overall seismic resilience of cities.

In summary, this study not only confirms the effectiveness of the proposed vis-coelastoplastic model in analyzing large-scale damage estimation but also provides new insights for future earthquake engineering research and practice. We hope to further enhance our ability to predict and mitigate earthquake disasters, ultimately contributing to the construction of safer and more resilient urban environments.

doi:10.6342/NTU202402645

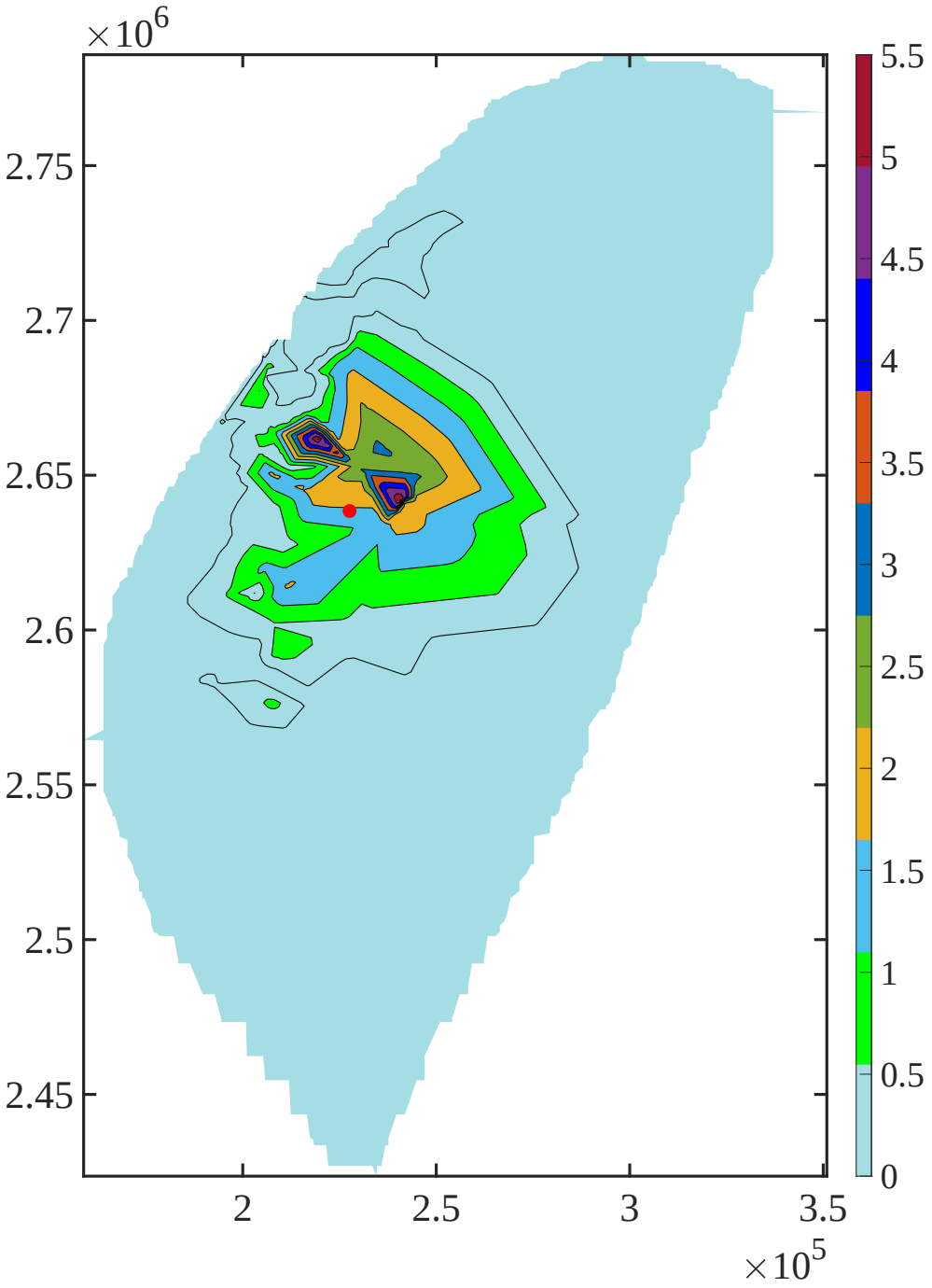

Figure 5.33: The plastic equivalent distribution

doi:10.6342/NTU202402645

5.3.1 CPU time for viscoelastoplastic analysis of asymmetric building structures

Section 5.3 We analyzed the equivalent plastic strain response of asymmetric structures using acceleration data recorded from 295 stations during the Chi-Chi earthquake event in Taiwan. In this subsection, we document the time taken to analyze these 295 stations. We used a 2022 MacBook air computer with chip processor is Apple M2 for the calculations. The computation time for each station is shown in Figure 5.34. The results indicate that using the viscoelastoplastic model proposed in this study, the average computation time for analyzing the acceleration time histories of 295 stations was 4.66194011 seconds. This high performance can be attributed to several factors:

1. Our model considers three compement responses, simplifying computational complexity while maintaining accuracy. 2. Accurate viscoelastoplastic behavior: The model incorporates precise representations of viscoelastoplastic behavior, enhancing the accuracy of results. 3. Elimination of complex nonlinear iterations: When asymmetric building structures enter plastic states due to seismic excitation, our model does not require complex nonlinear iterations. This feature significantly reduces the computational burden. 4. Optimized algorithm: We proposed an algorithm flow that ensures all computational results satisfy the conditions of the viscoelastoplastic model. Based on this algorithm flow, we developed an efficient numerical method and optimized code, further reducing computation time.

To better understand this performance, traditional nonlinear analysis methods might require hours or even days of computation time for such a large dataset. Our model achieves comparable accuracy in just a few seconds, representing a significant advance-

doi:10.6342/NTU202402645

ment in computational efficiency.

These results strongly demonstrate that the viscoelastoplastic model proposed in this study is an efficient and accurate simplified model. It can quickly process large datasets while maintaining high precision, making it a valuable tool for seismic analysis and design of asymmetric building structures. This model opens up new possibilities for large-scale seismic risk assessment and real-time structural health monitoring systems, where computational efficiency is crucial. In future work.

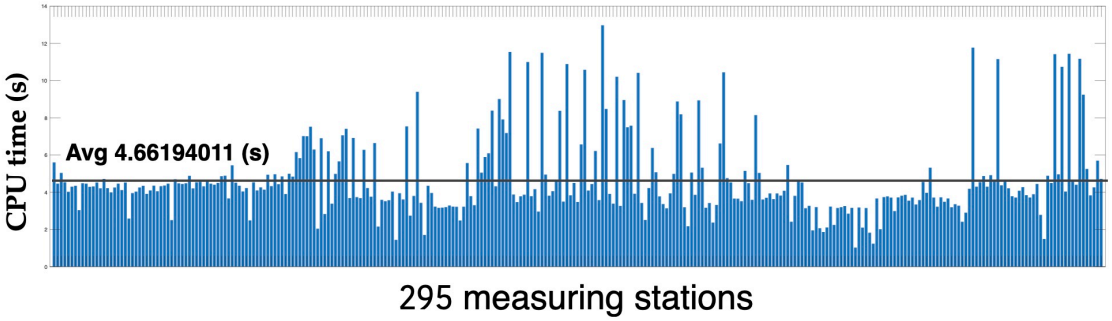

Figure 5.34: CPU time for viscoelastoplastic analysis of asymmetric building structures

5.4 Analysis of incident angle of seismic excitations on asymmetric building structures

In section 5.2, we learned that bidirectional analysis can more accurately capture the seismic response of asymmetric building structures. This section will further explore the seismic behavior of asymmetric building structures during earthquakes. The transmission of seismic forces actually occurs in the form of waves, while past structural analyses have mostly been conducted assuming seismic forces are transmitted through the principal axes. However, when seismic waves are transmitted to a building structure, they may not necessarily pass through the principal axes, but often have a certain angle of incidence. Therefore, this section will explore the impact of considering the angle of incidence of

doi:10.6342/NTU202402645

seismic waves on the seismic response of asymmetric building structures, examining the responses of both bidirectional coupled (BDC) seismic analysis and biunidirectional uncoupled (BUU) seismic force analysis.

5.4.1 Biunidirectional uncoupled analysis of asymmetric building structures

In the biunidirectional uncoupled (BUU) seismic analysis, we independently input the two acceleration time history data from the same station into the model, considering an angle of incidence for the analysis. The simplified concept is shown in Figure 5.35. We can express the form of external force input as follows:

$$\ddot{u}_{g_{\mathrm{EW}}}(\theta) = \ddot{u}_{g_{\mathrm{EW}}} \cos\theta, \tag{5.2}$$

$$\ddot{u}_{g_{\mathrm{NS}}}(\theta) = \ddot{u}_{g_{\mathrm{NS}}} \sin\theta, \tag{5.3}$$

where $\ddot{u}_{g_{\mathrm{EW}}}(\theta)$ represents the seismic force acceleration input of the east-west seismic wave with an incidence angle to the principal axis, and $\ddot{u}_{g_{\mathrm{NS}}}(\theta)$ represents the seismic force acceleration input of the north-south seismic wave with an incidence angle to the principal axis. During analysis, the two acceleration time history data are independently input into the model, considering the incidence angle between the seismic wave and the principal axis from 0° to 360° at one-degree intervals. The peak structural responses for each degree are recorded, including the peak interstory displacement and peak interstory shear force. The results of the two independent unidirectional analyses are then combined by taking the square root of the sum of their squares to represent the total structural response. These are represented in polar coordinates to show the asymmetric building structural response considering 360 degrees of incidence angles, exploring the impact of the incidence

doi:10.6342/NTU202402645

angle and comparing it with the results of bidirectional coupled (BDC) seismic analysis. The biunidirectional uncoupled (BUU) peak interstory displacement response and peak interstory shear force response are as follows:

$$q_{\max} = \sqrt{(q_{\mathrm{EW}}^{\max})^2 + (q_{\mathrm{NS}}^{\max})^2}, \tag{5.4}$$

$$Q_{\max} = \sqrt{(Q_{\mathrm{EW}}^{\max})^2 + (Q_{\mathrm{NS}}^{\max})^2}. \tag{5.5}$$

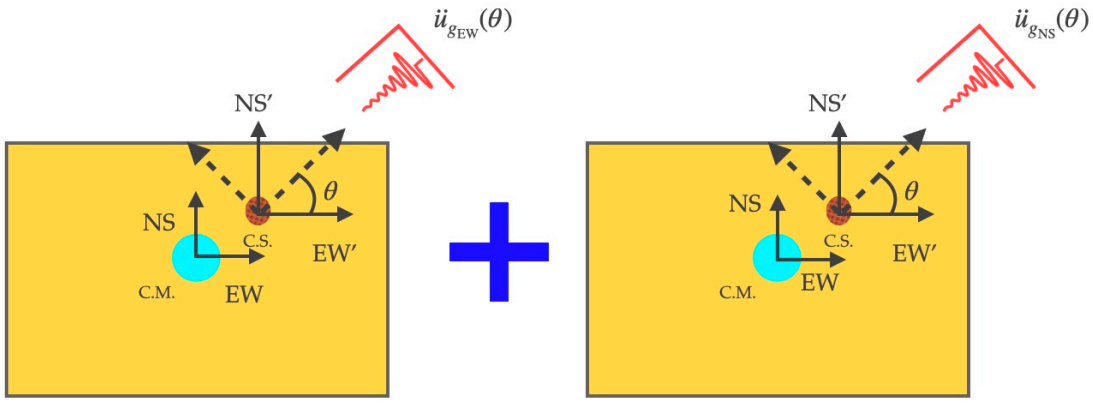

Figure 5.35: Schematic diagram of biunidirectional uncoupled (BUU) analysis of asymmetric building structures

5.4.2 Bidirectional coupled analysis of asymmetric building structures

In bidirectional coupled seismic analysis, we simultaneously input the bidirectional horizontal acceleration time history data from the same station into the model, considering an angle of incidence for the analysis. The simplified concept is shown in Figure 5.36.

doi:10.6342/NTU202402645

We can express the form of external force input as follows:

$$\begin{bmatrix} \ddot{u}_{g_{\mathrm{EW}}}(\theta) \\ \ddot{u}_{g_{\mathrm{NS}}}(\theta) \end{bmatrix} = \begin{bmatrix} \cos\theta & -\sin\theta \\ \sin\theta & \cos\theta \end{bmatrix} \begin{bmatrix} \ddot{u}_{g_{\mathrm{EW}}} \\ \ddot{u}_{g_{\mathrm{NS}}} \end{bmatrix}, \tag{5.6}$$

where $\ddot{u}_{g_{\mathrm{EW}}}(\theta)$ represents the seismic force acceleration input of the east-west seismic wave with an incidence angle to the principal axis, and $\ddot{u}_{g_{\mathrm{NS}}}(\theta)$ represents the seismic force acceleration input of the north-south seismic wave with an incidence angle to the principal axis. During analysis, the bidirectional horizontal acceleration time history data are simultaneously input into the model, considering the incidence angle between the seismic wave and the principal axis from 0° to 360° at one-degree intervals. The peak structural responses for each degree are recorded, specifically the peak interstory displacement and peak interstory shear force for each degree. These are represented in polar coordinates to show the structural response considering 360 degrees of incidence angles, exploring the impact of the incidence angle and comparing it with the results of biunidirectional uncoupled (BUU) seismic analysis. The bidirectional coupled (BDC) peak interstory displacement response and peak interstory shear force response are expressed as follows:

$$q_{\max} = \max_{\forall t} \left(\sqrt{(q_{\mathrm{EW}}(t))^2 + (q_{\mathrm{NS}}(t))^2} \right), \tag{5.7}$$

$$Q_{\max} = \max_{\forall t} \left(\sqrt{(Q_{\mathrm{EW}}(t))^2 + (Q_{\mathrm{NS}}(t))^2} \right). \tag{5.8}$$

doi:10.6342/NTU202402645

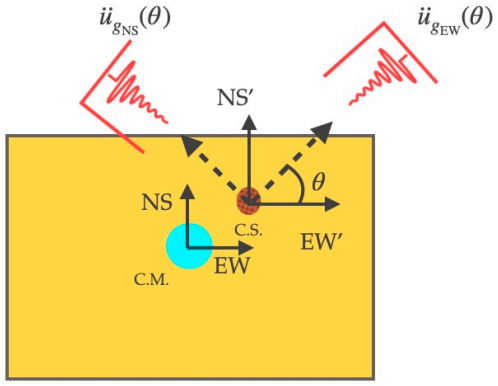

Figure 5.36: Schematic diagram of bidirectional coupled (BDC) analysis of asymmetric building structures

5.4.3 Comparisons of biunidirectional uncoupled (BUU) analysis and bidirectional coupled (BDC) analysis for asymmetric building structures

The results shown in Figures 5.37-5.56. The results indicate that for asymmetric building structures, when using bidirectional coupled (BDC) analysis, the angle of incidence of the earthquake significantly affects the structural response, both in terms of peak interstory displacement response and peak interstory shear force response. Consequently, the peak value graphs for Peak interstory displacement and peak interstory shear force considering 360 degrees of incidence angles are no longer circular but irregular in shape, which is vastly different from the results for symmetric structures. This situation is consistently demonstrated in the results analyzed from the acceleration data of all 10 stations using bidirectional earthquake input with consideration of incidence angles. When considering the angle of incidence for Peak interstory displacement response, biunidirectional uncoupled (BUU) analysis shows significant misestimation compared to bidirectional analysis. Specifically, for CHY041, TCU071, TCU079, TCU084, TCU065, TCU068, and TCU129, unidirectional analysis underestimates at most angles, while for

doi:10.6342/NTU202402645

CHY028, CHY101, and TCU052, biunidirectional uncoupled (BUU) analysis shows both over- and underestimation at certain angles. This clearly demonstrates that unidirectional analysis can significantly misestimate the Peak interstory displacement response. For peak interstory shear force response considering the angle of incidence, most angles also show that unidirectional analysis significantly underestimates compared to bidirectional coupled (BDC) analysis. These results clearly demonstrate that using biunidirectional uncoupled (BUU) analysis alone can seriously underestimate or misestimate the seismic response of asymmetric structures. Therefore, the accuracy and importance of bidirectional coupled (BDC) analysis become more significant. In conclusion, bidirectional coupled analysis (BDC) considering the angle of incidence of seismic waves can provide a more accurate assessment of structural seismic response, offering important reference value for earthquake engineering design and evaluation. Through the above analysis and graphical presentation, we can intuitively see the impact of seismic wave incidence angles on structural response, emphasizing the importance of bidirectional coupled (BDC) analysis.

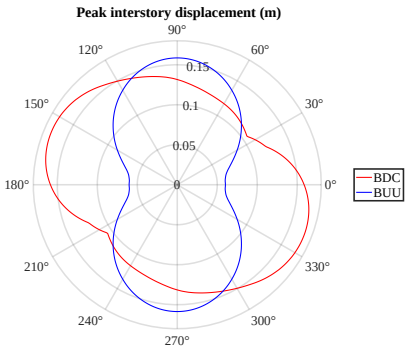

Figure 5.37: Peak interstory displacement responses of asymmetric building structures under different incidence angles (CHY028)

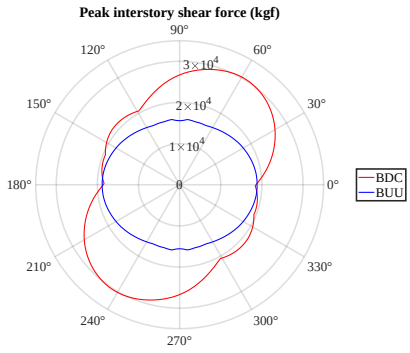

Figure 5.38: Peak interstory shear force responses of asymmetric building structures under different incidence angles (CHY028)

doi:10.6342/NTU202402645

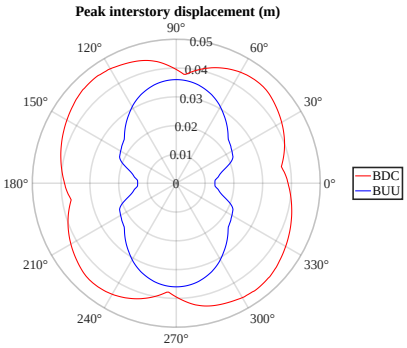

Figure 5.39: Peak interstory displacement responses of asymmetric building structures under different incidence angles (CHY041)

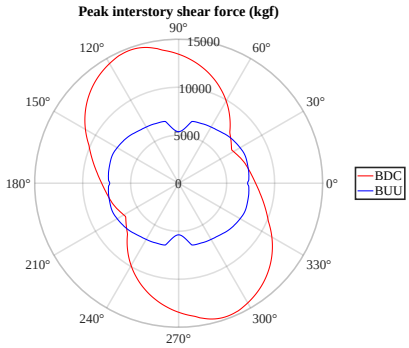

Figure 5.40: Peak interstory shear force responses of asymmetric building structures under different incidence angles (CHY041)

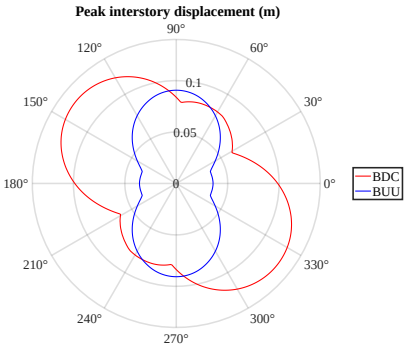

Figure 5.41: Peak interstory displacement responses of asymmetric building structures under different incidence angles (TCU071)

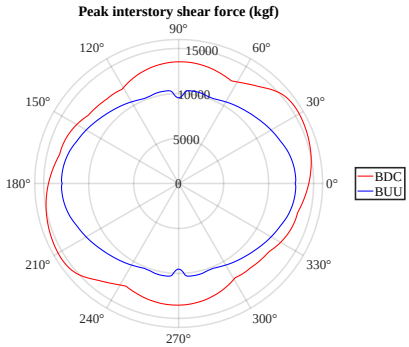

Figure 5.42: Peak interstory shear force responses of asymmetric building structures under different incidence angles (TCU071)

doi:10.6342/NTU202402645

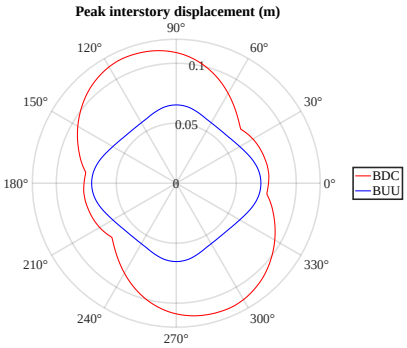

Figure 5.43: Peak interstory displacement responses of asymmetric building structures under different incidence angles (TCU079)

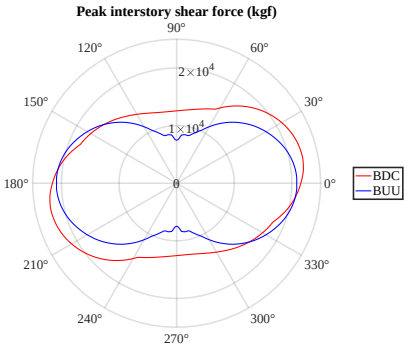

Figure 5.44: Peak interstory shear force responses of asymmetric building structures under different incidence angles (TCU079)

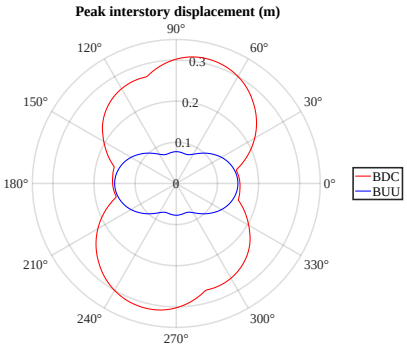

Figure 5.45: Peak interstory displacement responses of asymmetric building structures under different incidence angles (TCU084)

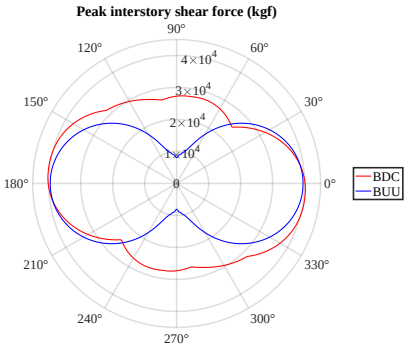

Figure 5.46: Peak interstory shear force responses of asymmetric building structures under different incidence angles (TCU084)

doi:10.6342/NTU202402645

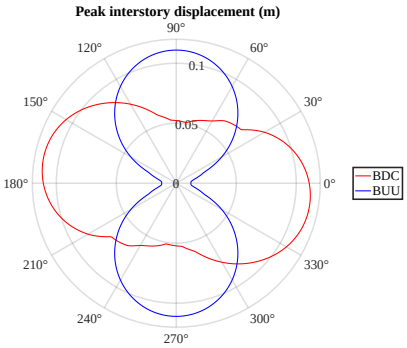

Figure 5.47: Peak interstory displacement responses of asymmetric building structures under different incidence angles (CHY101)

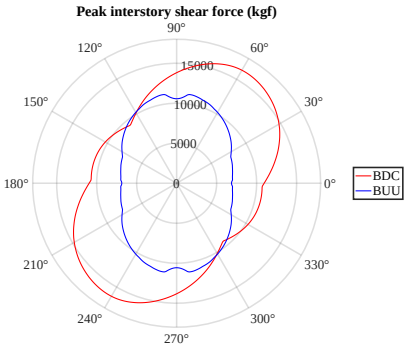

Figure 5.48: Peak interstory shear force responses of asymmetric building structures under different incidence angles (CHY101)

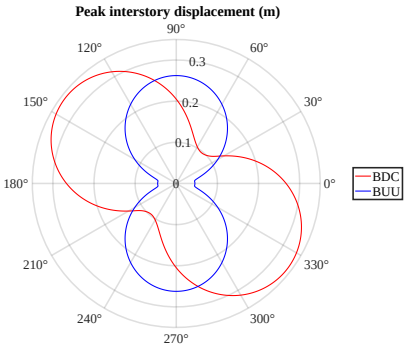

Figure 5.49: Peak interstory displacement responses of asymmetric building structures under different incidence angles (TCU052)

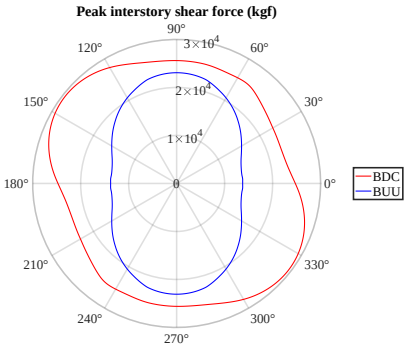

Figure 5.50: Peak interstory shear force responses of asymmetric building structures under different incidence angles (TCU052)

doi:10.6342/NTU202402645

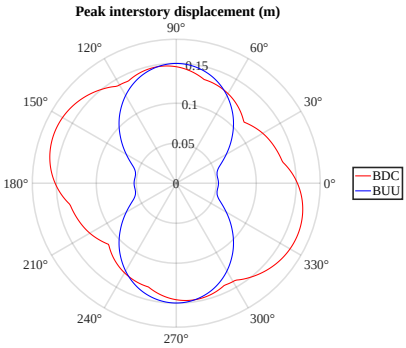

Figure 5.51: Peak interstory displacement responses of asymmetric building structures under different incidence angles (TCU065)

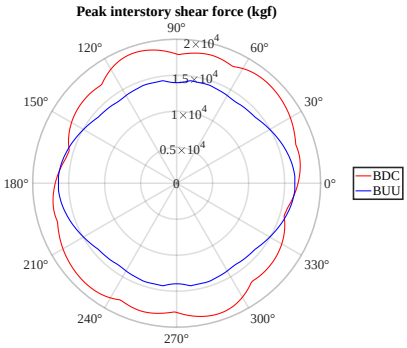

Figure 5.52: Peak interstory shear force responses of asymmetric building structures under different incidence angles (TCU065)

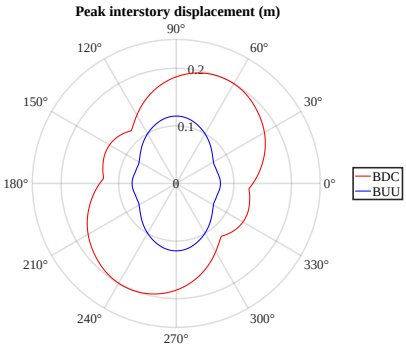

Figure 5.53: Peak interstory displacement responses of asymmetric building structures under different incidence angles (TCU068)

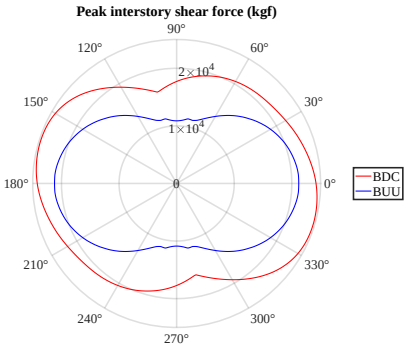

Figure 5.54: Peak interstory shear force responses of asymmetric building structures under different incidence angles (TCU068)

doi:10.6342/NTU202402645

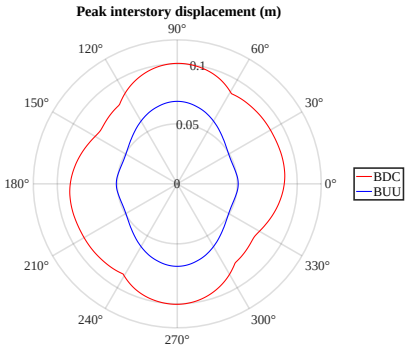

Figure 5.55: Peak interstory displacement responses of asymmetric building structures under different incidence angles (TCU129)

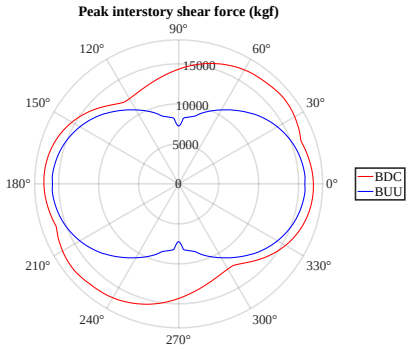

Figure 5.56: Peak interstory shear force responses of asymmetric building structures under different incidence angles (TCU129)

5.5 Influence of seismic peak ground acceleration for asymmetric building structures

This section utilizes acceleration data from 10 stations during the 1999 Chi-Chi earthquake event for detailed analysis and study of peak ground acceleration effects. In this study, the peak ground acceleration range is from 0.1g to 1g, with parametric analysis conducted at 0.1g intervals. The selected analysis parameters include: Equivalent plastic strain, Peak interstory displacement, peak interstory shear force, and Equivalent plastic strain rate. The analysis results are shown in Figures 5.57 to 5.67. The analysis results show that regardless of equivalent plastic strain, Peak interstory displacement, peak interstory shear force, or equivalent plastic strain rate, as the peak ground acceleration increases, the overall response trend of these parameters increases. Particularly in Figures 5.67a to 5.67d, we conducted an integrated analysis aimed at determining the response impact of velocity pulse-type earthquake acceleration time histories on asymmetric building structures. In this part of the study, five non-velocity pulse-type earthquake acceler-

doi:10.6342/NTU202402645

ation time histories (CHY028, CHY041, TCU071, TCU079, TCU084) and five velocity pulse-type earthquake acceleration time histories (CHY101, TCU052, TCU065, TCU068, TCU129) were selected. All responses are plotted on the same graph for comparison and analysis. It can be clearly seen from the graphs that records marked as "pulse" (such as CHY101, TCU052, etc.) usually lead to larger responses. This phenomenon can be observed in the Peak interstory displacement, peak interstory shear force, Equivalent plastic strain, and Equivalent plastic strain rate graphs, as shown in Figures 5.67a to 5.67d. In Figures 5.67b to 5.67d, these pulse-type records show significantly higher displacement responses at high PGA values compared to non-pulse records. This emphasizes the significant impact of velocity pulses in near-fault earthquakes on asymmetric building structures, potentially leading to greater Peak interstory displacement demands, energy input, and plastic damage. The results indicate that the behavior of asymmetric structures varies greatly under different earthquake records, highlighting the importance of considering multiple earthquake scenarios. Near-fault effects (pulse-type records) cause significant structural responses and require special attention, possibly necessitating additional design considerations to address larger Peak interstory displacement and peak interstory shear force demands, especially in terms of Peak interstory displacement. This underscores the strong influence of pulse-type earthquakes on asymmetric structures. Figures 5.67a and 5.67d show that pulse-type earthquakes cause significant plastic responses in asymmetric structures, thus requiring special attention to this effect. However, we can infer from this that earthquakes with velocity pulses do indeed cause more pronounced overall responses in building structures. It can also be observed that the response differences caused by different earthquake records are substantial, indicating that asymmetric structures are highly sensitive to earthquake input characteristics. These graphs reveal the complex response

doi:10.6342/NTU202402645

characteristics of asymmetric building structures under strong seismic actions. This emphasizes the need for detailed dynamic analysis when designing asymmetric structures, considering various earthquake scenarios. Particular attention should be paid to controlling large displacements and potential torsional effects to ensure structural safety. These findings emphasize the necessity of incorporating the effects of velocity pulse-type earthquakes in structural design to ensure buildings maintain adequate safety and stability during such seismic events. Future research should further explore responses under different structural types and design parameters to provide more comprehensive design guidance.

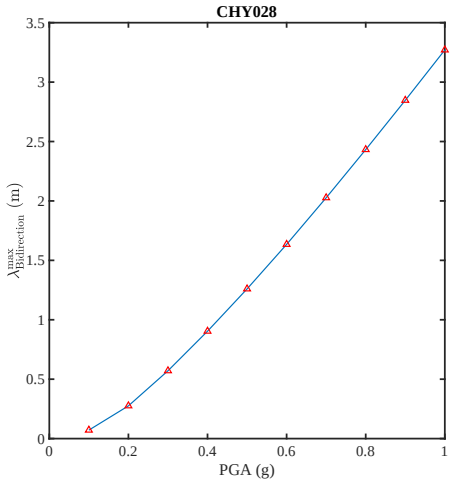

(a) Equivalent plastic strain

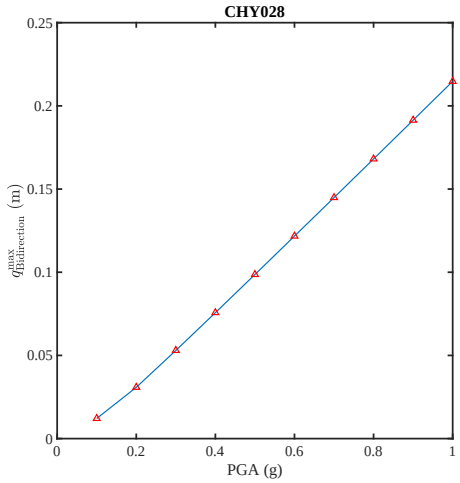

(b) Peak interstory displacement

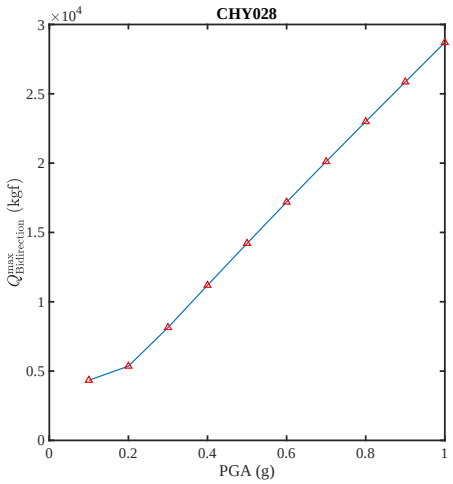

(c) Peak interstory shear force

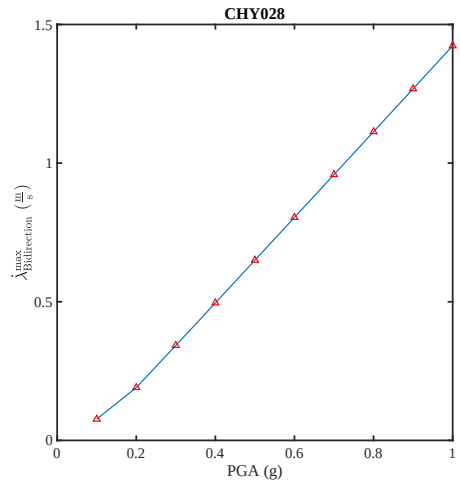

(d) Equivalent plastic strain rate

Figure 5.57: Analysis results of asymmetric building structures under different peak ground accelerations (PGA) at CHY028 station

doi:10.6342/NTU202402645

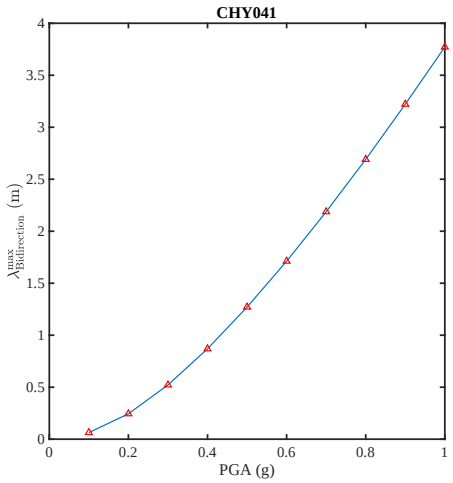

(a) Equivalent plastic strain

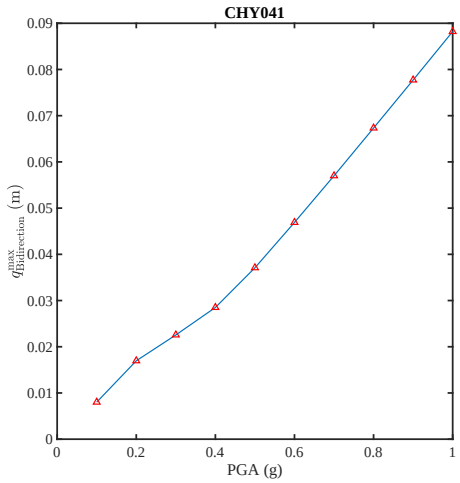

(b) Peak interstory displacement

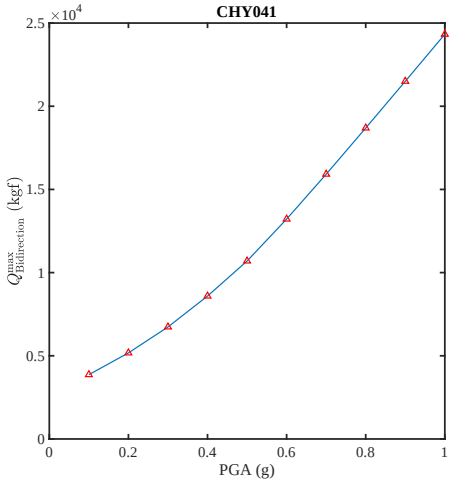

(c) Peak interstory shear force

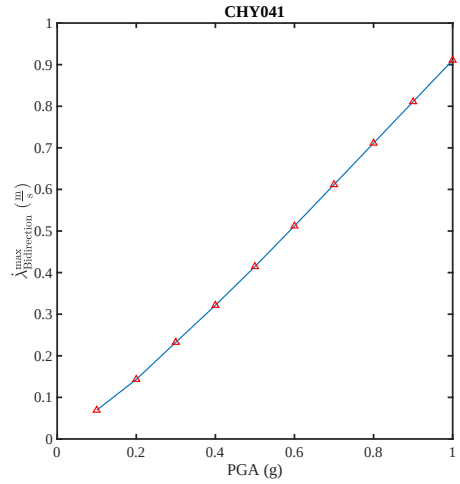

(d) Equivalent plastic strain rate

Figure 5.58: Analysis results of asymmetric building structures under different peak ground accelerations (PGA) at CHY041 station

doi:10.6342/NTU202402645

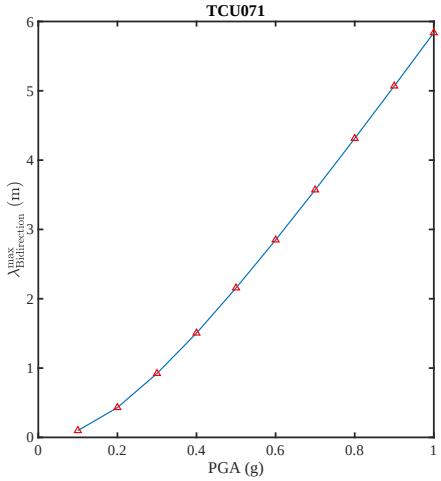

(a) Equivalent plastic strain

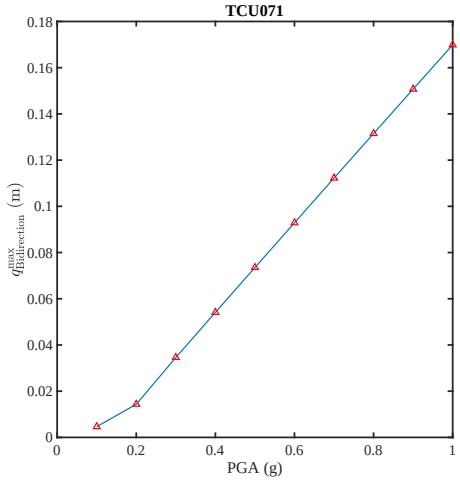

(b) Peak interstory displacement

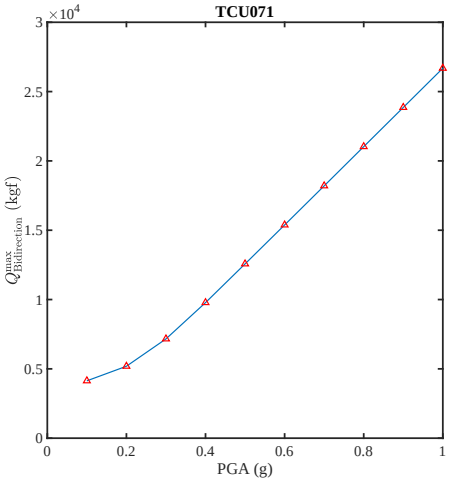

(c) Peak interstory shear force

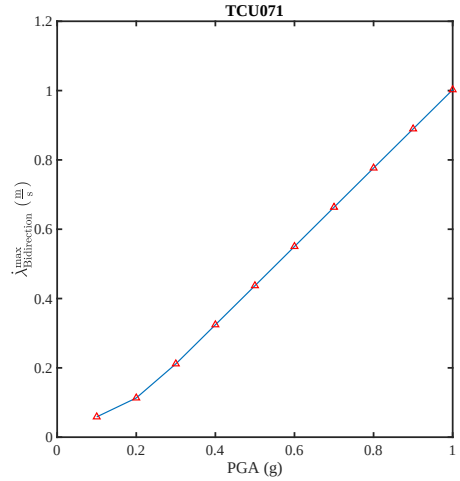

(d) Equivalent plastic strain rate

Figure 5.59: Analysis results of asymmetric building structures under different peak ground accelerations (PGA) at TCU071 station

doi:10.6342/NTU202402645

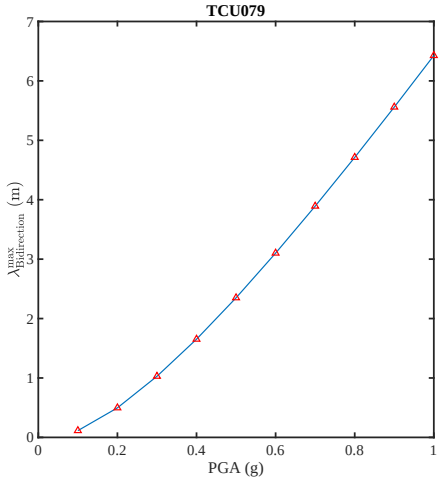

(a) Equivalent plastic strain

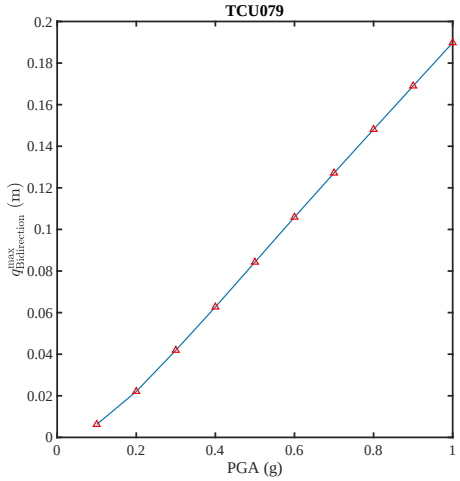

(b) Peak interstory displacement

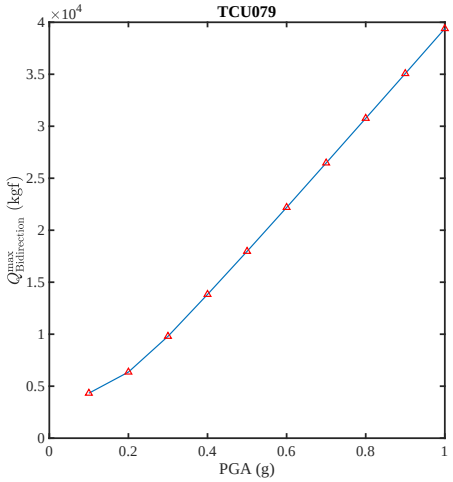

(c) Peak interstory shear force

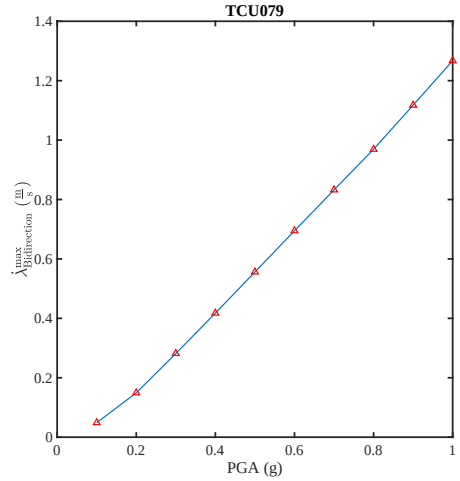

(d) Equivalent plastic strain rate

Figure 5.60: Analysis results of asymmetric building structures under different peak ground accelerations (PGA) at TCU079 station

doi:10.6342/NTU202402645

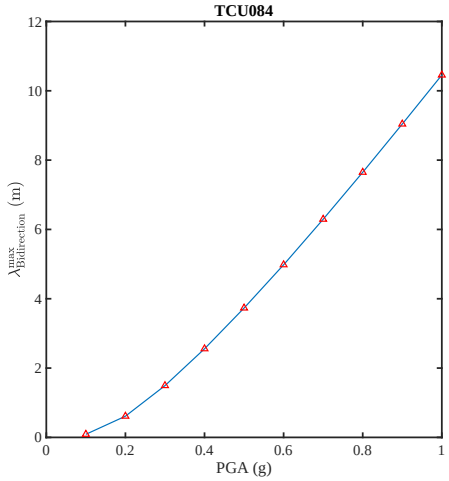

(a) Equivalent plastic strain

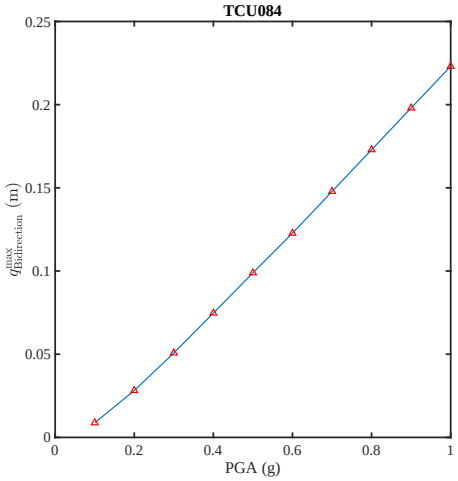

(b) Peak interstory displacement

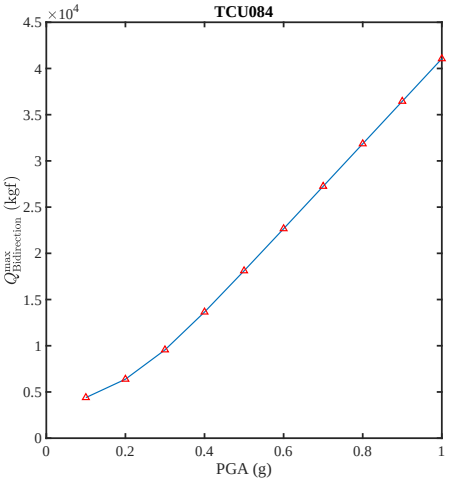

(c) Peak interstory shear force

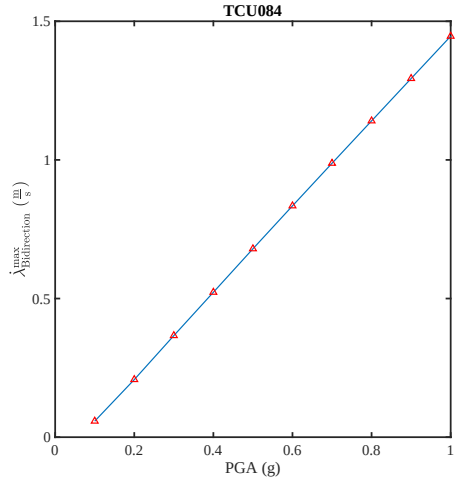

(d) Equivalent plastic strain rate

Figure 5.61: Analysis results of asymmetric building structures under different peak ground accelerations (PGA) at TCU084 station

doi:10.6342/NTU202402645

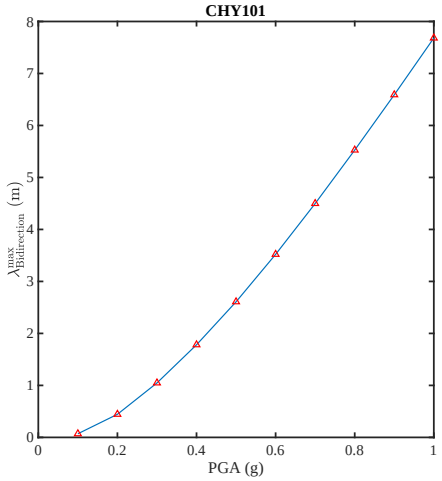

(a) Equivalent plastic strain

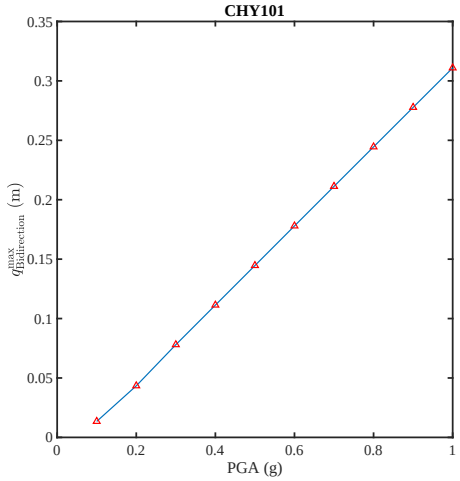

(b) Peak interstory displacement

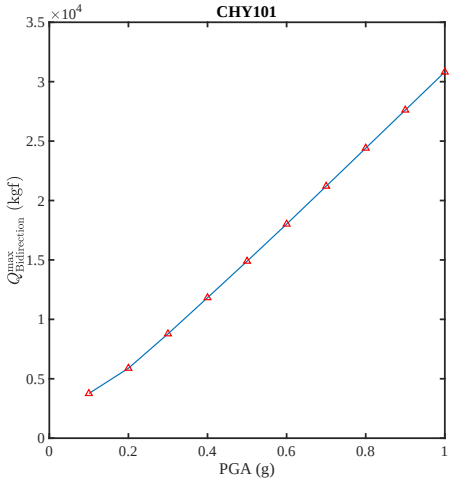

(c) Peak interstory shear force

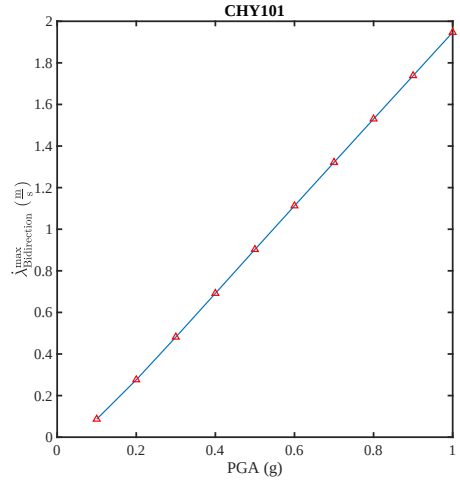

(d) Equivalent plastic strain rate

Figure 5.62: Analysis results of asymmetric building structures under different peak ground accelerations (PGA) at CHY101 station

doi:10.6342/NTU202402645

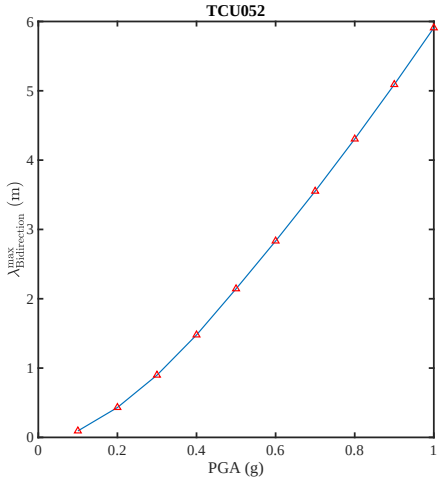

(a) Equivalent plastic strain

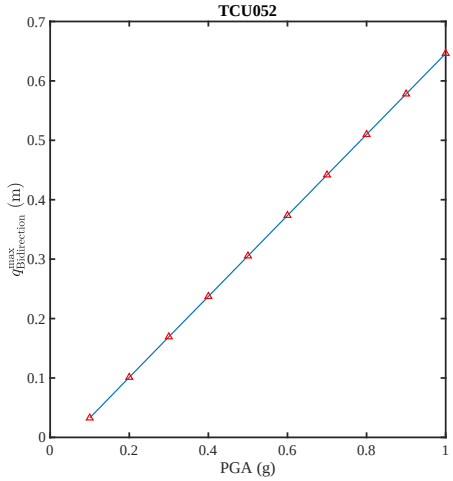

(b) Peak interstory displacement

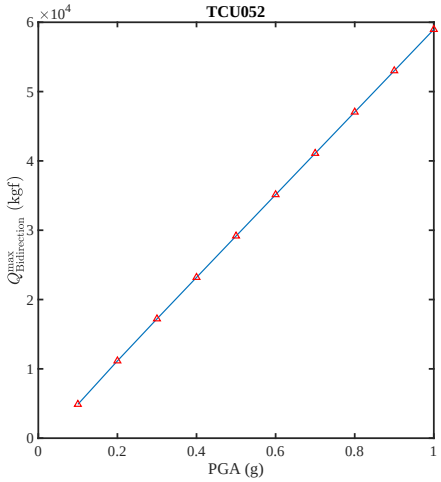

(c) Peak interstory shear force

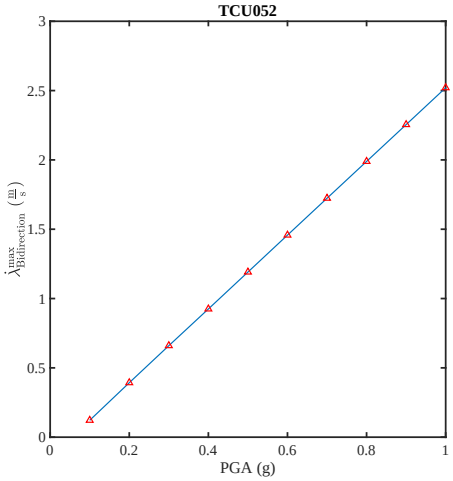

(d) Equivalent plastic strain rate

Figure 5.63: Analysis results of asymmetric building structures under different peak ground accelerations (PGA) at TCU052 station

doi:10.6342/NTU202402645

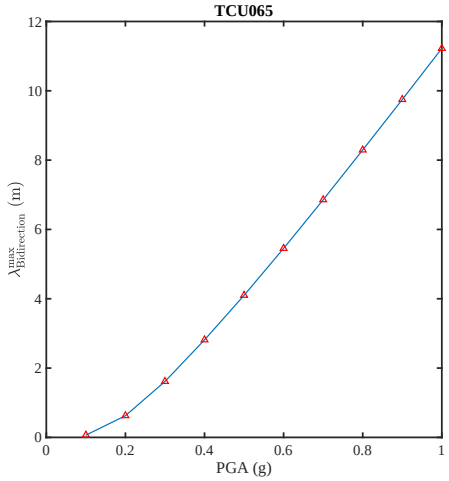

(a) Equivalent plastic strain

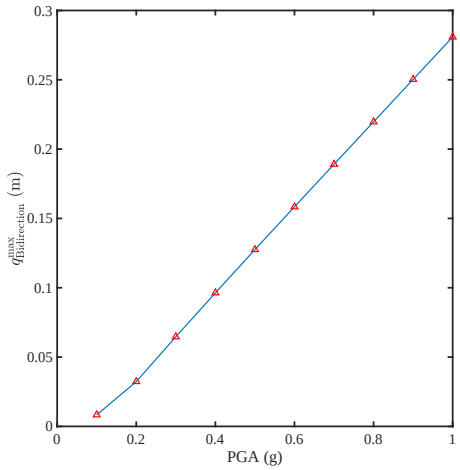

(b) Peak interstory displacement

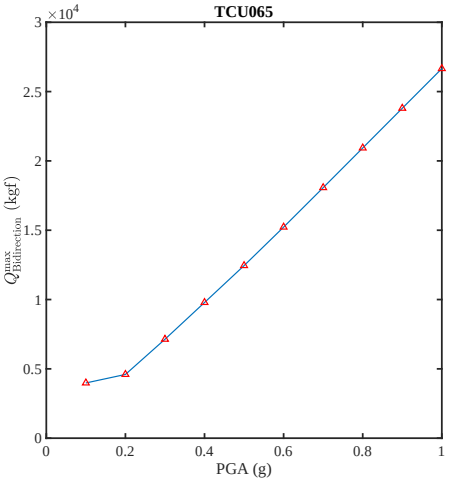

(c) Peak interstory shear force

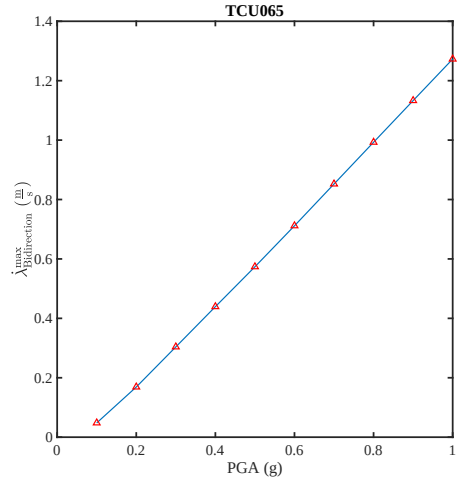

(d) Equivalent plastic strain rate

Figure 5.64: Analysis results of asymmetric building structures under different peak ground accelerations (PGA) at TCU065 station

doi:10.6342/NTU202402645

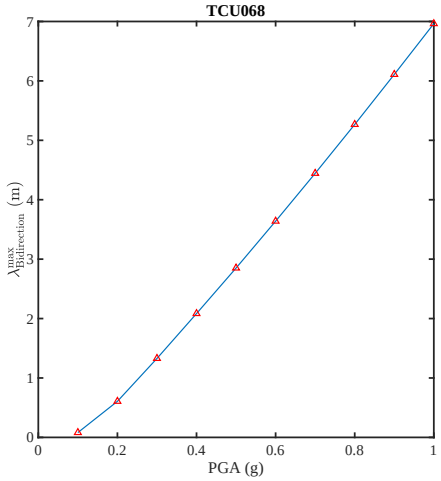

(a) Equivalent plastic strain

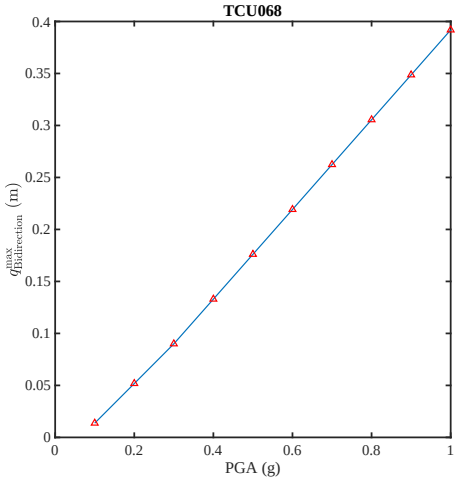

(b) Peak interstory displacement

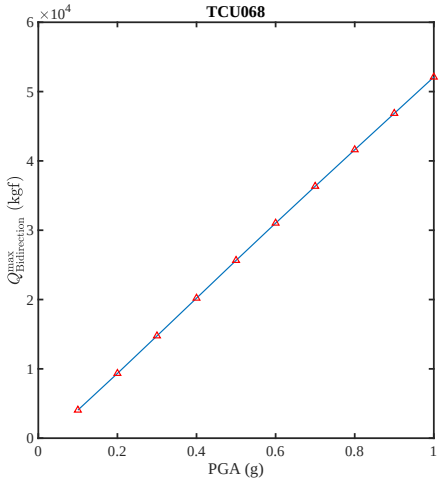

(c) Peak interstory shear force

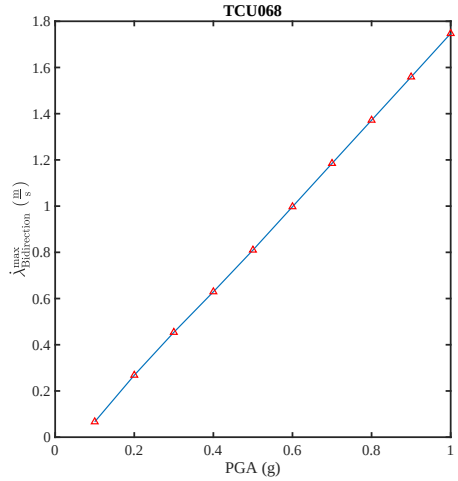

(d) Equivalent plastic strain rate

Figure 5.65: Analysis results of asymmetric building structures under different peak ground accelerations (PGA) at TCU068 station

doi:10.6342/NTU202402645

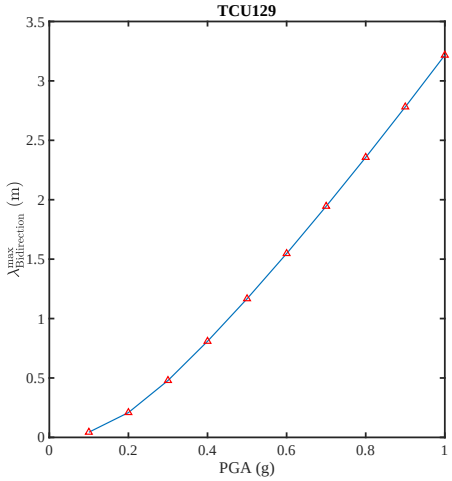

(a) Equivalent plastic strain

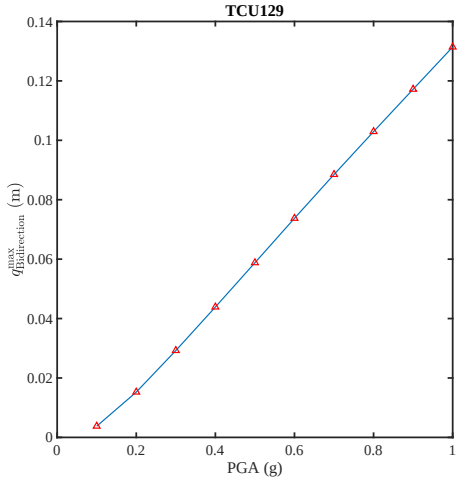

(b) Peak interstory displacement

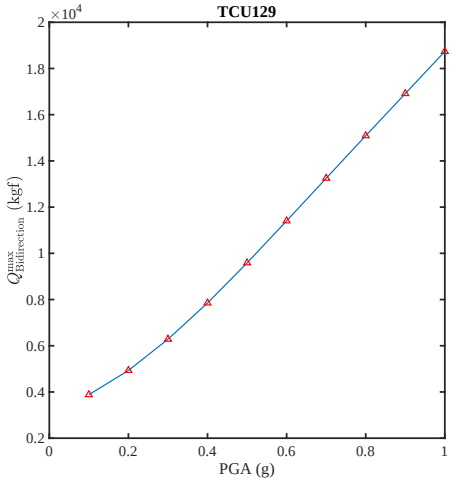

(c) Peak interstory shear force

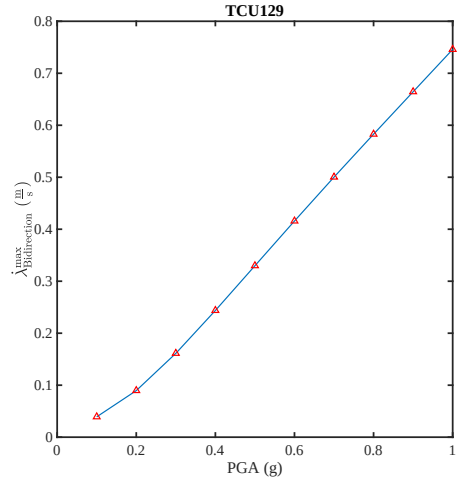

(d) Equivalent plastic strain rate

Figure 5.66: Analysis results of asymmetric building structures under different peak ground accelerations (PGA) at TCU129 station

doi:10.6342/NTU202402645

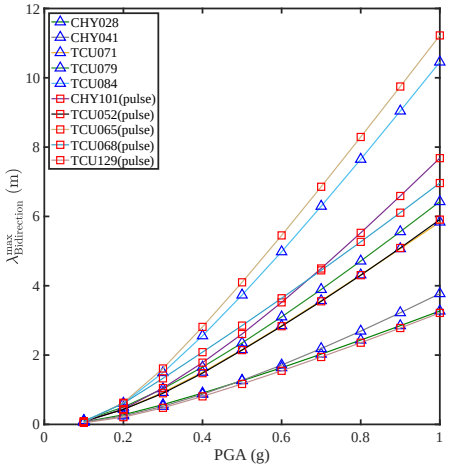

(a) Equivalent plastic strain

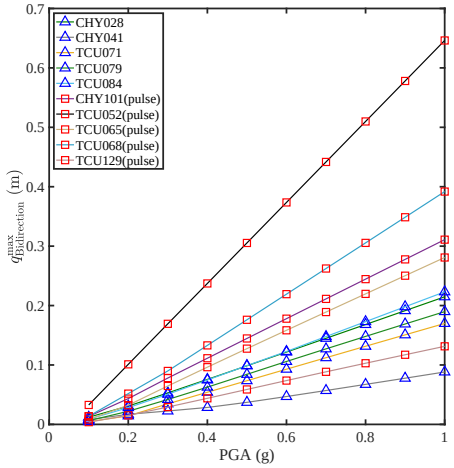

(b) Peak interstory displacement

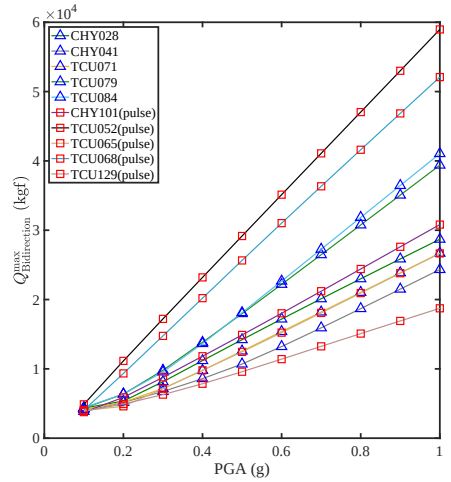

(c) Peak interstory shear force

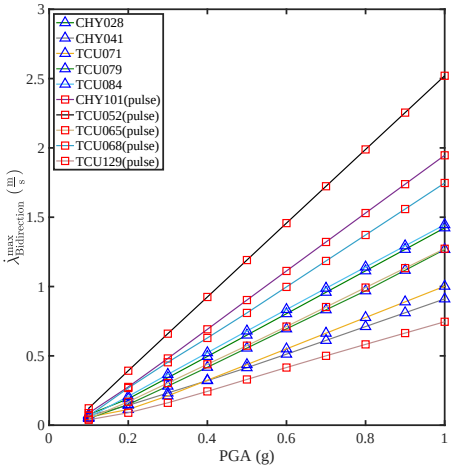

(d) Equivalent plastic strain rate

Figure 5.67: Comparisons of asymmetric structure responses under different peak ground accelerations at 10 stations for pulse-like and non-pulse-like earthquakes.

doi:10.6342/NTU202402645

doi:10.6342/NTU202402645

Chapter 6 Conclusions and future works

6.1 Conclusions

This study proposes two viscoelastoplastic models: a model with isotropic stiffness for analyzing symmetric building structures, and a model with anisotropic stiffness for analyzing asymmetric building structures. The isotropic stiffness model is a special case of the anisotropic stiffness model. Each model is further divided into viscoelastic and viscoelastoplastic systems. Based on the intrinsic symmetry of Lie groups and Lie algebras, the study first conducts high-precision numerical integration to obtain single-step analytical solutions for plastic internal variables, coupled with state-space representation for solving. The research provides detailed theoretical derivations and algorithmic procedures.

For model validation, the study uses bidirectional seismic acceleration as input and ensures the model satisfies viscoelastoplastic constraints through complementary trio conditions. Particularly, the verification of the $\mathbf{Q}_a$ trajectory, which exists only within or on the yield surface, not only confirms the correctness of the algorithm but also demonstrates the model's high accuracy in describing building structures behavior. This rigorous vali-

doi:10.6342/NTU202402645

dation process enhances the model's reliability and applicability.

The study also compares bidirectional and unidirectional seismic analyses for both symmetric and asymmetric structures. The results indicate that regardless of building structures symmetry, unidirectional analysis leads to misestimation or underestimation of several key responses, including equivalent plastic strain, inter-story displacement, inter-story shear force, and total number of time step of viscoelastoplastic phase. Notably, the equivalent plastic strain is significantly underestimated, with asymmetric structure analysis showing an average underestimation of 63.975% when using unidirectional analysis compared to bidirectional analysis. These findings highlight the importance and necessity of bidirectional analysis. The results not only demonstrate the significance of bidirectional analysis but also underscore the necessity of plastic analysis, as bidirectional viscoelastoplastic analysis can more accurately assess the plastic response of building structures after seismic events.

To further emphasize the importance and necessity of bidirectional viscoelastoplastic analysis, the study conducts large-scale bidirectional viscoelastoplastic analyses on symmetric and asymmetric building structures using acceleration data from stations across Taiwan during the Chi-Chi earthquake event. The equivalent plastic strain caused by each station's acceleration history is recorded and represented in isoequivalent plastic strain maps. The results show a higher trend of equivalent plastic strain in the central region for both symmetric and asymmetric structures, indicating higher plastic damage in this area. This aligns well with the actual damage statistics from the Chi-Chi earthquake event, confirming the model's ability to accurately predict the plastic response of building structures after seismic events. This not only validates the model's predictive capability but also provides a powerful tool for earthquake damage assessment and disaster prevention plan-

doi:10.6342/NTU202402645

ning. It also demonstrates the necessity of using bidirectional viscoelastoplastic analysis in building structures evaluations. Additionally, the CPU time for analyzing all Taiwan stations is provided, showing the high computational efficiency of the proposed model and algorithm, which does not require excessive waiting time for analysis.

The study further analyzes the effect of seismic force incidence angle on symmetric and asymmetric building structures. The results indicate that symmetric building structures are not significantly affected by the incidence angle, suggesting that this factor can be omitted when analyzing symmetric structures. However, for asymmetric building structures, the seismic incidence angle has a significant impact, recommending that future analyses of asymmetric structures should consider this effect. The results also show that for most incidence angles, biunidirectional uncouple (BUU) analysis tends to underestimate responses for both symmetric and asymmetric structures, further emphasizing the importance of bidirectional viscoelastoplastic analysis.

Lastly, the study conducts spectral acceleration analysis. The results show that equivalent plastic strain, peak inter-story drift, peak inter-story shear, and equivalent plastic strain rate all increase with rising peak ground acceleration. A comparison between velocity pulse-type and non-pulse-type earthquake histories reveals that certain velocity pulse-type earthquakes indeed cause higher building structures responses, especially evident in asymmetric structures. These findings provide crucial references for seismic hazard assessment and building structures design.

In conclusion, this study not only offers in-depth theoretical exploration and innovation but also provides rich insights for practical applications. The research results emphasize the importance of accurate viscoelastoplastic analysis and bidirectional analysis,

doi:10.6342/NTU202402645

while pointing out the risks of relying solely on elastic analysis and the necessity of conducting bidirectional analysis to avoid misestimation or underestimation of responses in unidirectional analysis. These findings have significant implications for improving the seismic performance of building structures, refining seismic design codes, and optimizing earthquake disaster assessment methods. Therefore, having an accurate viscoelastoplastic model for analysis is of paramount importance.

6.2 Future work

Future work for this research will involve conducting comprehensive full-scale experiments to further validate the proposed model. These experiments will not only consolidate theoretical findings but also provide practical insights into the model's behavior under real conditions.

Another significant extension of this study is the application of the model to high-rise building structures. This will require expanding the model to accommodate the increased complexity and different dynamic behaviors associated with taller building structures. The results will provide valuable contributions to the design and analysis of high-rise buildings.

Furthermore, emphasis will be placed on incorporating isolation layers. Simulating isolated building structures will help understand isolation techniques and further comprehend their viscoelastic or frictional behavior. This will involve detailed analysis and adjustments to the model to accurately reflect the behavior of isolated structures.

The inclusion of building structure foundations in the model will also be explored. This will enable a comprehensive analysis of the responses and interactions between the superstructure and substructure. Understanding these interactions is crucial for the overall

doi:10.6342/NTU202402645

stability and safety of buildings.

Additionally, the effects of axial forces and bending moments on the structure will be studied in more detail. This will involve refining the model to consider these forces and their impact on the structural integrity and performance of buildings.

To support the practical application of this research, user-friendly software with a good interface will be developed. This software will be designed for easy use by engineers and researchers, facilitating analysis and design processes based on the validated model. The goal is to create a tool that is both powerful and easy to use, bridging the gap between complex theoretical models and practical engineering solutions.

In conclusion, future work will focus on experimental validation, extension to high-rise structures, incorporation of isolation layers and structural foundations, detailed analysis of axial force and bending moment effects, and development of user-friendly software. These efforts aim to enhance the model's applicability and usability in real-world scenarios, ultimately contributing to safer and more efficient building designs.

doi:10.6342/NTU202402645

doi:10.6342/NTU202402645

References

[1] H. A. Abbas, M. R. Salman, and H. M. Ghaltan. Modelling analysis of earthquake impact on RC buildings in baghdad using SAP2000. Journal of Applied Engineering Design and Simulation, 3(2):49–56, 2023.

[2] A. Acharjya, A. Santra, and R. Roy. Estimating structural response to bidirectional seismic excitation using spectrum compatible motions: Performance of a pair of companion spectra. Earthquake Engineering & Structural Dynamics, 2024.

[3] K. Anastassiadis, A. Athanatopoulou, and T. Makarios. Equivalent static eccentricities in the simplified methods of seismic analysis of buildings. Earthquake Spectra, 14(1):1–34, 1998.

[4] R. Arvindreddy and M. Fernandes. Seismic analysis of RC regular and Irregular frame structures. Int. Res. J. Eng. Technol, 2:44–47, 2015.

[5] P. T. Brewick, E. A. Johnson, E. Sato, and T. Sasaki. Constructing and evaluating generalized models for a base-isolated structure. Structural Control and Health Monitoring, 25(11):e2243, 2018.

[6] A. K. Chopra and R. K. Goel. A modal pushover analysis procedure for estimating seismic demands for buildings. Earthquake Engineering & Structural Dynamics, 31(3):561–582, 2002.

doi:10.6342/NTU202402645

[7] A. K. Chopra and R. K. Goel. A modal pushover analysis procedure to estimate seismic demands for unsymmetric-plan buildings. Earthquake Engineering & Structural Dynamics, 33(8):903–927, 2004.

[8] A. T. Council. Seismic evaluation and retrofit of concrete buildings. Report No. SSC 96-01: ATC-40, 1, 1996.

[9] J. C. L. De Llera and A. K. Chopra. A simplified model for analysis and design of asymmetric-plan buildings. Earthquake Engineering & Structural Dynamics, 24(4):573–594, 1995.

[10] R. Divya and K. Murali. Comparative analysis of behaviour of horizontal and vertical irregular buildings with and without using shear walls by ETABS software. Materials Today: Proceedings, 52:1821–1830, 2022.

[11] F. E. FEMA 356 et al. Prestandard and commentary for the seismic rehabilitation of buildings. Federal Emergency Management Agency: Washington, DC, USA, 2000.

[12] A. Genikomsou and M. Polak. Finite element analysis of a reinforced concrete slab-column connection using ABAQUS. In Structures Congress 2014, pages 813–823, 2014.

[13] A. Guleria et al. Structural analysis of a multi-storeyed building using ETABS for different plan configurations. Int. J. Eng. Res. Technol, 3(5):1481–1485, 2014.

[14] H.-K. Hong and C.-S. Liu. Prandtl-reuss elastoplasticity: on-off switch and superposition formulae. International Journal of Solids and Structures, 34(33-34):4281–4304, 1997.

doi:10.6342/NTU202402645

[15] H.-K. Hong and C.-S. Liu. Internal symmetry in bilinear elastoplasticity. International Journal of Non-Linear Mechanics, 34(2):279–288, 1999.

[16] H.-K. Hong and C.-S. Liu. Internal symmetry in the constitutive model of perfect elastoplasticity. International Journal of Non-Linear Mechanics, 35(3):447–466, 2000.

[17] H.-K. Hong, L.-W. Liu, Y.-P. Shiao, and C.-J. Chang. Building structure with elastoplastic bilinear model under multi-dimensional earthquake forces. Journal of Mechanics, 38:598–609, 2022.

[18] S.-H. Hsu. 功能性支承橋梁考慮雙向耦合滑動之受震反應分析. Master's thesis, 國立成功大學, 06 2023.

[19] M. A. Hussain, S. C. Dutta, and S. Das. Seismic behaviour of structures under bidirectional ground motion: Does the angle of incidence have any influence? Soil Dynamics and Earthquake Engineering, 159:107328, 2022.

[20] A. Y. Ishlinsky. Some applications of statistics to description of laws of body deformation. Reports of the Academy of Science of the USSR, ONT, 9:583–590, 1944.

[21] M. Ismaeil, K. Elhadi, Y. Alashker, and I. E. Yousef. Seismic analysis and design of a multi-storey building located in haql city, ksa. Journal of Soft Computing in Civil Engineering, 1(2):35–51, 2017.

[22] W. D. Iwan. A distributed-element model for hysteresis and its steady-state dynamic response. Journal of Applied Mechanics, 33(4):893–900, 1966.

[23] K. Ji, Y. Ren, R. Wen, and C.-H. Kuo. Near-field velocity pulse-like ground motions

doi:10.6342/NTU202402645

on February 6, 2018 MW6. 4 Hualien, Taiwan earthquake and structural damage implications. Soil Dynamics and Earthquake Engineering, 126:105784, 2019.

[24] S. Kim, F. Kusuhara, and H. Shiohara. Analysis of RC slab–beam–column sub-assemblages subjected to bidirectional lateral cyclic loading using a new 3D macroelement. Earthquake Engineering & Structural Dynamics, 46(14):2519–2536, 2017.

[25] Z. Li and G. D. Hatzigeorgiou. Seismic damage analysis of RC structures using fiber beam-column elements. Soil Dynamics and Earthquake Engineering, 32(1):103–110, 2012.

[26] B.-Z. Lin, M.-C. Chuang, and K.-C. Tsai. Object-oriented development and application of a nonlinear structural analysis framework. Advances in Engineering Software, 40(1):66–82, 2009.

[27] J.-L. Lin and M.-C. Chuang. Simplified nonlinear modeling for estimating the seismic response of buildings. Engineering Structures, 279:115590, 2023.

[28] J.-L. Lin and K.-C. Tsai. Simplified seismic analysis of asymmetric building systems. Earthquake Engineering & Structural Dynamics, 36(4):459–479, 2007.

[29] J.-L. Lin and K.-C. Tsai. Seismic analysis of two-way asymmetric building systems under bi-directional seismic ground motions. Earthquake Engineering & Structural Dynamics, 37(2):305–328, 2008.

[30] C.-S. Liu. Two-dimensional bilinear oscillator: group-preserving scheme and steady-state motion under harmonic loading. International journal of non-linear mechanics, 38(10):1581–1602, 2003.

doi:10.6342/NTU202402645

[31] C.-S. Liu. A method of Lie-symmetry GL (n, R) for solving non-linear dynamical systems. International Journal of Non-Linear Mechanics, 52:85–95, 2013.

[32] C.-S. Liu, H.-K. Hong, and D.-Y. Liou. Two-dimensional friction oscillator: group-preserving scheme and handy formulae. Journal of Sound and Vibration, 266(1):49–74, 2003.

[33] K.-Y. Liu, L.-W. Liu, D.-G. Huang, and T.-L. Tsai. Viscoelastoplastic and incremental analysis of bridge with functional bearing. Journal of Sound and Vibration, 530:116926, 2022.

[34] Q. Luo, F. Dai, Y. Liu, M. Gao, Z. Li, and R. Jiang. Seismic performance assessment of velocity pulse-like ground motions under near-field earthquakes. Rock Mechanics and Rock Engineering, 54(8):3799–3816, 2021.

[35] G. Magliulo and R. Ramasco. Seismic response of three-dimensional r/c multi-storey frame building under uni-and bi-directional input ground motion. Earthquake Engineering & Structural Dynamics, 36(12):1641–1657, 2007.

[36] G. Nguyen and G. Nguyen. A thermodynamic approach to constitutive modelling of concrete using damage mechanics and plasticity theory. PhD thesis, Oxford University, UK, 2005.

[37] M. Perrault and P. Guéguen. Correlation between ground motion and building response using california earthquake records. Earthquake Spectra, 31(4):2027–2046, 2015.

[38] I. Peruš and P. Fajfar. On the inelastic torsional response of single-storey structures under bi-axial excitation. Earthquake engineering & structural dynamics, 34(8):931–941, 2005.

doi:10.6342/NTU202402645

[39] L. Prandtl. Ein gedankenmodell zur kinetischen theorie der festen körper. ZAMM-Journal of Applied Mathematics and Mechanics/Zeitschrift für Angewandte Mathematik und Mechanik, 8(2):85–106, 1928.

[40] P. Rathod and R. Chandrashekar. Seismic analysis of multistoried building for different plans using ETABS 2015. International Research Journal of Engineering and Technology (IRJET) Volume, 4:1101–8, 2017.

[41] J. C. Reyes and A. K. Chopra. Three-dimensional modal pushover analysis of buildings subjected to two components of ground motion, including its evaluation for tall buildings. Earthquake Engineering & Structural Dynamics, 40(7):789–806, 2011.

[42] A. Roy, A. Santra, and R. Roy. Estimating seismic response under bi-directional shaking per uni-directional analysis: Identification of preferred angle of incidence. Soil Dynamics and Earthquake Engineering, 106:163–181, 2018.

[43] J. Ruiz-García and J. M. Ramos-Cruz. Assessment of permanent drift demands in steel moment-resisting steel buildings due to recorded near-fault forward directivity earthquake ground motions and velocity pulse models. In Structures, volume 27, pages 1260–1273. Elsevier, 2020.

[44] H. Sucuoğlu, N. Eren, and R. Pinho. Interstory drift based scaling of bi-directional ground motions. Earthquake Engineering & Structural Dynamics, 51(15):3620–3638, 2022.

[45] T.-L. Tsai. 應用黏彈塑性理論於支承介面摩擦衰減之橋梁模型受近斷層地震反應分析. Master's thesis, 國立成功大學, 01 2022.

[46] Y.-P. Wang, W.-H. Liao, and C.-L. Lee. A state-space approach for dynamic analysis of sliding structures. Engineering Structures, 23(7):790–801, 2001.

doi:10.6342/NTU202402645

[47] Y.-T. Weng, K.-C. Tsai, P.-C. Chen, C.-C. Chou, Y.-R. Chan, S.-J. Jhuang, and Y.-Y. Wang. Seismic performance evaluation of a 34-story steel building retrofitted with response modification elements. Earthquake Engineering & Structural Dynamics, 38:759 – 781, 05 2009.

[48] I. Whiteman. A mathematical model depicting the stress-strain diagram and the hysteresis loop. Journal of Applied Mechanics, 26(1):95–100, 1959.

[49] W. Xiong, S.-J. Zhang, L.-Z. Jiang, and Y.-Z. Li. Introduction of the convex friction system (CFS) for seismic isolation. Structural Control and Health Monitoring, 24(1):e1861, 2017.

[50] M. Yılmaz and H. Can. Examination of buildings with different number of floors using non-linear time history analysis according to TBEC-2018 and EC 8 seismic codes. Advanced Engineering Days (AED), 8:49–51, 2023.

[51] X.-K. Zhu and B. N. Leis. Strength criteria and analytic predictions of failure pressure in line pipes. International Journal of Offshore and Polar Engineering, 14(02), 2004.

doi:10.6342/NTU202402645

doi:10.6342/NTU202402645

Appendix A — Viscoelastoplastic analysis of multi-story asymmetric building structures

A.1 Bilinear viscoelastoplastic of a multi-story in asymmetric building structures

Here, we will detail how to establish a bilinear viscoelastoplastic model for a multi-story asymmetric building structure. First, we can derive the equation of motion for this asymmetric building structure as follows:

$$\mathbf{m}_{si}\ddot{\mathbf{q}}_i + \mathbf{Q}_i - \mathbf{Q}_{i+1} = \mathbf{F}_i. \tag{A.1}$$

where $i = 1, 2, 3..., n$ and $\mathbf{Q}_{n+1} = \mathbf{0}$,

$$\mathbf{m}_{si} = \begin{bmatrix} m_{1i} & 0 & 0 \\ 0 & m_{i2} & 0 \\ 0 & 0 & I_{io} \end{bmatrix},$$

doi:10.6342/NTU202402645

$$\mathbf{q}_i = \begin{bmatrix} q_{i1} \\ q_{i2} \\ q_{i3} \end{bmatrix},$$

$$\mathbf{Q}_i = \begin{bmatrix} Q_{i1} \\ Q_{i2} \\ Q_{i3} \end{bmatrix},$$

$$\mathbf{F}_i = \begin{bmatrix} F_{i1} \\ F_{i2} \\ F_{i3} \end{bmatrix},$$

Among these, $\mathbf{m}_s$ is the mass matrix of ith story of the building structure, m_1 and m_2 are the masses of ith story of the building structure, and I_o is the rotational inertia of ith story of the building structure.$\mathbf{q}_i$ is the generalized displacement of ith story, q_{i1} is the interstory displacement in the 1st direction of ith story, q_{i2} is the interstory displacement in the 2nd direction of ith story, q_{i3} is the twist angle of ith story. $\mathbf{Q}_i$ is the generalized force of ith story, Q_{i1} is the interstory shear force in the 1st direction of ith story, Q_{i2} is the interstory shear force in the 2nd direction of ith story, Q_{i3} is the torque of ith story. $\mathbf{F}_i$ is the external force vector of ith story, F_{i1} is the external force in the 1st direction of ith story, F_{i2} is the external force in the 2nd direction of ith story, F_{i3} is the external torque of ith story.

The model proposed in this study considers not only elasticity but also elastoplasticity. For the elastoplastic part, we applied the bilinear elastoplastic model from plasticity theory to simulate the elastoplastic behavior of the building structure. The bilinear elasto-

doi:10.6342/NTU202402645

plastic model consists of an elastic part and a plastic part. The elastic part is composed of an elastic spring, while the plastic part consists of a plastic spring and a yield switch. Therefore, we can decompose the generalized displacement of ith story $\mathbf{q}_i$ into two parts: elastic displacement of ith story $\mathbf{q}_i^e$ and plastic displacement of ith story $\mathbf{q}_i^p$. As mentioned earlier, the model proposed in this study also considers the contribution of viscosity. Thus, we use a viscous damper to simulate the inherent damping of the building structure. Combining the viscous damper in parallel with the bilinear elastoplastic model results in the viscoelastoplastic model. The composition of the generalized shear force of ith story includes the elastoplastic shear force of ith story contributed by the elastoplastic model and the viscous damping force. The elastoplastic shear force of ith story of the building structure $\mathbf{Q}_i^{EP}$ is decomposed as active shear force of ith story $\mathbf{Q}_{ai}$, and back shear force of ith story $\mathbf{Q}_{bi}$. Considering all of the above, we can establish the mechanical components as shown in Figure A.1, and we can express the viscoelastoplastic model of ith story mathematically as follows:

$$\mathbf{q}_i = \mathbf{q}_i^e + \mathbf{q}_i^p, \tag{A.2}$$

$$\mathbf{Q}_i = \mathbf{Q}_i^{EP} + \mathbf{C}_i\dot{\mathbf{q}}_i, \tag{A.3}$$

$$\mathbf{Q}_i^{EP} = \mathbf{Q}_{ai} + \mathbf{Q}_{bi}, \tag{A.4}$$

$$\mathbf{Q}_i^{EP} = \mathbf{K}_{ei}\mathbf{q}_i^e, \tag{A.5}$$

doi:10.6342/NTU202402645

$$\dot{\mathbf{Q}}_{bi} = \mathbf{K}_{pi}\dot{\mathbf{q}}_i^p, \tag{A.6}$$

$$Q_{yi}\dot{\mathbf{q}}_i^p = \mathbf{Q}_{ai}^*\dot{\lambda}_i, \tag{A.7}$$

$$f_i\dot{\lambda}_i = 0, \tag{A.8}$$

$$f_i = \sqrt{\mathbf{Q}_{ai}^{\mathrm{T}}\mathbf{Y}_i\mathbf{Q}_{ai}} - Q_{yi} \leq 0, \tag{A.9}$$

$$\dot{\lambda}_i \geq 0, \tag{A.10}$$

where

$$\mathbf{Y}_i = (\mathbf{N}_i^{-1})^{\mathrm{T}}\mathbf{N}_i,$$

$$\mathbf{K}_{pi} = k_{pi}\mathbf{N}_i$$

$$\mathbf{Q}_{ai}^* = \mathbf{N}_i^{-1}\mathbf{Q}_{ai}$$

$$\dot{\mathbf{q}}_i^p = \frac{\dot{\lambda}_i}{Q_{yi}}\mathbf{N}_i^{-1}\mathbf{Q}_{ai}$$

where $\mathbf{Y}_i$ is yield matrix of ith story.

The Hooke's law of the elastic displacement is stated in Eq. (A.5) where the $\mathbf{K}_{ei}$ is elastic stiffness of ith story of building structures. Eq. (A.7) shows the plastic flow rule

doi:10.6342/NTU202402645

of ith story which relates the plastic displacement rate of ith story $\dot{\mathbf{q}}_i^p$ with the active shear force of ith story $\mathbf{Q}_{ai}^*$ multiplied by the rate of plastic equivalent of ith story $\dot{\lambda}_i$. The kinematic hardening rule of ith story of in Eq. (A.6) describes the back shear force of ith story which is proportional to the rate of generalized plastic displacement of ith story where the $\mathbf{K}_{pi}$ is kinematic-hardening stiffness of ith story. Eq. (A.8)- Eq. (A.10) are the complementary trios of ith story where Eq. (A.9) shows that the $||\mathbf{Q}_{ai}^*||$ cannot exceed the yielding force Q_{yi}, Eq. (A.10) means that the rate of plastic equivalent of ith story is non-negative, and the alternative condition of ith story Eq. (A.8) means that $f_i\dot{\lambda}_i$ must be zero for each case. Further, the bilinear elastoplastic model of ith story in Eq. (A.2)-Eq. (A.10) can be represented as a compact formulation as follows:

$$\dot{\mathbf{q}}_i = \mathbf{K}_{ei}^{-1}\dot{\mathbf{Q}}_i^{\mathrm{EP}} + \dot{\mathbf{q}}_i^p, \tag{A.11}$$

$$\dot{\mathbf{Q}}_{ai} = \mathbf{K}_{ei}\dot{\mathbf{q}}_i - (\mathbf{K}_{pi} + \mathbf{K}_{ei})\dot{\mathbf{q}}_i^p, \tag{A.12}$$

$$\dot{\mathbf{Q}}_{ai}^* = \mathbf{N}_i^{-1}\mathbf{K}_{ei}\dot{\mathbf{q}}_i - (\mathbf{N}_i^{-1}\mathbf{K}_{ei} + k_{pi}\mathbf{I})\frac{\dot{\lambda}_i}{Q_{yi}}\mathbf{Q}_{ai}^*, \tag{A.13}$$

$$Q_{yi}\dot{\mathbf{q}}_i^p = \mathbf{Q}_{ai}^*\dot{\lambda}_i, \tag{A.14}$$

$$f_i\dot{\lambda}_i = 0, \tag{A.15}$$

$$f_i = \sqrt{\mathbf{Q}_{ai}^{\mathrm{T}}\mathbf{Y}_i\mathbf{Q}_{ai}} - Q_{yi} \leq 0, \tag{A.16}$$

$$\dot{\lambda}_i \geq 0. \tag{A.17}$$

doi:10.6342/NTU202402645

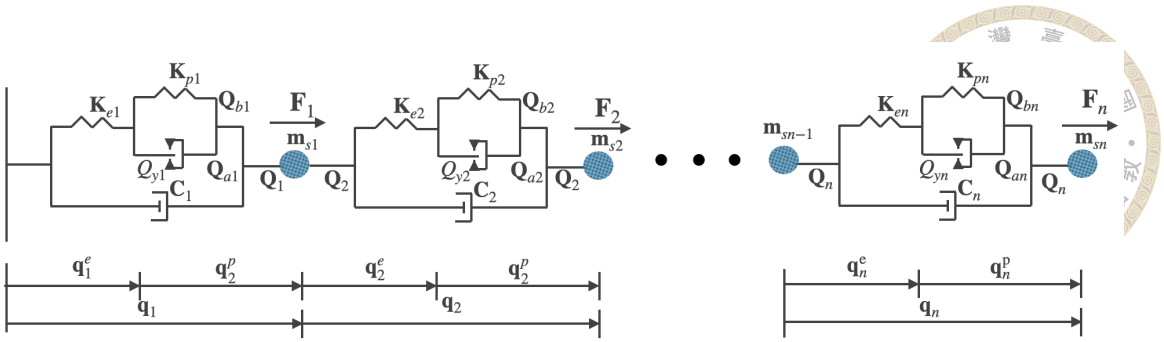

Figure A.1: Mechanical element of the three-component multi-story asymmetric building structure

A.2 The straining conditions and the sufficient and necessary conditions for the ith story viscoelastoplastic model

In order to provide a more detailed description of the viscoelastoplastic behavior of this model. We use the complementary trio relationship to better describe the viscoelastoplastic behavior of the building structures. Additionally, all these conditions need to be simultaneously satisfied. Eq. (A.8) represents an alternative condition, meaning that either $f_i = 0$ or $\dot{\lambda}_i = 0$ can be chosen. Eq. (A.9) is an admissible condition, while Eq. (A.10) ensures non-negative dissipation, meaning that the system will not have dissipations with negative energy.The following is a theoretical derivation. To accurately determine the system's switching to judge whether the system is in a viscoelastic or viscoelastoplastic state, the core idea is to combine the complementary trio as a switching mechanism. When the yield condition $(f_i = 0)$ is satisfied, it leads to $\dot{f}_i = 0$, therefore we have

$$\dot{f}_i = (\mathbf{Q}_{ai}^*)^{\mathrm{T}} \dot{\mathbf{Q}}_{ai}^* = 0.$$

doi:10.6342/NTU202402645

Substituting Eq. (A.13) into the above equations, we obtain:

$$(\mathbf{Q}_{ai}^{*})^{\mathrm{T}}\mathbf{N}_i^{-1}\mathbf{K}_{ei}\dot{\mathbf{q}}_i - (\mathbf{Q}_{ai}^{*})^{\mathrm{T}}(\mathbf{N}_i^{-1}\mathbf{K}_{ei} + k_{pi}\mathbf{I})\frac{\dot{\lambda}_i}{Q_{yi}}\mathbf{Q}_{ai}^{*} = 0. \tag{A.18}$$

Since $(\mathbf{Q}_{ai}^{*})^{\mathrm{T}}(\mathbf{N}_i^{-1}\mathbf{K}_{ei} + k_{pi}\mathbf{I})\mathbf{Q}_{ai}^{*} \geq 0$ for $\mathbf{Q}_{ai}^{*} \neq 0$, Eq. (A.15) is satisfied and we can obtain the straining conditions $\dot{\lambda}_i$

$$\dot{\lambda}_i = \frac{Q_{yi}(\mathbf{Q}_{ai}^{*})^{\mathrm{T}}\mathbf{N}_i^{-1}\mathbf{K}_{ei}\dot{\mathbf{q}}_i}{(\mathbf{Q}_{ai}^{*})^{\mathrm{T}}(\mathbf{N}_i^{-1}\mathbf{K}_{ei} + k_{pi}\mathbf{I})\mathbf{Q}_{ai}^{*}} > 0. \tag{A.19}$$

Therefore, we prove that

$$\text{if} \quad f_i = 0 \quad \text{and} \quad (\mathbf{Q}_{ai}^{*})^{\mathrm{T}}\mathbf{N}_i^{-1}\mathbf{K}_{ei}\dot{\mathbf{q}}_i > 0 \quad \text{then} \quad \dot{\lambda}_i = \frac{Q_{yi}(\mathbf{Q}_{ai}^{*})^{\mathrm{T}}\mathbf{N}_i^{-1}\mathbf{K}_{ei}\dot{\mathbf{q}}_i}{(\mathbf{Q}_{ai}^{*})^{\mathrm{T}}(\mathbf{N}_i^{-1}\mathbf{K}_{ei} + k_{pi}\mathbf{I})\mathbf{Q}_{ai}^{*}} > 0.$$

On the contray, if $\dot{\lambda}_i > 0$, Eq. (A.15) request $f_i = 0$, hence we obtain $\dot{f}_i = 0$ again. Further, this brings us to obtain the following condition

$$\text{if} \quad \dot{\lambda}_i = 0 \quad \text{then} \quad f_i = 0 \quad \text{and} \quad (\mathbf{Q}_{ai}^{*})^{\mathrm{T}}\mathbf{N}_i^{-1}\mathbf{K}_{ei}\dot{\mathbf{q}}_i > 0.$$

In summary, we have the sufficient and necessary condition of the viscoelastoplastic model.

$$\left\{f_i = 0 \text{ and } (\mathbf{Q}_{ai}^{*})^{\mathrm{T}}\mathbf{N}_i^{-1}\mathbf{K}_{ei}\dot{\mathbf{q}}_i > 0\right\} \Leftrightarrow \left\{\dot{\lambda}_i = \frac{Q_{yi}(\mathbf{Q}_{ai}^{*})^{\mathrm{T}}\mathbf{N}_i^{-1}\mathbf{K}_{ei}\dot{\mathbf{q}}_i}{(\mathbf{Q}_{ai}^{*})^{\mathrm{T}}(\mathbf{N}_i^{-1}\mathbf{K}_{ei} + k_{pi}\mathbf{I})\mathbf{Q}_{ai}^{*}}\right\} \Leftrightarrow \{\dot{\lambda}_i > 0\}.$$

It is logically equivalent to the following on-off criterion of the viscoelastoplastic model.

$$\dot{\lambda}_i = \begin{cases} \frac{Q_{yi}(\mathbf{Q}_{ai}^{*})^{\mathrm{T}}\mathbf{N}_i^{-1}\mathbf{K}_{ei}\mathbf{q}_i}{(\mathbf{Q}_{ai}^{*})^{\mathrm{T}}(\mathbf{N}_i^{-1}\mathbf{K}_{ei}+k_{pi}\mathbf{I})\mathbf{Q}_{ai}^{*}} & \text{if} \quad f_i = 0 \quad \text{and} \quad (\mathbf{Q}_{ai}^{*})^{\mathrm{T}}\mathbf{N}_i^{-1}\mathbf{K}_{ei}\dot{\mathbf{q}}_i > 0 \\ 0 & \text{if} \quad f_i < 0 \quad \text{or} \quad (\mathbf{Q}_{ai}^{*})^{\mathrm{T}}\mathbf{N}_i^{-1}\mathbf{K}_{ei}\dot{\mathbf{q}}_i \leq 0 \end{cases}. \tag{A.20}$$

Based on the above derivation, we can know that this bilinear viscoelastoplastic model combined with plastic flow rules and complementary trio can more completely

doi:10.6342/NTU202402645

describe the viscoelastoplastic behavior of the building structure.

A.3 Numerical integration based on internal symmetry

This section aims to address difficult of numerical integration caused by the nonlinear term when the system is in the viscoelastoplastic phase. Firstly, from Eq. (A.9), we know that when the system is in the plastic phase, $f_i = 0$, implying $(\mathbf{Q}^*_{ai})^{\mathrm{T}}\mathbf{Q}^*_{ai} = Q^2_{yi}$. Here, we discuss asymmetric building structures, which means that the stiffness in all directions and the radius of the yield surface can be different. Therefore, the yield surface in the $\mathbf{Q}^*_{ai}$ space can be an ellipse. To solve for $\mathbf{Q}^*_{ai}$, we transform the $\mathbf{Q}^*_{ai}$ into augmented force space. Next, we will proceed with the theoretical derivation of the ith story Minkowski spacetime.

A.3.1 Internal symmetry in Minkowski spacetime

First, we start from Eq. (A.13), which can be rewritten as follows:

$$\dot{\mathbf{Q}}^*_{ai} + k_{pi}\frac{\dot{\lambda}_i}{Q_{yi}}\mathbf{Q}^*_{ai} = \mathbf{N}_i^{-1}\mathbf{K}_{ei}(\dot{\mathbf{q}}_i - \dot{\mathbf{q}}_i^p). \tag{A.21}$$

If the integrating factor as $X_{0i} = \exp(\frac{k_{pi}\lambda_i}{Q_{yi}})$ is found and multiplies by Eq. (A.21) we have:

$$X_{0i}\dot{\mathbf{Q}}^*_{ai} + k_{pi}X_{0i}\frac{\dot{\lambda}_i}{Q_{yi}}\mathbf{Q}^*_{ai} = X_{0i}\mathbf{N}_i^{-1}\mathbf{K}_{ei}(\dot{\mathbf{q}}_i - \dot{\mathbf{q}}_i^p). \tag{A.22}$$

doi:10.6342/NTU202402645

Then, dividing Eq. (A.22) by Q_{yi}, we have:

$$\frac{d}{dt}\left[\frac{X_{0i}\mathbf{Q}_{ai}^{*}}{Q_{yi}}\right]=\frac{X_{0i}}{Q_{yi}}\mathbf{N}_{i}^{-1}\mathbf{K}_{ei}(\dot{\mathbf{q}}_{i}-\dot{\mathbf{q}}_{i}^{p}). \tag{A.23}$$

Beside the formulation of $\dot{\lambda}_i$ in Eq. (A.19),we derive another form of $\dot{\lambda}_i$ for the expoloration of internal stmmetry.Multipling both sides of Eq. (A.21) by $(\mathbf{Q}_{ai}^{*})^{\mathrm{T}}$, we have

$$(\mathbf{Q}_{ai}^{*})^{\mathrm{T}}\dot{\mathbf{Q}}_{ai}^{*}+k_{pi}\frac{\dot{\lambda}_{i}}{Q_{yi}}(\mathbf{Q}_{ai}^{*})^{\mathrm{T}}\mathbf{Q}_{ai}^{*}=(\mathbf{Q}_{ai}^{*})^{\mathrm{T}}\mathbf{N}_{i}^{-1}\mathbf{K}_{ei}(\dot{\mathbf{q}}_{i}-\dot{\mathbf{q}}_{i}^{p}). \tag{A.24}$$

In case of $\dot{\lambda}_i > 0$, we know that $f_i = 0$, $(\mathbf{Q}_{ai}^{*})^{\mathrm{T}}\mathbf{Q}_{ai}^{*} = Q_{yi}^{2}$, and $\dot{f}_i = 0$, $(\mathbf{Q}_{ai}^{*})^{\mathrm{T}}\dot{\mathbf{Q}}_{ai}^{*} = 0$. Substituting them into Eq. (A.24), we get:

$$k_{pi}Q_{yi}\dot{\lambda}_{i}=(\mathbf{Q}_{ai}^{*})^{\mathrm{T}}\mathbf{N}_{i}^{-1}\mathbf{K}_{ei}(\dot{\mathbf{q}}_{i}-\dot{\mathbf{q}}_{i}^{p}). \tag{A.25}$$

If $\frac{(\mathbf{Q}_{ai}^{*})^{\mathrm{T}}\mathbf{N}_{i}^{-1}\mathbf{K}_{ei}(\dot{\mathbf{q}}_{i}-\dot{\mathbf{q}}_{i}^{p})}{k_{pi}} > 0$, then

$$\dot{\lambda}_{i}=\frac{(\mathbf{Q}_{ai}^{*})^{\mathrm{T}}\mathbf{N}_{i}^{-1}\mathbf{K}_{ei}(\dot{\mathbf{q}}_{i}-\dot{\mathbf{q}}_{i}^{p})}{k_{pi}Q_{yi}}. \tag{A.26}$$

Next, differentiating X_{0i} with respect to time yields the following relationship:

$$\frac{d}{dt}\left[X_{0i}\right]=\frac{k_{pi}\dot{\lambda}_{i}}{Q_{yi}}X_{0i}=\frac{X_{0i}}{Q_{yi}}\frac{(\mathbf{Q}_{ai}^{*})^{\mathrm{T}}\mathbf{N}_{i}^{-1}\mathbf{K}_{ei}(\dot{\mathbf{q}}_{i}-\dot{\mathbf{q}}_{i}^{p})}{Q_{yi}}=\frac{[\mathbf{N}_{i}^{-1}\mathbf{K}_{ei}(\dot{\mathbf{q}}_{i}-\dot{\mathbf{q}}_{i}^{p})]^{\mathrm{T}}}{Q_{yi}}X_{0i}\frac{\mathbf{Q}_{ai}^{*}}{Q_{yi}}. \tag{A.27}$$

The augmented force vector is defined by:

$$\mathbf{X}_{i}=\begin{bmatrix}\mathbf{X}_{si}\\ X_{0i}\end{bmatrix}=\begin{bmatrix}X_{0i}\frac{\mathbf{Q}_{ai}^{*}}{Q_{yi}}\\ X_{0i}\end{bmatrix}. \tag{A.28}$$

doi:10.6342/NTU202402645

We refer to it as the (3+1)-dimensional augmented force vector. We now transform the elastoplastic bilinear model to defined in the generalized force space into model within the augmented force space $\mathbf{X}_i$. Combining Eq. (A.23) and Eq. (A.27), we obtain the dynamical system of augmented force under viscoelastoplastic phase as follows:

$$\frac{d}{dt}\begin{bmatrix} \frac{X_{0i}\mathbf{Q}^*_{ai}}{Q_{yi}} \\ X_{0i} \end{bmatrix} = \frac{1}{Q_{yi}}\begin{bmatrix} 0 & \boldsymbol{\eta}_i \\ \boldsymbol{\eta}_i^{\mathrm{T}} & 0 \end{bmatrix}\begin{bmatrix} X_{0i}\frac{\mathbf{Q}^*_{ai}}{Q_{yi}} \\ X_{0i} \end{bmatrix} =: \mathbf{A}_i\mathbf{X}_i, \tag{A.29}$$

where $\boldsymbol{\eta}_i = [\mathbf{N}_i^{-1}\mathbf{K}_{ei}(\dot{\mathbf{q}}_i - \dot{\mathbf{q}}_i^p)]$ and $\mathbf{g}$ is the Minkowski metric as follows:

$$\mathbf{g} = \begin{bmatrix} \mathbf{I} & \mathbf{0} \\ \mathbf{0} & -1 \end{bmatrix}.$$

According to Eq. (A.9), the Minkowski metric $\mathbf{g}$ and Eq. (A.28), we further distinguish between two correspondences

$$\|\mathbf{Q}^*_{ai}\| = Q_{yi} \Longleftrightarrow \mathbf{X}_i\mathbf{g}\mathbf{X}_i = 0,$$

$$\|\mathbf{Q}^*_{ai}\| < Q_{yi} \Longleftrightarrow \mathbf{X}_i\mathbf{g}\mathbf{X}_i < 0.$$

The generalized active force vector in generalized active force space corresponds to an augmented force vector $\mathbf{X}_i$ of Minkowski spacetime $\mathbb{M}^{3+1}$. By using the coordinates, we convert the non-liner model to a system $\dot{\mathbf{X}}_i = \mathbf{A}_i\mathbf{X}_i$, and state matrix $\mathbf{A}_i$ satisfies

$$\mathbf{A}_i^{\mathrm{T}}\mathbf{g} + \mathbf{g}\mathbf{A}_i = \mathbf{0}, \tag{A.30}$$

Therefore, $\mathbf{A}_i$ is an element of the real Lie algebra so(3,1).

In the viscoelastoplastic phase, the solution of Eq. (A.29) can be expressed by the

doi:10.6342/NTU202402645

following augmented force transformation formula:

$$\mathbf{X}_i(t) = \left[\mathbf{G}_i(t)\mathbf{G}_i^{-1}(t_1)\right]\mathbf{X}_i(t_1),$$

where $\mathbf{G}_i(t)$ is the fundamental solution of Eq. (A.29) and it satisfies

$$\dot{\mathbf{G}}_i(t) = \mathbf{A}_i\mathbf{G}_i,$$

$$\mathbf{G}_i(0) = \mathbf{I}_4.$$

Based on the above mentioned property on $\mathbf{G}_i(t)$

$$\mathbf{G}_i^{\mathrm{T}}(t)\mathbf{g}\mathbf{G}_i(t) = \mathbf{g}. \tag{A.31}$$

Hence,the fundamental solution $\mathbf{G}_i(t)$ is an element of Lie algebra so(3,1). In the case of constant vector $\dot{\boldsymbol{\eta}}_i$, $\mathbf{A}_i$ is a constant matrix, and the system Eq. (A.29) become linear. Then the matrix exponent $\exp(\mathbf{A}_i\Delta t)$ can be used to play the role of the fundamental solution $\mathbf{G}_i(t_{k+1}, t_k)$ in the period of t_k to $t_{k+1} = t_k + \Delta t$, i.e.

$$\mathbf{G}(t_{k+1}, t_k) = \exp(\mathbf{A}_i\Delta t) = \begin{bmatrix} \mathbf{I}_n + \frac{a_i - 1}{\|\boldsymbol{\eta}_i(t_k)\|^2}\boldsymbol{\eta}_i(t_k)\boldsymbol{\eta}_i^{\mathrm{T}}(t_k) & \frac{b_i}{\|\boldsymbol{\eta}_i(t_k)\|}\boldsymbol{\eta}_i(t_k) \\ \frac{b_i}{\|\boldsymbol{\eta}_i(t_k)\|}\boldsymbol{\eta}_i^{\mathrm{T}}(t_k) & a_i \end{bmatrix}, \tag{A.32}$$

where

$$a_i = \cosh\left(\frac{\|\boldsymbol{\eta}_i(t_k)\|}{Q_{yi}}\Delta t\right), \tag{A.33}$$

$$b_i = \sinh\left(\frac{\|\boldsymbol{\eta}_i(t_k)\|}{Q_{yi}}\Delta t\right). \tag{A.34}$$

doi:10.6342/NTU202402645

Substituting the above expression into Eq. (A.29) and Eq. (A.32), we obtain:

$$\mathbf{X}_i(t_{k+1}) = \mathbf{G}_i(t_{k+1}, t_k)\mathbf{X}_i(t_k), \tag{A.35}$$

$$\begin{bmatrix} \frac{X_{0i}(t_{k+1})\mathbf{Q}^*_{ai}(t_{k+1})}{Q_{yi}} \\ X_{0i}(t_{k+1}) \end{bmatrix} = \begin{bmatrix} \mathbf{I}_n + \frac{a_i-1}{\|\boldsymbol{\eta}_i(t_k)\|^2}\boldsymbol{\eta}_i(t_k)\boldsymbol{\eta}_i^{\mathrm{T}}(t_k) & \frac{b_i}{\|\boldsymbol{\eta}_i(t_k)\|}\boldsymbol{\eta}_i(t_k) \\ \frac{b_i}{\|\boldsymbol{\eta}_i(t_k)\|}\boldsymbol{\eta}_i^{\mathrm{T}}(t_k) & a_i \end{bmatrix} \begin{bmatrix} X_{0i}(t_k)\frac{\mathbf{Q}^*_{ai}(t_k)}{Q_{yi}} \\ X_{0i}(t_k) \end{bmatrix}. \tag{A.36}$$

From Eq. (A.36), we have obtained the closed-form solution for $\mathbf{Q}_{ai}$ as follows:

$$\mathbf{Q}_{ai}(t_{k+1}) = \frac{X_{0i}(t_{k+1})\mathbf{Q}^*_{ai}(t_{k+1})}{Q_{yi}} \frac{Q_{yi}}{X_{0i}(t_{k+1})}. \tag{A.37}$$

In the above derivation, we utilized the transformation of $\mathbf{Q}^*_{ai}$ space to augmented force space and employed the Group-preserving integration (GPI) method to derive the closed-form solution for $\mathbf{Q}^*_{ai}$. That will be advantageous for solving the viscoelastoplastic-phase system. In the next section, we will represent the two-phase system in the form of state-space representation, it will become clearer why we need to solve for $\mathbf{Q}^*_{ai}$ and how we address the nonlinear behavior in the viscoelastoplastic-phase.

A.4 Total state-space representation

We can divide the entire system into an viscoelastic phase and multiple viscoelasto-plastic phases. In this section, we use the state-space representation method to represent the system, which is a very advantageous tool for analyzing dynamic systems. Furthermore, when the system enters the viscoelastic-plastic stage, we utilize the closed-form solution, $\mathbf{Q}^*_a$, derived in Section A.3, and combine it with the state-space representation

doi:10.6342/NTU202402645

method for analysis. Below, we will conduct the theoretical derivation of the system's state-space representation method. From the equation, we can derive the equation of motion for the ith story as follows:

$$\mathbf{m}_{si}\ddot{\mathbf{q}}_i + \mathbf{Q}_i - \mathbf{Q}_{i+1} = \mathbf{F}_i,$$

where $i = 1, 2, 3..., n$ and $\mathbf{Q}_{n+1} = \mathbf{0}$. Next, we define the momentum equation for the system as follows:

$$\mathbf{P}_{si} = \mathbf{m}_{si}\dot{\mathbf{q}}_i. \tag{A.38}$$

We differentiate Eq. (A.38) wich represent to the time and obtain::

$$\dot{\mathbf{P}}_{si} = \mathbf{m}_{si}\ddot{\mathbf{q}}_i. \tag{A.39}$$

Substituting Eq. (A.39) into the equation of motion Eq. (A.1), we get:

$$\dot{\mathbf{P}}_{si} = -\mathbf{Q}_i + \mathbf{Q}_{i+1} + \mathbf{F}_i. \tag{A.40}$$

Next, we will derive the state-space representation for the system.

A.4.1 The ith story is viscoelastic-phase system

If the i-th story is a viscoelastic-phase system, we first select the state parameters as $\mathbf{P}_{si}$, $\mathbf{q}_i$, and $\mathbf{Q}_i$. First, we substitute Eq. (A.5) into Eq. (A.3) to obtain $\mathbf{Q}_i = \mathbf{K}_{ei}\mathbf{q}_i^e + \mathbf{C}_i\dot{\mathbf{q}}_i$, and then we differentiate it as follows:

$$\dot{\mathbf{Q}}_i = \mathbf{K}_{ei}\dot{\mathbf{q}}_i^e + \mathbf{C}_i\ddot{\mathbf{q}}_i. \tag{A.41}$$

doi:10.6342/NTU202402645

From Eq. (A.2), we know that $\dot{\mathbf{q}}_i^e = \dot{\mathbf{q}}_i - \dot{\mathbf{q}}_i^p$. Substituting this into Eq. (A.41), we get:

$$\dot{\mathbf{Q}}_i = \mathbf{K}_{ei}(\dot{\mathbf{q}}_i - \dot{\mathbf{q}}_i^p) + \mathbf{C}_i\ddot{\mathbf{q}}_i. \tag{A.42}$$

Since $\dot{\mathbf{q}}_i^p = \mathbf{0}$ from Eq. (A.8), Eq. (A.42) can be rewritten as follows:

$$\dot{\mathbf{Q}}_i = \mathbf{K}_{ei}\dot{\mathbf{q}}_i + \mathbf{C}_i\ddot{\mathbf{q}}_i. \tag{A.43}$$

From the equation of motion, we know that $\ddot{\mathbf{q}}_i = -\mathbf{m}_{si}^{-1}[-\mathbf{Q}_i + \mathbf{Q}_{i+1} + \mathbf{F}_i]$, and from Eq. (A.38), we know that $\dot{\mathbf{q}}_i = \mathbf{m}_{si}^{-1}\mathbf{P}_{si}$. Therefore, Eq. (A.43) can be rewritten as follows:

$$\dot{\mathbf{Q}}_i = \mathbf{K}_{ei}\mathbf{m}_{si}^{-1}\mathbf{P}_{si} + \mathbf{C}_i\mathbf{m}_{si}^{-1}\left[-\mathbf{Q}_i + \mathbf{Q}_{i+1} + \mathbf{F}_i\right]. \tag{A.44}$$

In Eq. (A.44), if the $(i+1)$th-story is viscoelastic-phase, then $\mathbf{Q}_{i+1}$ is as follows:

$$\mathbf{Q}_{i+1} = \mathbf{Q}_{i+1} \tag{A.45}$$

In Eq. (A.44), if the $(i+1)$th-story is viscoelastoplastic-phase, then $\mathbf{Q}_{i+1}$ is as follows:

$$\mathbf{Q}_{i+1} = \mathbf{Q}_{a(i+1)} + \mathbf{Q}_{b(i+1)} + \mathbf{C}_{(i+1)}\mathbf{m}_{\mathrm{s(i+1)}}^{-1}\mathbf{P}_{\mathrm{s}(i+1)} \tag{A.46}$$

A.4.2 The ith story is viscoelastoplastic-phase system

If the i-th story is a viscoelastoplastic-phase system, we first select the state parameters as $\mathbf{P}_{si}$, $\mathbf{q}_i$, and $\mathbf{Q}_{bi}$.First, from Eq. (A.3) and Eq. (A.4), we know that $\mathbf{Q}_i = \mathbf{Q}_{ai} + \mathbf{Q}_{bi} + \mathbf{C}_i\dot{\mathbf{q}}_i$. We substitute this into Eq. (A.40) as follows:

$$\dot{\mathbf{P}}_{si} = -\mathbf{Q}_{ai} - \mathbf{Q}_{bi} - \mathbf{C}_i\dot{\mathbf{q}}_i + \mathbf{Q}_{i+1} + \mathbf{F}_i. \tag{A.47}$$

doi:10.6342/NTU202402645

We know from Eq. (A.47) that $\dot{\mathbf{q}}_i = \mathbf{m}_{si}^{-1}\mathbf{P}_{si}$. Substituting this into Eq. (A.40), we get:

$$\dot{\mathbf{P}}_{si} = -\mathbf{Q}_{ai} - \mathbf{Q}_{bi} - \mathbf{C}_i\mathbf{m}_{si}^{-1}\mathbf{P}_{si} + \mathbf{Q}_{i+1} + \mathbf{F}_i. \tag{A.48}$$

In Section A.3.1, we have already solved for the closed form of $\mathbf{Q}_{ai}^*$, so $\mathbf{Q}_{ai}$, $\dot{\mathbf{Q}}_{ai}$ and $\dot{\mathbf{Q}}_{ai}^*$ is known. From Eq. (A.12), we can know $\dot{\mathbf{q}}_i^p$ as follows:

$$\dot{\mathbf{q}}_i^p = [\mathbf{K}_{pi} + \mathbf{K}_{ei}]^{-1}\mathbf{K}_{ei}\dot{\mathbf{q}}_i - [\mathbf{K}_{pi} + \mathbf{K}_{ei}]^{-1}\dot{\mathbf{Q}}_{ai}. \tag{A.49}$$

We can also know $\dot{\mathbf{Q}}_{bi}$ from Eq. (A.6) as follows:

$$\begin{aligned}\dot{\mathbf{Q}}_{bi} &= \mathbf{K}_{pi}[\mathbf{K}_{pi} + \mathbf{K}_{ei}]^{-1}\mathbf{K}_{ei}\dot{\mathbf{q}}_i - \mathbf{K}_{pi}[\mathbf{K}_{pi} + \mathbf{K}_{ei}]^{-1}\dot{\mathbf{Q}}_{ai}, \\ &= \mathbf{K}_{pi}[\mathbf{K}_{pi} + \mathbf{K}_{ei}]^{-1}\mathbf{K}_{ei}\mathbf{m}_{si}^{-1}\mathbf{P}_{si} - \mathbf{K}_{pi}[\mathbf{K}_{pi} + \mathbf{K}_{ei}]^{-1}\dot{\mathbf{Q}}_{ai}.\end{aligned} \tag{A.50}$$

In Eq. (A.48), if the $(i+1)$th-story is viscoelastic-phase, then $\mathbf{Q}_{i+1}$ is as follows:

$$\mathbf{Q}_{i+1} = \mathbf{Q}_{i+1} \tag{A.51}$$

In Eq. (A.48), if the $(i+1)$th-story is viscoelastoplastic-phase, then $\mathbf{Q}_{i+1}$ is as follows:

$$\mathbf{Q}_{i+1} = \mathbf{Q}_{a(i+1)} + \mathbf{Q}_{b(i+1)} + \mathbf{C}_{(i+1)}\mathbf{m}_{s(i+1)}^{-1}\mathbf{P}_{s(i+1)} \tag{A.52}$$

doi:10.6342/NTU202402645